Development of picture-change corrected relativistic quantum chemical methods and its applications to homogeneous catalytic reactions

描像変化補正による相対論的量子化学手法の開発と均一系触媒反応への応用

February, 2024

Chinami TAKASHIMA
髙島　千波

Development of picture-change corrected relativistic quantum chemical methods and its applications to homogeneous catalytic reactions

描像変化補正による相対論的量子化学手法の開発と均一系触媒反応への応用

February, 2024

Waseda University Graduate School of Advanced Science and Engineering

Department of Chemistry and Biochemistry, Research on Electronic State Theory

Chinami TAKASHIMA
髙島　千波

Table of contents

List of abbreviations

2c	Two-component
4c	Four-component
AO	Atomic orbital
CAM	Coulomb-attenuating method
CC	Coupled cluster
CCSD	Coupled cluster with singles and doubles
CCSD(T)	CCSD with perturbative triples
CD	Cholesky decomposition
CPU	Central processing unit
DC	Divide and conquer
DFT	Density functional theory
ERI	Electron repulsion integral
FON	Fractional occupation number
GAMESS	General Atomic and Molecular Electronic Structure System
HFx	Hartree–Fock exchange
HOMO	Highest occupied molecular orbital
IOTC	Infinite-order two-component
$Ir(ppy)_3$	Tris-(2-phenylpyridinato) iridium (III)
IRC	Intrinsic reaction coordinate
KS	Kohn–Sham
LC	Long-range corrected
LRD	Local response dispersion
LUD	Lower-upper decomposition
LUMO	lowest unoccupied molecular orbital
LUT	Local unitary transformation
MO	Molecular orbital
MP2	Second-order Møller–Plesset
NBO	Natural bond orbital
NESC	Normalized elimination of the small component
NMR	Nuclear magnetic resonance
OEI	One-electron integral
PBF	Primitive basis function
PCC	Picture change correction, picture-change corrected
PCE	Picture change error
RS	Range-separated
(*S*)-BINAP	(*S*)-2,2′-bis(diphenylphosphino)-1,1′-binaphthyl
(*S*)-SEGPHOS	(*S*)- 5,5'-bis(diphenylphosphino)-4,4'-bi-1,3-benzodioxole
SCF	Self-consistent field
SIE	Self-interaction error
TEI	Two-electron integral
TS	Transition state
vdW	van der Waals
X2C	Exact two-component

Chapter 1 General introduction

Quantum Chemistry predicts molecular properties and chemical reactions by describing electronic states based on the Schrödinger equation developed in 1926. Recent advances of computers and software facilitate the use of quantum chemical calculations not only by theoretical chemists but also by experimental chemists. Particularly, the DFT has become the most familiar methods due to its good balance between computational costs and accuracy.

Relativistic effects are essential when simulating chemical properties of compounds including higher row elements in the periodic table. The Schrödinger equation, which is in the nonrelativistic framework, describes relativistic effects by pseudopotential or effective core potential methods, where inner-shell electrons are represented by potential with parameters. Relativistic treatment of all electrons is possible by using the Dirac equation, which satisfies the requirements of the special relativity proposed in 1928,[1] as a fundamental equation. The 4c theory, which solves the Dirac equation directly, gives highly accurate results, while it requires complicated calculations due to explicitly treatments of both positive and negative-energy states. The 2c theory extracts or decouples the positive-energy state from the 4c Hamiltonian and uses the positive-energy states as an electronic Hamiltonian. The 2c Hamiltonian is proved to be equivalent to the 4c Hamiltonian under the no-pair approximation that assumes particles and antiparticles do not interact. The IOTC Hamiltonian, which is one of exact two-component Hamiltonians, was proposed for one-electron Hamiltonian in 2002,[2] followed by the extension to many-electron systems in 2008.[3] Furthermore, the LUT scheme, which is an accurate and efficient method based on the IOTC Hamiltonian, was developed in 2012.[4,5]

In the 2c theory, the pictures of wave functions change along the transformation of

Hamiltonian from 4c to 2c. Without consideration of the operators with respect to the 2c wave functions, the corresponding expectation values involve the error, namely, PCE. From a viewpoint of the transformation of the one-electron Dirac Hamiltonian, the error due to neglecting the PCC of the two-electron operator can also be called PCE. Most quantum chemical programs widely used today, cannot perform the PCC methods for expectation values. However, in 2017, it was pointed out that the PCE of electron density, which is the fundamental variable of DFT, cannot be ignored.[6]

Against these backgrounds, this thesis attempts to extend the availability and applicability of PCC methods based on the IOTC Hamiltonian by developing novel theories and publishing to de facto standard quantum chemical program. Besides, the relativistic quantum chemistry is applied to the analysis of transition metal catalysts containing higher-row elements. This thesis consists of nine chapters including this chapter as the general introduction. The remainder of this thesis is as follows.

Chapter 2 summarizes the theoretical background of the 2c theory: Dirac equation, PCC of operators, IOTC Hamiltonian, and LUT scheme.

Chapters 3 and 4 explain the acceleration methods for TEIs, which is a bottleneck of IOTC Hamiltonian. IOTC Hamiltonian for two-electron term requires evaluation and unitary transformation of several types of TEIs. The computational costs for evaluation and unitary transformation of TEIs are proportional to fourth and fifth power of system size, respectively.

Chapter 3 describes the efficient algorithm for evaluation of TEIs based on the matrix decomposition. TEIs can be regarded as a matrix by labeling them with pairs of orbitals belonging to two electrons (distribution). Utilizing the symmetric characteristics of nonrelativistic ERIs, the efficient algorithm based on the CD was proposed in 2003. On the other hand, TEIs for spin-free IOTC Hamiltonian are categorized into three types; two are symmetric and one is asymmetric. In this chapter, CD is applied to two types of symmetric

TEIs and LUD of asymmetric TEIs is formulated and implemented. The proposed method can reduce the number of calculation while controlling the accuracy by introducing threshold to truncate decomposition.

Chapter 4 proposes a more efficient algorithm for the LUT scheme, which is assisted by database of relativistic TEIs. LUT for TEI calculates only one-center integrals with relativistic Hamiltonian and treats multi-center integrals as in the nonrelativistic method. Focusing on the fact that the values of atomic-center TEIs depend only on the elemental species and basis function, independent of the molecular structures, this chapter constructs the database of atomic center TEIs. In practical calculations, the proposed algorithm reads the integral values from the database avoiding the explicit evaluation and unitary transformation of TEIs. Numerical assessments show that the proposed algorithm enables the constant computational costs for TEIs regardless of the system size. Furthermore, calculations of transition metal complexes by using the proposed algorithm can be performed at similar computational costs to nonrelativistic cases.

Chapter 5 explains the RS-DFT based on the IOTC Hamiltonian. RS-DFT separates the two-electron operator into long- and short-range terms. LC-DFT, which is one of the RS DFT, calculates exchange energy as long-range HFx integrals and short-range exchange functional. This chapter formulates and implements the IOTC transformation with and without LUT scheme for separated two-electron operators. Application of this method to the potential energy curve of Rn dimer indicates the importance of consideration of relativistic effects and long-range correction simultaneously.

Chapter 6 examines the PCE in the FON states based on the 2c DFT. By adding HFx into exchange energy, the HOMO of noble gas atoms, Ne to Rn, is approximately constant with respect to changes in the occupation number, which satisfies the physical requirement. The PCE is small in valence orbital. On the other hand, 1s orbital is not constant with respect to the occupation number and requires large ratio of HFx. The PCE is not negligible

in higher row elements such as Rn. Furthermore, PCC influences on the delocalization error, which is represented by the total energy deviation from the behavior of the exact energy.

Chapter 7 explains the implementation of the PCC methods into the public version of GAMESS program, which is a program package developed by researchers around the world and distributed free of charge. The IOTC and LUT-IOTC Hamiltonians for one-electron operator have been implemented so far into GAMESS. This chapter describes the implementation of the PCC methods for two-electron and density operators based on the IOTC Hamiltonian with and without the LUT scheme. The LUT-IOTC Hamiltonian for one- and two-electron operators is also utilized for electron correlation methods such as MP2, CCSD, and CCSD(T), as well as the linear-scaling DC method.

Chapter 8 elucidates that the relativistic effects play a key role in C-H activation using cationic iridium catalysts. Experiments reported that the cationic Ir(I)-diphosphine catalysts causes the deuterium substitution of *N*-phenylbenzamide, whereas Rh(I)-diphosphine catalysts are scarcely effective. In this chapter, energy diagrams by relativistic calculations show large difference in reaction energies between Ir and Rh, while nonrelativistic results show the same tendency in Ir and Rh. This is due to the considerably stabilized product rationalized by stronger interaction in Ir–H and Ir–C bonds by relativistic self-consistent *d*-orbital expansion of Ir, followed by the relatively low reaction barrier.

Chapter 9 refers to general conclusion and perspectives on the field of this study.

References

1. P.A.M. Dirac, *Proc. R. soc. Lond. Ser. A-Contain. Pap. Math. Phys. Character* **117**, 610 (1928).

2. M. Barysz and A.J. Sadlej, *J. Chem. Phys.* **116**, 2696 (2002).

3. J. Seino and M. Hada, *Chem. Phys. Lett.* **461**, 327 (2008).

4. J. Seino and H. Nakai, *J. Chem. Phys.* **136**, 244102 (2012).

5. J. Seino and H. Nakai, *J. Chem. Phys.* **137**, 144101 (2012).

6. T. Oyama, Y. Ikabata, J. Seino, and H. Nakai, *Chem. Phys. Lett.* **680**, 37 (2017).

Chapter 2 Theoretical backgrounds

This chapter explains several methods to incorporate relativistic effects into quantum chemistry. The pseudopotentials[1] are used based on the nonrelativistic Schrödinger equation,[2] while it cannot describe all electrons explicitly. The Dirac equation[3] satisfies the relativistic requirements, thus exact solutions for all electron calculations are obtained. The direct solution of the Dirac equation is termed the 4c theory. The 4c theory treats both positive- and negative-energy states, which are related to electronic and positronic states. The 2c theory transforms the Dirac Hamiltonian and only treats positive-energy states, namely, electronic states, which are important for chemistry. With these backgrounds, this chapter briefly describes the theoretical backgrounds: Dirac Hamiltonian, the PCC of expectation values, and IOTC Hamiltonian.

2.1 Dirac Hamiltonian

Special relativity[4] demands that the laws of physics have the same expressions in all the inertial frames of reference. Space and time must be treated equivalently in coordinate transformation, termed the Lorentz invariance. The Schrödinger equation, the fundamental equation of quantum mechanics, does not satisfy the Lorentz invariance since it is a second-order derivative for space and a first-order derivative for time. Equation based on the quantum electrodynamics fully satisfies the Lorentz invariance although the effects of electrodynamics are negligibly small in the electronic states in molecules.

In the quantum chemistry, the fundamental equation is the Dirac equation, which satisfies the Lorentz invariance only for electron motion. The Dirac equation is a first-order derivative for both time and space as follows:

$$\boldsymbol{H}_4^{\mathrm{D}}\Psi_4 = E\Psi_4, \tag{2.1.1}$$

where Ψ_4, E, and $\boldsymbol{H}_4^{\mathrm{D}}$ is wavefunction, energy, and one-particle operator termed the Dirac Hamiltonian, respectively. The explicit formula of Dirac Hamiltonian is a 4×4 matrix as follows:

$$\boldsymbol{H}_4^{\mathrm{D}} = \begin{pmatrix} \boldsymbol{V} & c\boldsymbol{\sigma}\cdot\boldsymbol{p} \\ c\boldsymbol{\sigma}\cdot\boldsymbol{p} & \boldsymbol{V} - 2c^2\mathbf{1}_2 \end{pmatrix}, \tag{2.1.2}$$

with external potential $\boldsymbol{V}$, the speed of light c, momentum operator $\boldsymbol{p}$, Pauli matrix $\boldsymbol{\sigma}$. and the n×n identity matrix $\mathbf{1}_n$. The Dirac Hamiltonian inherently includes spin. The solution of Dirac Hamiltonian consists of positive- and negative-energy states as the large and small components.

Basically, the Dirac equation is solved by the 4c theory. As a 4c Hamiltonian, the one-electron Dirac Hamiltonian is combined with a two-electron operator such as the Coulomb interaction[5] representing instantaneous electron-electron repulsion,

$$\boldsymbol{G}_{ij}^{\mathrm{C}} = \frac{1}{r_{ij}}\mathbf{1}_4, \tag{2.1.3}$$

the Gaunt[6] operator including internal magnetic interaction,

$$\boldsymbol{G}_{ij}^{\mathrm{G}} = -\frac{\boldsymbol{\alpha}_i\cdot\boldsymbol{\alpha}_j}{r_{ij}}\mathbf{1}_4, \tag{2.1.4}$$

and the Breit operator[7] adding retardant interaction to the Gaunt operator,

$$\boldsymbol{G}_{ij}^{\mathrm{B}} = -\frac{1}{r_{ij}}\left\{\boldsymbol{\alpha}_i\cdot\boldsymbol{\alpha}_j + \frac{\left(\boldsymbol{\alpha}_i\cdot r_{ij}\right)\left(\boldsymbol{\alpha}_j\cdot r_{ij}\right)}{r_{ij}^{\,2}}\right\}\mathbf{1}_4. \tag{2.1.5}$$

Here, r_{ij} is the distance between two electrons, and $\boldsymbol{\alpha}_l$ represents the following matrix,

$$\boldsymbol{\alpha}_l = \begin{pmatrix} \mathbf{0}_2 & \boldsymbol{\sigma}_l \\ \boldsymbol{\sigma}_l & \mathbf{0}_2 \end{pmatrix} \qquad (l = x, y, z), \tag{2.1.6}$$

where $\mathbf{0}_2$ is a 2×2 zero matrix. Due to the dimension of the Dirac Hamiltonian, the wavefunction Ψ_4 have four components ψ_1, ψ_2, ψ_3, and ψ_4 as

$$\Psi_4 = \begin{pmatrix} \psi_1 \\ \psi_2 \\ \psi_3 \\ \psi_4 \end{pmatrix} = \begin{pmatrix} \psi_\alpha^L \\ \psi_\beta^L \\ \psi_\alpha^S \\ \psi_\beta^S \end{pmatrix}, \tag{2.1.7}$$

where ψ^L and ψ^S are large and small spinors, which mainly correspond to electronic and positronic states, respectively, with α and β spin states. Although the 4c theory satisfies the chemical accuracy, it suffers from several problems, such as large computational costs and variational collapse due to the existence of negative-energy states.

2.2 2c theory and PCC

An alternative approach to solve the Dirac equation is the 2c theory that eliminates small components or decouples the positive- and negative-energy states in the 4c Hamiltonian. The 2c Hamiltonians for one-electron system, such as the Foldy–Woutheysen Hamiltonian,[8] Douglas–Kroll–Hess Hamiltonian,[9–13] regular approximation,[14,15] and normalized elimination of the small component method,[16] have been widely studied. The accuracy and computational costs of 2c Hamiltonians depend on the degree of elimination or separation of the negative-energy state. X2C[17–21] and IOTC[22] Hamiltonians, which exactly decouple positive- and negative-energy states by unitary transformation in one-electron system, are proved to be equivalent to the 4c Dirac Hamiltonian under no-pair approximation[23] that does not consider the explicit positron–electron coupling. Some of these one-electron Hamiltonians are available for many-electron system by considering the unitary transformation of the two-electron operator simultaneously.[24–28]

When considering the expectation values in 2c theory, PCC of operators along the transformation of the Hamiltonian must be considered. The PCC based on the unitary transformation[29] is explained here. The 4c Dirac Hamiltonian is separated into positive- and negative-energy states, $\boldsymbol{h}_2^+$ and $\boldsymbol{h}_2^-$, by block-diagonalization as follows:

$$\boldsymbol{U}^{\dagger}\boldsymbol{H}_4^{\mathrm{D}}\boldsymbol{U} \approx \begin{pmatrix} \boldsymbol{h}_2^{+} & \boldsymbol{0}_2 \\ \boldsymbol{0}_2 & \boldsymbol{h}_2^{-} \end{pmatrix}. \tag{2.2.1}$$

As mentioned above, X2C and IOTC Hamiltonians completely separate $\boldsymbol{h}_2^{+}$ and $\boldsymbol{h}_2^{-}$, thus the right- and left-hand sides of Eq. (2.2.1) are equivalent. $\boldsymbol{h}_2^{+}$ is used as the electronic Hamiltonian. The 2c electronic wavefunction Ψ_2^{+} is determined as the solution of Eq. (2.2.2):

$$\begin{pmatrix} \boldsymbol{h}_2^{+} & \boldsymbol{0}_2 \\ \boldsymbol{0}_2 & \boldsymbol{h}_2^{-} \end{pmatrix} \begin{pmatrix} \Psi_2^{+} \\ 0 \end{pmatrix} = E \begin{pmatrix} \Psi_2^{+} \\ 0 \end{pmatrix}. \tag{2.2.2}$$

Multiplying $\boldsymbol{U}$ from the left of both sides of Eq. (2.2.2), the following equation is obtained:

$$\boldsymbol{H}_4^{\mathrm{D}}\boldsymbol{U} \begin{pmatrix} \Psi_2^{+} \\ 0 \end{pmatrix} = E\boldsymbol{U} \begin{pmatrix} \Psi_2^{+} \\ 0 \end{pmatrix}. \tag{2.2.3}$$

Here, Eq. (2.2.3) is none other than Eq. (2.1.1). Therefore, the following relation between 4c and 2c wavefunctions is established:

$$\Psi_4 = \boldsymbol{U} \begin{pmatrix} \Psi_2^{+} \\ 0 \end{pmatrix}. \tag{2.2.4}$$

The expectation values of arbitrary 4c operators $\boldsymbol{X}$ are represented as

$$\langle X \rangle = \langle \Psi_4 | \boldsymbol{X} | \Psi_4 \rangle, \tag{2.2.5}$$

where

$$\boldsymbol{X} = \begin{pmatrix} \boldsymbol{X}_{11} & \boldsymbol{X}_{12} \\ \boldsymbol{X}_{21} & \boldsymbol{X}_{22} \end{pmatrix}. \tag{2.2.6}$$

According to Eqs. (2.2.4) and (2.2.5), the expectation values of 4c and 2c pictures are related by the following equation:

$$\begin{aligned}\left\langle \Psi_4 \middle| \boldsymbol{X} \middle| \Psi_4 \right\rangle &= \left\langle \Psi_2^+ \quad 0 \middle| \boldsymbol{U}^\dagger \boldsymbol{X} \boldsymbol{U} \middle| \begin{matrix} \Psi_2^+ \\ 0 \end{matrix} \right\rangle \\ &= \left\langle \Psi_2^+ \quad 0 \middle| \begin{pmatrix} \left[\boldsymbol{U}^\dagger \boldsymbol{X} \boldsymbol{U}\right]_{11} & \left[\boldsymbol{U}^\dagger \boldsymbol{X} \boldsymbol{U}\right]_{12} \\ \left[\boldsymbol{U}^\dagger \boldsymbol{X} \boldsymbol{U}\right]_{21} & \left[\boldsymbol{U}^\dagger \boldsymbol{X} \boldsymbol{U}\right]_{22} \end{pmatrix} \middle| \begin{matrix} \Psi_2^+ \\ 0 \end{matrix} \right\rangle \\ &= \left\langle \Psi_2^+ \middle| \left[\boldsymbol{U}^\dagger \boldsymbol{X} \boldsymbol{U}\right]_{11} \middle| \Psi_2^+ \right\rangle . \end{aligned} \tag{2.2.7}$$

Here, the pictures of operators are changed from 4c picture $\boldsymbol{X}$ to 2c picture $[\boldsymbol{U}^\dagger \boldsymbol{X} \boldsymbol{U}]_{11}$. The PCEs are occasionally not negligible in chemical and physical properties, thus PCC by the formula in the last line of Eq (2.2.7) is necessary. However, calculations that ignore the PC are practically performed by using $\boldsymbol{X}_{11}$ instead of $[\boldsymbol{U}^\dagger \boldsymbol{X} \boldsymbol{U}]_{11}$. PCE for the expectation value of $\boldsymbol{X}$ is defined as follows:

$$\left\langle \Psi_2^+ \middle| \left[\boldsymbol{U}^\dagger \boldsymbol{X} \boldsymbol{U}\right]_{11} \middle| \Psi_2^+ \right\rangle - \left\langle \Psi_2^+ \middle| \boldsymbol{X}_{11} \middle| \Psi_2^+ \right\rangle . \tag{2.2.8}$$

2.3 IOTC Hamiltonian

As mentioned in Subsection 2.2, the 2c theory requires the comprehensive transformations that cover other operators as well as the one-electron Dirac Hamiltonian. This thesis uses IOTC Hamiltonian, one of the most accurate 2c Hamiltonian. This subsection explains the IOTC transformation of one-electron Dirac Hamiltonian, the extension of IOTC Hamiltonian to the two-electron operator, and treatment of density operator.

2.3.1 One-electron operator

IOTC transformation of the Dirac Hamiltonian is performed by a two-step unitary transformation,

$$\boldsymbol{U} = \boldsymbol{U}_0 \boldsymbol{U}_1 . \tag{2.3.1}$$

The first step is the free-particle Foldy–Wouthuysen transformation,

$$\boldsymbol{U}_0 = \begin{pmatrix} K\mathbf{1}_2 & \alpha K\boldsymbol{B} \\ \alpha K\boldsymbol{B} & -K\mathbf{1}_2 \end{pmatrix}, \tag{2.3.2}$$

where α, K, and B are represented as

$$\alpha = \frac{1}{c},\ K = \sqrt{\frac{e_p + 1}{2e_p}},\ \boldsymbol{B} = b\boldsymbol{\sigma}\cdot\boldsymbol{p},\ b = \frac{1}{e_p + 1},\ e_p = \sqrt{1 + \alpha^2 p^2}\ , \tag{2.3.3}$$

with the speed of light c and momentum operator $\boldsymbol{p}$. $\boldsymbol{U}_0$ is defined to block-diagonalize Dirac Hamiltonian for free particle i.e., the electron is free from the external potential $\boldsymbol{V}$ ($\boldsymbol{V}$ = $\mathbf{0}$). When $\boldsymbol{V}$ is not equal to $\mathbf{0}$, the Dirac Hamiltonian is transformed as

$$\begin{aligned} \boldsymbol{H}_1 &= \boldsymbol{U}_0^{\dagger}\boldsymbol{H}_4^{\mathrm{D}}\boldsymbol{U}_0 \\ &= \begin{pmatrix} K\mathbf{1}_2 & \alpha K\boldsymbol{B} \\ \alpha K\boldsymbol{B} & -K\mathbf{1}_2 \end{pmatrix} \begin{pmatrix} \boldsymbol{V} & c\boldsymbol{\sigma}\cdot\boldsymbol{p} \\ c\boldsymbol{\sigma}\cdot\boldsymbol{p} & \boldsymbol{V} - 2c^2\mathbf{1}_2 \end{pmatrix} \begin{pmatrix} K\mathbf{1}_2 & \alpha K\boldsymbol{B} \\ \alpha K\boldsymbol{B} & -K\mathbf{1}_2 \end{pmatrix}, \end{aligned} \tag{2.3.4}$$

by using $\boldsymbol{U}_0 = \boldsymbol{U}_0^{\dagger}$. The unitary transformation $\boldsymbol{U}_1$ is defined to block-diagonalize $\boldsymbol{H}_1$ as follows:

$$\boldsymbol{H}^{\mathrm{IOTC}} = \boldsymbol{U}_1^{\dagger}\boldsymbol{H}_1\boldsymbol{U}_1 = \begin{pmatrix} \boldsymbol{h}_2^{+} & \mathbf{0}_2 \\ \mathbf{0}_2 & \boldsymbol{h}_2^{-} \end{pmatrix}. \tag{2.3.5}$$

The explicit formula of $\boldsymbol{U}_1$ is

$$\boldsymbol{U}_1 = \begin{pmatrix} \left(\mathbf{1}_2 + \boldsymbol{Y}\boldsymbol{Y}^{\dagger}\right)^{-1/2} & \left(\mathbf{1}_2 + \boldsymbol{Y}\boldsymbol{Y}^{\dagger}\right)^{-1/2}\boldsymbol{Y}^{\dagger}p^{-1}\boldsymbol{\sigma}\cdot\boldsymbol{p} \\ -\left(\mathbf{1}_2 + \boldsymbol{Y}\boldsymbol{Y}^{\dagger}\right)^{-1/2}\boldsymbol{\sigma}\cdot\boldsymbol{p}p^{-1}\boldsymbol{Y} & -\left(\mathbf{1}_2 + \boldsymbol{Y}\boldsymbol{Y}^{\dagger}\right)^{-1/2} \end{pmatrix}. \tag{2.3.6}$$

$\boldsymbol{Y}$ is the operator that is determined by solving non-linear equation

$$\begin{aligned} e_p\boldsymbol{Y} + \boldsymbol{Y}e_p = {} & \alpha^3\left(pKb\boldsymbol{V}K - p^{-1}K\boldsymbol{\sigma}\cdot\boldsymbol{p}\boldsymbol{V}\boldsymbol{\sigma}\cdot\boldsymbol{p}bK\right) \\ & + \alpha^2\left(p^{-1}K\boldsymbol{\sigma}\cdot\boldsymbol{p}\boldsymbol{V}\boldsymbol{\sigma}\cdot\boldsymbol{p}p^{-1}K\boldsymbol{Y} - \boldsymbol{Y}K\boldsymbol{V}K\right) \\ & + \alpha^4\left(pKb\boldsymbol{V}bKp\boldsymbol{Y} - \boldsymbol{Y}Kb\boldsymbol{\sigma}\cdot\boldsymbol{p}\boldsymbol{V}\boldsymbol{\sigma}\cdot\boldsymbol{p}bK\right) \\ & + \alpha^3\boldsymbol{Y}\left(Kb\boldsymbol{\sigma}\cdot\boldsymbol{p}\boldsymbol{V}\boldsymbol{\sigma}\cdot\boldsymbol{p}Kp^{-1} - K\boldsymbol{V}Kbp\right)\boldsymbol{Y}, \end{aligned} \tag{2.3.7}$$

numerically. One-electron Hamiltonian $\boldsymbol{h}_2^{+}$ is represented by

$$\boldsymbol{h}_2^{+} = \boldsymbol{\Omega}^{\dagger}\boldsymbol{G}\boldsymbol{\Omega}\,, \tag{2.3.8}$$

with

$$\boldsymbol{\Omega} = \left(\mathbf{1}_2 + \boldsymbol{Y}^\dagger \boldsymbol{Y}\right)^{-1/2}, \tag{2.3.9}$$

and

$$\begin{aligned}\boldsymbol{G} = {} & p^2 b \mathbf{1}_2 + K\boldsymbol{V}K + \alpha^2 Kb\boldsymbol{\sigma}\cdot\boldsymbol{p}\boldsymbol{V}\boldsymbol{\sigma}\cdot\boldsymbol{p}bK \\ & + \alpha\left(K\boldsymbol{V}bKp - Kb\boldsymbol{\sigma}\cdot\boldsymbol{p}\boldsymbol{V}\boldsymbol{\sigma}\cdot\boldsymbol{p}p^{-1}K\right)\boldsymbol{Y} \\ & + \alpha\boldsymbol{Y}^\dagger\left(Kbp\boldsymbol{V}K - Kp^{-1}\boldsymbol{\sigma}\cdot\boldsymbol{p}\boldsymbol{V}\boldsymbol{\sigma}\cdot\boldsymbol{p}bK\right) \\ & + \boldsymbol{Y}^\dagger\left(\frac{p^2}{1-e_p} + p^{-1}K\boldsymbol{\sigma}\cdot\boldsymbol{p}\boldsymbol{V}\boldsymbol{\sigma}\cdot\boldsymbol{p}Kp^{-1} + \alpha^2 pKb\boldsymbol{V}bKp\right)\boldsymbol{Y}.\end{aligned} \tag{2.3.10}$$

The 2c theory can consider the spin-free and spin-dependent terms, separately. Introducing the Dirac relation for two arbitrary vector operators $\boldsymbol{A}$ and $\boldsymbol{B}$,

$$\left(\boldsymbol{\sigma}\cdot\boldsymbol{A}\right)\left(\boldsymbol{\sigma}\cdot\boldsymbol{B}\right) = \boldsymbol{A}\cdot\boldsymbol{B} + \mathrm{i}\boldsymbol{\sigma}\cdot\left(\boldsymbol{A}\times\boldsymbol{B}\right), \tag{2.3.11}$$

the Pauli matrices $\boldsymbol{\sigma}$ are separated:

$$\boldsymbol{\sigma}\cdot\boldsymbol{p}\boldsymbol{V}\boldsymbol{\sigma}\cdot\boldsymbol{p} = \boldsymbol{p}\boldsymbol{V}\cdot\boldsymbol{p} + \mathrm{i}\boldsymbol{\sigma}\cdot\left(\boldsymbol{p}\boldsymbol{V}\times\boldsymbol{p}\right), \tag{2.3.12}$$

where i represents the imaginary part. The first and second terms of the right-hand side of Eq. (2.3.12) represent the spin-free and spin-dependent terms, respectively. The remainder of this thesis deals with the spin-free term that does not involve $\boldsymbol{\sigma}$.

2.3.2 Two-electron operator

This subsection describes the IOTC Hamiltonian for many-electron systems. Along the IOTC transformation for one-electron Hamiltonian, the picture of wavefunction is transformed into the 2c picture. Calculating two-electron term using electron-electron interactions such as Eqs. (2.1.3)–(2.1.5) generates the PCE because two-electron term is expressed as expectation values of the two-electron interaction operator. PCC is accomplished by considering the IOTC transformation of both one-electron Dirac Hamiltonian and electron-electron interaction operator simultaneously.

Many-electron unitary transformation is approximated by a direct product of one-electron unitary transformation $\boldsymbol{U}(i)$ as

$$\boldsymbol{U}(i,j,\cdots)\approx\boldsymbol{U}(i)\otimes\boldsymbol{U}(j)\otimes\cdots. \tag{2.3.14}$$

The one- and two-electron Hamiltonians are block-diagonalized into positive- and negative-energy states:

$$\boldsymbol{U}^{\dagger}(i,j,\cdots)\left[\sum_{i}\boldsymbol{H}_4^{\mathrm{D}}(i)+\sum_{i>j}\boldsymbol{G}_4(i,j)\right]\boldsymbol{U}(i,j,\cdots)\approx\begin{pmatrix}\boldsymbol{H}_2^{+} & \boldsymbol{0}_2\\ \boldsymbol{0}_2 & \boldsymbol{H}_2^{-}\end{pmatrix}, \tag{2.3.15}$$

where $\boldsymbol{G}_4$ represents the 4c two-electron interaction, such as the Coulomb, Gaunt, and Breit operators, and $\boldsymbol{H}_2^{+}$ and $\boldsymbol{H}_2^{-}$ are the positive- and negative-energy states, respectively. Positive-energy state is used as electronic Hamiltonian as follows:

$$\boldsymbol{H}_2^{+}\approx\sum_{i}\boldsymbol{h}_2^{+}(i)+\sum_{i>j}\boldsymbol{g}_2^{++}(i,j), \tag{2.3.16}$$

where $\boldsymbol{g}_2^{++}$ is the two-particle electronic state. The electron-positron coupling terms, which are also obtained as a result of the unitary transformation, are nonzero, but are assumed to be negligible.[27]

In this thesis, the Coulomb interaction is adopted as a two-electron operator. The explicit formula for the spin-free part of $\boldsymbol{g}_2^{++}$ is given by

$$\boldsymbol{g}_2^{\mathrm{sf}}(i,j)=\boldsymbol{g}_2^{\mathrm{sf1}}(i,j)+\boldsymbol{g}_2^{\mathrm{sf2}}(i,j)+\boldsymbol{g}_2^{\mathrm{sf3}}(i,j) \tag{2.3.17}$$

with

$$\boldsymbol{g}_2^{\mathrm{sf1}}(i,j)=\boldsymbol{M}_i\boldsymbol{M}_j\left\lfloor\frac{1}{r_{ij}}\boldsymbol{1}_2\right\rfloor\boldsymbol{M}_j\boldsymbol{M}_i, \tag{2.3.18}$$

$$\boldsymbol{g}_2^{\mathrm{sf2}}(i,j)=P(i,j)\left(\boldsymbol{d}_i\boldsymbol{M}_j\left\lfloor\boldsymbol{p}_i\frac{1}{r_{ij}}\boldsymbol{1}_2\cdot\boldsymbol{p}_i\right\rfloor\boldsymbol{M}_j\boldsymbol{d}_i\right), \tag{2.3.19}$$

and

$$\boldsymbol{g}_2^{\mathrm{sf3}}(i,j)=\boldsymbol{d}_i\boldsymbol{d}_j\left\lfloor\boldsymbol{p}_i\left(\boldsymbol{p}_j\frac{1}{r_{ij}}\boldsymbol{1}_2\cdot\boldsymbol{p}_j\right)\cdot\boldsymbol{p}_i\right\rfloor\boldsymbol{d}_i\boldsymbol{d}_j, \tag{2.3.20}$$

where

$$\boldsymbol{M} = K\left(\mathbf{1}_2 + bp\boldsymbol{Y}\right)\boldsymbol{\Omega} \tag{2.3.21}$$

and

$$\boldsymbol{d} = K\left(\alpha b\mathbf{1}_2 - p^{-1}\boldsymbol{Y}\right)\boldsymbol{\Omega}\,. \tag{2.3.22}$$

$P(i,j)$ is an operator that satisfies

$$P(i,j)O(i,j) = O(i,j) + O(j,i) \tag{2.3.23}$$

for an arbitrary two-electron operator, $O(i,j)$. $\boldsymbol{g}_2^{\mathrm{sf1}}$, $\boldsymbol{g}_2^{\mathrm{sf2}}$, and $\boldsymbol{g}_2^{\mathrm{sf3}}$ denote the Coulomb-like, Darwin-like, and specific spin-free interaction terms, respectively. The Coulomb-like term mainly corresponds to the electron repulsion, whereas the other two terms are higher-order relativistic terms.

In practical calculations, a matrix transformation method that adopts the resolution of identity using the eigenvectors of $\boldsymbol{p}^2$,

$$1 \approx \sum_k |k\rangle\langle k|, \tag{2.3.24}$$

is applied[30] because a direct evaluation of two-electron integrals for $\boldsymbol{g}_2^{\mathrm{sf1}}$, $\boldsymbol{g}_2^{\mathrm{sf2}}$, and $\boldsymbol{g}_2^{\mathrm{sf3}}$ is difficult. Commonly, $\{k\}$ are represented by the linear combination of PBFs for AOs $\{\chi\}$. The explicit formulae of matrix representations of the TEIs for $\boldsymbol{g}_2^{\mathrm{sf1}}$, $\boldsymbol{g}_2^{\mathrm{sf2}}$, and $\boldsymbol{g}_2^{\mathrm{sf3}}$ are

$$\begin{aligned}&\left\langle \chi_\mu\chi_\nu \left| \boldsymbol{g}_2^{\mathrm{sf1}} \right| \chi_\lambda\chi_\sigma \right\rangle \\ &= \sum_{k_a k_b k_c k_d} \left\langle \chi_\mu \left| \boldsymbol{M}_i \right| k_a \right\rangle \left\langle \chi_\nu \left| \boldsymbol{M}_j \right| k_b \right\rangle \left\langle k_a k_b \left| 1/r_{ij}\mathbf{1}_2 \right| k_c k_d \right\rangle \left\langle k_c \left| \boldsymbol{M}_i \right| \chi_\lambda \right\rangle \left\langle k_d \left| \boldsymbol{M}_j \right| \chi_\sigma \right\rangle,\end{aligned} \tag{2.3.25}$$

$$\begin{aligned}&\left\langle \chi_\mu\chi_\nu \left| \boldsymbol{g}_2^{\mathrm{sf2}} \right| \chi_\lambda\chi_\sigma \right\rangle \\ &= \sum_{k_a k_b k_c k_d} \left\langle \chi_\mu \left| \boldsymbol{d}_i \right| k_a \right\rangle \left\langle \chi_\nu \left| \boldsymbol{M}_j \right| k_b \right\rangle \left\langle k_a k_b \left| \boldsymbol{p}_i 1/r_{ij}\mathbf{1}_2 \cdot \boldsymbol{p}_i \right| k_c k_d \right\rangle \left\langle k_c \left| \boldsymbol{d}_i \right| \chi_\lambda \right\rangle \left\langle k_d \left| \boldsymbol{M}_j \right| \chi_\sigma \right\rangle,\end{aligned} \tag{2.3.26}$$

and

$$\left\langle \chi_\mu \chi_\nu \left| \boldsymbol{g}_2^{\mathrm{sf3}} \right| \chi_\lambda \chi_\sigma \right\rangle$$
$$= \sum_{k_a k_b k_c k_d} \left\langle \chi_\mu \left| \boldsymbol{d}_i \right| k_a \right\rangle \left\langle \chi_\nu \left| \boldsymbol{d}_j \right| k_b \right\rangle \left\langle k_a k_b \left| \boldsymbol{p}_i \left[\boldsymbol{p}_j 1/r_{ij} \mathbf{1}_2 \cdot \boldsymbol{p}_j \right] \cdot \boldsymbol{p}_i \right| k_c k_d \right\rangle \left\langle k_c \left| \boldsymbol{d}_i \right| \chi_\lambda \right\rangle \left\langle k_d \left| \boldsymbol{d}_j \right| \chi_\sigma \right\rangle, \tag{2.3.27}$$

where μ, ν, λ, and σ are the indices of AOs and a, b, c, and d are those of PBFs, respectively. For the calculation of the two-electron terms of the IOTC Hamiltonian, the evaluation of primitive integrals $\left\langle k_a k_b \left| 1/r_{ij} \mathbf{1}_2 \right| k_c k_d \right\rangle$, $\left\langle k_a k_b \left| \boldsymbol{p}_i 1/r_{ij} \mathbf{1}_2 \cdot \boldsymbol{p}_i \right| k_c k_d \right\rangle$, and $\left\langle k_a k_b \left| \boldsymbol{p}_i \left[\boldsymbol{p}_j 1/r_{ij} \mathbf{1}_2 \cdot \boldsymbol{p}_j \right] \cdot \boldsymbol{p}_i \right| k_c k_d \right\rangle$, and transformation of primitive integrals by matrix elements $\left\langle \chi_\mu \left| \boldsymbol{M}_i \right| k_a \right\rangle$ and $\left\langle \chi_\mu \left| \boldsymbol{d}_i \right| k_a \right\rangle$, which are represented as $M_{\mu a}$ and $d_{\mu \mathrm{a}}$, respectively, are required. The transformation is a time-consuming step in the calculation of the IOTC Hamiltonian.

2.3.3 Density operator

This subsection describes the PCC of electron density.[31,32] DFT,[33] which is widely used by users of computational chemistry, adopts an electron density ρ as a fundamental variable. According to the KS procedure,[34] the total energy of DFT is expressed as

$$E^{\mathrm{KS}} = \sum_i \left\langle \varphi_i \left| h(i) \right| \varphi_i \right\rangle + \int\int d\mathbf{r}_i d\mathbf{r}_j g(i,j) \rho(\mathbf{r}_i) \rho(\mathbf{r}_j) + E_{\mathrm{XC}}[\rho], \tag{2.3.28}$$

with the i-th KS orbital φ_i and one-electron Hamiltonian h. The first term denotes the kinetic energy and interaction between electron density and external potential. The second term is the Coulomb interaction of electron density. Introducing φ_i into Eq. (2.3.28), the second term is evaluated by the expectation value of the two-electron operator, $\sum_{i>j} \left\langle \varphi_i \varphi_j \left| g(i,j) \right| \varphi_i \varphi_j \right\rangle$, which is calculated by the same procedure in the wave-function theory. The third term represents the exchange-correlation term, which is a functional of ρ. ρ is represented as the expectation value of the density operator δ as follows:

$$\begin{aligned}\rho(\mathbf{r}) &= \sum_{\mu\nu} P_{\mu\nu} \langle \chi_\mu | \delta | \chi_\nu \rangle \\ &= \sum_{\mu\nu} P_{\mu\nu} \chi_\mu^*(\mathbf{r}) \chi_\nu(\mathbf{r}).\end{aligned} \tag{2.3.29}$$

The expansion of φ_i by a set of AOs $\{\chi_\mu\}$ and MO coefficient $c_{\mu i}$ as

$$\varphi_i = \sum_\mu c_{\mu i} \chi_\mu \,, \tag{2.3.30}$$

and density matrix $\boldsymbol{P}$, which is represented as

$$P_{\mu\nu} = \sum_i c_{\mu i}^* c_{\nu i} \,, \tag{2.3.31}$$

are introduced in Eq. (2.3.29). In nonrelativistic calculations, ρ is calculated by the product of AOs as the second line of Eq. (2.3.29). When extending DFT to the 2c theory, PCC of density operator is necessary besides the unitary transformation of one- and two-electron operators provided in the previous subsections.

PCC of density operator is performed by the IOTC transformation as follows:

$$\boldsymbol{U}_1^\dagger \boldsymbol{U}_0^\dagger \delta \mathbf{1}_4 \boldsymbol{U}_0 \boldsymbol{U}_1 = \begin{pmatrix} \boldsymbol{\delta}^+ & 0_2 \\ 0_2 & \boldsymbol{\delta}^- \end{pmatrix}. \tag{2.3.32}$$

The electronic state $\boldsymbol{\delta}^+$

$$\begin{aligned}\boldsymbol{\delta}^+(\mathbf{r}'-\mathbf{r}) = \left(1+\boldsymbol{Y}^\dagger\boldsymbol{Y}\right)^{-1/2} \big[& K\delta(\mathbf{r}'-\mathbf{r})\mathbf{1}_2 K + \alpha^2 Kb\boldsymbol{\sigma}\cdot\boldsymbol{p}\delta(\mathbf{r}'-\mathbf{r})\mathbf{1}_2\boldsymbol{\sigma}\cdot\boldsymbol{p}bK \\ & + \alpha\left(K\delta(\mathbf{r}'-\mathbf{r})\mathbf{1}_2 bKp - Kb\boldsymbol{\sigma}\cdot\boldsymbol{p}\delta(\mathbf{r}'-\mathbf{r})\mathbf{1}_2\boldsymbol{\sigma}\cdot\boldsymbol{p}p^{-1}K\right) \\ & + \alpha\boldsymbol{Y}^\dagger\left(Kpb\delta(\mathbf{r}'-\mathbf{r})\mathbf{1}_2 K - p^{-1}K\boldsymbol{\sigma}\cdot\boldsymbol{p}\delta(\mathbf{r}'-\mathbf{r})\mathbf{1}_2\boldsymbol{\sigma}\cdot\boldsymbol{p}bK\right) \\ & + \boldsymbol{Y}^\dagger\left(p^{-1}K\boldsymbol{\sigma}\cdot\boldsymbol{p}\delta(\mathbf{r}'-\mathbf{r})\mathbf{1}_2\boldsymbol{\sigma}\cdot\boldsymbol{p}Kp^{-1} + \alpha^2 pKb\delta(\mathbf{r}'-\mathbf{r})\mathbf{1}_2 bKp\right)\boldsymbol{Y}\big]\left(1+\boldsymbol{Y}^\dagger\boldsymbol{Y}\right)^{-1/2} \\ = {} & \boldsymbol{M}^\dagger\delta(\mathbf{r}'-\mathbf{r})\mathbf{1}_2\boldsymbol{M} + \boldsymbol{d}^\dagger\boldsymbol{\sigma}\cdot\boldsymbol{p}\delta(\mathbf{r}'-\mathbf{r})\mathbf{1}_2\boldsymbol{\sigma}\cdot\boldsymbol{p}\boldsymbol{d}\end{aligned} \tag{2.3.33}$$

is used as the density operator. The spin-free term of density operator is given by

$$\boldsymbol{\delta}^{\mathrm{sf}}(\mathbf{r}'-\mathbf{r}) = \boldsymbol{M}^\dagger\delta(\mathbf{r}'-\mathbf{r})\mathbf{1}_2\boldsymbol{M} + \boldsymbol{d}^\dagger\boldsymbol{p}\delta(\mathbf{r}'-\mathbf{r})\mathbf{1}_2\cdot\boldsymbol{p}\boldsymbol{d}\,, \tag{2.3.34}$$

eliminating the spin-dependent term from Eq. (2.3.33). The electron density at the spin-free level is represented as

$$\rho^{\mathrm{sf}}(\mathbf{r}) = \sum_{\mu\nu} P_{\mu\nu} \left[\left\langle \chi_\mu \middle| \boldsymbol{M}^\dagger \delta(\mathbf{r}' - \mathbf{r}) \mathbf{1}_2 \boldsymbol{M} \middle| \chi_\nu \right\rangle + \left\langle \chi_\mu \middle| \boldsymbol{d}^\dagger \boldsymbol{p} \delta(\mathbf{r}' - \mathbf{r}) \mathbf{1}_2 \cdot \boldsymbol{p}\boldsymbol{d} \middle| \chi_\nu \right\rangle \right]. \tag{2.3.35}$$

Transforming integrals included in Eq. (2.3.35) from coordinate to momentum space, the first and second terms are respectively represented as

$$\begin{aligned} &\left\langle \chi_\mu \middle| \boldsymbol{M}^\dagger \delta(\mathbf{r}' - \mathbf{r}) \mathbf{1}_2 \boldsymbol{M} \middle| \chi_\nu \right\rangle \\ &= \sum_{kk'k''k'''} \left\langle \chi_\mu \middle| k \right\rangle \left\langle k \middle| \boldsymbol{M}^\dagger \middle| k' \right\rangle \left\langle k' \middle| \delta(\mathbf{r}' - \mathbf{r}) \mathbf{1}_2 \middle| k'' \right\rangle \left\langle k'' \middle| \boldsymbol{M} \middle| k''' \right\rangle \left\langle k''' \middle| \chi_\nu \right\rangle \\ &= \sum_{kk'k''k'''} C^\dagger_{\mu k} M^\dagger_{kk'} D_{k'k''} M_{k''k'''} C_{k'''\nu} \end{aligned} \tag{2.3.36}$$

and

$$\begin{aligned} &\left\langle \chi_\mu \middle| \boldsymbol{d}^\dagger \boldsymbol{p} \delta(\mathbf{r}' - \mathbf{r}) \mathbf{1}_2 \cdot \boldsymbol{p}\boldsymbol{d} \middle| \chi_\nu \right\rangle \\ &= \sum_{kk'k''k'''} \left\langle \chi_\mu \middle| k \right\rangle \left\langle k \middle| \boldsymbol{d}^\dagger \middle| k' \right\rangle \left\langle k' \middle| \boldsymbol{p} \delta(\mathbf{r}' - \mathbf{r}) \mathbf{1}_2 \cdot \boldsymbol{p} \middle| k'' \right\rangle \left\langle k'' \middle| \boldsymbol{d} \middle| k''' \right\rangle \left\langle k''' \middle| \chi_\nu \right\rangle \\ &= \sum_{kk'k''k'''} C^\dagger_{\mu k} d^\dagger_{kk'} \Delta_{k'k''} d_{k''k'''} C_{k'''\nu}. \end{aligned} \tag{2.3.37}$$

The matrix representation is given by

$$\rho^{\mathrm{sf}}(\mathbf{r}) = \boldsymbol{P}\boldsymbol{C}^\dagger \left(\boldsymbol{M}^\dagger \boldsymbol{D} \boldsymbol{M} + \boldsymbol{d}^\dagger \boldsymbol{\Delta} \boldsymbol{d} \right) \boldsymbol{C}\,. \tag{2.3.38}$$

The character of delta function leads to $\boldsymbol{D}$ and $\boldsymbol{\Delta}$ respectively expressed as follows:

$$\begin{aligned} D_{k'k''} &= \left\langle k' \middle| \delta(\mathbf{r}' - \mathbf{r}) \mathbf{1}_2 \middle| k'' \right\rangle \\ &= \sum_\alpha \sum_\beta c^*_{\alpha k'} c_{\beta k''} \left\langle \zeta_\alpha(\mathbf{r}') \middle| \delta(\mathbf{r}' - \mathbf{r}) \mathbf{1}_2 \middle| \zeta_\beta(\mathbf{r}') \right\rangle \\ &= \sum_\alpha \sum_\beta c^*_{\alpha k'} c_{\beta k''} \zeta_\alpha(\mathbf{r}) \zeta_\beta(\mathbf{r}) \end{aligned} \tag{2.3.39}$$

and

$$\begin{aligned} \Delta_{k'k''} &= \left\langle k' \middle| \boldsymbol{p} \delta(\mathbf{r}' - \mathbf{r}) \mathbf{1}_2 \cdot \boldsymbol{p} \middle| k'' \right\rangle \\ &= \sum_\alpha \sum_\beta c^*_{\alpha k'} c_{\beta k''} \left\langle \zeta_\alpha(\mathbf{r}') \middle| -i\nabla_{\mathbf{r}'} \delta(\mathbf{r}' - \mathbf{r}) \mathbf{1}_2 \cdot (-i\nabla_{\mathbf{r}'}) \middle| \zeta_\beta(\mathbf{r}') \right\rangle \\ &= -\sum_\alpha \sum_\beta c^*_{\alpha k'} c_{\beta k''} \left[\left[\zeta_\alpha(\mathbf{r}') \delta(\mathbf{r}' - \mathbf{r}) \mathbf{1}_2 \nabla_{\mathbf{r}'} \zeta_\beta(\mathbf{r}') \right]_{-\infty}^{\infty} - \left\langle \nabla_{\mathbf{r}'} \zeta_\alpha(\mathbf{r}') \middle| \delta(\mathbf{r}' - \mathbf{r}) \mathbf{1}_2 \middle| \nabla_{\mathbf{r}'} \zeta_\beta(\mathbf{r}') \right\rangle \right] \\ &= \sum_\alpha \sum_\beta c^*_{\alpha k'} c_{\beta k''} \left\{ \nabla_{\mathbf{r}} \zeta_\alpha(\mathbf{r}) \right\} \left\{ \nabla_{\mathbf{r}} \zeta_\beta(\mathbf{r}) \right\}. \end{aligned} \tag{2.3.40}$$

By using the following unitary-transformed basis function

$$\begin{aligned}\chi_\mu{}'(\mathbf{r}) &= \sum_{kk'} |k\rangle\langle k|\boldsymbol{M}|k'\rangle\langle k'|\chi_\mu\rangle \\ &= \sum_{kk'}\left(\sum_\alpha c_{\alpha k}\zeta_\beta(\mathbf{r})\right)\langle k|\boldsymbol{M}|k'\rangle\langle k'|\chi_\mu\rangle\end{aligned} \tag{2.3.41}$$

and

$$\begin{aligned}\chi_\mu{}''(\mathbf{r}) &= \sum_{kk'} |\nabla k\rangle\langle k|\boldsymbol{d}|k'\rangle\langle k'|\chi_\mu\rangle \\ &= \sum_{kk'}\left(\sum_\alpha c_{\alpha k}\nabla_{\mathbf{r}}\zeta_\beta(\mathbf{r})\right)\langle k|\boldsymbol{d}|k'\rangle\langle k'|\chi_\mu\rangle,\end{aligned} \tag{2.3.42}$$

Eqs. (2.3.36) and (2.3.37) are rewritten as

$$\langle\chi_\mu|\boldsymbol{M}^\dagger\delta(\mathbf{r}'-\mathbf{r})\mathbf{1}_2\boldsymbol{M}|\chi_\nu\rangle = \chi_\mu{}'(\mathbf{r})\chi_\nu{}'(\mathbf{r}) \tag{2.3.43}$$

and

$$\langle\chi_\mu|\boldsymbol{d}^\dagger\boldsymbol{p}\delta(\mathbf{r}'-\mathbf{r})\mathbf{1}_2\cdot\boldsymbol{p}\boldsymbol{d}|\chi_\nu\rangle = \chi_\mu{}''(\mathbf{r})\chi_\nu{}''(\mathbf{r}), \tag{2.3.44}$$

respectively. The formation of electron density is also rewritten as

$$\rho^{\mathrm{sf}}(\mathbf{r}) = \sum_{\mu\nu} P_{\mu\nu}\left[\chi_\mu{}'(\mathbf{r})\chi_\nu{}'(\mathbf{r}) + \chi_\mu{}''(\mathbf{r})\chi_\nu{}''(\mathbf{r})\right]. \tag{2.3.45}$$

This formula leads to the gradient of electron density as follows:

$$\begin{aligned}\nabla_{\mathbf{r}}\rho^{\mathrm{sf}}(\mathbf{r}) = &\sum_{\mu\nu} P_{\mu\nu}\left[\left\{\nabla_{\mathbf{r}}\chi_\mu{}'(\mathbf{r})\right\}\left\{\chi_\nu{}'(\mathbf{r})\right\} + \left\{\chi_\mu{}'(\mathbf{r})\right\}\left\{\nabla_{\mathbf{r}}\chi_\nu{}'(\mathbf{r})\right\}\right] \\ &+\sum_{\mu\nu} P_{\mu\nu}\left[\left\{\nabla_{\mathbf{r}}\chi_\mu{}''(\mathbf{r})\right\}\left\{\chi_\nu{}''(\mathbf{r})\right\} + \left\{\chi_\mu{}''(\mathbf{r})\right\}\left\{\nabla_{\mathbf{r}}\chi_\nu{}''(\mathbf{r})\right\}\right].\end{aligned} \tag{2.3.46}$$

The kinetic energy density τ is derived in the same manner:

$$\begin{aligned}\tau(\mathbf{r}) &= \frac{1}{2}\sum_i \langle\varphi_i|\,\boldsymbol{p}\delta(\mathbf{r}_i-\mathbf{r})\mathbf{1}_2\cdot\boldsymbol{p}|\varphi_i\rangle \\ &= \frac{1}{2}\sum_{\mu\nu} P_{\mu\nu}\langle\chi_\mu(\mathbf{r}')|\,\boldsymbol{p}\delta(\mathbf{r}'-\mathbf{r})\mathbf{1}_2\cdot\boldsymbol{p}\,|\chi_\nu(\mathbf{r}')\rangle \\ &= \frac{1}{2}\sum_{\mu\nu} P_{\mu\nu}\langle\chi_\mu(\mathbf{r}')|(-i\nabla)\delta(\mathbf{r}'-\mathbf{r})\mathbf{1}_2\cdot(-i\nabla)|\chi_\nu(\mathbf{r}')\rangle \\ &= -\frac{1}{2}\sum_{\mu\nu} P_{\mu\nu}\langle\chi_\mu(\mathbf{r}')|\nabla\delta(\mathbf{r}'-\mathbf{r})\mathbf{1}_2\cdot\nabla|\chi_\nu(\mathbf{r}')\rangle.\end{aligned} \tag{2.3.47}$$

Eq. (2.3.47) is rewritten as

$$\tau(\mathbf{r}) = \frac{1}{2}\left\langle \nabla\chi_\mu(\mathbf{r}') \middle| \delta(\mathbf{r}'-\mathbf{r})\mathbf{1}_2 \middle| \nabla\chi_\nu(\mathbf{r}') \right\rangle \tag{2.3.48}$$

by replacing the integrals as

$$\begin{aligned}
&\left\langle \chi_\mu(\mathbf{r}') \middle| \nabla\delta(\mathbf{r}'-\mathbf{r})\mathbf{1}_2 \cdot \nabla \middle| \chi_\nu(\mathbf{r}') \right\rangle \\
&= \int \mathrm{d}\mathbf{r}' \chi_\mu(\mathbf{r}') \nabla\delta(\mathbf{r}'-\mathbf{r})\mathbf{1}_2 \cdot \nabla\chi_\nu(\mathbf{r}') \\
&= \left[\chi_\mu(\mathbf{r}')\delta(\mathbf{r}'-\mathbf{r})\mathbf{1}_2 \cdot \nabla\chi_\nu(\mathbf{r}') \right]_{-\infty}^{\infty} - \int \mathrm{d}\mathbf{r}' \nabla\chi_\mu(\mathbf{r}') \nabla\delta(\mathbf{r}'-\mathbf{r})\mathbf{1}_2 \cdot \nabla\chi_\nu(\mathbf{r}') \\
&= -\left\langle \nabla\chi_\mu(\mathbf{r}') \middle| \delta(\mathbf{r}'-\mathbf{r})\mathbf{1}_2 \middle| \nabla\chi_\nu(\mathbf{r}') \right\rangle .
\end{aligned} \tag{2.3.49}$$

The spin-free term of PCC kinetic energy density is given by

$$\tau_{\mathrm{SF}}^{+} = \frac{1}{2}\sum_{\mu\nu} P_{\mu\nu} \left[\nabla\chi_\mu'(\mathbf{r}) \cdot \nabla\chi_\nu'(\mathbf{r}) + \nabla\chi_\mu''(\mathbf{r}) \cdot \nabla\chi_\nu''(\mathbf{r}) \right]. \tag{2.3.50}$$

The exchange-correlation integral is represented as

$$\begin{aligned}
v_{\mu\nu}^{\mathrm{XC}} = \int \mathrm{d}\mathbf{r} \Bigg[& \frac{\partial\varepsilon_{\mathrm{XC}}}{\partial\rho} \left\langle \chi_\mu(\mathbf{r}') \middle| \delta(\mathbf{r}'-\mathbf{r})\mathbf{1}_2 \middle| \chi_\nu(\mathbf{r}') \right\rangle \\
& + \frac{\partial\varepsilon_{\mathrm{XC}}}{\partial\nabla\rho} \cdot \left\langle \nabla\chi_\mu(\mathbf{r}') \middle| \delta(\mathbf{r}'-\mathbf{r})\mathbf{1}_2 \middle| \chi_\nu(\mathbf{r}') \right\rangle \\
& + \frac{\partial\varepsilon_{\mathrm{XC}}}{\partial\nabla\rho} \cdot \left\langle \chi_\mu(\mathbf{r}') \middle| \delta(\mathbf{r}'-\mathbf{r})\mathbf{1}_2 \middle| \nabla\chi_\nu(\mathbf{r}') \right\rangle \\
& + \frac{\partial\varepsilon_{\mathrm{XC}}}{\partial\tau} \cdot \left\langle \nabla\chi_\mu(\mathbf{r}') \middle| \delta(\mathbf{r}'-\mathbf{r})\mathbf{1}_2 \middle| \nabla\chi_\nu(\mathbf{r}') \right\rangle \Bigg],
\end{aligned} \tag{2.3.51}$$

with exchange-correlation energy density $\varepsilon_{\mathrm{XC}}$. This is calculated by the summation of weight w_{g} at the grid point g as

$$\begin{aligned}
v_{\mu\nu}^{\mathrm{XC}} = \sum_{\mathrm{g}} w_{\mathrm{g}} \Bigg[& \frac{\partial\varepsilon_{\mathrm{XC}}}{\partial\rho} \left\langle \chi_\mu(\mathbf{r}') \middle| \delta(\mathbf{r}'-\mathbf{r}_g)\mathbf{1}_2 \middle| \chi_\nu(\mathbf{r}') \right\rangle \\
& + \frac{\partial\varepsilon_{\mathrm{XC}}}{\partial\nabla\rho} \cdot \left\langle \nabla\chi_\mu(\mathbf{r}') \middle| \delta(\mathbf{r}'-\mathbf{r}_g)\mathbf{1}_2 \middle| \chi_\nu(\mathbf{r}') \right\rangle \\
& + \frac{\partial\varepsilon_{\mathrm{XC}}}{\partial\nabla\rho} \cdot \left\langle \chi_\mu(\mathbf{r}') \middle| \delta(\mathbf{r}'-\mathbf{r}_g)\mathbf{1}_2 \middle| \nabla\chi_\nu(\mathbf{r}') \right\rangle \\
& + \frac{\partial\varepsilon_{\mathrm{XC}}}{\partial\tau} \cdot \left\langle \nabla\chi_\mu(\mathbf{r}') \middle| \delta(\mathbf{r}'-\mathbf{r}_g)\mathbf{1}_2 \middle| \nabla\chi_\nu(\mathbf{r}') \right\rangle \Bigg].
\end{aligned} \tag{2.3.52}$$

PCC exchange-correlation integral is given by

$$
\begin{aligned}
v_{\mu\nu}^{\mathrm{XC}} = \sum_{\mathrm{g}} w_{\mathrm{g}} \Bigg[& \frac{\partial \varepsilon_{\mathrm{XC}}}{\partial \rho} \Big[\chi_\mu'(\mathbf{r}_{\mathrm{g}}) \chi_\nu'(\mathbf{r}_{\mathrm{g}}) + \chi_\mu''(\mathbf{r}_{\mathrm{g}}) \chi_\nu''(\mathbf{r}_{\mathrm{g}}) \Big] \\
& + \frac{\partial \varepsilon_{\mathrm{XC}}}{\partial \nabla \rho} \cdot \Big[\nabla \chi_\mu'(\mathbf{r}_{\mathrm{g}}) \chi_\nu'(\mathbf{r}_{\mathrm{g}}) + \nabla \chi_\mu''(\mathbf{r}_{\mathrm{g}}) \chi_\nu''(\mathbf{r}_{\mathrm{g}}) \Big] \\
& + \frac{\partial \varepsilon_{\mathrm{XC}}}{\partial \nabla \rho} \cdot \Big[\chi_\mu'(\mathbf{r}_{\mathrm{g}}) \cdot \nabla \chi_\nu'(\mathbf{r}_{\mathrm{g}}) + \chi_\mu''(\mathbf{r}_{\mathrm{g}}) \cdot \nabla \chi_\nu''(\mathbf{r}_{\mathrm{g}}) \Big] \\
& + \frac{\partial \varepsilon_{\mathrm{XC}}}{\partial \tau} \cdot \Big[\nabla \chi_\mu'(\mathbf{r}_{\mathrm{g}}) \cdot \nabla \chi_\nu'(\mathbf{r}_{\mathrm{g}}) + \nabla \chi_\mu''(\mathbf{r}_{\mathrm{g}}) \cdot \nabla \chi_\nu''(\mathbf{r}_{\mathrm{g}}) \Big] \Bigg].
\end{aligned}
\tag{2.3.53}
$$

2.4 LUT scheme

Although the IOTC Hamiltonian realizes high accuracy close to 4c Hamiltonian, the unitary transformation is a time-consuming step; the computational costs for one-electron, two-electron, and density operators scale as $O(n^3)$, $O(n^5)$, and $O(n^3)$ with respect to the number of PBFs n. Efficient techniques to accelerate the unitary transformation have been proposed based on the locality of relativistic effects.[35–46] Nakai group has developed the LUT scheme based on the IOTC Hamiltonian.[40–42] The concept of the LUT is similar to that of the diagonal local approximation method for the one-electron system proposed by Peng and Reiher.[43,44] These efficient schemes have extended to calculations of molecular properties, such as molecular gradient[47–50] and NMR shielding constant.[51,52] This subsection briefly describes the LUT scheme.

LUT introduces two approximations. First, total transformation is approximated as direct summation of the transformations for subsystems:

$$
\boldsymbol{U} \approx \left[\boldsymbol{U}^A \oplus \boldsymbol{U}^B \oplus \boldsymbol{U}^C \oplus \cdots \right], \tag{2.4.1}
$$

where A, B, C, … represent the subsystems that do not intersect each other. Individual atoms are usually adopted as subsystems. This approximation is based on the locality of relativistic interactions that the relativistic effect is dominant in each atom rather than bonding regions. Second, the locality of the unitary transformation is introduced. When the distance between an electron and a subsystem is long, the relativistic effects of the kinetic

energy, nucleus–electron, and electron–electron interactions become small. Consequently, the operators behave as they do in the nonrelativistic case. Thus, the electronic components of the Hamiltonian, $\boldsymbol{H}_2^+$, are presented as

$$\boldsymbol{H}_2^+ \approx \sum_i \boldsymbol{h}_2^{\mathrm{LUT}}(i) + \sum_{i>j} \boldsymbol{g}_2^{\mathrm{LUT}}(i,j), \tag{2.4.2}$$

where $\boldsymbol{h}_2^{\mathrm{LUT}}$ and $\boldsymbol{g}_2^{\mathrm{LUT}}$ are the approximated electronic components of the 2c one- and two-electron operators, respectively. Here, the matrix elements of $\boldsymbol{h}_2^{\mathrm{LUT}}$ with $\{\chi_\mu\}$ are expressed as

$$\left\langle \chi_\mu^A \middle| \boldsymbol{h}_2^{\mathrm{LUT}} \middle| \chi_\nu^B \right\rangle = \begin{cases} \left\langle \chi_\mu^A \middle| \boldsymbol{T}^+ + \boldsymbol{V}_A^+ + \sum_{C\neq A} \boldsymbol{V}_C^{\mathrm{Nonrel.}} \middle| \chi_\nu^B \right\rangle & (A=B) \\ \left\langle \chi_\mu^A \middle| \boldsymbol{T}^{\mathrm{NR}} + \boldsymbol{V}_A^+ + \boldsymbol{V}_B^+ + \sum_{C\neq A,B} \boldsymbol{V}_C^{\mathrm{NR}} \middle| \chi_\nu^B \right\rangle & (A\neq B, R_{AB}\le\tau) \\ \left\langle \chi_\mu^A \middle| \boldsymbol{T}^{\mathrm{NR}} + \sum_C \boldsymbol{V}_C^{\mathrm{NR}} \middle| \chi_\nu^B \right\rangle & (A\neq B, R_{AB}>\tau), \end{cases} \tag{2.4.3}$$

where $\boldsymbol{V}$ is the nucleus–electron attraction, and $\boldsymbol{T}$ is the kinetic energy. Superscripts Nonrel. and + denote the nonrelativistic and relativistic operators, respectively. Note that $\boldsymbol{T}^+$ depends on the positions of nuclei because $\boldsymbol{T}^+$ is constructed by the operator that includes the nuclear-electron attraction potential. The relativistic effects are dominant for $\boldsymbol{T}^+$ in the atomic domains and for $\boldsymbol{V}^+$ in the atomic domains and interatomic interactions with the nearest-neighbor atoms. τ is the cutoff threshold for the distance, R_{AB}, between atoms A and B. The matrix representation of $\boldsymbol{g}_2^{\mathrm{LUT}}$ is written as

$$\left\langle \chi_\mu\chi_\nu \middle| \boldsymbol{g}_2^{\mathrm{LUT}} \middle| \chi_\lambda\chi_\sigma \right\rangle = \begin{cases} \left\langle \chi_\mu^A\chi_\nu^A \middle| \boldsymbol{g}_2^{++}(i,j) \middle| \chi_\lambda^A\chi_\sigma^A \right\rangle & \text{(one-center)} \\ \left\langle \chi_\mu^A\chi_\nu^B \middle| 1/r_{ij} \middle| \chi_\lambda^C\chi_\sigma^D \right\rangle & \text{(multicenter).} \end{cases} \tag{2.4.4}$$

Only the one-center TEIs are treated by relativistic transformation. The effects of relativistic transformations in multi-center TEIs are ignored.

The concept of LUT is also applied to the density operator.[32] Unitary transformation

of the density operator is performed when two AOs in the integral in Eqs. (2.3.36) and (2.3.37) belong to the same atom. Otherwise, nonrelativistic density operator is adopted. The electron density based on the LUT scheme is as follows:

$$\begin{aligned}\rho^{\mathrm{LUT}}(\mathbf{r}) &= \sum_i \langle \varphi_i | \delta^{\mathrm{LUT}}(\mathbf{r}'-\mathbf{r}) | \varphi_i \rangle \\ &= \begin{cases} \sum_i \sum_{\mu\nu} c_{\mu i}^* c_{\nu i} \langle \chi_\mu^A | \delta^{+}(\mathbf{r}'-\mathbf{r}) | \chi_\nu^B \rangle & (A=B) \\ \sum_i \sum_{\mu\nu} c_{\mu i}^* c_{\nu i} \langle \chi_\mu^A | \delta^{\mathrm{Nonrel.}}(\mathbf{r}'-\mathbf{r}) | \chi_\nu^B \rangle & (A\neq B), \end{cases}\end{aligned} \tag{2.4.5}$$

where

$$\langle \chi_\mu^A | \delta^{\mathrm{Nonrel.}}(\mathbf{r}-\mathbf{r}') | \chi_\nu^B \rangle = \chi_\mu^A(\mathbf{r})\,\chi_\nu^B(\mathbf{r}). \tag{2.4.6}$$

The time-consuming step of the LUT scheme is reduced to the unitary transformation in subsystems, i.e. the individual atoms. Therefore, the computational costs of LUT for one- and two-electron and density operators are of the scale $O(n)$.

References

1. M. Dolg and X. Cao, *Chem. Rev.* **112**, 403 (2012).

2. E. Schrödinger, *Ann. Phys.* **384**, 361 (1926).

3. P.A.M. Dirac, *Proc. R. soc. Lond. Ser. A-Contain. Pap. Math. Phys. Character*, **117**, 610 (1928).

4. A. Einstein, *Ann. Phys.* **322**, 891 (1905).

5. R.E. Moss, *Advanced molecular quantum mechanics* (Chapman and Hall, London, 1973).

6. G. Breit, *Phys. Rev.* **34**, 553 (1929).

7. G. Breit, *Phys. Rev.* **39**, 616 (1932).

8. L.L. Foldy and S.A. Wouthuysen, *Phys. Rev.* **78**, 29 (1950).

9. M. Douglas and N.M. Kroll, *Ann. Phys.* **82**, 89 (1974).

10. B.A. Hess, *Phys. Rev. A*, **33**, 3742 (1986).

11. T. Nakajima and K. Hirao, *J. Chem. Phys.* **113**, 7786 (2000).

12. A. Wolf, M. Reiher, and B.A. Hess, *J. Chem. Phys.* **117**, 9215 (2002).

13. M. Reiher, *Theor. Chem. Acc.* **116**, 241 (2006).

14. E. Lenthe, E.J. Baerends, and J.G. Snijders, *J. Chem. Phys.* **99**, 4597 (1993).

15. E. van Lenthe, E.J. Baerends, and J.G. Snijders, *J. Chem. Phys.* **101**, 9783 (1994).

16. K.G. Dyall, *J. Chem. Phys.* **106**, 9618 (1997).

17. M. Reiher and A. Wolf, *J. Chem. Phys.* **121**, 2037 (2004).

18. W. Kutzelnigg and W. Liu, *Mol. Phys.* **104**, 2225 (2006).

19. W. Liu and D. Peng, *J. Chem. Phys.* **125**, 044102 (2006).

20. M. Iliaš and T. Saue, *J. Chem. Phys.* **126**, 064102 (2007).

21. W. Liu and D. Peng, *J. Chem. Phys.* **131**, 031104 (2009).

22. M. Barysz and A.J. Sadlej, *J. Chem. Phys.* **116**, 2696 (2002).

23. J. Sucher, *Phys. Rev. A*, **22**, 348 (1980).

24. R. Samzow, B.A. Hess, and G. Jansen, *J. Chem. Phys.* **96**, 1227 (1992).

25. T. Nakajima and K. Hirao, *J. Chem. Phys.* **119**, 4105 (2003).

26. J. Seino and M. Hada, *Chem. Phys. Lett.* **442**, 134 (2007).

27. J. Seino and M. Hada, *Chem. Phys. Lett.* **461**, 327 (2008).

28. J. Sikkema, L. Visscher, T. Saue, and M. Iliaš, *J. Chem. Phys.* **131**, 124116 (2009).

29. J. Seino, W. Uesugi, and M. Hada, *J. Chem. Phys.* **132**, 164108 (2010).

30. B.A. Hess, *Phys. Rev. A*, **32**, 756 (1985).

31. T. Oyama, Y. Ikabata, J. Seino, and H. Nakai, *Chem. Phys. Lett.* **680**, 37 (2017).

32. Y. Ikabata, T. Oyama, M. Hayami, J. Seino, and H. Nakai, *J. Chem. Phys.* **150**, 164104 (2019).

33. P. Hohenberg and W. Kohn, *Phys. Rev.* **136**, B864 (1964).

34. W. Kohn and L. J. Sham, *Phys. Rev.* **140**, A1133 (1965).

35. L. Gagliardi, N.C. Handy, A.G. Ioannou, C. Skylaris, S. Spencer, A. Willetts, and A. M. Simper, *Chem. Phys. Lett.* **283**, 187 (1998).

36. K.G. Dyall, *J. Comput. Chem.* **23**, 786 (2002).

37. D. Peng, W. Liu, Y. Xiao, and L. Cheng, *J. Chem. Phys.* **127**, 104106 (2007).

38. A.V. Matveev and N. Rösch, *J. Chem. Phys.* **128**, 244102 (2008).

39. J. Thar and B. Kirchner, *J. Chem. Phys.* **130**, 124103 (2009).

40. J. Seino and H. Nakai, *J. Chem. Phys.* **136**, 244102 (2012).

41. J. Seino and H. Nakai, *J. Chem. Phys.* **137**, 144101 (2012).

42. J. Seino and H. Nakai, *J. Chem. Phys.* **139**, 034109 (2013).

43. D. Peng and M. Reiher, *J. Chem. Phys.* **136**, 244108 (2012).

44. D. Peng, N. Middendorf, F. Weigend, and M. Reiher, *J. Chem. Phys.* **138**, 184105 (2013).

45. J. Liu and L. Cheng, *J. Chem. Phys.* **148**, 144108 (2018).

46. S. Knecht, M. Repisky, H.J.A. Jensen, and T. Saue, *J. Chem. Phys.* **157**, 114106 (2022).

47. Y. Nakajima, J. Seino, and H. Nakai, *J. Chem. Phys.* **139**, 244107 (2013).

48. Y. Nakajima, J. Seino, and H. Nakai, *J. Chem. Theory Comput.* **12**, 2181 (2016).

49. Y.J. Franzke, N. Middendorf, and F. Weigend, *J. Chem. Phys.* **148**, 104110 (2018).

50. W. Zou, G. Guo, B. Suo, and W. Liu, *J. Chem. Theory Comput.* **16**, 1541 (2020).

51. Y.J. Franzke and F. Weigend, *J. Chem. Theory Comput.* **15**, 1028 (2019).

52. H. Zhu, C. Gao, M. Filatov, and W. Zou, *Phys. Chem. Chem. Phys.* **22**, 26776 (2020).

Chapter 3 Acceleration of TEIs utilizing matrix decomposition*

3.1 Introduction

The relativistic treatment of two-electron interactions is computationally expensive because it requires evaluations of several types of TEIs and their relativistic transformations, such as Eqs. (2.3.25)–(2.3.27). As mentioned in the Chapter 2, the computational costs of the two-electron term of the IOTC Hamiltonian, for example, are of scale $O(N^5)$, where N represents the number of PBFs owing to the unitary transformation of the TEIs. To perform transformation efficiently, several methods have been proposed that focus on the locality of the relativistic effect[1–9] including the LUT scheme. The LUT scheme achieves linear-scaling computational time with respect to the molecular size within chemical accuracy.

This chapter focuses on the acceleration technique for evaluation of TEIs. In the framework of nonrelativistic calculations, CD was utilized for the efficient evaluation of ERIs, taking advantage of the symmetric characteristics of the ERI matrix.[10–13] Here, ERIs, which are one of the TEIs, represent Coulomb interaction by the inverse of the distance between two electrons. TEIs other than ERIs also arise in the relativistic calculations due to the relativistic treatment of two-electron operators. Practically, TEIs are approximated as an incomplete CD integral matrix. A related idea was adopted for density fitting, also called the resolution-of-identity approximation, which describes the TEIs as an inner projection in terms of an auxiliary basis.[14,15] The CD approach is more general because it does not require an auxiliary basis. Furthermore, errors caused by the approximation can be controlled by the CD threshold. So far, the CD scheme has been applied to various

* Reproduced from the article by Chinami Takashima and Hiromi Nakai, *Chem. Phys. Lett.* **828**, 140714 (2023).

wavefunction theories such as the Hartree–Fock,[12,13] MP2,[12,16] CC,[17] complete active space-self-consistent field methods,[18,19] and multiconfiguration second-order perturbation theory.[20] The CD method has also been utilized in property calculations such as that of molecular gradient,[18,21,22] polarizability,[23–25] optical rotation,[24,26] and chemical shift with the use of gauge-including atomic orbitals.[27–29] Highly efficient techniques for the CD of ERIs have been developed realizing drastically reduction of the computational costs compared to earlier algorithms.[30,31]

This chapter examined the application of CD for evaluating TEIs using the IOTC Hamiltonian. Furthermore, extension to the lower-upper decomposition (LUD) was investigated to accommodate the asymmetric TEI matrices. The remainder of this chapter is organized as follows: Section 3.2 summarizes the algorithm and implementation of the proposed method. Section 3.3 presents the results of numerical assessments. Finally, concluding remarks are presented in Section 3.4.

3.2 Algorithm and implementation

3.2.1 Symmetry of TEIs in the two-electron IOTC Hamiltonian

Generally, two kinds of notation for TEIs are used. One is the Dirac notation:

$$\left\langle \chi_\mu \chi_\nu \middle| \chi_\lambda \chi_\sigma \right\rangle = \int\int d\mathbf{r}_i d\mathbf{r}_j \chi_\mu^*(\mathbf{r}_i)\chi_\nu^*(\mathbf{r}_j) g(i,j) \chi_\lambda(\mathbf{r}_i)\chi_\sigma(\mathbf{r}_j), \tag{3.2.1}$$

and the other is the Mulliken notation:

$$\left(\chi_\mu \chi_\nu \middle| \chi_\lambda \chi_\sigma\right) = \int\int d\mathbf{r}_i d\mathbf{r}_j \chi_\mu^*(\mathbf{r}_i)\chi_\lambda^*(\mathbf{r}_j) g(i,j) \chi_\nu(\mathbf{r}_i)\chi_\sigma(\mathbf{r}_j). \tag{3.2.2}$$

This chapter uses the Mulliken notation. The matrix representations of TEIs for two-electron IOTC Hamiltonian provided in Eqs. (2.3.25)–(2.3.27) are rewritten in Mulliken notation as follows:

$$\begin{aligned} &\left(\chi_\mu \chi_\nu \middle| \chi_\lambda \chi_\sigma\right)^{\mathrm{sf1}} \\ &= \sum_{k_a k_b k_c k_d} \left(\chi_\mu \middle| \boldsymbol{M}_i \middle| k_a\right)\left(\chi_\nu \middle| \boldsymbol{M}_i \middle| k_b\right)\left(k_a k_b \middle| 1/r_{ij}\mathbf{1}_2 \middle| k_c k_d\right)\left(k_c \middle| \boldsymbol{M}_j \middle| \chi_\lambda\right)\left(k_d \middle| \boldsymbol{M}_j \middle| \chi_\sigma\right), \end{aligned} \tag{3.2.3}$$

$$\left(\chi_\mu\chi_\nu\middle|\chi_\lambda\chi_\sigma\right)^{\mathrm{sf2}}$$
$$=\sum_{k_ak_bk_ck_d}\left(\chi_\mu\middle|\boldsymbol{d}_i\middle|k_a\right)\left(\chi_\nu\middle|\boldsymbol{d}_i\middle|k_b\right)\left(k_ak_b\middle|\boldsymbol{p}_i1/r_{ij}\mathbf{1}_2\cdot\boldsymbol{p}_i\middle|k_ck_d\right)\left(k_c\middle|\boldsymbol{M}_j\middle|\chi_\lambda\right)\left(k_d\middle|\boldsymbol{M}_j\middle|\chi_\sigma\right), \tag{3.2.4}$$

and

$$\left(\chi_\mu\chi_\nu\middle|\chi_\lambda\chi_\sigma\right)^{\mathrm{sf3}}$$
$$=\sum_{k_ak_bk_ck_d}\left(\chi_\mu\middle|\boldsymbol{d}_i\middle|k_a\right)\left(\chi_\nu\middle|\boldsymbol{d}_i\middle|k_b\right)\left(k_ak_b\middle|\boldsymbol{p}_i\left[\boldsymbol{p}_j1/r_{ij}\mathbf{1}_2\cdot\boldsymbol{p}_j\right]\cdot\boldsymbol{p}_i\middle|k_ck_d\right)\left(k_c\middle|\boldsymbol{d}_j\middle|\chi_\lambda\right)\left(k_d\middle|\boldsymbol{d}_j\middle|\chi_\sigma\right), \tag{3.2.5}$$

where superscripts sf1, sf2, and sf3 represent the TEIs of the Coulomb-like $\boldsymbol{g}_2^{\mathrm{sf1}}$, Darwin-like $\boldsymbol{g}_2^{\mathrm{sf2}}$, and specific spin-free interaction terms $\boldsymbol{g}_2^{\mathrm{sf3}}$, respectively. The angular momentum of the PBFs in $\left(k_ak_b\middle|\boldsymbol{p}_i1/r_{ij}\mathbf{1}_2\cdot\boldsymbol{p}_i\middle|k_ck_d\right)$ and $\left(k_ak_b\middle|\boldsymbol{p}_i\left[\boldsymbol{p}_j1/r_{ij}\mathbf{1}_2\cdot\boldsymbol{p}_j\right]\cdot\boldsymbol{p}_i\middle|k_ck_d\right)$ increased or decreased by one and two from the original value, respectively, because $\boldsymbol{p}_j=-\mathrm{i}\nabla_{r_j}$. Note that the symmetry of three TEIs is difference, namely, $\left(\chi_\mu\chi_\nu\middle|\chi_\lambda\chi_\sigma\right)^{\mathrm{sf2}}$ is asymmetric for two electrons *i* and *j*, that is

$$\left(\chi_\mu\chi_\nu\middle|\chi_\lambda\chi_\sigma\right)\neq\left(\chi_\lambda\chi_\sigma\middle|\chi_\mu\chi_\nu\right), \tag{3.2.6}$$

while $\left(\chi_\mu\chi_\nu\middle|\chi_\lambda\chi_\sigma\right)^{\mathrm{sf1}}$ and $\left(\chi_\mu\chi_\nu\middle|\chi_\lambda\chi_\sigma\right)^{\mathrm{sf3}}$ are symmetric for *i* and *j*, i.e.,

$$\left(\chi_\mu\chi_\nu\middle|\chi_\lambda\chi_\sigma\right)=\left(\chi_\lambda\chi_\sigma\middle|\chi_\mu\chi_\nu\right). \tag{3.2.7}$$

3.2.2 Matrix decomposition of TEIs

This section explains the methodology of CD and LUD of the primitive integrals in Eqs. (3.2.3)–(3.2.7). Consider the matrix representation of TEI $\boldsymbol{V}$ as

$$\begin{aligned}V_{ab,cd}&=\left(k_ak_b\middle|g(i,j)\middle|k_ck_d\right)\\&=\int\int d\mathbf{r}_id\mathbf{r}_jk_a^*\left(\mathbf{r}_i\right)k_c^*\left(\mathbf{r}_j\right)g(i,j)k_b\left(\mathbf{r}_i\right)k_d\left(\mathbf{r}_j\right)\\&=\left(ab\,|\,cd\right).\end{aligned} \tag{3.2.8}$$

The two indices, *ab* and *cd* in Eq. (3.2.8), are called the overlap distribution. Throughout this chapter, the overlap distribution is represented by capital letters *I*, *J*, *K*, ….

When $\boldsymbol{V}$ is a symmetric matrix, it can be decomposed by the Cholesky procedure into a product of the lower triangular matrix $\boldsymbol{L}$ and its transpose as follows:

$$\boldsymbol{V} = \boldsymbol{L}\boldsymbol{L}^{\mathrm{T}}. \tag{3.2.9}$$

Note that $\boldsymbol{V}$ must be factorized by a pivoting procedure with truncation because $\boldsymbol{V}$ is not a positive-definite but a positive-semidefinite matrix and occasionally has a negative definite part due to the round off errors on computers.[12] The formulas of the diagonal and off-diagonal elements of $\boldsymbol{L}$ are given by

$$L_{JJ} = \left(V_{JJ} - \sum_{K=1}^{J-1} L_{JK}^2 \right)^{1/2} \tag{3.2.10}$$

and

$$L_{IJ} = \left(V_{IJ} - \sum_{K=1}^{J-1} L_{IK} L_{JK} \right) / L_{JJ} \qquad \left(I = J+1, J+2, \cdots, M \right), \tag{3.2.11}$$

respectively, where *M* is the number of rows in $\boldsymbol{L}$.

Figure 3.1(a) shows the algorithm used to obtain the elements of $\boldsymbol{L}$. In the first step, all diagonal elements of the primitive integrals are calculated, followed by the selection of the largest diagonal element V_{JJ} in the *J*-th iteration as the pivot. Using V_{JJ}, the diagonal element $\boldsymbol{L}$ is calculated as follows:

$$L_{JJ} \leftarrow \sqrt{V_{JJ}}. \tag{3.2.12}$$

Next, the partial column of $\boldsymbol{V}$ is obtained, followed by the calculation of the corresponding partial column of $\boldsymbol{L}$ using Eq. (3.2.11). Then, stored diagonal elements are updated as

$$V_{II} \leftarrow V_{II} - L_{IJ}^2 \quad \left(I = J+1, J+2, \ldots, M \right). \tag{3.2.13}$$

If the largest element among the updated diagonal terms is smaller than the threshold δ, the procedure is terminated. The subsequent elements of $\boldsymbol{V}$ are discarded. The number of iteration steps at the end of the procedure *R* becomes the rank of the truncated $\boldsymbol{L}$, which

corresponds to the number of columns. The matrix elements of $\boldsymbol{V}$ are approximated by the matrix elements of $\boldsymbol{L}$ as follows:

$$V_{ab,cd} \approx \sum_{K}^{R} L_{ab,K} L_{cd,K} \,. \tag{3.2.14}$$

As the absolute value of the error with the approximation in Eq. (3.2.14) becomes less than δ in all elements of $\boldsymbol{V}$ from the Cauchy–Schwarz inequality,[12] δ determines the accuracy of the decomposition. CD is applicable to both $\left(k_a k_b \middle| 1/r_{ij}\mathbf{1}_2 \middle| k_c k_d\right)$ and $\left(k_a k_b \middle| \boldsymbol{p}_i \left[\boldsymbol{p}_j 1/r_{ij}\mathbf{1}_2 \cdot \boldsymbol{p}_j\right] \cdot \boldsymbol{p}_i \middle| k_c k_d\right)$.

For the asymmetric matrix $\left(k_a k_b \middle| \boldsymbol{p}_i 1/r_{ij}\mathbf{1}_2 \cdot \boldsymbol{p}_i \middle| k_c k_d\right)$, LUD, which is a more general case of CD, is applied. The LUD is the factorization of a square matrix into the product of a lower triangular matrix $\boldsymbol{L}$ and an upper triangular matrix $\boldsymbol{U}$. In this study, the diagonal elements of $\boldsymbol{L}$ were set to one. Subsequently, the off-diagonal elements of $\boldsymbol{L}$ and $\boldsymbol{U}$ are evaluated as

$$L_{IJ} = \left(V_{IJ} - \sum_{K=1}^{J-1} L_{IJ} U_{KJ} \right) \Big/ U_{JJ} \qquad (I > J) \tag{3.2.15}$$

and

$$U_{IJ} = V_{IJ} - \sum_{K=1}^{I-1} L_{IK} U_{KJ} \qquad (I \le J) \,. \tag{3.2.16}$$

Figure 3.1(b) shows the algorithm used to obtain elements of $\boldsymbol{L}$ and $\boldsymbol{U}$. As shown in Eq. (3.2.15), the calculation of the off-diagonal elements of $\boldsymbol{L}$ requires a division by the diagonal elements of $\boldsymbol{U}$. A pivoting procedure was necessary to prevent division by zero. Although partial pivoting that permutates either rows or columns is generally sufficient, this study adopts full pivoting to introduce truncation by a threshold, as in the case of CD. The first step is the calculation of all diagonal elements of $\boldsymbol{V}$, followed by selecting the largest diagonal element in V_{JJ} in the J-th iteration as the pivot and calculating the partial column and row of $\boldsymbol{V}$. Using V_{JJ}, the corresponding diagonal elements of $\boldsymbol{U}$ are obtained by

$$U_{JJ} \leftarrow V_{JJ} \,. \tag{3.2.17}$$

The corresponding columns and rows of $\boldsymbol{L}$ and $\boldsymbol{U}$ are computed using the elements calculated in $\boldsymbol{V}$ and U_{JJ} using Eqs. (3.2.15) and (3.2.16). Then, stored diagonal elements are updated as follows:

$$V_{II} \leftarrow V_{II} - L_{IJ}^2 \quad \left(I = J+1, J+2, \ldots, M\right). \tag{3.2.18}$$

The procedure is continued until the largest element in the updated diagonal elements becomes smaller than the threshold δ. The number of iterations at the end of the procedure, R, becomes the rank of the truncated $\boldsymbol{L}$ and $\boldsymbol{U}$, which corresponds to the number of columns or rows. The matrix element of $\boldsymbol{V}$ is approximated by elements of $\boldsymbol{L}$ and $\boldsymbol{U}$ as follows:

$$V_{ab,cd} \approx \sum_{K}^{R} L_{ab,K} U_{K,cd} \,. \tag{3.2.18}$$

Since the Cauchy–Schwarz inequality does not hold good, the relationship between δ and the error in approximated TEIs is unclear, different from the case of CD.

3.2.3 IOTC transformation of $\boldsymbol{L}$ and $\boldsymbol{U}$ and construction of the Fock matrix

The transformations of $\boldsymbol{L}$ and $\boldsymbol{U}$ by $\boldsymbol{M}$ and $\boldsymbol{d}$, corresponding to Eqs. (3.2.3)–(3.2.5), are performed analogously as the transformation of AO to MO of the Cholesky matrices.[12] The general expressions of elements in the transformed matrices are

$$L_{\mu\nu,K}^{\text{trans}} = \sum_{a}\sum_{b} X_{\mu a} X_{\nu b} L_{ab,K} \quad (X = M, d) \tag{3.2.19}$$

for symmetric terms, and

$$L_{\mu\nu,K}^{\text{trans}} = \sum_{a}\sum_{b} d_{\mu a} d_{\nu b} L_{ab,K} \tag{3.2.20}$$

and

$$U_{\mu\nu,K}^{\text{trans}} = \sum_{a}\sum_{b} M_{\mu a} M_{\nu b} U_{ab,K} \tag{3.2.21}$$

for an asymmetric term. The two-electron term of Fock matrix $\boldsymbol{G}$ is constructed from the transformed matrices $\boldsymbol{L}^{\text{trans}}$ and $\boldsymbol{U}^{\text{trans}}$ in a self-consistent field (SCF) calculation. For

simplicity, superscript "trans" is omitted hereafter. The matrix element of $\boldsymbol{G}$ for the restricted Hartree–Fock method is expressed as

$$G_{\mu\nu} = \sum_i \sum_{\lambda\sigma} C_{\lambda i} C^*_{\sigma i} \left[2\left(\chi_\mu \chi_\nu \mid \chi_\lambda \chi_\sigma\right) - \left(\chi_\mu \chi_\sigma \mid \chi_\lambda \chi_\nu\right) \right], \tag{3.2.22}$$

with MO coefficients C, where the first and second terms are Coulomb and exchange terms, respectively. As the TEIs are given by the sum of $\left(\chi_\mu \chi_\nu \middle| \chi_\lambda \chi_\sigma\right)^{\mathrm{sf1}}$, $\left(\chi_\mu \chi_\nu \middle| \chi_\lambda \chi_\sigma\right)^{\mathrm{sf2}}$, and $\left(\chi_\mu \chi_\nu \middle| \chi_\lambda \chi_\sigma\right)^{\mathrm{sf3}}$ in the two-electron IOTC method, $\boldsymbol{G}$ can be divided into three terms:

$$G_{\mu\nu} = G^{\mathrm{sf1}}_{\mu\nu} + G^{\mathrm{sf2}}_{\mu\nu} + G^{\mathrm{sf3}}_{\mu\nu}. \tag{3.2.23}$$

$G^{\mathrm{sf1}}_{\mu\nu}$ and $G^{\mathrm{sf3}}_{\mu\nu}$ were constructed using $\boldsymbol{L}$ as follows: The Coulomb term $G^{\mathrm{sfx,C}}_{\mu\nu}$ (x = 1, 3) is given by

$$\begin{aligned} G^{\mathrm{sfx,C}}_{\mu\nu} &\approx 2 \sum_i \sum_{\lambda\sigma} C_{\lambda i} C^*_{\sigma i} \sum_{K=1}^{R} L_{\mu\nu,K} L_{\lambda\sigma,K} \\ &= 2 \sum_{\lambda\sigma} P_{\lambda\sigma} \sum_{K=1}^{R} L_{\mu\nu,K} L_{\lambda\sigma,K} \\ &= 2 \sum_{K=1}^{R} L_{\mu\nu,K} \sum_{\lambda\sigma} P_{\lambda\sigma} L_{\lambda\sigma,K} \end{aligned} \tag{3.2.24}$$

and the exchange term $G^{\mathrm{sfx,E}}_{\mu\nu}$ (x = 1, 3) by

$$\begin{aligned} G^{\mathrm{sfx,E}}_{\mu\nu} &\approx -\sum_i \sum_{\lambda\sigma} C^*_{\sigma i} \left[\sum_{K=1}^{R} L_{\mu\sigma,K} L_{\lambda\nu,K} \right] C_{\lambda i} \\ &= -\sum_{K=1}^{R} L'_{\mu,K} L'_{\lambda,K}. \end{aligned} \tag{3.2.25}$$

Here, $\boldsymbol{L}$**'** is MO transformed $\boldsymbol{L}$ given by

$$L'_{\mu,K} = \sum_i \sum_{\sigma} C_{\sigma i} L_{\mu\sigma,K}\ . \tag{3.2.26}$$

Similarly, $G^{\mathrm{sf2}}_{\mu\nu}$ was constructed using $\boldsymbol{L}$ and $\boldsymbol{U}$. The Coulomb term $G^{\mathrm{sf2,C}}_{\mu\nu}$ and exchange term $G^{\mathrm{sf2,E}}_{\mu\nu}$ are given by

$$
\begin{aligned}
G_{\mu\nu}^{\mathrm{sf2,C}} &\approx 2\sum_{i}\sum_{\lambda\sigma} C_{\lambda i} C_{\sigma i}^{*} \left[\sum_{K=1}^{R} L_{\mu\nu,K} U_{K,\lambda\sigma} + \sum_{K=1}^{R} L_{\lambda\sigma,K} U_{K,\mu\nu} \right] \\
&= 2\sum_{\lambda\sigma} P_{\lambda\sigma} \left[\sum_{K=1}^{R} L_{\mu\nu,K} U_{K,\lambda\sigma} + \sum_{K=1}^{R} L_{\lambda\sigma,K} U_{K,\mu\nu} \right] \\
&= 2\sum_{K=1}^{R} \left[L_{\mu\nu,K} \sum_{\lambda\sigma} P_{\lambda\sigma} U_{K,\lambda\sigma} + U_{K,\mu\nu} \sum_{\lambda\sigma} P_{\lambda\sigma} L_{\lambda\sigma,K} \right]
\end{aligned}
\tag{3.2.25}
$$

and

$$
\begin{aligned}
G_{\mu\nu}^{\mathrm{sf2,E}} &\approx -\sum_{i}\sum_{\lambda\sigma} C_{\sigma i}^{*} \left[\sum_{K=1}^{R} L_{\mu\sigma,K} U_{K,\lambda\nu} + \sum_{K=1}^{R} L_{\lambda\nu,K} U_{K,\mu\sigma} \right] C_{\lambda i} \\
&= -\sum_{K=1}^{R} \left[L'_{\mu,K} U'_{K,\lambda} + L'_{\lambda,K} U'_{K,\mu} \right]
\end{aligned}
\tag{3.2.26}
$$

with Eq. (3.2.26) and MO transformed $\boldsymbol{U}$,

$$
U'_{K,\mu} = \sum_{i}\sum_{\sigma} C_{\sigma i} U_{K,\mu\sigma} \,. \tag{3.2.27}
$$

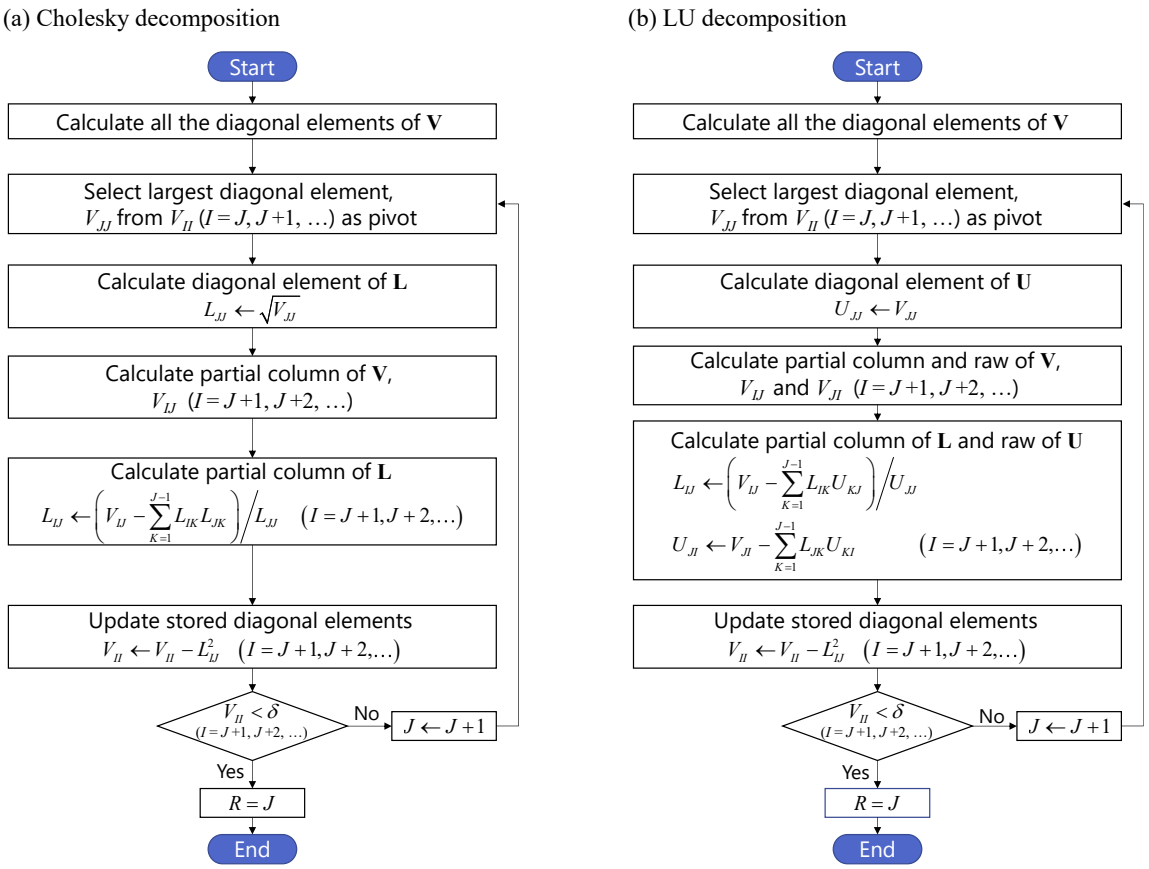

Figure 3.1. Algorithms of (a) CD and (b) LUD of TEIs.

3.3 Numerical assessments

3.3.1 Computational details

This section assesses the performance of the present methods, which were implemented to the modified version of GAMESS program.[32] The threshold for the integral screenings and the cutoffs in the reference calculations, namely the conventional two-electron IOTC Hamiltonian, was set to 1.0×10^{-12}. Numerical tests were performed for noble gas atoms, Ne, Ar, Kr, Xe, and Rn; hydrogen halides, HX (X = F, Cl, Br, I, and At); and hydrogen bromide chains, $(HBr)_n$ (n = 2–4). The intramolecular distances of H–X were fixed at 0.970, 1.350, 1.500, 1.710, and 1.729 Å for H–F, H–Cl, H–Br, H–I, and H–At, respectively. The intermolecular distances in $(HBr)_n$ were 2.53 Å. The H–Br–H and Br–H–Br bond angles were 120° and 180°, respectively. As basis sets, Sapporo-DZP-2012[33,34] for H to Ar and Sapporo-DKH3-DZP-2012[35] for Br to Rn were adopted in an uncontracted manner. In addition, the uncontracted Sapporo-*X*ZP-2012 (*X* = D, T, or Q) basis sets with and without diffuse functions[33–35] for boron, including the *s*, *p*, *d*, *f*, and *g* functions, were used to examine the accuracy of the approximated integral values. For example, the sizes of the Sapporo-*X*ZP-2012 basis sets for boron are summarized in Table 3.1.

Table 3.1. Sizes of the Sapporo-*X*ZP-2012 (*X* = D, T, or Q) basis sets without/with diffuse functions for the boron element. The abbreviations, primitive functions, total number of primitive basis functions (PBFs) are listed.

	abbreviation	functions	# of PBFs
Sapporo-DZP-2012	DZP	(9s5p2d)	36
Sapporo-DZP-2012 + diffuse	DZP+d	(10s6p3d)	46
Sapporo-TZP-2012	TZP	(10s6p3d2f)	66
Sapporo-TZP-2012 + diffuse	TZP+d	(11s7p4d3f)	86
Sapporo-QZP-2012	QZP	(12s8p4d3f2g)	120
Sapporo-QZP-2012 + diffuse	QZP+d	(13s9p5d4f3g)	155

3.3.2 Accuracy

The maximal absolute error (MaxAE) $\varepsilon_{\max}$ of approximated primitive TEIs was defined as

$$\varepsilon_{\max} = \begin{cases} \max\left| \sum_{K}^{R} L_{ab,K} L_{cd,K} - \left(k_a k_b \left| \boldsymbol{g}_2^{\mathrm{sfx}} \right| k_c k_d\right) \right| & (x = 1,3) \\ \max\left| \sum_{K}^{R} L_{ab,K} U_{K,cd} - \left(k_a k_b \left| \boldsymbol{g}_2^{\mathrm{sfx}} \right| k_c k_d\right) \right| & (x = 2). \end{cases} \tag{3.3.1}$$

The calculations were performed with $\delta = 10^{-4}$, 10^{-5}, 10^{-6}, 10^{-7}, 10^{-8}, and 10^{-9}. Figure 3.2 shows $\varepsilon_{\max}$ in logarithms of (a) Coulomb-like, (b) specific spin-free interaction, and (c) Darwin-like terms in the calculations of the B atom by six types of basis sets. MaxAE $\varepsilon_{\max}$ depends mainly on δ and slightly on the type of basis function in the Coulomb-like and specific spin-free interaction terms and is close to the δ value. The results confirmed that the errors in the approximated primitive integrals in symmetric terms for electrons i and j are well controlled below a threshold value, not only for the s, p, and d functions but also for high angular momentum, such as the f and g functions. The MaxAEs $\varepsilon_{\max}$ in the Darwin-like term shown in Figure 3.2(c) change with the type of basis function. Although the values of $\varepsilon_{\max}$ fluctuate around ten times larger than δ, the approximation errors by LUD TEI matrix in the asymmetric term are still controllable by δ. Figures 3.3 and 3.4 show the results of BH and BH_3. As shown in Figures 3.3 and 3.4 , the errors of primitive integrals in molecules can be also controlled by δ.

Table 3.2 shows the total energy deviations (in hartree) obtained by the present method with $\delta = 10^{-4}$, 10^{-5}, 10^{-6}, 10^{-7}, 10^{-8}, and 10^{-9} and the conventional two-electron IOTC Hamiltonian for noble gas atoms and HX and $(HBr)_n$ molecules. Total energies obtained by using the conventional two-electron IOTC Hamiltonian are shown in parentheses. As δ becomes smaller, the absolute values of energy deviations tend to decrease: within 1 μhartree at $\delta \leq 10^{-6}$ for Ne, Ae, Xe, HF, HCl, and HI, and $\delta \leq 10^{-7}$ for Kr, Rn, $(HBr)_n$ (n = 1-4), and HAt. Although heavier-element systems appear to require a smaller threshold for

accuracy, the total energies converge to those of the conventional two-electron IOTC Hamiltonian, even for the fifth- and sixth-row elements, where relativistic effects are essential. The energies of the molecules converged to those obtained using the conventional two-electron IOTC Hamiltonian, as in the case of atoms.

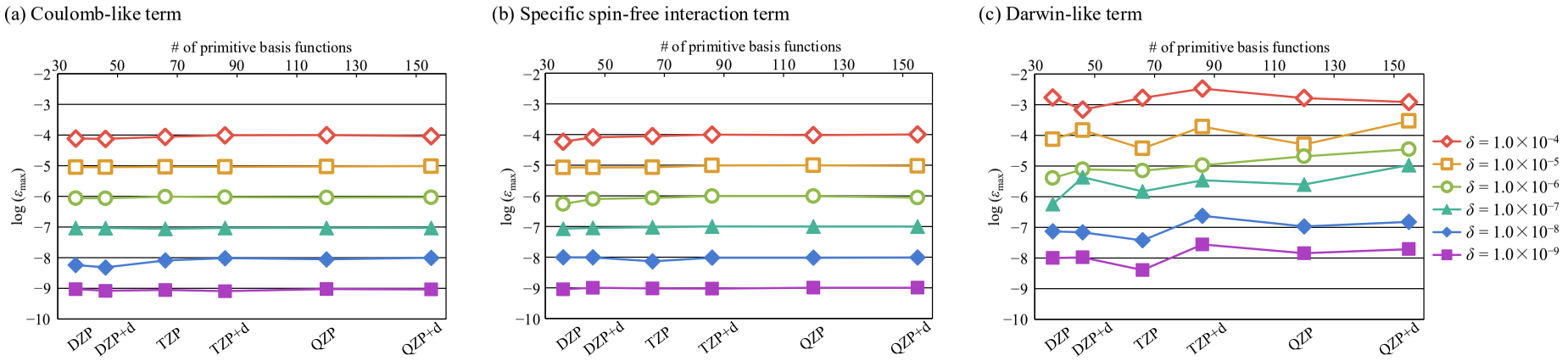

Figure 3.2. Maximal absolute errors of the approximated primitive TEIs $\varepsilon_{\max}$ in (a) Coulomb-like, (b) specific spin-free interaction, and (c) Darwin-like terms in the calculations of B atom. Sapporo-*X*ZP-2012 (X = D, T, or Q) basis sets without/with diffuse functions were used. As the threshold of the decomposition δ, 10^{-4}, 10^{-5}, 10^{-6}, 10^{-7}, 10^{-8}, and 10^{-9} were examined.

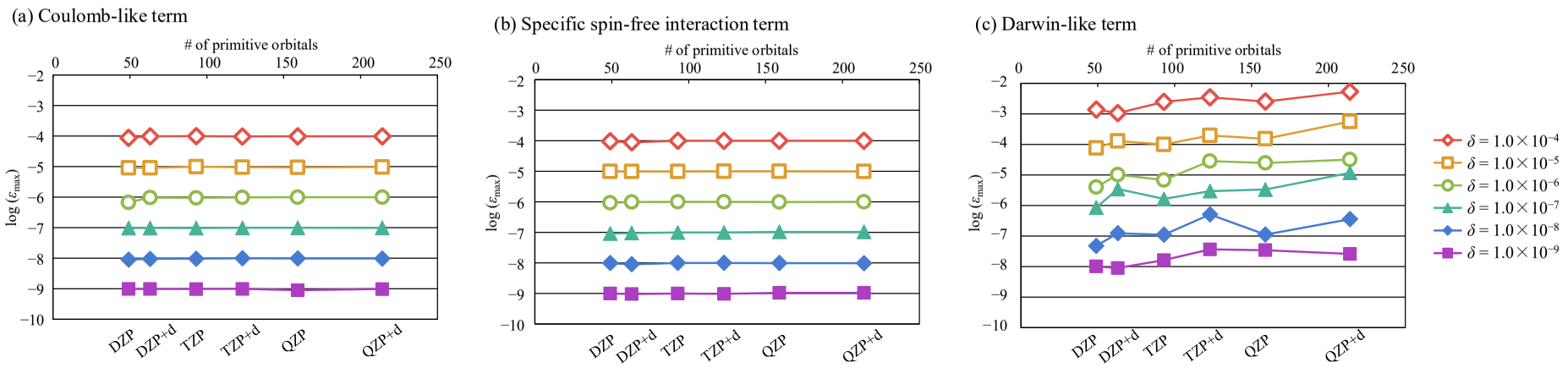

Figure 3.3. Maximal absolute errors of the approximated primitive TEIs ε_{max} in (a) Coulomb-like, (b) specific spin-free interaction, and (c) Darwin-like terms in the calculations of BH molecule. Sapporo-*X*ZP-2012 (*X* = D, T, or Q) basis sets without/with diffuse functions were used. As the threshold of the decomposition δ, 10^{-4}, 10^{-5}, 10^{-6}, 10^{-7}, 10^{-8}, and 10^{-9} were examined.

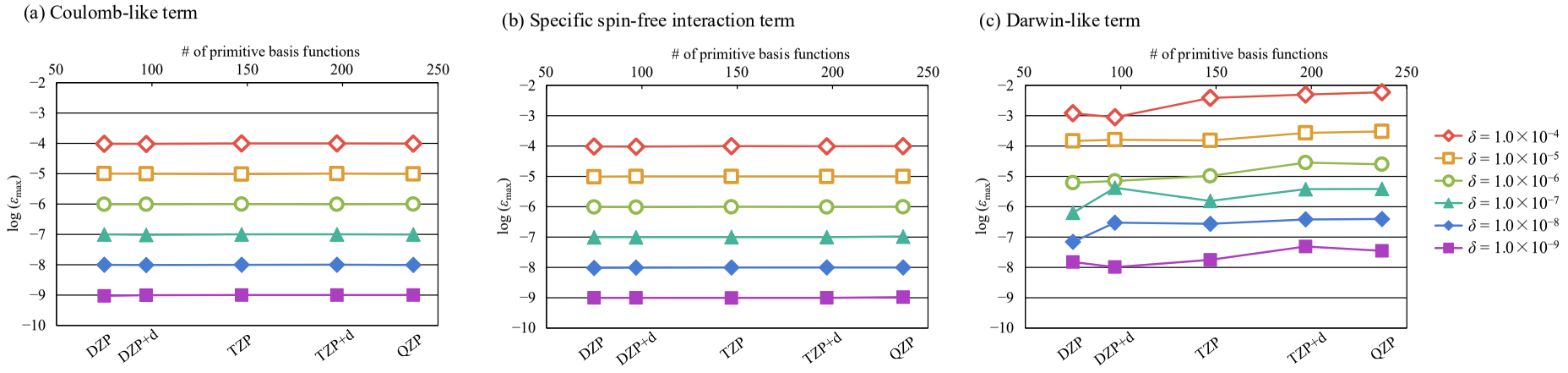

Figure 3.4. Maximal absolute errors of the approximated primitive TEIs $\varepsilon_{\max}$ in (a) Coulomb-like, (b) specific spin-free interaction, and (c) Darwin-like terms in the calculations of BH_3 molecule. Sapporo-*X*ZP-2012 (*X* = D, T, or Q) basis sets without/with diffuse functions were used. As the threshold of the decomposition δ, 10^{-4}, 10^{-5}, 10^{-6}, 10^{-7}, 10^{-8}, and 10^{-9} were examined.

Table 3.2. Deviations in total energy (in hartree) obtained by the present method with various thresholds and the conventional two-electron IOTC Hamiltonian of noble gas atoms and HX molecules. The total energies obtained by the conventional method are shown in parentheses.

δ	Ne	Ar	Kr	Xe	Rn
10^{-4}	−0.00000039	0.00008967	0.00005084	0.00044503	0.00124063
10^{-5}	0.00000115	−0.00000142	−0.00002169	0.00003563	0.00008069
10^{-6}	−0.00000001	−0.00000080	0.00000128	−0.00000096	−0.00000702
10^{-7}	0.00000002	0.00000018	0.00000008	0.00000041	−0.00000080
10^{-8}	0.00000001	0.00000000	0.00000000	0.00000002	−0.00000001
10^{-9}	0.00000000	0.00000000	0.00000000	0.00000001	0.00000000
	(−128.62675909)	(−528.63333826)	(−2788.73419359)	(−7445.50196731)	(−23573.33393888)

δ	HF	HCl	HBr	HI	HAt
10^{-4}	0.00000094	−0.00011900	0.00005708	0.00024925	0.00110454
10^{-5}	0.00000257	−0.00000983	−0.00002045	0.00003160	0.00008063
10^{-6}	0.00000016	−0.00000027	0.00000110	−0.00000083	−0.00000669
10^{-7}	0.00000000	0.00000008	0.00000008	0.00000028	0.00000014
10^{-8}	0.00000000	0.00000000	0.00000000	0.00000002	0.00000006
10^{-9}	0.00000000	0.00000000	0.00000000	0.00000000	0.00000004
	(−100.10822894)	(−461.51776971)	(−2605.51611690)	(−7115.13559819)	(−22883.68495904)

δ	$(HBr)_2$	$(HBr)_3$	$(HBr)_4$
10^{-4}	0.00011314	0.00017337	0.00023010
10^{-5}	−0.00004381	−0.00006181	−0.00008607
10^{-6}	0.00000212	0.00000307	0.00000406
10^{-7}	0.00000022	0.00000029	0.00000039
10^{-8}	0.00000006	0.00000001	0.00000002
10^{-9}	0.00000005	0.00000000	0.00000000
	(−5211.03068965)	(−7816.54595192)	(−10422.06140162)

3.3.3 Efficiency

Figure 3.5 provides the ratios (in %) of the number of nonzero elements in $\boldsymbol{L}^{\text{trans}}$ and $\boldsymbol{U}^{\text{trans}}$ obtained by the present method with the threshold δ of 10^{-9} and 10^{-4} with respect to those of nonzero IOTC-transformed TEIs of noble gas atoms and HX molecules. The ratios of the Coulomb-like term (Figures 3.5(a) and (b)), specific spin-free interaction term (Figures 3.5(c) and (d)), and Darwin-like term (Figures 3.5(e) and (f)) decreased rapidly when a higher-row element was included. The results of two threshold δ indicate the same tendency although smaller δ obviously gives larger ratios. The ratios of the Coulomb-like term are from ~74% (~75%) for Ne (HF) to ~15% (~12%) for Rn (HAt) at the threshold δ of 10^{-9}. The ratios of the specific spin-free interaction term, which are ~90% (~145%) for He (HF) and ~15% (~33%) for Rn (HAt) at the threshold δ of 10^{-9} are larger than those of the Coulomb-like term. As shown in Table 3.3, the number of nonzero IOTC-transformed TEIs of the specific spin-free interaction term is smaller than that of the Coulomb-like term, whereas the numbers of primitive TEIs of both terms shown in Table 3.4 are similar. The integral values of the specific spin-free interaction term become small because of the transformation matrix $\boldsymbol{d}$ shown in Eq. (3.2.4), some of which were removed. Consequently, the ratios of the Coulomb-like and specific spin-free interaction terms indicate difference tendencies. Some of the ratios the specific spin-free interaction term exceeded 100%, because values that are close to zero are obtained as elements in matrix $\boldsymbol{L}$ along the decomposition and the TEI matrix is commonly sparse due to zero integrals derived from symmetry and cutting the small integrals off with the threshold of 10^{-12}. Similar trends can be seen in the other terms. The ratios of the Darwin-like term in the range ~76% (~77%) for Ne (HF) to ~32% (~27%) for Rn (HAt) at the threshold δ of 10^{-9} are larger than those of the Coulomb-like term and smaller than those of the specific spin-free interaction term except for Kr, Xe, and Rn. The Darwin-like term is transformed by matrix $\boldsymbol{d}$ only for either electrons i or j whereas the specific spin-free interaction term is transformed for both

electrons i and j. Thus, the integral values and number of TEIs of the Darwin-like term are not as small as those of the specific spin-free interaction term. Comparing the results of noble gas atoms (Figures 3.5(a), (c), and (e)) with those of HX (Figures 3.5(b), (d), and (f)), the ratios of HX are larger than those of same row noble gas atoms in specific spin-free interaction terms and indicate values comparable to those of the same row noble gas atoms in Coulomb- and Darwin-like terms.

Figure 3.6 shows the system-size dependence of the number of nonzero IOTC-transformed TEIs obtained by the conventional two-electron IOTC Hamiltonian and $\boldsymbol{L}^{\mathrm{trans}}$ and $\boldsymbol{U}^{\mathrm{trans}}$ obtained by the present method with a threshold δ of 10^{-4} and 10^{-9} in the calculations for $(\mathrm{HBr})_n$ (n = 1–4). The theoretical value of the number of TEIs N^{tot}, which is of the scale $O(n^4)$, is also shown. Figures 3.6(a)–(c) show the results for the Coulomb-like, specific spin-free interaction, and Darwin-like terms, respectively. The conventional values were reduced from N^{tot} owing to the sparsity of the TEI matrix. The order of scaling obtained by δ of 10^{-4} and 10^{-9} are close in the three terms. Although the order of scaling of the present method is close to that of the conventional two-electron IOTC Hamiltonian, the prefactor is small in the present calculation. Comparing the three terms, the scaling of the specific spin-free interaction term was smaller than that of the other terms. The interatomic two-electron interactions decrease as n increases. This is presumed to be more apparent in the specific spin-free interaction term than in the other two terms, because the integral values of the specific spin-free interaction term are particularly small owing to the transformation matrix $\boldsymbol{d}$.

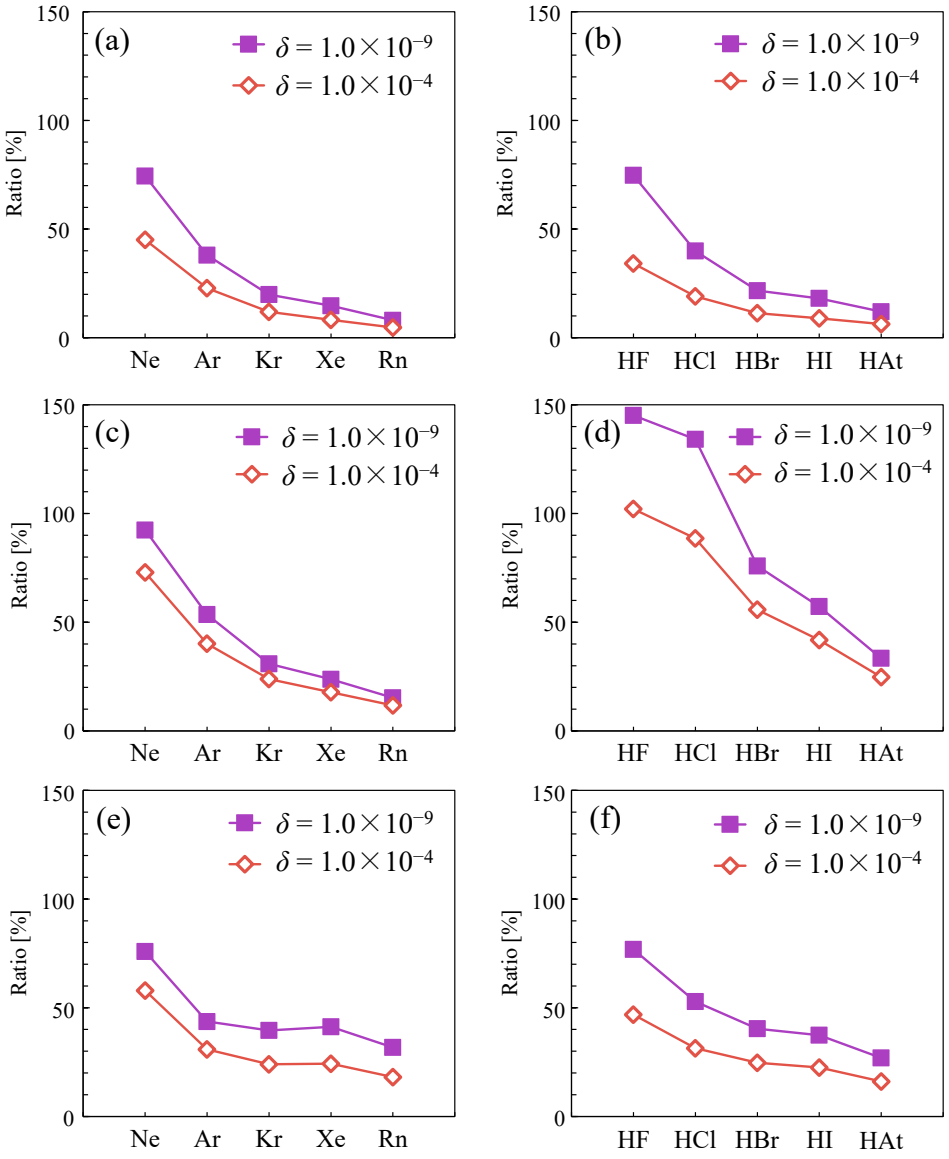

Figure 3.5. Ratios (in %) of the number of nonzero elements in $\boldsymbol{L}^{\text{trans}}$ (and $\boldsymbol{U}^{\text{trans}}$) obtained by the present method with the threshold δ of 10^{-4} and 10^{-9} with respect to the number of nonzero IOTC-transformed TEIs obtained by the conventional two-electron IOTC Hamiltonian. (a) and (b) are the Coulomb-like term, (c) and (d) are the specific spin-free interaction term, and (e) and (f) are the Darwin-like term. (a), (c), and (e) correspond to the results of noble gas atoms, and (b), (d), and (f) correspond to those of HX.

Table 3.3. Numbers of nonzero elements in IOTC-transformed matrix of decomposition $\boldsymbol{L}^{\text{trans}}$ and $\boldsymbol{U}^{\text{trans}}$ in Coulomb-like, specific spin-free interaction, and Darwin-like terms of rare gas atoms and HX molecules at $\delta = 10^{-4}$, 10^{-5}, 10^{-6}, 10^{-7}, 10^{-8}, and 10^{-9}. The values of Darwin-like term are the sum of the number of elements in both $\boldsymbol{L}^{\text{trans}}$ and $\boldsymbol{U}^{\text{trans}}$. Numbers of nonzero IOTC-transformed TEIs of three terms in conventional two-electron IOTC method (Conv.) are also provided. The ratios (in %) of the number of the matrix elements with respect to those of the TEIs obtained by conventional method are shown in parentheses.

	δ						Conv.
	10^{-4}	10^{-5}	10^{-6}	10^{-7}	10^{-8}	10^{-9}	
Coulomb-like term							
Ne	15789 (45.1)	17664 (50.4)	20028 (57.2)	20961 (59.9)	23559 (67.3)	26058 (74.4)	35017
Ar	96322 (22.8)	112075 (26.5)	121264 (28.7)	131881 (31.2)	153416 (36.3)	160612 (38.0)	422360
Kr	677040 (12.0)	757184 (13.4)	851248 (15.0)	951252 (16.8)	1050799 (18.6)	1124672 (19.9)	5664546
Xe	1229052 (8.3)	1462917 (9.8)	1630273 (11.0)	1789384 (12.0)	1989041 (13.4)	2187131 (14.7)	14868055
Rn	4455411 (4.8)	5196566 (5.5)	5815672 (6.2)	6245963 (6.7)	6900661 (7.4)	7535490 (8.0)	93705998
HF	138423 (34.2)	170618 (42.1)	200126 (49.4)	227838 (56.3)	269664 (66.6)	302672 (74.7)	404982
HCl	576077 (19.0)	707286 (23.3)	808627 (26.7)	922766 (30.4)	1091963 (36.0)	1209056 (39.9)	3030641
HBr	3279725 (11.3)	3780121 (13.1)	4392629 (15.2)	5037458 (17.4)	5731761 (19.8)	6264012 (21.7)	28906285
HI	5496114 (8.9)	6665404 (10.8)	7654041 (12.4)	8837628 (14.4)	9932460 (16.1)	11135588 (18.1)	61514129
HAt	17809902 (6.3)	21085681 (7.5)	24309949 (8.6)	26919672 (9.6)	30182603 (10.7)	33708228 (12.0)	281424214

Table 3.3. Continued.

	δ						Conv.
	10^{-4}	10^{-5}	10^{-6}	10^{-7}	10^{-8}	10^{-9}	
Specific spin-free interaction term							
Ne	24780 (72.9)	27185 (79.9)	28269 (83.1)	29921 (88.0)	30824 (90.6)	31423 (92.4)	34008
Ar	158270 (40.1)	170817 (43.3)	184451 (46.7)	195164 (49.4)	202012 (51.2)	211398 (53.6)	394743
Kr	1191961 (23.9)	1260724 (25.3)	1345312 (27.0)	1406927 (28.2)	1485381 (29.8)	1540737 (30.9)	4988808
Xe	2173670 (17.8)	2392659 (19.6)	2541174 (20.8)	2697593 (22.1)	2819918 (23.1)	2900945 (23.8)	12207402
Rn	8084872 (11.7)	8819089 (12.8)	9264146 (13.4)	9761345 (14.1)	10172415 (14.7)	10500933 (15.2)	69044978
HF	230958 (102.1)	259380 (114.6)	285291 (126.1)	305836 (135.2)	320749 (141.8)	328351 (145.1)	226262
HCl	885688 (88.6)	1021331 (102.1)	1116418 (111.6)	1234809 (123.5)	1290837 (129.1)	1341390 (134.1)	1000017
HBr	4530312 (55.8)	4983957 (61.4)	5331683 (65.6)	5696429 (70.1)	5982670 (73.7)	6164088 (75.9)	8123034
HI	7127766 (41.8)	7960831 (46.7)	8642605 (50.7)	9182323 (53.9)	9525013 (55.9)	9751475 (57.2)	17049341
HAt	22212311 (24.7)	24624117 (27.4)	26471206 (29.5)	27880083 (31.0)	28895522 (32.2)	29978978 (33.4)	89817474
Darwin-like term							
Ne	40190 (58.0)	44232 (63.8)	47123 (68.0)	50171 (72.3)	51830 (74.7)	52609 (75.9)	69345
Ar	258250 (30.9)	288646 (34.5)	313684 (37.5)	335771 (40.1)	349656 (41.8)	365477 (43.7)	836522
Kr	2608623 (24.0)	3036120 (27.9)	3442301 (31.6)	3726979 (34.2)	4045384 (37.2)	4309909 (39.6)	10884910
Xe	6737919 (24.3)	7536157 (27.1)	8649549 (31.2)	9535564 (34.4)	10536315 (38.0)	11447007 (41.2)	27758065
Rn	27151393 (18.1)	31329272 (20.9)	34762452 (23.1)	38727309 (25.8)	43208337 (28.8)	47707058 (31.8)	150207029
HF	353780 (46.9)	406021 (53.8)	463471 (61.4)	503314 (66.7)	542358 (71.9)	579813 (76.9)	754394
HCl	1423292 (31.4)	1652834 (36.4)	1875082 (41.3)	2088286 (46.0)	2232160 (49.2)	2398667 (52.8)	4538638
HBr	8590990 (24.7)	9870869 (28.3)	11121681 (31.9)	12147470 (34.9)	13104040 (37.6)	14063359 (40.4)	34837789
HI	15333118 (22.5)	17519908 (25.7)	19524909 (28.7)	21662651 (31.8)	23685269 (34.8)	25456335 (37.4)	68059524
HAt	52640165 (16.1)	59660186 (18.2)	65840035 (20.1)	72645848 (22.2)	80464979 (24.6)	88052790 (26.9)	327132645

Table 3.4. Numbers of nonzero elements in primitive decomposed matrix ***L*** and ***U*** in Coulomb-like, specific spin-free interaction, and Darwin-like terms of rare gas atoms and HX molecules at $\delta = 10^{-4}$, 10^{-5}, 10^{-6}, 10^{-7}, 10^{-8}, and 10^{-9}. The values of Darwin-like term are the sum of the number of elements in both ***L*** and ***U***. Numbers of nonzero primitive TEIs of three terms in conventional two-electron IOTC method (Conv.) are also provided. The ratios (in %) of the number of the matrix elements with respect to those of the TEIs obtained by conventional method are shown in parentheses.

	δ						Conv.
	10^{-4}	10^{-5}	10^{-6}	10^{-7}	10^{-8}	10^{-9}	
Coulomb-like term							
Ne	14022 (40.4)	15477 (44.6)	17234 (49.7)	17912 (51.6)	19741 (56.9)	21407 (61.7)	34680
Ar	90598 (21.6)	104339 (24.9)	112175 (26.8)	121122 (28.9)	138916 (33.2)	144697 (34.5)	418878
Kr	646428 (11.9)	720903 (13.2)	807882 (14.8)	899537 (16.5)	989857 (18.2)	1056569 (19.4)	5448734
Xe	1174736 (8.5)	1396377 (10.0)	1554455 (11.2)	1703829 (12.3)	1890327 (13.6)	2074072 (14.9)	13899535
Rn	4230703 (5.7)	4941149 (6.7)	5530667 (7.5)	5938758 (8.1)	6558264 (8.9)	7161183 (9.7)	73647760
HF	125587 (40.6)	151546 (48.9)	174226 (56.3)	194567 (62.8)	223627 (72.2)	245390 (79.2)	309698
HCl	545083 (29.7)	661631 (36.1)	749636 (40.9)	846817 (46.2)	987747 (53.9)	1083064 (59.1)	1832317
HBr	3181618 (23.6)	3650278 (27.1)	4219850 (31.3)	4814514 (35.7)	5449548 (40.4)	5934420 (44.0)	13487230
HI	5501984 (19.6)	6624477 (23.6)	7565527 (26.9)	8690995 (30.9)	9732789 (34.6)	10873892 (38.7)	28126582
HAt	18585711 (15.6)	21848698 (18.4)	25032846 (21.1)	27592610 (23.2)	30875068 (26.0)	34405513 (29.0)	118824602

Table 3.4 Continued.

	δ						Conv.
	10^{-4}	10^{-5}	10^{-6}	10^{-7}	10^{-8}	10^{-9}	
Specific spin-free interaction term							
Ne	20779 (59.9)	22506 (64.9)	23304 (67.2)	24687 (71.2)	25788 (74.4)	26334 (75.9)	34680
Ar	144347 (34.4)	155319 (37.0)	167543 (39.9)	177440 (42.3)	185396 (44.2)	197717 (47.1)	419457
Kr	1140123 (20.5)	1208835 (21.7)	1295478 (23.3)	1365872 (24.5)	1458265 (26.2)	1541523 (27.7)	5563725
Xe	2111208 (14.7)	2338327 (16.3)	2496507 (17.4)	2693034 (18.8)	2883970 (20.1)	3022709 (21.1)	14332579
Rn	7983054 (10.3)	8748192 (11.2)	9224909 (11.9)	9822326 (12.6)	10328096 (13.3)	10767893 (13.8)	77819134
HF	204931 (64.6)	230442 (72.6)	256210 (80.8)	280307 (88.4)	302731 (95.4)	318562 (100.4)	317263
HCl	889177 (46.0)	1030137 (53.2)	1135311 (58.7)	1292937 (66.8)	1396708 (72.2)	1518381 (78.5)	1935035
HBr	5567285 (35.4)	6193826 (39.4)	6762927 (43.1)	7442512 (47.4)	8185274 (52.1)	8867267 (56.5)	15706915
HI	9856670 (28.6)	11145142 (32.3)	12390845 (35.9)	13577159 (39.4)	14924269 (43.3)	16047803 (46.5)	34482580
HAt	34974628 (21.8)	38864910 (24.2)	42123521 (26.2)	45899740 (28.6)	49000454 (30.5)	52386973 (32.6)	160750582
Darwin-like term							
Ne	34960 (50.9)	38327 (55.8)	41063 (59.8)	44321 (64.5)	46252 (67.3)	47092 (68.6)	68694
Ar	228344 (27.3)	255091 (30.5)	280124 (33.5)	304197 (36.4)	321583 (38.5)	340813 (40.8)	836322
Kr	1721370 (15.6)	1933289 (17.5)	2126163 (19.2)	2279635 (20.6)	2446159 (22.1)	2571905 (23.3)	11060802
Xe	3383617 (11.9)	3672909 (12.9)	4045407 (14.2)	4330998 (15.2)	4691392 (16.5)	5026489 (17.7)	28434054
Rn	12103686 (7.9)	13443174 (8.8)	14498819 (9.4)	15701935 (10.2)	17026505 (11.1)	18348701 (12.0)	153430713
HF	319323 (51.1)	369017 (59.1)	430838 (68.9)	477383 (76.4)	523144 (83.7)	564011 (90.3)	624919
HCl	1381376 (36.9)	1620737 (43.3)	1873213 (50.0)	2143575 (57.2)	2335799 (62.4)	2553272 (68.2)	3745797
HBr	8428881 (29.4)	9706642 (33.8)	11040375 (38.5)	12241185 (42.7)	13403926 (46.7)	14525587 (50.6)	28693772
HI	15529288 (25.5)	17605797 (28.9)	19661621 (32.2)	21941334 (36.0)	24254823 (39.8)	26276514 (43.1)	60968887
HAt	53038788 (19.8)	59519882 (22.2)	65472756 (24.5)	72136351 (27.0)	80151936 (29.9)	87879663 (32.8)	267637211

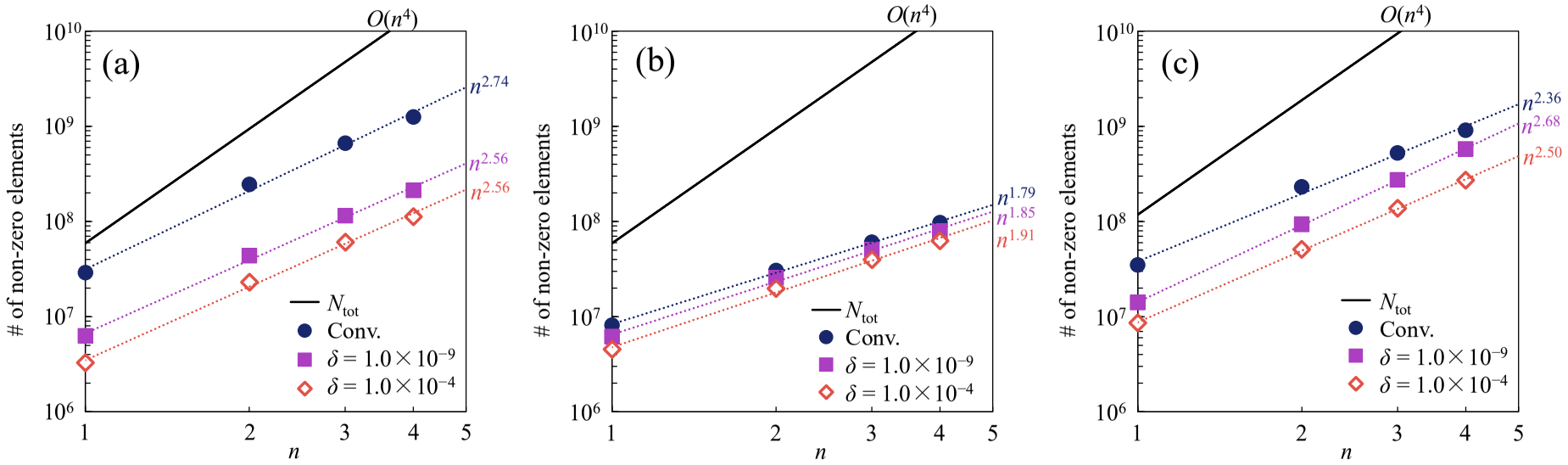

Figure 3.6. System-size dependence of the number of nonzero IOTC-transformed TEIs obtained by the conventional two-electron IOTC Hamiltonian (Conv.) and $\boldsymbol{L}^{\text{trans}}$ (and $\boldsymbol{U}^{\text{trans}}$) obtained by the present method with the threshold δ of 10^{-4} and 10^{-9} in the calculations for $(\text{HBr})_n$ (n = 1-4). The theoretical value of the number of the TEIs N^{tot} is also shown. (a), (b), and (c) correspond to the Coulomb-like, specific spin-free interaction, and Darwin-like terms, respectively.

3.4 Conclusion

This chapter demonstrated matrix decomposition techniques for TEIs using the spin-free two-electron IOTC Hamiltonian. CD was used for the symmetric TEI matrices. The LUD, which is a general CD method, was applied to the asymmetric TEI matrix.

The performance of the proposed method was numerically assessed for atoms and molecules, including heavy elements. The validity of the matrix decomposition techniques of TEI was confirmed for relativistic method. The proposed methods can significantly reduce the storage requirements of TEIs without loss of accuracy. Examination of the approximated primitive TEIs showed that the errors of the symmetric TEI matrix were less than the decomposition threshold, and the errors of the asymmetric TEI matrix could be controlled by the decomposition threshold despite error fluctuations. The total energy deviations tended to decrease with smaller decomposition thresholds. Total energies of both atoms and molecules were obtained with an error of less than 1 μhartree when the decomposition threshold is 10^{-7}. This indicated that the decomposition threshold determined the accuracy of the proposed method. The efficiency assessments showed that the number of nonzero elements in the decomposed matrix became considerably smaller than that of nonzero IOTC-transformed TEIs obtained by the conventional two-electron IOTC Hamiltonian especially in the fifth and sixth row elements. The advantage of matrix decomposition increases importantly when calculating heavy elements where relativistic effects are inevitable. The computational costs of the present methods have small prefactors for the system-size dependence in $(HBr)_n$ calculations. The efficiencies were different among three terms. The characters of the three primitive TEIs are different because the angular momenta of PBFs in the Darwin-like and specific spin-free interaction terms increase or decrease compared to those of Coulomb-like term due to the momentum operator. Transformation matrices $\boldsymbol{M}$ and $\boldsymbol{d}$ also have different characters. Therefore, it implies that the differences due to the angular momenta and the character of the IOTC

transformation matrices influence the efficiencies of each term in the proposed method.

References

1. K.G. Dyall, *J. Comput. Chem.* **23**, 786 (2002).

2. D. Peng, W. Liu, Y. Xiao, and L. Cheng, *J. Chem. Phys.* **127**, 104106 (2007).

3. J. Seino and H. Nakai, *J. Chem. Phys.* **137**, 144101 (2012).

4. J. Seino and H. Nakai, *J. Chem. Phys.* **136**, 244102 (2012).

5. J. Seino and H. Nakai, *J. Chem. Phys.* **139**, 034109 (2013).

6. D. Peng and M. Reiher, *J. Chem. Phys.* **136**, 244108 (2012).

7. D. Peng, N. Middendorf, F. Weigend, and M. Reiher, *J. Chem. Phys.* **138**, 184105 (2013).

8. J. Liu and L. Cheng, *J. Chem. Phys.* **148**, 144108 (2018).

9. S. Knecht, M. Repisky, H.J.A. Jensen, and T. Saue, *J. Chem. Phys.* **157**, 114106 (2022).

10. N.H.F. Beebe and J. Linderberg, *Int. J. Quantum Chem.* **12**, 683 (1977).

11. I. Røeggen and E. Wisløff-Nilssen, *Chem. Phys. Lett.* **132**, 154 (1986).

12. H. Koch, A. Sánchez de Merás, and T.B. Pedersen, *J. Chem. Phys.* **118**, 9481 (2003).

13. I. Røeggen and T. Johansen, *J. Chem. Phys.* **128**, 194107 (2008).

14. J.L. Whitten, *J. Chem. Phys.* **58**, 4496 (1973).

15. O. Vahtras, J. Almlöf, and M.W. Feyereisen, *Chem. Phys. Lett.* **213**, 514 (1993).

16. F. Aquilante and T.B. Pedersen, *Chem. Phys. Lett.* **449**, 354 (2007).

17. E. Epifanovsky, D. Zuev, X. Feng, K. Khistyaev, Y. Shao, and A.I. Krylov, *J. Chem. Phys.* **139**, 134105 (2013).

18. F. Aquilante, T.B. Pedersen, R. Lindh, B.O. Roos, A. Sánchez de Merás, and H. Koch, *J. Chem. Phys.* **129**, 024113 (2008).

19. T. Nottoli, J. Gauss, and F. Lipparini, *J. Chem. Theory Comput.* **17**, 6819 (2021).

20. F. Aquilante, P. Malmqvist, T.B. Pedersen, A. Ghosh, and B.O. Roos, *J. Chem. Theory Comput.* **4**, 694 (2008).

21. D.W. O'neal and J. Simons, *Int. J. Quantum Chem.* **36**, 673 (1989).

22. X. Feng, E. Epifanovsky, J. Gauss, and A.I. Krylov, *J. Chem. Phys.* **151**, 014110 (2019).

23. T.B. Pedersen, H. Koch, L. Boman, and Sánchez de Merás, Alfredo M. J., *Chem. Phys. Lett.* **393**, 319 (2004).

24. I. García Cuesta, T. B. Pedersen, H. Koch, and A.M.J. Sánchez de Merás, *Chem. Phys. Lett.* **390**, 170 (2004).

25. I. García Cuesta, J. Sánchez Marín, T.B. Pedersen, H. Koch, and A.M.J. Sánchez de Merás, *Phys. Chem. Chem. Phys.* **10**, 361 (2008).

26. T.D. Crawford, L.S. Owens, M.C. Tam, P.R. Schreiner, and H. Koch, *J. Am. Chem. Soc.* **127**, 1368 (2005).

27. S. Burger, F. Lipparini, J. Gauss, and S. Stopkowicz, *J. Chem. Phys.* **155**, 074105 (2021).

28. S. Blaschke and S. Stopkowicz, *J. Chem. Phys.* **156**, 044115 (2022).

29. J. Gauss, S. Blaschke, S. Burger, T. Nottoli, F. Lipparini, and S. Stopkowicz, *Mol. Phys.* **121**, 11 (2022).

30. S.D. Folkestad, E.F. Kjønstad, and H. Koch, *J. Chem. Phys.* **150**, 194112 (2019).

31. T. Zhang, X. Liu, E.F. Valeev, and X. Li, *J. Phys. Chem. A* **125**, 4258 (2021).

32. G.M.J. Barca, C. Bertoni, L. Carrington, D. Datta, N. De Silva, J.E. Deustua, D.G. Fedorov, J.R. Gour, A.O. Gunina, E. Guidez, T. Harville, S. Irle, J. Ivanic, K. Kowalski, S.S. Leang, H. Li, W. Li, J.J. Lutz, I. Magoulas, J. Mato, V. Mironov, H. Nakata, B.Q. Pham, P. Piecuch, D. Poole, S.R. Pruitt, A.P. Rendell, L.B. Roskop, K. Ruedenberg, T. Sattasathuchana, M.W. Schmidt, J. Shen, L. Slipchenko, M. Sosonkina, V. Sundriyal, A. Tiwari, J.L. Galvez Vallejo, B. Westheimer, M. Włoch, P. Xu, F. Zahariev, and M.S. Gordon, *J. Chem. Phys.* **152**, 154102 (2020).

33. T. Noro, M. Sekiya, and T. Koga, *Theor. Chem. Acc.* **109**, 85 (2003).

34. T. Noro, M. Sekiya, and T. Koga, *Theor. Chem. Acc.* **131**, 1124 (2012).

35. T. Noro, M. Sekiya, and T. Koga, *Theor. Chem. Acc.* **132**, 1363 (2013).

Chapter 4 Database of TEIs in 2c relativistic calculations[†]

4.1 Introduction

In this chapter, the author modifies the LUT scheme for two-electron operators based on the IOTC Hamiltonian to realize more efficient calculations. The scheme utilizes a database containing atomic (one-center) unitary transformed TEIs calculated in advance. The novel algorithm for the unitary transformation of TEIs in terms of elements is implemented. This chapter is organized as follows. Section 4.2 summarizes the algorithm and implementation of the proposed scheme. In Sec. 4.3, numerical assessments are presented. Finally, concluding remarks are provided in Sec. 4.4.

4.2 Algorithm and implementation

This section describes the algorithm for constructing and utilizing the database of relativistically transformed one-center TEIs. In Eq. (2.4.4), the one-center transformation of TEIs is a time-consuming process for small- and medium-sized molecules. The reason is that the computational cost per atom scales as $O(N_P^5)$ with respect to the number of PBFs per atom (or element), N_P, because the resolution of identity approximation is used.[1] Thus, the total computational cost scales as $O(N_A * N_P^5)$, where N_A is the number of atoms. Note that the total computational cost without the LUT technique scales as $O(N_A^5 * N_P^5)$.

Here, the author should recall that the one-center transformed TEIs depend only on the atom species, i.e., the element, when the same basis set is used for the same element. Thus, one can reuse the same one-center transformed TEIs for different atoms of the same element,

[†] Reproduced from the article by Chinami Takashima, Junji Seino, and Hiromi Nakai, *Chem. Phys. Lett.* **777**, 138691 (2021).

for example, by saving to and reading from a database disk. Consequently, the computational cost can be reduced to $O(N_E{*}N_P{}^5)$, where N_E is the number of elements. This discussion is based on the assumption that N_P is the same for each atom and each element. Furthermore, if one assumes that the number of atoms of each element, $n_A{}^E$, is constant, N_A becomes $n_A{}^E{*}N_E$. Therefore, the acceleration ratio is estimated to be $n_A{}^E$.

Based on these considerations, the author developed a new algorithm in order to use a database. The algorithm was implemented by modifying the GAMESS program.[2] Figure 4.1 shows the conventional and proposed database-assisted algorithms for the two-electron LUT-IOTC Hamiltonian assuming a disk-based SCF procedure. The proposed algorithm for the direct SCF procedure can be extended straightforwardly. As shown in Figure 4.1, four steps are involved: Step I for the construction of the database of one-center transformed TEIs, Step II for the calculations and transformations of the TEIs, and Steps III and IV for the construction and diagonalization of the Fock matrix, respectively.

The conventional algorithm starts at Step II, because Step I is unique to the proposed algorithm. In Step II of the conventional algorithm, the multi-center nonrelativistic TEIs are calculated and stored in a disk file. Then, the one-center relativistic TEIs are calculated and stored on the disk in each atomic loop, where the one-center TEIs without operators $\boldsymbol{d}$ and $\boldsymbol{M}$ in Eqs. (2.3.18)–(2.3.20) of Chapter 2 are evaluated; subsequently, Eqs. (2.3.18)–(2.3.20) are transformed by introducing operators $\boldsymbol{d}$ and $\boldsymbol{M}$. In Step III, the skeleton Fock matrix elements are constructed by multiplying the nonrelativistic TEIs with the density matrix elements and are added to the core matrix, which is obtained from the one-electron relativistic integrals. Furthermore, another set of skeleton Fock matrix elements is obtained by using the one-center relativistic TEIs and the density matrix elements, and these elements are added to the aforementioned Fock matrix in each atomic loop. In Step IV, the Fock matrix is diagonalized.

In the proposed database-assisted algorithm, one-center relativistic TEIs are calculated

and stored to a database disk, as shown in Step I. Thus, the atomic loop for the calculations and transformations of one-center relativistic TEIs is not needed in Step II. Consequently, only the multi-center nonrelativistic TEIs are evaluated. The difference from the conventional algorithm in Step III is the addition of the contributions of the one-center relativistic TEIs to the Fock matrix. First, the one-center relativistic TEIs are read from the database disk in an element loop. Then, the TEIs are assigned to the corresponding indices of the atomic orbitals of a molecule, and their contributions are added to the Fock matrix in an atomic loop. Note that the element loop should be changed if different basis sets are used for the same element. No modification of Step IV is needed. The proposed database-assisted method gives the molecular energies that are equivalent to those given by the conventional method. Furthermore, the present method is simply available not only for the HF method but also for DFT, which applies to one-center relativistic TEIs for the Coulomb and the HF exchange terms. Although the present method can be extended straightforwardly to the nonrelativistic calculation, the high efficiency is not expected because the computational costs for multi-center TEIs are dominant.

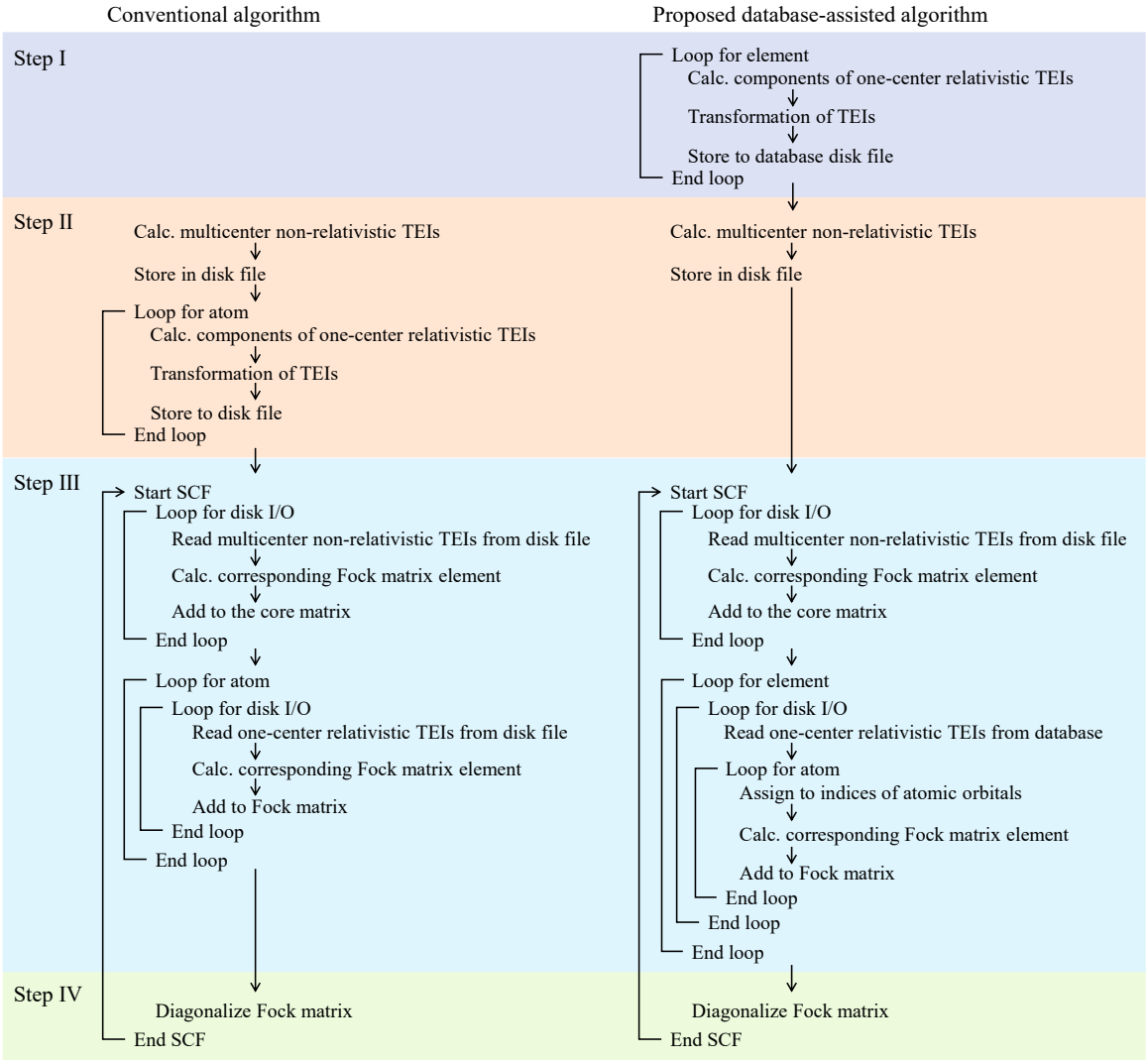

Figure 4.1. Comparison between the conventional and proposed database-assisted algorithms for the two-electron LUT-IOTC Hamiltonian. Step I: construction of a database of unitary transformed TEIs, Step II: calculation and transformation of TEIs, Step III: construction of Fock matrix, and Step IV: diagonalization of Fock matrix

4.3 Numerical assessments

4.3.1 Computational details

This section details the performance of the proposed algorithm. The spin-free LUT-IOTC Hamiltonian for one- and two-electron term[3], which is denoted as 1e2eLUT-IOTC in this chapter, are applied. The cutoff distance for the one-electron LUT was set to 3.5 Å. The implementations and computations reported in this chapter were based on the modified version of the GAMESS program. All calculations were performed on a single core of a Quad Core Intel® Xeon® Gold 5122 central processing unit (CPU) at 3.60 GHz.

Numerical tests were performed for one-dimensional hydrogen halide chains $(HX)_n$ (X = Cl and At, $n = 1, 2, \ldots, 50$), three-dimensional gold clusters Au_n ($n = 1, 2, \ldots, 20$), $Ir(ppy)_3$, cycloheptatrienyl trimetal sandwich complex $Pt_3(C_7H_7)_2(HCN)_3$, and $PtCl_2(NH_3)_2$. The author choses the systems in the following reasons. $(HX)_n$ and Au_n are suitable to examine the size dependence of computational cost. $(HX)_n$ are quasi-one-dimensional models, which consist of heavy and light atoms alternately. This system is the simplest and illustrates the effectiveness of LUT. Au_n are three-dimensional models of heavy element aggregation, which are more complicated. $Ir(ppy)_3$, $PtCl_2(NH_3)_2$, and $PtCl_2(NH_3)_2$ are test molecules for actual three-dimensional calculations with various combinations of heavy and light atoms. $Ir(ppy)_3$ provides the effect in one heavy atom and several light atoms. $Pt_3(C_7H_7)_2(HCN)_3$ gives the effect in three heavy and several light atoms. $PtCl_2(NH_3)_2$ consists of one heavy atom and several light atoms with the smaller size than $Ir(ppy)_3$. Their geometries are illustrated in Figure 4.2. The structures, except for $(HX)_n$ and Au_n, were optimized by using the Hartree–Fock method, Stuttgart–Dresden pseudo potential[4] for Pt and Ir, and 6-31G(d,p) basis sets[5,6] for the other atoms. The restricted Hartree–Fock method was adopted for the single-point energy calculations. Two categories of basis sets were used, namely, segmented and general contractions, for the all-electron Gaussian-type functions for elements of the first to sixth periods. The basis sets adopted for segmented contraction

were the Sapporo(-DKH3)-XZP-2012 (X = D or T) basis set with/without diffuse functions[7–9] and the Jorge-XZP-DKH (X = D or T) basis set.[10] The basis sets for general contraction were the ANO-DK3 basis set[11] and the Dyall double- (dz) or triple-zeta (tz) basis set.[12] To evaluate the multi-center TEIs, the default option in the GAMESS program was adopted, which includes a combination of the rotated axis code, ERIC precursor transfer equation code, and Rys quadrature.

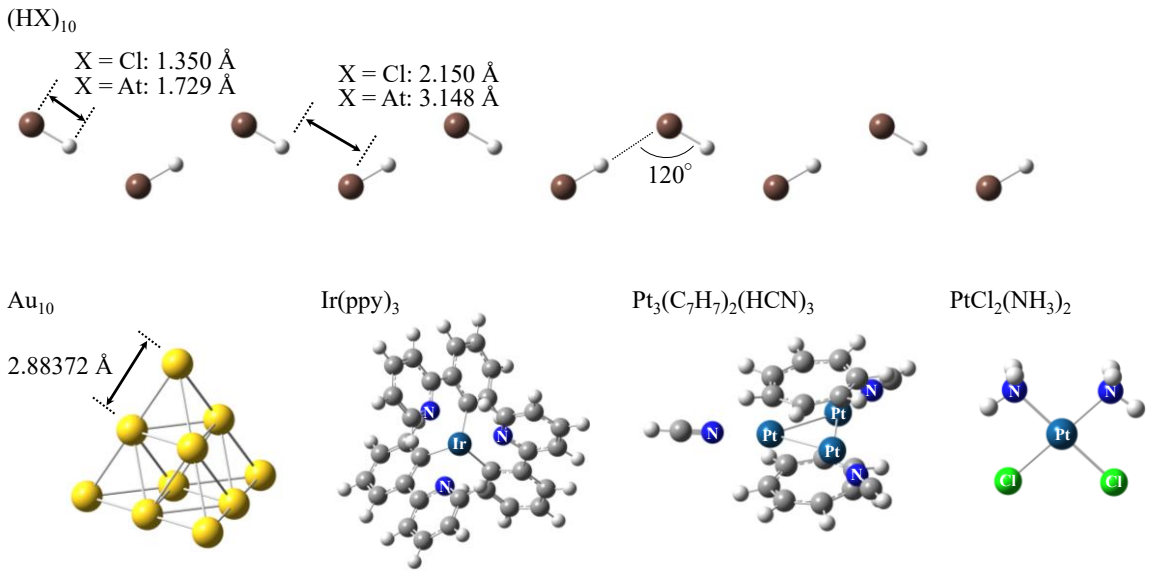

Figure 4.2. Geometries of $(HX)_{10}$ (X = Cl and At), Au_{10}, $Ir(ppy)_3$, $Pt_3(C_7H_7)_2(HCN)_3$, and $PtCl_2(NH_3)_2$.

4.3.2 Constructed database

This subsection describes the constructed database. Table 4.1 summarizes the required disk space in megabytes (MB) for the one-center relativistic TEIs obtained using Eq. (2.4.4) in Chapter 2 and several contracted basis sets. The value represents the sum of the disk space for all the elements shown in the element column. The disk space depends on the number of contracted basis functions. Thus, the disk space values for general contraction are smaller than those for segmented contraction. The maxima are 3209.26 MB for Jorge-TZP-DKH (segmented contraction) and 152.41 MB for Dyall dz (general contraction). Therefore, most current computer resources can easily store the database.

Table 4.1. Required disk space (in MB) of one-center relativistic TEIs for five segmented and three general-contracted basis sets.

Basis set	Element	Disk space [MB]
Segmented contraction		
Sapporo(-DKH3)-DZP-2012	H-Rn	1051.99
Sapporo(-DKH3)-DZP-2012+diffuse	H-Rn	2990.12
Sapporo(-DKH3)-TZP-2012	H-Ba, Hf-Rn	1759.80
Jorge-DZP-DKH	H-Lr	920.71
Jorge-TZP-DKH	H-Lr	3209.26
General contraction		
ANO-DK3	H-Rn	53.77
Dyall dz	K-Lr	152.41
Dyall tz	K-Xe, Ba-Rn	56.17

4.3.3 Efficiency

This subsection describes the system-size dependence of the CPU time required for the transformation of the TEIs in the 1e2eLUT-IOTC calculations. Figure 4.3 illustrates the results for (a) $(HCl)_n$ (n = 1, 2, …, 50) and (b) $(HAt)_n$ (n = 1, 2, …, 30). Here, the Sapporo(-DKH3)-DZP-2012 basis set was employed. The results for the 1e2eLUT-IOTC Hamiltonian based on the conventional and proposed database-assisted algorithms are shown. For comparison, the results for 1e2eIOTC without the LUT are also plotted. Here, n is shown on the horizontal axis. The vertical axis represents the CPU time in seconds. For $(HCl)_n$, the CPU time required for the 1e2eIOTC Hamiltonian scales as $n^{4.72}$. The scaling is close to the theoretical scaling, which is $O(N_A^5 * N_P^5)$, because n is proportional to the product of the number of atoms (N_A) and the number of primitive functions (N_P). For the conventional 1e2eLUT-IOTC Hamiltonian, the CPU time scales as $n^{0.99}$, which is almost the same as the theoretical scaling, $O(N_A * N_P^5)$. Here, n is proportional to N_A and constant with respect to N_P. The proposed 1e2eLUT-IOTC Hamiltonian scales as 0.00, which is also the same as the theoretical scaling, $O(N_E * N_P^5)$, because N_E and N_P are constant with respect to n. In large molecules, 1e2eLUT-IOTC requires significantly less CPU time than 1e2eIOTC when both algorithms are used. Here, the acceleration ratio, r_{Acc}, are defined as

$$r_{Acc} = t_{Conv} / t_{Prop}, \tag{4.3.1}$$

where t_{Conv} and t_{Prop} are the CPU times required for the conventional and proposed 1e2eLUT-IOTC Hamiltonians, respectively. The ratios are plotted in Figure 4.3. Here, t_{Prop} includes the time required to construct the database in Step I. Thus, r_{Acc} corresponds to n, i.e., n_A^E, as defined in Sec. 4.2. In the actual calculations, the CPU time required for the transformation of the TEIs using the proposed algorithm becomes zero because Step I is not needed.

The results for $(HAt)_n$ are similar to those for $(HCl)_n$, although the prefactor is larger.

Note that the calculations of $(HAt)_2$ and larger using 1e2eIOTC were difficult in the current computing environment.

Figure 4.4 presents the system-size dependence of the acceleration ratio, r_{Acc}, [Eq. (4.3.1)] for the total CPU time required for the HF calculations of one-dimensional $(HAt)_n$ and three-dimensional Au_n. Note that r_{Acc} does not correspond to $n_A{}^E$ because t_{Conv} and t_{Prop} include the computational times required for all steps. For small and medium-sized molecules, the acceleration ratio is large and decreases monotonically because the transformations of the TEIs are dominant. By contrast, for large molecules, the calculation of the TEIs or SCF is dominant because the transformation of the TEIs exhibits linear scaling. The slope of r_{Acc} for $(HAt)_n$ is different from that for Au_n because the number of nonzero multi-center TEIs for $(HAt)_n$ increases slowly owing to screening by the Schwarz inequality.

Figure 4.5 shows the memory size in MB required to save the one-center TEIs using the conventional and proposed 1e2eLUT-IOTC Hamiltonians for Au_n. For the conventional algorithm, the scaling is $O(n^{1.00})$ because the one-center TEIs for each atom are stored. Thus, the memory size required for large systems containing hundreds of heavy atoms becomes very large. For the proposed database-assisted algorithm, the scaling is $O(n^{0.00})$ because the TEIs for an atom are stored once for each basis set. The required memory size is approximately 10 MB. Thus, even for large molecules, the in-core method, which stores the TEIs in memory, can be adopted to reduce the number of times the disk is loaded during the SCF procedure.

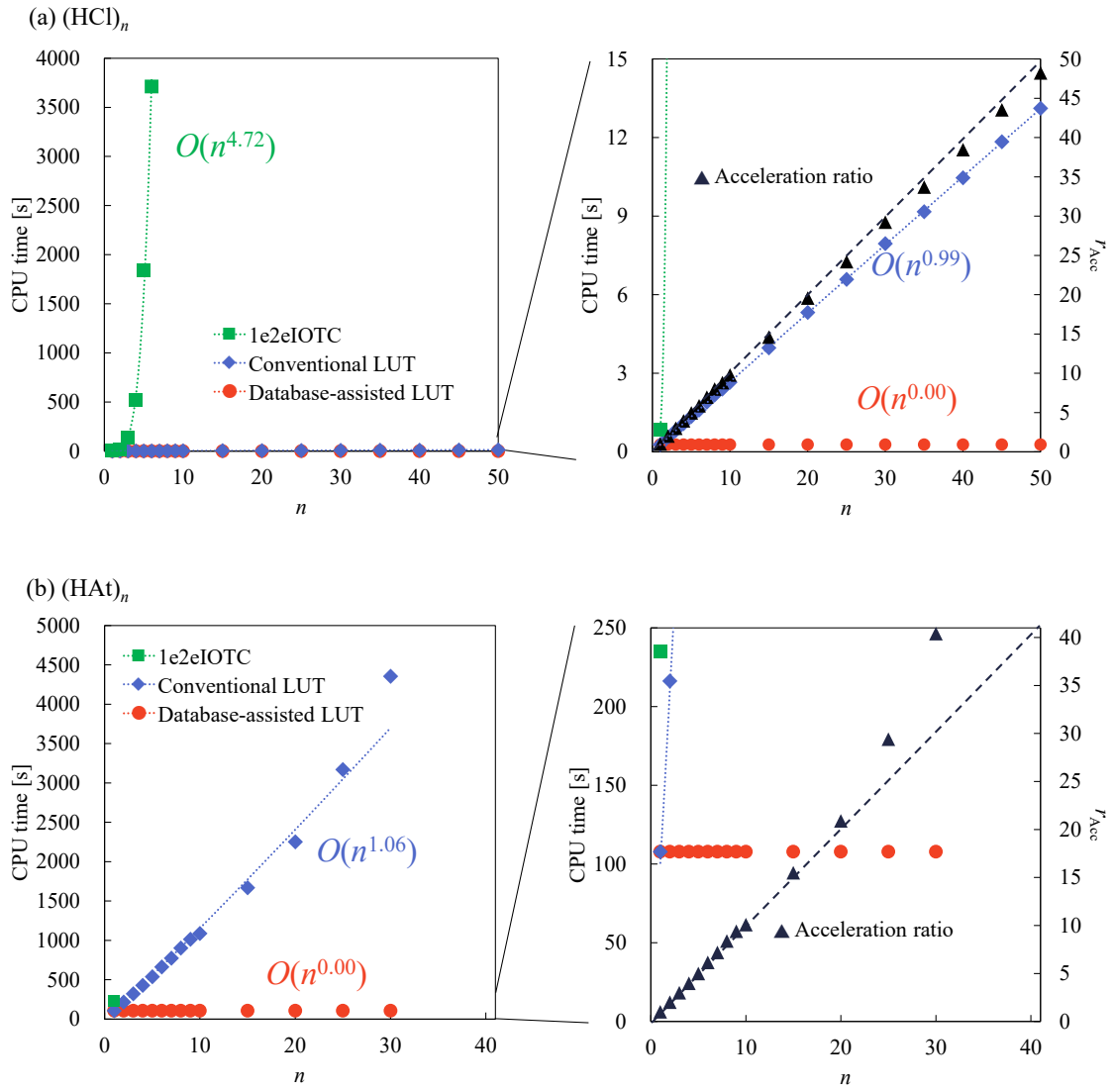

Figure 4.3. System-size dependence of the CPU time (in s) for transformation of TEIs in (a) $(HCl)_n$ and (b) $(HAt)_n$ calculated using the 1e2eIOTC and 1e2eLUT-IOTC Hamiltonians based on the conventional and proposed database-assisted algorithms. Acceleration ratio r_{Acc} is also plotted.

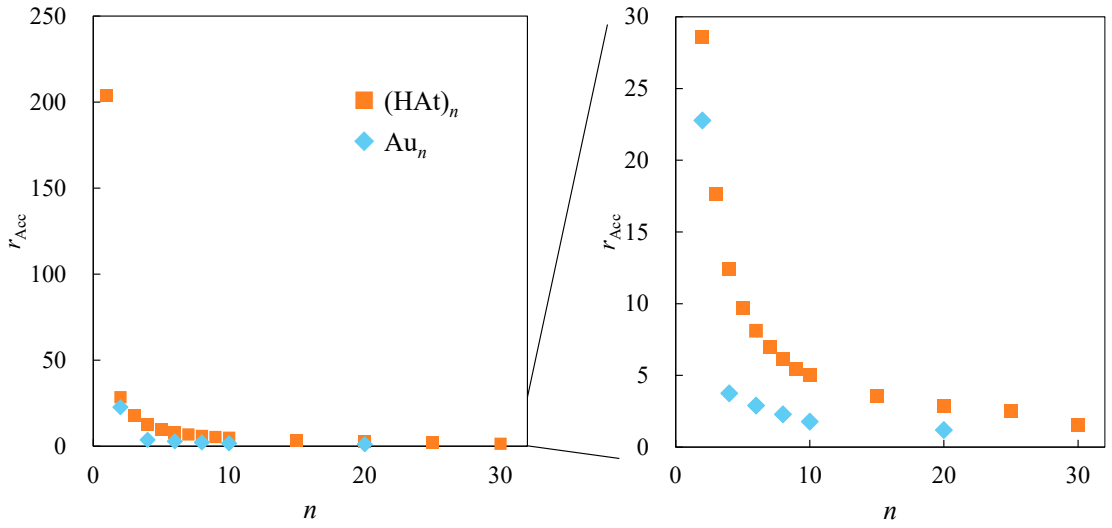

Figure 4.4. Acceleration ratio r_{Acc} for total CPU time t required for HF calculations of (HAt)$_n$ and Au$_n$.

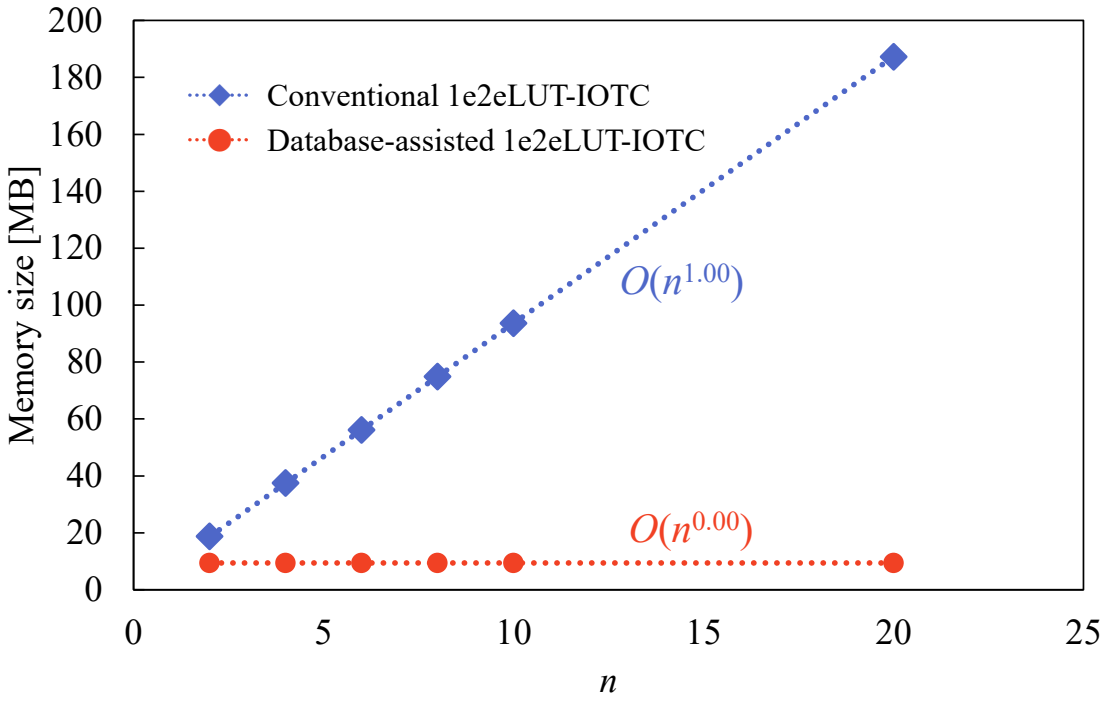

Figure 4.5. Memory size (in MB) required to save one-center TEIs in the 1e2eLUT-IOTC Hamiltonian using the conventional and proposed database-assisted algorithms for Au$_n$.

4.3.4 Application to metal complexes

This subsection details the computational time required for $Ir(ppy)_3$ and $Pt_3(C_7H_7)_2(HCN)_3$ molecules. Table 4.2 summarizes the CPU time (in seconds) of the four steps in the HF calculations: the one-electron integral (OEI) and the initial guess calculated using the extended Hückel method in a minimal basis sets used in a default option of GAMESS, TEI, and SCF procedure. The total CPU time is also shown. The OEI and TEI include the calculations and transformations of the integrals. The nonrelativistic Hamiltonian and the conventional and proposed 1e2eLUT-IOTC Hamiltonians were used. The wall-clock time is shown in parentheses, and the bottom row shows the number of SCF cycles. For all the methods, the times required for the TEI and SCF procedures are the bottlenecks in the entire calculation. In the nonrelativistic Hamiltonian, the times required for the OEI and TEI are less than those in the conventional 1e2eLUT-IOTC Hamiltonian for both molecules because the transformations are also performed in 1e2eLUT-IOTC. The time required for the SCF calculation for $Ir(ppy)_3$ is more than that in 1e2eLUT-IOTC because the nonrelativistic Hamiltonian requires more SCF cycles. The proposed 1e2eLUT-IOTC Hamiltonian differs from the conventional one only in the TEI step. The CPU times required for the TEI for $Ir(ppy)_3$ and $Pt_3(C_7H_7)_2(HCN)_3$ are reduced from 1492.73 and 2095.54 s for the conventional 1e2eLUT-IOTC Hamiltonian to 1175.37 and 1160.93 s for the proposed one, respectively. The acceleration ratio, r_{Acc}, for the entire calculation is 1.09 for $Ir(ppy)_3$ and 1.25 for $Pt_3(C_7H_7)_2(HCN)_3$. These results are quantitatively consistent with the theoretical estimates in Sec. 4.2 because the $n_{\mathrm{A}}^{\mathrm{E}}$ values for heavy elements are one and three $Ir(ppy)_3$ and $Pt_3(C_7H_7)_2(HCN)_3$, respectively.

Table 4.2. CPU time (in s) required for the four steps in the HF calculations in nonrelativistic and 1e2eLUT-IOTC Hamiltonians using the conventional (Conv.) and proposed database-assisted (Prop.) algorithms for $Ir(ppy)_3$ and $Pt_3(C_7H_7)_2(HCN)_3$ molecules: one-electron integral (OEI), initial guess (Guess) calculated using the extended Hückel calculation in a minimal basis sets, two-electron integral (TEI), and SCF procedure. The corresponding wall-clock times (in s) are shown in parentheses. The number of SCF cycles is also presented.

Molecule	$Ir(ppy)_3$						$Pt_3(C_7H_7)_2(HCN)_3$					
Method	Nonrelativistic		LUT-IOTC				Nonrelativistic		LUT-IOTC			
			Conv.		Prop.				Conv.		Prop.	
OEI	0.77	(0.79)	2.48	(3.14)	2.48	(2.73)	2.31	(2.92)	2.28	(2.54)	2.31	(2.92)
Guess	1.95	(2.14)	1.95	(2.15)	1.94	(2.02)	0.92	(1.10)	0.92	(1.02)	0.92	(1.10)
TEI	1201.67	(1491.1)	1492.73	(1527.37)	1175.37	(1176.64)	2095.54	(2098.11)	1160.93	(1162.83)	2095.54	(2098.11)
SCF	8560.46	(53681.54)	3727.89	(18993.15)	3620.71	(17507.40)	2805.41	(16261.77)	2769.05	(14732.54)	2805.41	(16261.77)
Total	9764.85	(55175.57)	5225.05	(20525.81)	4800.50	(18688.79)	4904.18	(18363.90)	3933.18	(15898.93)	4904.18	(18363.90)
# of SCF cycles	35		16		16		21		21		21	

4.3.5 Basis set dependence of computational cost

This subsection explains the basis-set dependence of the total CPU time at the HF level for $PtCl_2(NH_3)_2$. Table 4.3 summarizes the numbers of PBFs and AOs for Pt and the other elements, the total CPU time, and the acceleration ratio. The adopted basis sets are the same as those in Table 4.1. For the Dyall dz and tz basis sets, the ANO-DK3 basis set was used for light elements such as H, N, and Cl. The results for the conventional and proposed database-assisted 1e2eLUT-IOTC Hamiltonians are shown. As reported in the previous subsection, the time-consuming steps are the calculations and transformations of the TEIs and the SCF procedure. The times required for the calculations of the multi-center TEIs and the SCF procedure depend primarily on the number of AOs in an entire molecule. By contrast, the time required for the transformations of the one-center TEIs depends on the number of PBFs in heavy elements. Thus, in segmented contraction, the total time for the proposed 1e2eLUT-IOTC Hamiltonian is related to the number of AOs for all elements. However, the difference between the conventional and proposed 1e2eLUT-IOTC Hamiltonians is related to the number of AOs for Pt. The acceleration ratio, r_{Acc}, [Eq. (4.3.1)] is large; the maximum and minimum values are 9.07 for Sapporo(-DKH3)-DZP-2012 and 1.97 for Jorge-TZP-DKH, respectively. The general contracted basis sets require a longer total CPU time than the segmented contracted basis sets because the algorithm for multi-center TEIs was not optimized for general contraction. The other trends are the same as those of the segmented contracted basis sets.

Table 4.3. Basis-set dependence of the CPU time (in s) for HF calculations in the 1e2eLUT-IOTC Hamiltonian for $PtCl_2(NH_3)_2$ using the conventional (Conv.) and proposed database-assisted (Prop.) algorithms. The numbers of PBFs and AOs for Pt and the other elements and the acceleration ratio, r_{Acc}, are also tabulated.

	# of PBFs		# of AOs		Total time [s]		r_{Acc}
	Pt	Other	Pt	Other	Conv.	Prop.	
Segmented contraction							
Sapporo(-DKH3)-DZP-2012	262	288	76	126	282.25	31.11	9.07
Sapporo(-DKH3)-DZP-2012+diffuse	282	352	96	190	519.52	114.80	4.53
Sapporo(-DKH3)-TZP-2012	305	528	115	308	1038.44	316.15	3.28
Jorge-DZP-DKH	170	192	73	112	54.00	12.05	4.48
Jorge-TZP-DKH	198	332	99	252	219.59	111.24	1.97
General contraction							
ANO-DK3	286	206	46	34	412.14	136.53	3.02
Dyall dz	233	206	49	34	226.57	104.41	2.17
Dyall tz	292	206	49	34	523.88	189.89	2.76

4.4 Conclusion

In this chapter, the author provided an efficient scheme for the LUT method using an element loop and a one-center relativistic TEI database. The basic idea of the present scheme was originated from the fact that the relativistic effect in the one-center TEIs, which is dominant in all the TEIs, depends only on a combination of an element and a basis set. The author implemented the scheme for the 1e2eIOTC Hamiltonian with a spin-free formalism.

The previous LUT scheme using an atomic loop reduced the computational scale from $O(N_A{}^5 * N_P{}^5)$ to $O(N_A * N_P{}^5)$ theoretically, where N_A and N_P were the number of atoms and that of primitive basis functions per atom (or element), respectively. On the contrary, the present LUT scheme using an element loop achieved the computational scale from $O(N_E * N_P{}^5)$, where N_E was the number of elements. Namely, the previous and present schemes correspond to the linear- and zero-scalings with respect to the system size, respectively. It should be noticed that the data-base assisted algorithm can be accomplished by using the element-loop scheme.

The efficiency of the present database-assisted algorithm was numerically assessed for hydrogen halide chains, $(HX)_n$ (X = Cl and At), Au_n, $Ir(ppy)_3$, $Pt_3(C_7H_7)_2(HCN)_3$, and $PtCl_2(NH_3)_2$. The computational time and required memory size for the proposed algorithm were confirmed to be smaller than those for the previous algorithm.

References

1. B.A. Hess, *Phys. Rev. A*, **32**, 756 (1985).

2. G.M.J. Barca, C. Bertoni, L. Carrington, D. Datta, N. De Silva, J.E. Deustua, D.G. Fedorov, J.R. Gour, A.O. Gunina, E. Guidez, T. Harville, S. Irle, J. Ivanic, K. Kowalski, S.S. Leang, H. Li, W. Li, J.J. Lutz, I. Magoulas, J. Mato, V. Mironov, H. Nakata, B.Q. Pham, P. Piecuch, D. Poole, S.R. Pruitt, A.P. Rendell, L.B. Roskop, K. Ruedenberg, T. Sattasathuchana, M.W. Schmidt, J. Shen, L. Slipchenko, M. Sosonkina, V. Sundriyal, A. Tiwari, J.L. Galvez Vallejo, B. Westheimer, M. Włoch, P. Xu, F. Zahariev, and M.S. Gordon, *J. Chem. Phys.* **152**, 154102 (2020).

3. J. Seino and H. Nakai, *J. Chem. Phys.* **137**, 144101 (2012).

4. D. Figgen, K.A. Peterson, M. Dolg, and H. Stoll, *J. Chem. Phys.* **130**, 164108 (2009).

5. P.C. Hariharan and J.A. Pople, *Theor. Chim. Acta*, **28**, 213 (1973).

6. M.M. Francl, W.J. Pietro, W.J. Hehre, J.S. Binkley, M.S. Gordon, D.J. DeFrees, and J.A. Pople, *J. Chem. Phys.* **77**, 3654 (1982).

7. T. Noro, M. Sekiya, and T. Koga, *Theor. Chem. Acc.* **109**, 85 (2003).

8. T. Noro, M. Sekiya, and T. Koga, *Theor. Chem. Acc.* **131**, 1124 (2012).

9. T. Noro, M. Sekiya, and T. Koga, *Theor. Chem. Acc.* **132**, 1363 (2013).

10. F.E. Jorge, A. Canal Neto, G.G. Camiletti, and S.F. Machado, *J. Chem. Phys.* **130**, 064108 (2009).

11. T. Tsuchiya, M. Abe, T. Nakajima, and K. Hirao, *J. Chem. Phys.* **115**, 4463 (2001).

12. K.G. Dyall, *Theor. Chem. Acc.* **115**, 441 (2006).

Chapter 5 RS-DFT with IOTC Hamiltonian‡

5.1 Introduction

The KS-DFT[1] is one of the most popular methods for performing quantum chemical calculations because it ensures optimum balance between accuracy and computational costs. RS-DFT,[2] which separates two-electron interactions into long- and short-range parts, is an extension of the KS-DFT. The RS-DFT utilizes the wave function theory to improve the KS-DFT from the perspective of a strong-correlation system[3,4] and weak intermolecular interactions.[5,6] The LC-DFT,[7–24] which incorporates long-range interactions by introducing range separation to exchange functionals, is also commonly used. The LC-DFT provides more adequate descriptions of the vdW interaction,[25] excitation spectra,[9] optical response properties,[26] and orbital energies.[27]

For the calculations of heavy element systems, the range-separation method was extended to the framework of the 4c relativistic theory, which is the fundamental approach to describe relativistic effects in quantum chemistry.[28–31] In terms of 2c theory, the one-electron regular approximation[32,33] and normalized elimination of the small component[34] Hamiltonians were extended to the range-separation method by combination with the LC-DFT.

In this chapter, the range separation method is introduced to the IOTC Hamiltonian in the framework of the LC-DFT by implementing range-separated terms of two-electron operators resulting from their IOTC transformation. The LUT scheme is also applied. The remainder of this chapter is organized as follows. In Section 5.2, the author explains the theoretical aspects of range separation of TEIs in the two-electron IOTC Hamiltonian and

‡ Reprinted with permission from the article by Chinami Takashima and Hiromi Nakai, https://doi.org/10.1021/acs.jctc.3c01102. Copyright 2024 American Chemical Society.

LUT scheme. Section 5.3 presents the computational details of this chapter. Section 5.4 presents the numerical assessment of the present method, followed by Section 5.5, which delineates the conclusion of this chapter.

5.2 Theory and implementation

5.2.1 LC-DFT based on the IOTC Hamiltonian

This subsection explains the derivation of the energy expression of LC-DFT by using the IOTC Hamiltonian. The derivation is started with the 4c Hamiltonian. The LC method treats long-range exchange interaction $E_{\mathrm{X}}^{\mathrm{lr}}$ as HFx integrals.[7] The two-electron operator is separated into the short-range and long-range terms as

$$\boldsymbol{G}_4^{\mathrm{C}} = \boldsymbol{G}_4^{\mathrm{C,sr}} + \boldsymbol{G}_4^{\mathrm{C,lr}}, \tag{5.2.1}$$

where the short-range term $\boldsymbol{G}_4^{\mathrm{C,sr}}$ adopts the complementary error function

$$\boldsymbol{G}_4^{\mathrm{C,sr}}(i,j) = \frac{1-\mathrm{erf}\left(\mu r_{ij}\right)}{r_{ij}}\mathbf{1}_4, \tag{5.2.2}$$

and the long-range term $\boldsymbol{G}_4^{\mathrm{C,lr}}$ employs the error function

$$\boldsymbol{G}_4^{\mathrm{C,lr}}(i,j) = \frac{\mathrm{erf}\left(\mu r_{ij}\right)}{r_{ij}}\mathbf{1}_4. \tag{5.2.3}$$

Here, μ is a range-separation parameter that determines the ratio of short- and long-range terms. Using $\boldsymbol{G}_4^{\mathrm{C,lr}}$, $E_{\mathrm{X}}^{\mathrm{lr}}$ is calculated as

$$E_{\mathrm{X}}^{\mathrm{lr}} = -\frac{1}{2}\sum_{i=1}^{N}\sum_{j=1}^{N}\int\int d\mathbf{r}_1 d\mathbf{r}_2 \psi_i^*(\mathbf{r}_1)\psi_j^*(\mathbf{r}_2)\boldsymbol{G}_4^{\mathrm{C,lr}}(1,2)\psi_j(\mathbf{r}_1)\psi_i(\mathbf{r}_2). \tag{5.2.4}$$

Short-range HFx integral $E_{\mathrm{X}}^{\mathrm{sr}}$ used in LC-DFT, such as ωB97X series,[18,19] LC-ωPBE,[13] CAM,[10] and orbital-specific hybrid functional[24] is also calculated with respect to $\boldsymbol{G}_4^{\mathrm{C,sr}}$ in the same manner as in Eq. (5.2.4).

To adopt a two-electron IOTC Hamiltonian for a range-separated operator, unitary transformations in Eq. (2.3.14) are performed on $\boldsymbol{G}_4^{\mathrm{C,sr}}$ and $\boldsymbol{G}_4^{\mathrm{C,lr}}$. Here, replacing $1/r_{ij}$ in Eqs. (2.3.18)-(2.3.20) by $\left(1-\mathrm{erf}\left(\mu r_{ij}\right)\right)/r_{ij}$ and $\mathrm{erf}\left(\mu r_{ij}\right)/r_{ij}$ yields the short- and long-range parts of $\boldsymbol{g}_2^{\mathrm{sf}}$, respectively. The explicit expressions for range separation of $\boldsymbol{g}_2^{\mathrm{sf}}$ are as follows:

$$\begin{aligned}\boldsymbol{g}_2^{\mathrm{sf}}\left(i,j\right) &= \boldsymbol{g}_2^{\mathrm{sf,sr}}\left(i,j\right)+\boldsymbol{g}_2^{\mathrm{sf,lr}}\left(i,j\right)\\ &= \boldsymbol{g}_2^{\mathrm{sf1,sr}}\left(i,j\right)+\boldsymbol{g}_2^{\mathrm{sf1,lr}}\left(i,j\right)+\boldsymbol{g}_2^{\mathrm{sf2,sr}}\left(i,j\right)+\boldsymbol{g}_2^{\mathrm{sf2,lr}}\left(i,j\right)+\boldsymbol{g}_2^{\mathrm{sf3,sr}}\left(i,j\right)+\boldsymbol{g}_2^{\mathrm{sf3,lr}}\left(i,j\right),\end{aligned} \tag{5.2.5}$$

where

$$\boldsymbol{g}_2^{\mathrm{sf1,sr}}\left(i,j\right)=\boldsymbol{M}_i\boldsymbol{M}_j\left[\frac{1-\mathrm{erf}\left(\mu r_{ij}\right)}{r_{ij}}\mathbf{1}_2\right]\boldsymbol{M}_j\boldsymbol{M}_i, \tag{5.2.6}$$

$$\boldsymbol{g}_2^{\mathrm{sf1,lr}}\left(i,j\right)=\boldsymbol{M}_i\boldsymbol{M}_j\left[\frac{\mathrm{erf}\left(\mu r_{ij}\right)}{r_{ij}}\mathbf{1}_2\right]\boldsymbol{M}_j\boldsymbol{M}_i, \tag{5.2.7}$$

$$\boldsymbol{g}_2^{\mathrm{sf2,sr}}\left(i,j\right)=P\left(i,j\right)\left(\boldsymbol{d}_i\boldsymbol{M}_j\left[\boldsymbol{p}_i\frac{1-\mathrm{erf}\left(\mu r_{ij}\right)}{r_{ij}}\mathbf{1}_2\cdot\boldsymbol{p}_i\right]\boldsymbol{M}_j\boldsymbol{d}_i\right), \tag{5.2.8}$$

$$\boldsymbol{g}_2^{\mathrm{sf2,lr}}\left(i,j\right)=P\left(i,j\right)\left(\boldsymbol{d}_i\boldsymbol{M}_j\left[\boldsymbol{p}_i\frac{\mathrm{erf}\left(\mu r_{ij}\right)}{r_{ij}}\mathbf{1}_2\cdot\boldsymbol{p}_i\right]\boldsymbol{M}_j\boldsymbol{d}_i\right), \tag{5.2.9}$$

$$\boldsymbol{g}_2^{\mathrm{sf3,sr}}\left(i,j\right)=\boldsymbol{d}_i\boldsymbol{d}_j\left[\boldsymbol{p}_i\left(\boldsymbol{p}_j\frac{1-\mathrm{erf}\left(\mu r_{ij}\right)}{r_{ij}}\mathbf{1}_2\cdot\boldsymbol{p}_j\right)\cdot\boldsymbol{p}_i\right]\boldsymbol{d}_j\boldsymbol{d}_i, \tag{5.2.10}$$

and

$$\boldsymbol{g}_2^{\mathrm{sf3,lr}}\left(i,j\right)=\boldsymbol{d}_i\boldsymbol{d}_j\left[\boldsymbol{p}_i\left(\boldsymbol{p}_j\frac{\mathrm{erf}\left(\mu r_{ij}\right)}{r_{ij}}\mathbf{1}_2\cdot\boldsymbol{p}_j\right)\cdot\boldsymbol{p}_i\right]\boldsymbol{d}_j\boldsymbol{d}_i. \tag{5.2.11}$$

$E_{\mathrm{X}}^{\mathrm{lr}}$ and $E_{\mathrm{X}}^{\mathrm{sr}}$ are calculated as using Eqs. (5.2.12) and (5.2.13), respectively.

$$E_{\mathrm{X}}^{\mathrm{lr}}=-\frac{1}{2}\sum_{i=1}^{N}\sum_{j=1}^{N}\int\int d\mathbf{r}_1 d\mathbf{r}_2\varphi_i^*\left(\mathbf{r}_1\right)\varphi_j^*\left(\mathbf{r}_2\right)\boldsymbol{g}_2^{\mathrm{sf,lr}}\left(1,2\right)\varphi_j\left(\mathbf{r}_1\right)\varphi_i\left(\mathbf{r}_2\right) \tag{5.2.12}$$

$$E_{\mathrm{X}}^{\mathrm{sr}} = -\frac{1}{2}\sum_{i=1}^{N}\sum_{j=1}^{N}\int\int d\mathbf{r}_1 d\mathbf{r}_2 \varphi_i^*(\mathbf{r}_1)\varphi_j^*(\mathbf{r}_2)\boldsymbol{g}_2^{\mathrm{sf,sr}}(1,2)\varphi_j(\mathbf{r}_1)\varphi_i(\mathbf{r}_2) \tag{5.2.13}$$

As described in Chapter 2, LUT scheme for two-electron Hamiltonian only treats one-center, i.e., atomic-center TEIs by the relativistic operator and the others are calculated as nonrelativistic TEIs. Similarly, the TEIs of the range-separated two-electron operator consist of one-center TEIs of $\boldsymbol{g}_2^{\mathrm{sf,lr}}$ or $\boldsymbol{g}_2^{\mathrm{sf,sr}}$ and multicenter TEIs of nonrelativistic operators $\mathrm{erf}(\mu r_{12})/r_{12}$ or $(1-\mathrm{erf}(\mu r_{12}))/r_{12}$.

5.2.2 TEIs of range-separated two-electron operators in IOTC Hamiltonian

This subsection describes the implementation of the range-separated two-electron terms in the IOTC Hamiltonian. The evaluation method reported by Seino et al.[35] was extended. Based on the expansion of φ_i by $\{\chi_\mu\}$ (Eq. (2.3.30) in Chapter2), the AO-based TEIs with respect to $\boldsymbol{g}_2^{\mathrm{sfx,lr}}$ (x =1, 2, and 3),

$$\left\langle \chi_\mu\chi_\nu \middle| \boldsymbol{g}_2^{\mathrm{sfx,lr}} \middle| \chi_\lambda\chi_\sigma \right\rangle = \int\int d\mathbf{r}_1 d\mathbf{r}_2 \chi_\mu^*(\mathbf{r}_1)\chi_\nu^*(\mathbf{r}_2)\boldsymbol{g}_2^{\mathrm{sfx,lr}}(1,2)\chi_\lambda(\mathbf{r}_1)\chi_\sigma(\mathbf{r}_2), \tag{5.2.14}$$

are calculated to obtain $E_{\mathrm{X}}^{\mathrm{lr}}$. The matrix representations of the TEIs for $\boldsymbol{g}_2^{\mathrm{sfx,lr}}$ are

$$\begin{aligned}&\left\langle \chi_\mu\chi_\nu \middle| \boldsymbol{g}_2^{\mathrm{sf1,lr}} \middle| \chi_\lambda\chi_\sigma \right\rangle \\ &= \sum_{k_a k_b k_c k_d} \left\langle \chi_\mu \middle| \boldsymbol{M}_1 \middle| k_a \right\rangle \left\langle \chi_\nu \middle| \boldsymbol{M}_2 \middle| k_b \right\rangle \left\langle k_a k_b \middle| \mathrm{erf}(\mu r_{12})/r_{12}\,\mathbf{1}_2 \middle| k_c k_d \right\rangle \left\langle k_c \middle| \boldsymbol{M}_1 \middle| \chi_\lambda \right\rangle \left\langle k_d \middle| \boldsymbol{M}_2 \middle| \chi_\sigma \right\rangle,\end{aligned} \tag{5.2.15}$$

$$\begin{aligned}&\left\langle \chi_\mu\chi_\nu \middle| \boldsymbol{g}_2^{\mathrm{sf2,lr}} \middle| \chi_\lambda\chi_\sigma \right\rangle \\ &= \sum_{k_a k_b k_c k_d} \left\langle \chi_\mu \middle| \boldsymbol{d}_1 \middle| k_a \right\rangle \left\langle \chi_\nu \middle| \boldsymbol{M}_2 \middle| k_b \right\rangle \left\langle k_a k_b \middle| \boldsymbol{p}_1\,\mathrm{erf}(\mu r_{12})/r_{12}\,\mathbf{1}_2 \cdot \boldsymbol{p}_1 \middle| k_c k_d \right\rangle \left\langle k_c \middle| \boldsymbol{d}_1 \middle| \chi_\lambda \right\rangle \left\langle k_d \middle| \boldsymbol{M}_2 \middle| \chi_\sigma \right\rangle,\end{aligned} \tag{5.2.16}$$

and

$$\begin{aligned}&\left\langle \chi_\mu\chi_\nu \middle| \boldsymbol{g}_2^{\mathrm{sf3,lr}} \middle| \chi_\lambda\chi_\sigma \right\rangle \\ &= \sum_{k_a k_b k_c k_d} \left\langle \chi_\mu \middle| \boldsymbol{d}_1 \middle| k_a \right\rangle \left\langle \chi_\nu \middle| \boldsymbol{d}_2 \middle| k_b \right\rangle \left\langle k_a k_b \middle| \boldsymbol{p}_1 \left[\boldsymbol{p}_2\,\mathrm{erf}(\mu r_{12})/r_{12}\,\mathbf{1}_2 \cdot \boldsymbol{p}_2 \right] \cdot \boldsymbol{p}_1 \middle| k_c k_d \right\rangle \left\langle k_c \middle| \boldsymbol{d}_1 \middle| \chi_\lambda \right\rangle \left\langle k_d \middle| \boldsymbol{d}_2 \middle| \chi_\sigma \right\rangle.\end{aligned} \tag{5.2.17}$$

Consequently, the TEIs that require explicit calculations are those that appear in Eqs. (5.2.15)-(5.2.17):

$$\left\langle k_a k_b \left| \mathrm{erf}\left(\mu r_{12}\right)/r_{12}\,\mathbf{1}_2 \right| k_c k_d \right\rangle$$

$$\left\langle k_a k_b \left| \boldsymbol{p}_1 \,\mathrm{erf}\left(\mu r_{12}\right)/r_{12}\,\mathbf{1}_2 \cdot \boldsymbol{p}_1 \right| k_c k_d \right\rangle$$

$$\left\langle k_a k_b \left| \boldsymbol{p}_1 \left[\boldsymbol{p}_2 \,\mathrm{erf}\left(\mu r_{12}\right)/r_{12}\,\mathbf{1}_2 \cdot \boldsymbol{p}_2 \right] \cdot \boldsymbol{p}_1 \right| k_c k_d \right\rangle .$$

The first integral can be evaluated using the same algorithm as that required for the ERIs in a nonrelativistic framework. Considering $p_1 = -\mathrm{i}\nabla_{\mathbf{r}_1}$, the second and third TEIs are written as

$$\left\langle k_a k_b \left| \boldsymbol{p}_1 \,\mathrm{erf}\left(\mu r_{12}\right)/r_{12}\,\mathbf{1}_2 \cdot \boldsymbol{p}_1 \right| k_c k_d \right\rangle = \left\langle \nabla_{\mathbf{r}_1} k_a k_b \left| \mathrm{erf}\left(\mu r_{12}\right)/r_{12}\,\mathbf{1}_2 \right| \nabla_{\mathbf{r}_1} k_c k_d \right\rangle \tag{5.2.18}$$

and

$$\left\langle k_a k_b \left| \boldsymbol{p}_1 \left[\boldsymbol{p}_2 \,\mathrm{erf}\left(\mu r_{12}\right)/r_{12}\,\mathbf{1}_2 \cdot \boldsymbol{p}_2 \right] \cdot \boldsymbol{p}_1 \right| k_c k_d \right\rangle = \left\langle \nabla_{\mathbf{r}_1} k_a \nabla_{\mathbf{r}_2} k_b \left| \mathrm{erf}\left(\mu r_{12}\right)/r_{12}\,\mathbf{1}_2 \right| \nabla_{\mathbf{r}_1} k_c \nabla_{\mathbf{r}_2} k_d \right\rangle . \tag{5.2.19}$$

When Gaussian-type functions are adopted as $\{k\}$, $\nabla_{\mathbf{r}_1} k_a$ is represented by Gaussian-type functions that have different angular momenta from those of k_a. Thus, the TEIs on the right-hand side of Eqs. (5.2.18) and (5.2.19) can be calculated using a similar algorithm as that used for $\left\langle k_a k_b \left| \mathrm{erf}\left(\mu r_{12}\right)/r_{12}\,\mathbf{1}_2 \right| k_c k_d \right\rangle$.

Although the author reports the long-range part in the spin-free framework in this chapter, this method can be extended in a straightforward manner. Short-range HFx integrals $E_{\mathrm{X}}^{\mathrm{sr}}$ are obtained by the same procedure using operator $\boldsymbol{g}_2^{\mathrm{sfx,sr}}$ (x =1, 2, and 3). In the case of double-hybrid functionals,[36] TEIs in the perturbative second-order correlation part should be calculated using the operators in Eqs. (2.3.18)–(2.3.20). Similar formulae are applicable to spin-dependent component of long-range and short-range terms

(summarized in Appendix of this chapter). Spin-dependent calculations require variables such as the OEIs, TEIs, orbital coefficients, and Fock matrices to be treated in complex numbers. Although the program becomes considerably different from that in the nonrelativistic case, spin-dependent terms can be implemented using program packages like RAQET,[37] which support complex variables.

5.3 Numerical assessments

5.3.1 Computational details

This subsection explains the calculation conditions of the numerical assessments. The one-electron spin-free IOTC (two-electron nonrelativistic, denoted as 1eIOTC), one- and two-electron spin-free IOTC Hamiltonian (1e2eIOTC), and the LUT scheme for these (LUT-IOTC) were adopted. 1e2eIOTC indicates that the unitary transformation was applied to both full-range and range-separated two-electron operators, i.e., $1/r_{ij}$ and $\mathrm{erf}\left(\mu r_{ij}\right)/r_{ij}$, respectively. The spin-free (LUT-)IOTC transformation of density operator, $\boldsymbol{\delta}^{\mathrm{sf}}$ for the IOTC Hamiltonian and $\boldsymbol{\delta}^{\mathrm{LUT}}$ for the LUT-IOTC Hamiltonian was also considered. The cutoff distance τ for the one-electron LUT was set to 3.5 Å. Nonrelativistic, IOTC, and LUT-IOTC calculations were performed using the modified version of the GAMESS program.[38] As the 4c DFT, the spin-free Dirac–Coulomb (SFDC) calculations were performed using the DIRAC program.[39] All the CPU times were measured based on a single core of AMD EPYC™ E7763 (2.45 GHz, 64 cores).

Numerical experiments were conducted on noble gas atoms, namely, He, Ne, Ar, Kr, Xe, and Rn; their dimers (He_2, Ne_2, Ar_2, Kr_2, Xe_2, and Rn_2); hydrogen halides (HX; X= F, Cl, Br, I, and At); and bond cleavage reactions involving Pb and Ge complexes that are a part of the HEAVYSB11[40] benchmark set. In case of hydrogen halides, experimental bond lengths[41] with values of 0.9168, 1.2746, 1.4144, and 1.6092 Å were utilized for HF, HCl,

HBr, and HI molecules, respectively. An HAt bond length of 1.718 Å, as per the optimized value reported by Gomes and Visscher,[42] was used in the calculations. Additionally, one-dimensional HX chains, denoted as $(HX)_n$ (where X = F or At), were also subjected to analysis. For $(HF)_n$, the intramolecular and intermolecular distances were fixed at 0.970 and 1.530 Å, respectively. Conversely, for $(HAt)_n$, the corresponding distances were established as 1.729 and 3.148 Å, respectively. In both cases, the H–X–H and X–H–X bond angles were maintained at 120° and 180°, respectively. Potential energy curves were computed for noble gas dimers. To account for basis set superposition errors, the counterpoise method[43] was employed. Moreover, dispersion contributions were factored in utilizing the LRD method.[44] Equilibrium bond lengths R_e and dissociation energies D_e were extracted from a Morse potential fit based on equidistant points with a step length of 0.01 Å, both backward and forward along the bond distance, encompassing 10 points in total. The resulting Morse potential curve enabled the determination of the lowest energy.

The Becke's exchange (B88)[45] in conjunction with the Lee–Yang–Parr correlation[46] (BLYP), B88 exchange paired with one-parameter progressive correlation[47] (BOP), and Becke-3–parameter–Lee–Yang–Parr (B3LYP)[48] functionals were employed as the exchange-correlation functionals. Additionally, LC-BLYP (μ = 0.189,[14] 0.33,[9] and 0.47[15]), LC-BOP[7] (μ = 0.47), and CAM-B3LYP[10] functionals were utilized as range-separated functionals. The basis sets used in this study were Sapporo-DZP-2012+d for the first to third row elements[49,50] and Sapporo-DKH3-DZP-2012+d for the fourth and fifth row elements.[50,51] These basis sets were applied in a contracted form for the computations concerning $(HAt)_n$ and in an uncontracted form for all other calculations. For the analysis of bond cleavage reactions, the basis sets used did not include diffuse functions.

5.3.2 Deviation from 4c Hamiltonian

This subsection discusses the accuracy of the range separation method in the context

of the 1e2eIOTC Hamiltonian, with a focus on deviations from the SFDC values. Table 5.1 presents the total energy deviations (in hartree) for noble gas atoms, as determined by nonrelativistic and IOTC Hamiltonians, using the BLYP, LC-BLYP, B3LYP, and CAM-B3LYP functionals. The reference SFDC values are provided in parentheses. The energy deviation observed in LC-DFT are of the same order as those observed in the corresponding functionals without the LC method. The nonrelativistic Hamiltonian yields large errors across all functionals and elements. By contrast, the 1eIOTC Hamiltonian considerably reduces these errors, although they remain relatively pronounced for heavier elements. The results obtained using both 1e2eIOTC Hamiltonians with $\boldsymbol{\delta}^{\mathrm{sf}}$ exhibit strong agreement with the reference SFDC values. Notably, errors in the 1eIOTC Hamiltonian are smaller than those of the 1eIOTC Hamiltonian with $\boldsymbol{\delta}^{\mathrm{sf}}$. This discrepancy arises from the error cancellation effect stemming from the negative values in 1e2eIOTC Hamiltonians. The comprehensive IOTC transformation of both one- and two-electron operators and the density operator is essential in LC-DFT calculations. Furthermore, the energy deviations from SFDC values exhibit minimal dependence on the choice of basis sets, as illustrated in Tables 5.2–5.4.

Table 5.5 presents the orbital energy deviations for the Rn atom (in hartree), as determined by nonrelativistic and IOTC Hamiltonians employing the BLYP and LC-BLYP functionals. The reference SFDC values are indicated in parentheses. These deviations exhibit a consistent trend with the total energy deviations. The nonrelativistic Hamiltonian yields large errors, while the holistic IOTC transformation of one- and two-electron as well as density operators effectively reproduces the SFDC results. Errors in individual orbitals primarily depend on relativistic treatments and exhibit quasi-independence from the choice of the range-separate parameter. A common pattern observed in both nonrelativistic and IOTC Hamiltonians is that *s* and *p* orbitals tend to exhibit larger errors compared to *d* and *f* orbitals, suggesting that inner-shell orbitals are more significantly influenced by

relativistic effects than their outer-shell counterparts. Additionally, the nonrelativistic Hamiltonian overestimates orbital energies of *s* and *p* orbitals while underestimating those of *d* and *f* orbitals, compared to the SFDC energies. This behavior aligns with the shrinkage of inner-shell orbitals and expansion of outer-shell orbitals.

Table 5.1. Total energy deviation (in hartree) of noble gas atoms obtained by nonrelativistic and IOTC Hamiltonians from 4c Hamiltonian using BLYP, LC-BLYP (μ = 0.189, 0.33, and 0.47), B3LYP, and CAM-B3LYP functionals. IOTC transformation for one-electron (1e), two-electron (2e), and density operator ($\boldsymbol{\delta}^{\mathrm{sf}}$) was examined. The reference SFDC values are shown in parentheses.

		Nonrelativistic	1eIOTC	1eIOTC with $\boldsymbol{\delta}^{\mathrm{sf}}$	1e2eIOTC	1e2eIOTC with $\boldsymbol{\delta}^{\mathrm{sf}}$	(SFDC)
He							
	BLYP	0.000132	0.000020	0.000064	−0.000043	0.000000	(−2.901151)
	LC-BLYP (μ = 0.189)	0.000130	0.000021	0.000062	−0.000041	0.000000	(−2.860187)
	LC-BLYP (μ = 0.33)	0.000128	0.000022	0.000061	−0.000038	0.000000	(−2.862495)
	LC-BLYP (μ = 0.47)	0.000127	0.000023	0.000059	−0.000036	0.000000	(−2.871390)
	B3LYP	0.000130	0.000023	0.000057	−0.000034	0.000000	(−2.902225)
	CAM-B3LYP	0.000129	0.000023	0.000057	−0.000033	0.000000	(−2.895608)
Ne							
	BLYP	0.145635	0.006365	0.014243	−0.007884	−0.000001	(−129.062596)
	LC-BLYP (μ = 0.189)	0.145535	0.006416	0.014232	−0.007821	−0.000001	(−128.927377)
	LC-BLYP (μ = 0.33)	0.145420	0.006453	0.014218	−0.007770	−0.000001	(−128.903626)
	LC-BLYP (μ = 0.47)	0.145299	0.006490	0.014201	−0.007716	−0.000001	(−128.903021)
	B3LYP	0.144975	0.006668	0.012809	−0.006145	−0.000001	(−129.031594)
	CAM-B3LYP	0.145103	0.006545	0.012884	−0.006343	−0.000001	(−129.047192)
Ar							
	BLYP	1.874055	0.052874	0.101627	−0.048827	−0.000024	(−529.387682)
	LC-BLYP (μ = 0.189)	1.873644	0.053055	0.101603	−0.048621	−0.000024	(−529.196260)
	LC-BLYP (μ = 0.33)	1.873173	0.053188	0.101573	−0.048458	−0.000024	(−529.150163)
	LC-BLYP (μ = 0.47)	1.872748	0.053321	0.101540	−0.048292	−0.000023	(−529.127525)
	B3LYP	1.868787	0.053412	0.091437	−0.038081	−0.000021	(−529.329712)
	CAM-B3LYP	1.869937	0.052617	0.091974	−0.039414	−0.000021	(−529.404586)

Table 5.1. Continued.

		Nonrelativistic	1eIOTC	1eIOTC with $\boldsymbol{\delta}^{\mathrm{sf}}$	1e2eIOTC	1e2eIOTC with $\boldsymbol{\delta}^{\mathrm{sf}}$	(SFDC)
Kr							
	BLYP	36.949097	0.586170	1.006724	−0.421984	−0.000592	(−2790.772595)
	LC-BLYP (μ = 0.189)	36.947048	0.586934	1.006667	−0.421162	−0.000591	(−2790.484613)
	LC-BLYP (μ = 0.33)	36.944735	0.587498	1.006596	−0.420526	−0.000591	(−2790.399639)
	LC-BLYP (μ = 0.47)	36.942528	0.588052	1.006514	−0.419887	−0.000591	(−2790.355417)
	B3LYP	36.888814	0.577957	0.906110	−0.329142	−0.000399	(−2790.570517)
	CAM-B3LYP	36.902074	0.571163	0.911312	−0.341176	−0.000413	(−2790.833830)
Xe							
	BLYP	214.451097	2.444200	3.974525	−1.535082	−0.000305	(−7449.245992)
	LC-BLYP (μ = 0.189)	214.445951	2.445886	3.974416	−1.533297	−0.000318	(−7448.887145)
	LC-BLYP (μ = 0.33)	214.440170	2.447132	3.974288	−1.531931	−0.000327	(−7448.773083)
	LC-BLYP (μ = 0.47)	214.434461	2.448358	3.974141	−1.530566	−0.000337	(−7448.705194)
	B3LYP	214.202609	2.382933	3.578199	−1.197924	0.000482	(−7448.785471)
	CAM-B3LYP	214.256842	2.360142	3.598703	−1.241189	0.000635	(−7449.304200)
Rn							
	BLYP	1712.553415	13.223952	21.273169	−8.092406	−0.003583	(−23583.958589)
	LC-BLYP (μ = 0.189)	1712.536892	13.228214	21.272925	−8.087938	−0.003633	(−23583.494933)
	LC-BLYP (μ = 0.33)	1712.518274	13.231367	21.272644	−8.084529	−0.003665	(−23583.332108)
	LC-BLYP (μ = 0.47)	1712.499450	13.234474	21.272326	−8.081129	−0.003697	(−23583.231096)
	B3LYP	1711.136714	12.889248	19.178587	−6.300707	0.016593	(−23582.195271)
	CAM-B3LYP	1711.444189	12.768754	19.286218	−6.530045	0.016470	(−23583.390542)

Table 5.2. Total energy deviation (in hartree) of noble gas atoms obtained by nonrelativistic and IOTC Hamiltonians from SFDC Hamiltonian using BLYP, LC-BLYP (μ = 0.189, 0.33, and 0.47), B3LYP, and CAM-B3LYP functionals. Uncontracted Sapporo(-DKH3)-DZP-2012 basis sets were used. The reference SFDC values are provided in parentheses.

		Nonrelativistic	1eIOTC	1eIOTC with $\boldsymbol{\delta}^{sf}$	1e2eIOTC	1e2eIOTC with $\boldsymbol{\delta}^{sf}$	(SFDC)
He							
	BLYP	0.000132	0.000021	0.000064	−0.000044	0.000000	(−2.899065)
	LC-BLYP (μ = 0.189)	0.000130	0.000022	0.000063	−0.000041	0.000000	(−2.857572)
	LC-BLYP (μ = 0.33)	0.000129	0.000023	0.000062	−0.000039	0.000000	(−2.859756)
	LC-BLYP (μ = 0.47)	0.000128	0.000024	0.000060	−0.000036	0.000000	(−2.869061)
	B3LYP	0.000130	0.000024	0.000058	−0.000034	0.000000	(−2.900673)
	CAM-B3LYP	0.000129	0.000024	0.000057	−0.000033	0.000000	(−2.893825)
Ne							
	BLYP	0.145625	0.006379	0.014254	−0.007872	0.000007	(−129.043110)
	LC-BLYP (μ = 0.189)	0.145527	0.006431	0.014243	−0.007810	0.000007	(−128.906633)
	LC-BLYP (μ = 0.33)	0.145417	0.006468	0.014230	−0.007759	0.000008	(−128.882692)
	LC-BLYP (μ = 0.47)	0.145302	0.006504	0.014213	−0.007705	0.000007	(−128.883623)
	B3LYP	0.144969	0.006679	0.012818	−0.006137	0.000005	(−129.015852)
	CAM-B3LYP	0.145099	0.006557	0.012893	−0.006334	0.000006	(−129.030715)
Ar							
	BLYP	1.874127	0.052947	0.101699	−0.048754	0.000048	(−529.386586)
	LC-BLYP (μ = 0.189)	1.873727	0.053139	0.101687	−0.048538	0.000060	(−529.194929)
	LC-BLYP (μ = 0.33)	1.873246	0.053259	0.101644	−0.048388	0.000047	(−529.149051)
	LC-BLYP (μ = 0.47)	1.872800	0.053370	0.101589	−0.048244	0.000025	(−529.126726)
	B3LYP	1.868837	0.053463	0.091488	−0.038030	0.000030	(−529.328918)
	CAM-B3LYP	1.869989	0.052668	0.092025	−0.039363	0.000030	(−529.403764)

Table 5.2. Continued.

		Nonrelativistic	1eIOTC	1eIOTC with $\boldsymbol{\delta}^{sf}$	1e2eIOTC	1e2eIOTC with $\boldsymbol{\delta}^{sf}$	(SFDC)
Kr							
	BLYP	36.949113	0.586174	1.006728	−0.421980	−0.000588	(−2790.772124)
	LC-BLYP (μ = 0.189)	36.947071	0.586938	1.006672	−0.421158	−0.000588	(−2790.484057)
	LC-BLYP (μ = 0.33)	36.944760	0.587502	1.006601	−0.420522	−0.000587	(−2790.399208)
	LC-BLYP (μ = 0.47)	36.942551	0.588057	1.006518	−0.419883	−0.000587	(−2790.355103)
	B3LYP	36.888831	0.577961	0.906114	−0.329138	−0.000395	(−2790.570152)
	CAM-B3LYP	36.902094	0.571167	0.911316	−0.341172	−0.000409	(−2790.833470)
Xe							
	BLYP	214.450898	2.444191	3.974515	−1.535091	−0.000314	(−7449.246062)
	LC-BLYP (μ = 0.189)	214.445759	2.445875	3.974405	−1.533307	−0.000328	(−7448.887199)
	LC-BLYP (μ = 0.33)	214.439980	2.447121	3.974276	−1.531942	−0.000339	(−7448.773196)
	LC-BLYP (μ = 0.47)	214.434268	2.448347	3.974130	−1.530576	−0.000348	(−7448.705330)
	B3LYP	214.202411	2.382924	3.578189	−1.197933	0.000473	(−7448.785575)
	CAM-B3LYP	214.256646	2.360132	3.598692	−1.241199	0.000625	(−7449.304319)
Rn							
	BLYP	1712.552748	13.223370	21.272589	−8.092988	−0.004164	(−23583.957984)
	LC-BLYP (μ = 0.189)	1712.536291	13.227635	21.272347	−8.088517	−0.004210	(−23583.494331)
	LC-BLYP (μ = 0.33)	1712.517686	13.230786	21.272065	−8.085110	−0.004245	(−23583.331580)
	LC-BLYP (μ = 0.47)	1712.498841	13.233890	21.271744	−8.081713	−0.004280	(−23583.230600)
	B3LYP	1711.136055	12.888669	19.178009	−6.301286	0.016015	(−23582.194717)
	CAM-B3LYP	1711.443564	12.768175	19.285640	−6.530624	0.015892	(−23583.390016)

Table 5.3. Total energy deviation (in hartree) of noble gas atoms obtained by nonrelativistic and IOTC Hamiltonians from SFDC Hamiltonian using BLYP, LC-BLYP (μ = 0.189, 0.33, and 0.47), B3LYP, and CAM-B3LYP functionals. Uncontracted Sapporo(-DKH3)-TZP-2012 basis sets were used. The reference SFDC values are provided in parentheses.

		Nonrelativistic	1eIOTC	1eIOTC with $\boldsymbol{\delta}^{\mathrm{sf}}$	1e2eIOTC	1e2eIOTC with $\boldsymbol{\delta}^{\mathrm{sf}}$	(SFDC)
He							
	BLYP	0.000140	0.000019	0.000064	−0.000045	0.000000	(−2.906429)
	LC-BLYP (μ = 0.189)	0.000138	0.000020	0.000063	−0.000043	0.000000	(−2.865254)
	LC-BLYP (μ = 0.33)	0.000136	0.000021	0.000061	−0.000040	0.000000	(−2.867487)
	LC-BLYP (μ = 0.47)	0.000135	0.000022	0.000060	−0.000038	0.000000	(−2.876462)
	B3LYP	0.000138	0.000022	0.000058	−0.000035	0.000000	(−2.907583)
	CAM-B3LYP	0.000137	0.000022	0.000057	−0.000035	0.000000	(−2.900882)
Ne							
	BLYP	0.145967	0.006388	0.014258	−0.007876	−0.000001	(−129.094125)
	LC-BLYP (μ = 0.189)	0.145868	0.006438	0.014247	−0.007814	−0.000001	(−128.958557)
	LC-BLYP (μ = 0.33)	0.145756	0.006475	0.014233	−0.007764	−0.000001	(−128.935039)
	LC-BLYP (μ = 0.47)	0.145640	0.006511	0.014216	−0.007710	−0.000001	(−128.935289)
	B3LYP	0.145307	0.006687	0.012823	−0.006140	−0.000001	(−129.064463)
	CAM-B3LYP	0.145436	0.006564	0.012898	−0.006337	−0.000001	(−129.079933)
Ar							
	BLYP	1.874011	0.052850	0.101604	−0.048853	−0.000050	(−529.390946)
	LC-BLYP (μ = 0.189)	1.873600	0.053031	0.101579	−0.048648	−0.000050	(−529.199343)
	LC-BLYP (μ = 0.33)	1.873132	0.053165	0.101550	−0.048485	−0.000050	(−529.153454)
	LC-BLYP (μ = 0.47)	1.872709	0.053297	0.101517	−0.048320	−0.000050	(−529.131050)
	B3LYP	1.868745	0.053388	0.091413	−0.038107	−0.000047	(−529.333177)
	CAM-B3LYP	1.869896	0.052593	0.091950	−0.039441	−0.000048	(−529.408058)

Table 5.3. Continued.

		Nonrelativistic	1eIOTC	1eIOTC with $\boldsymbol{\delta}^{sf}$	1e2eIOTC	1e2eIOTC with $\boldsymbol{\delta}^{sf}$	(SFDC)
Kr							
	BLYP	36.949068	0.586048	1.006603	−0.422104	−0.000712	(−2790.772255)
	LC-BLYP (μ = 0.189)	36.947026	0.586813	1.006547	−0.421281	−0.000711	(−2790.484180)
	LC-BLYP (μ = 0.33)	36.944716	0.587377	1.006476	−0.420645	−0.000710	(−2790.399316)
	LC-BLYP (μ = 0.47)	36.942508	0.587932	1.006393	−0.420006	−0.000710	(−2790.355187)
	B3LYP	36.888785	0.577836	0.905989	−0.329263	−0.000519	(−2790.570249)
	CAM-B3LYP	36.902049	0.571042	0.911191	−0.341296	−0.000533	(−2790.833567)
Xe							
	BLYP	214.458601	2.451736	3.982060	−1.527548	0.007228	(−7449.255044)
	LC-BLYP (μ = 0.189)	214.453475	2.453423	3.981952	−1.525763	0.007216	(−7448.896144)
	LC-BLYP (μ = 0.33)	214.447698	2.454669	3.981825	−1.524396	0.007207	(−7448.782124)
	LC-BLYP (μ = 0.47)	214.441986	2.455895	3.981678	−1.523030	0.007198	(−7448.714264)
	B3LYP	214.210123	2.390475	3.585740	−1.190384	0.008021	(−7448.794553)
	CAM-B3LYP	214.264363	2.367684	3.606244	−1.233649	0.008174	(−7449.313283)
Rn							
	BLYP	1712.552619	13.223486	21.272702	−8.092871	−0.004050	(−23583.960826)
	LC-BLYP (μ = 0.189)	1712.536170	13.227750	21.272459	−8.088402	−0.004098	(−23583.497100)
	LC-BLYP (μ = 0.33)	1712.517557	13.230901	21.272176	−8.084995	−0.004133	(−23583.334256)
	LC-BLYP (μ = 0.47)	1712.498700	13.234006	21.271856	−8.081596	−0.004166	(−23583.233260)
	B3LYP	1711.135964	12.888785	19.178122	−6.301169	0.016129	(−23582.197508)
	CAM-B3LYP	1711.443453	12.768290	19.285752	−6.530508	0.016005	(−23583.392756)

Table 5.4. Total energy deviation (in hartree) of noble gas atoms obtained by nonrelativistic and IOTC Hamiltonians from SFDC Hamiltonian using BLYP, LC-BLYP (μ = 0.189, 0.33, and 0.47), B3LYP, and CAM-B3LYP functionals. Uncontracted Sapporo(-DKH3)-TZP-2012+d basis sets were used. The reference SFDC values are provided in parentheses.

		Nonrelativistic	1eIOTC	1eIOTC with $\boldsymbol{\delta}^{sf}$	1e2eIOTC	1e2eIOTC with $\boldsymbol{\delta}^{sf}$	(SFDC)
He							
	BLYP	0.000140	0.000019	0.000064	−0.000045	0.000000	(−2.906756)
	LC-BLYP (μ = 0.189)	0.000138	0.000020	0.000063	−0.000043	0.000000	(−2.865710)
	LC-BLYP (μ = 0.33)	0.000136	0.000021	0.000061	−0.000040	0.000000	(−2.867905)
	LC-BLYP (μ = 0.47)	0.000135	0.000022	0.000060	−0.000038	0.000000	(−2.876744)
	B3LYP	0.000138	0.000022	0.000057	−0.000035	0.000000	(−2.907802)
	CAM-B3LYP	0.000137	0.000022	0.000057	−0.000034	0.000000	(−2.901129)
Ne							
	BLYP	0.145978	0.006385	0.014257	−0.007878	−0.000001	(−129.102314)
	LC-BLYP (μ = 0.189)	0.145880	0.006435	0.014246	−0.007816	−0.000001	(−128.967239)
	LC-BLYP (μ = 0.33)	0.145766	0.006472	0.014232	−0.007765	−0.000001	(−128.943532)
	LC-BLYP (μ = 0.47)	0.145646	0.006509	0.014215	−0.007712	−0.000001	(−128.942935)
	B3LYP	0.145312	0.006685	0.012822	−0.006141	−0.000001	(−129.071486)
	CAM-B3LYP	0.145441	0.006562	0.012897	−0.006338	−0.000001	(−129.087120)
Ar							
	BLYP	1.874012	0.052849	0.101602	−0.048855	−0.000051	(−529.392053)
	LC-BLYP (μ = 0.189)	1.873601	0.053029	0.101578	−0.048650	−0.000052	(−529.200600)
	LC-BLYP (μ = 0.33)	1.873130	0.053163	0.101548	−0.048487	−0.000052	(−529.154489)
	LC-BLYP (μ = 0.47)	1.872706	0.053295	0.101515	−0.048321	−0.000052	(−529.131874)
	B3LYP	1.868743	0.053386	0.091412	−0.038109	−0.000049	(−529.334086)
	CAM-B3LYP	1.869894	0.052591	0.091948	−0.039443	−0.000049	(−529.408950)

Table 5.4. Continued.

		Nonrelativistic	1eIOTC	1eIOTC with $\boldsymbol{\delta}^{sf}$	1e2eIOTC	1e2eIOTC with $\boldsymbol{\delta}^{sf}$	(SFDC)
Kr							
	BLYP	36.949387	0.586316	1.006870	−0.421836	−0.000444	(−2790.772590)
	LC-BLYP (μ = 0.189)	36.947340	0.587080	1.006813	−0.421014	−0.000443	(−2790.484586)
	LC-BLYP (μ = 0.33)	36.945028	0.587644	1.006743	−0.420377	−0.000443	(−2790.399613)
	LC-BLYP (μ = 0.47)	36.942821	0.588199	1.006660	−0.419739	−0.000442	(−2790.355406)
	B3LYP	36.889104	0.578104	0.906257	−0.328994	−0.000251	(−2790.570500)
	CAM-B3LYP	36.902365	0.571309	0.911459	−0.341027	−0.000265	(−2790.833812)
Xe							
	BLYP	214.450695	2.443847	3.974171	−1.535437	−0.000660	(−7449.247932)
	LC-BLYP (μ = 0.189)	214.445555	2.445534	3.974063	−1.533652	−0.000673	(−7448.889041)
	LC-BLYP (μ = 0.33)	214.439777	2.446780	3.973936	−1.532285	−0.000682	(−7448.774969)
	LC-BLYP (μ = 0.47)	214.434069	2.448006	3.973789	−1.530920	−0.000691	(−7448.707084)
	B3LYP	214.202210	2.382582	3.577847	−1.198277	0.000128	(−7448.787390)
	CAM-B3LYP	214.256445	2.359791	3.598352	−1.241542	0.000281	(−7449.306109)
Rn							
	BLYP	1712.552599	13.223491	21.272707	−8.092867	−0.004046	(−23583.961056)
	LC-BLYP (μ = 0.189)	1712.536079	13.227755	21.272465	−8.088397	−0.004093	(−23583.497359)
	LC-BLYP (μ = 0.33)	1712.517455	13.230906	21.272182	−8.084990	−0.004127	(−23583.334516)
	LC-BLYP (μ = 0.47)	1712.498626	13.234010	21.271862	−8.081592	−0.004162	(−23583.233502)
	B3LYP	1711.135941	12.888790	19.178127	−6.301165	0.016133	(−23582.197731)
	CAM-B3LYP	1711.443395	12.768295	19.285757	−6.530503	0.016010	(−23583.392990)

Table 5.5. Orbital energy deviation (in hartree) of Rn atom obtained by nonrelativistic (Nonrel.) and IOTC Hamiltonians from 4c Hamiltonian using BLYP and LC-BLYP (μ = 0.189, 0.33, and 0.47) functionals. The reference SFDC value are shown in parentheses.

	Nonrel.	1eIOTC	1eIOTC w/ $\boldsymbol{\delta}^{\mathrm{sf}}$	1e2eIOTC	1e2eIOTC w/ $\boldsymbol{\delta}^{\mathrm{sf}}$	(SFDC)
BLYP						
1*s*	412.3708	9.0938	13.2110	−4.1629	−0.0074	(−3619.4264)
2*s*	111.6033	1.2138	1.7872	−0.5800	−0.0019	(−658.4915)
2*p*	33.6494	0.8523	0.8186	0.0326	−0.0014	(−561.3627)
3*s*	28.0375	0.2470	0.3797	−0.1342	−0.0005	(−161.4652)
3*p*	9.6960	0.1702	0.1621	0.0078	−0.0004	(−133.8916)
3*d*	−0.9692	0.0640	0.0586	0.0053	−0.0001	(−105.9791)
4*s*	7.2136	0.0552	0.0902	−0.0354	−0.0002	(−38.4741)
4*p*	2.2729	0.0340	0.0319	0.0020	−0.0001	(−29.3946)
4*d*	−0.4289	0.0061	0.0047	0.0014	0.0000	(−19.0154)
4*f*	−1.0054	−0.0069	−0.0079	0.0011	0.0000	(−7.9255)
5*s*	1.4953	0.0097	0.0175	−0.0079	−0.0001	(−7.3784)
5*p*	0.3119	0.0044	0.0038	0.0006	0.0000	(−4.7112)
5*d*	−0.2171	−0.0012	−0.0015	0.0004	0.0000	(−1.6816)
6*s*	0.1812	0.0009	0.0021	−0.0012	0.0000	(−0.7935)
6*p*	−0.0023	0.0001	0.0000	0.0001	0.0000	(−0.2782)
LC-BLYP (μ = 0.189)						
1*s*	412.3694	9.0944	13.2109	−4.1622	−0.0074	(−3619.5226)
2*s*	111.6020	1.2140	1.7872	−0.5798	−0.0019	(−658.5969)
2*p*	33.6485	0.8524	0.8186	0.0326	−0.0014	(−561.4687)
3*s*	28.0358	0.2471	0.3797	−0.1341	−0.0005	(−161.5724)
3*p*	9.6949	0.1702	0.1621	0.0078	−0.0004	(−133.9994)
3*d*	−0.9701	0.0640	0.0586	0.0053	−0.0001	(−106.0871)
4*s*	7.2124	0.0552	0.0902	−0.0353	−0.0002	(−38.5805)
4*p*	2.2718	0.0340	0.0319	0.0020	−0.0001	(−29.5013)
4*d*	−0.4300	0.0061	0.0047	0.0014	0.0000	(−19.1228)
4*f*	−1.0064	−0.0069	−0.0079	0.0011	0.0000	(−8.0332)
5*s*	1.4952	0.0097	0.0175	−0.0079	−0.0001	(−7.4871)
5*p*	0.3113	0.0044	0.0038	0.0006	0.0000	(−4.8192)
5*d*	−0.2181	−0.0012	−0.0015	0.0004	0.0000	(−1.7863)
6*s*	0.1801	0.0009	0.0021	−0.0012	0.0000	(−0.9039)
6*p*	−0.0029	0.0001	0.0000	0.0001	0.0000	(−0.3725)

Table 5.5. Continued.

	Nonrel.	1eIOTC	1eIOTC w/ $\boldsymbol{\delta}^{\mathrm{sf}}$	1e2eIOTC	1e2eIOTC w/ $\boldsymbol{\delta}^{\mathrm{sf}}$	(SFDC)
LC-BLYP (μ = 0.33)						
1*s*	412.3679	9.0948	13.2108	−4.1617	−0.0074	(−3619.5890)
2*s*	111.6004	1.2141	1.7872	−0.5797	−0.0019	(−658.6704)
2*p*	33.6472	0.8523	0.8185	0.0326	−0.0014	(−561.5426)
3*s*	28.0340	0.2471	0.3797	−0.1340	−0.0005	(−161.6476)
3*p*	9.6935	0.1702	0.1621	0.0078	−0.0004	(−134.0748)
3*d*	−0.9713	0.0640	0.0586	0.0053	−0.0001	(−106.1626)
4*s*	7.2110	0.0553	0.0902	−0.0353	−0.0002	(−38.6554)
4*p*	2.2704	0.0340	0.0319	0.0020	−0.0001	(−29.5763)
4*d*	−0.4312	0.0061	0.0047	0.0014	0.0000	(−19.1982)
4*f*	−1.0078	−0.0069	−0.0079	0.0011	0.0000	(−8.1073)
5*s*	1.4945	0.0097	0.0175	−0.0079	−0.0001	(−7.5654)
5*p*	0.3099	0.0044	0.0038	0.0006	0.0000	(−4.8964)
5*d*	−0.2197	−0.0012	−0.0016	0.0004	0.0000	(−1.8506)
6*s*	0.1809	0.0009	0.0021	−0.0012	0.0000	(−0.9763)
6*p*	−0.0034	0.0001	0.0000	0.0001	0.0000	(−0.4114)
LC-BLYP (μ = 0.47)						
1*s*	412.3664	9.0952	13.2107	−4.1612	−0.0074	(−3619.6533)
2*s*	111.5988	1.2142	1.7871	−0.5795	−0.0019	(−658.7416)
2*p*	33.6460	0.8523	0.8185	0.0326	−0.0014	(−561.6142)
3*s*	28.0323	0.2472	0.3797	−0.1340	−0.0005	(−161.7207)
3*p*	9.6922	0.1702	0.1621	0.0078	−0.0004	(−134.1482)
3*d*	−0.9724	0.0639	0.0585	0.0053	−0.0001	(−106.2359)
4*s*	7.2097	0.0553	0.0902	−0.0353	−0.0002	(−38.7289)
4*p*	2.2691	0.0340	0.0319	0.0020	−0.0001	(−29.6500)
4*d*	−0.4324	0.0061	0.0046	0.0014	0.0000	(−19.2717)
4*f*	−1.0092	−0.0069	−0.0079	0.0011	0.0000	(−8.1773)
5*s*	1.4938	0.0097	0.0175	−0.0079	−0.0001	(−7.6437)
5*p*	0.3085	0.0044	0.0038	0.0007	0.0000	(−4.9715)
5*d*	−0.2217	−0.0012	−0.0016	0.0004	0.0000	(−1.9014)
6*s*	0.1851	0.0010	0.0021	−0.0012	0.0000	(−1.0283)
6*p*	−0.0029	0.0001	0.0000	0.0001	0.0000	(−0.4325)

5.3.3 Accuracy of LUT

This subsection provides insight into the accuracy of the LUT scheme within the range separation method for the two-electron term. Table 5.6 presents the total energies of HX molecules (in hartree) obtained using various approaches: 1e2eLUT-IOTC Hamiltonian with $\boldsymbol{\delta}^{\mathrm{LUT}}$, 1e2eIOTC Hamiltonian with $\boldsymbol{\delta}^{\mathrm{sf}}$, and the SFDC Hamiltonian. BLYP, LC-BLYP, B3LYP, and CAM-B3LYP functionals were employed for calculations. Δ^{LUT} represents the energy deviations of LUT-IOTC from IOTC, i.e., the difference between 1e2eLUT-IOTC Hamiltonian with $\boldsymbol{\delta}^{\mathrm{LUT}}$ and 1e2eIOTC Hamiltonian with $\boldsymbol{\delta}^{\mathrm{sf}}$. Δ^{SFDC} represents the energy deviations of 1e2eIOTC Hamiltonian with $\boldsymbol{\delta}^{\mathrm{sf}}$ from the SFDC Hamiltonian. Notably, both Δ^{SFDC} and Δ^{LUT} exhibit minimal dependence on the range-separation parameter. The absolute values of Δ^{LUT} are approximately on the order of 10^{-5} hartree, which is remarkably small, particularly for heavier-element systems. In comparison to Δ^{SFDC}, these deviations are one-tenth in HBr, one hundredth in HI, and one-thousandth in HAt. These findings affirm that the LUT scheme serves as a reliable approximation to the 4c theory.

Table 5.7 provides the total energies in $(\mathrm{HF})_n$ and $(\mathrm{HAt})_n$ molecules (in hartree), which were computed using 1e2eLUT-IOTC Hamiltonians with $\boldsymbol{\delta}^{\mathrm{LUT}}$, as well as 1e2eIOTC Hamiltonians with $\boldsymbol{\delta}^{\mathrm{sf}}$. BLYP and LC-BLYP functionals with $\mu = 0.33$ were employed as exchange-correlation functionals. Although Δ^{LUT} increases as n becomes larger, Δ^{LUT} remains less than 1 millihartree per unit. Thus, the accuracy of the LUT scheme within LC-DFT remains acceptable even for large-scale molecules. In terms of differences between the two functionals, Δ^{LUT} for LC-BLYP is slightly smaller than that for BLYP, except for cases where $n = 1$. This observation suggests that the effects of LUT in the long-range region are comparatively smaller for two-electron interactions than for the electron density.

Table 5.6. Total energy (in hartree) of HX molecules obtained using1e2eLUT-IOTC Hamiltonian with $\boldsymbol{\delta}^{\mathrm{LUT}}$ (E^{LUT}), 1e2eIOTC Hamiltonian with $\boldsymbol{\delta}^{\mathrm{sf}}$ (E^{IOTC}), and 4c Hamiltonian (E^{SFDC}). Δ^{LUT} represents the deviations of E^{LUT} from E^{IOTC}. Δ^{SFDC} represents the deviations of E^{IOTC} from E^{SFDC}.

	E^{LUT}	Δ^{LUT}	E^{IOTC}	Δ^{SFDC}	E^{SFDC}
HF					
BLYP	−100.543614	0.000029	−100.543642	0.000000	−100.543642
LC-BLYP (μ = 0.189)	−100.416731	0.000029	−100.416759	0.000000	−100.416759
LC-BLYP (μ = 0.33)	−100.398683	0.000028	−100.398711	0.000000	−100.398711
LC-BLYP (μ = 0.47)	−100.397707	0.000028	−100.397734	0.000000	−100.397734
B3LYP	−100.515432	0.000027	−100.515459	0.000000	−100.515459
CAM-B3LYP	−100.527942	0.000027	−100.527969	0.000000	−100.527969
HCl					
BLYP	−462.258826	−0.000008	−462.258817	−0.000019	−462.258798
LC-BLYP (μ = 0.189)	−462.070298	−0.000010	−462.070288	−0.000019	−462.070269
LC-BLYP (μ = 0.33)	−462.025211	−0.000010	−462.025201	−0.000019	−462.025182
LC-BLYP (μ = 0.47)	−462.001248	−0.000010	−462.001238	−0.000019	−462.001220
B3LYP	−462.206224	−0.000005	−462.206219	−0.000016	−462.206203
CAM-B3LYP	−462.272085	−0.000006	−462.272079	−0.000016	−462.272063
HBr					
BLYP	−2607.542663	−0.000014	−2607.542649	−0.000628	−2607.542021
LC-BLYP (μ = 0.189)	−2607.253897	−0.000016	−2607.253880	−0.000627	−2607.253254
LC-BLYP (μ = 0.33)	−2607.168506	−0.000018	−2607.168487	−0.000626	−2607.167861
LC-BLYP (μ = 0.47)	−2607.122745	−0.000020	−2607.122725	−0.000625	−2607.122100
B3LYP	−2607.345601	−0.000012	−2607.345589	−0.000441	−2607.345148
CAM-B3LYP	−2607.595326	−0.000014	−2607.595312	−0.000460	−2607.594851

Table 5.6. Continued.

		E^{LUT}	Δ^{LUT}	E^{IOTC}	Δ^{SFDC}	E^{SFDC}
HI						
	BLYP	−7118.805152	−0.000020	−7118.805133	0.001305	−7118.806437
	LC-BLYP (μ = 0.189)	−7118.442754	−0.000022	−7118.442732	0.001297	−7118.444029
	LC-BLYP (μ = 0.33)	−7118.326952	−0.000022	−7118.326929	0.001292	−7118.328221
	LC-BLYP (μ = 0.47)	−7118.256755	−0.000023	−7118.256733	0.001286	−7118.258019
	B3LYP	−7118.363480	−0.000017	−7118.363463	0.002414	−7118.365877
	CAM-B3LYP	−7118.863530	−0.000018	−7118.863512	0.002482	−7118.865994
HAt						
	BLYP	−22894.069198	−0.000011	−22894.069188	−0.015455	−22894.053733
	LC-BLYP (μ = 0.189)	−22893.600109	−0.000012	−22893.600097	−0.015486	−22893.584611
	LC-BLYP (μ = 0.33)	−22893.434234	−0.000012	−22893.434221	−0.015509	−22893.418712
	LC-BLYP (μ = 0.47)	−22893.329648	−0.000013	−22893.329635	−0.015531	−22893.314104
	B3LYP	−22892.346210	−0.000008	−22892.346202	0.005928	−22892.352130
	CAM-B3LYP	−22893.510246	−0.000009	−22893.510237	0.005494	−22893.515731

Table 5.7 Total energy (in hartree) of $(HF)_n$ and $(HAt)_n$ obtained using 1e2eLUT-IOTC Hamiltonian with $\boldsymbol{\delta}^{LUT}$ (E^{LUT}) and 1e2eIOTC Hamiltonian with $\boldsymbol{\delta}^{sf}$ (E^{IOTC}). BLYP and LC-BLYP (μ = 0.33) were used. Δ^{LUT} represents the deviations of E^{LUT} from E^{IOTC}.

molecule	n	BLYP			LC-BLYP (μ = 0.33)		
		E^{LUT}	E^{IOTC}	Δ^{LUT}	E^{LUT}	E^{IOTC}	Δ^{LUT}
HF							
	1	−100.542761	−100.542785	0.000024	−100.397424	−100.397448	0.000024
	2	−201.091142	−201.091121	−0.000021	−200.806609	−200.806599	−0.000010
	3	−301.644768	−301.644684	−0.000084	−301.221020	−301.220960	−0.000060
	4	−402.200322	−402.200167	−0.000155	−401.637354	−401.637237	−0.000117
	5	−502.756711	−502.756481	−0.000230	−502.054510	−502.054332	−0.000178
	6	−603.313539	−603.313232	−0.000308	−602.472102	−602.471862	−0.000241
	7	−703.870605	−703.870219	−0.000386	−702.889928	−702.889624	−0.000304
	8	−804.427819	−804.427355	−0.000464	−803.307903	−803.307535	−0.000368
	9	−904.985127	−904.984584	−0.000543	−903.725970	−903.725538	−0.000432
	10	−1005.542501	−1005.541879	−0.000622	−1004.144102	−1004.143606	−0.000496
HAt							
	1	−22892.592562	−22892.592554	−0.000009	−22891.956879	−22891.956869	−0.000010
	2	−45785.185613	−45785.185284	−0.000329	−45783.915584	−45783.915259	−0.000325
	3	−68677.778945	−68677.778166	−0.000778	−68675.874519	−68675.873755	−0.000764
	4	−91570.372316	−91570.371080	−0.001235	−91567.833482	−91567.832271	−0.001211

Efficiency of LUT

This subsection demonstrates the computational costs of the two-electron term based on the IOTC and LUT-IOTC Hamiltonians. Figure 5.1 shows the system-size dependence of the CPU time for the calculation of TEIs required for the range-separated two-electron operators in the context of IOTC, LUT-IOTC, and nonrelativistic Hamiltonians, particularly in the calculations of $(HF)_n$ and $(HAt)_n$. The results for LUT-IOTC include the CPU time required for evaluating multicenter nonrelativistic TEIs as well as primitive TEIs, as described in Eqs. (5.2.15)–(5.2.17) for individual atoms. In the calculations of $(HF)_n$, the CPU times of IOTC, LUT-IOTC, and nonrelativistic Hamiltonians scale as $n^{2.92}$, $n^{2.45}$, and $n^{2.74}$, respectively. Computational costs of IOTC and nonrelativistic Hamiltonians exhibit similar scaling tendencies, which are proportional to approximately the cube of the system size. The LUT scheme slightly reduces the scaling of computational costs. In the calculations of $(HAt)_n$, the CPU times for IOTC, LUT-IOTC, and nonrelativistic Hamiltonians scale as $n^{2.17}$, $n^{1.14}$, and $n^{2.19}$, respectively. The computational costs for IOTC and nonrelativistic Hamiltonians resemble those observed in $(HF)_n$ calculations, displaying a similar scaling trend. However, the computational costs for LUT-IOTC exhibit nearly linear scaling, in contrast to the $(HF)_n$ calculations. This variation arises from the fact that in $(HAt)_n$ calculations, the CPU time for one-center primitive TEIs plays a significantly larger role in the total CPU time for TEIs, leading to increased CPU time proportional to the number of atoms. In $(HF)_n$ calculations, multicenter nonrelativistic TEIs dominate the total CPU time for TEIs, thus aligning the order of computational costs for TEIs closely with that of nonrelativistic TEIs. Detailed CPU times for TEIs are provided in Table 5.8.

Figure 5.2 shows the system-size dependence of the CPU time for unitary transformation of TEIs required for range-separated two-electron operators in the context of IOTC and LUT-IOTC Hamiltonians, focusing on calculations involving $(HF)_n$ and $(HAt)_n$. For IOTC Hamiltonian calculations, the CPU times scale as $n^{4.60}$ for $(HF)_n$ and $n^{4.96}$

for $(HAt)_n$. The LUT scheme clearly reduces the computational costs, with scaling behavior of $n^{1.00}$ for $(HF)_n$ and $n^{1.02}$ for $(HAt)_n$. The calculated scaling agrees well with theoretical quintic- and linear-scaling for IOTC and LUT-IOTC Hamiltonians, respectively. Detailed CPU times for TEIs are provided in Table 5.9.

As shown in Figures 5.3 and 5.4 and Tables 5.10 and 5.11, the CPU times required for full-range two-electron operators, $1/r_{ij}$ and $\boldsymbol{g}_2^{\mathrm{sf}}$, are close to those of range-separated two-electron operators. The total computational cost for the two-electron term in the LC-DFT calculations is approximately twice that for the functional without the LC method.

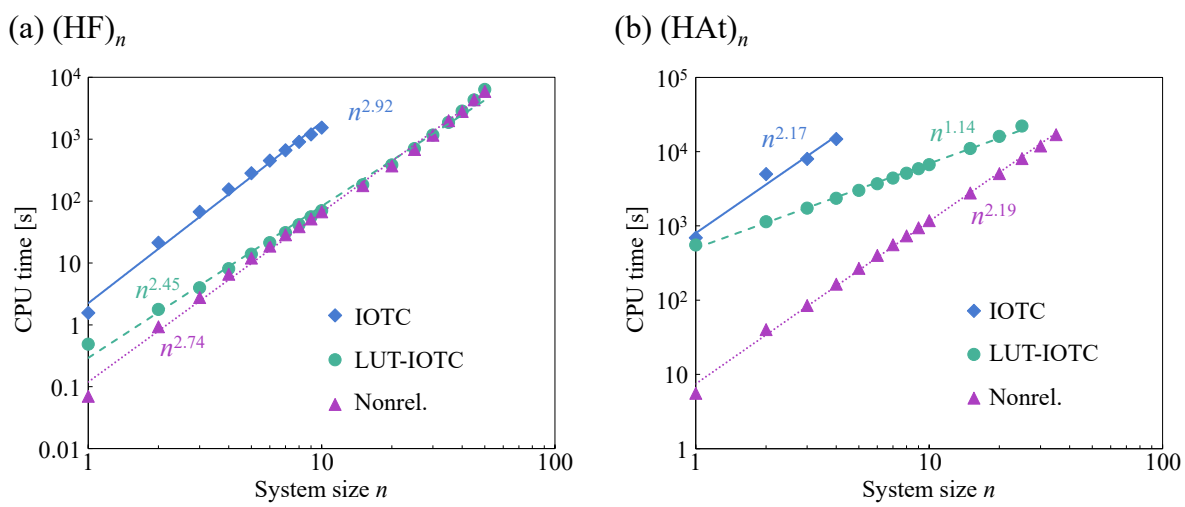

Figure 5.1. System-size dependence of CPU time (in s) for TEIs required for range-separated two-electron operators using IOTC, LUT-IOTC, and nonrelativistic Hamiltonians in calculation of $(HF)_n$ and $(HAt)_n$. CPU times were measured by a single core of AMD EPYC™ E7763 (2.45 GHz, 64 core).

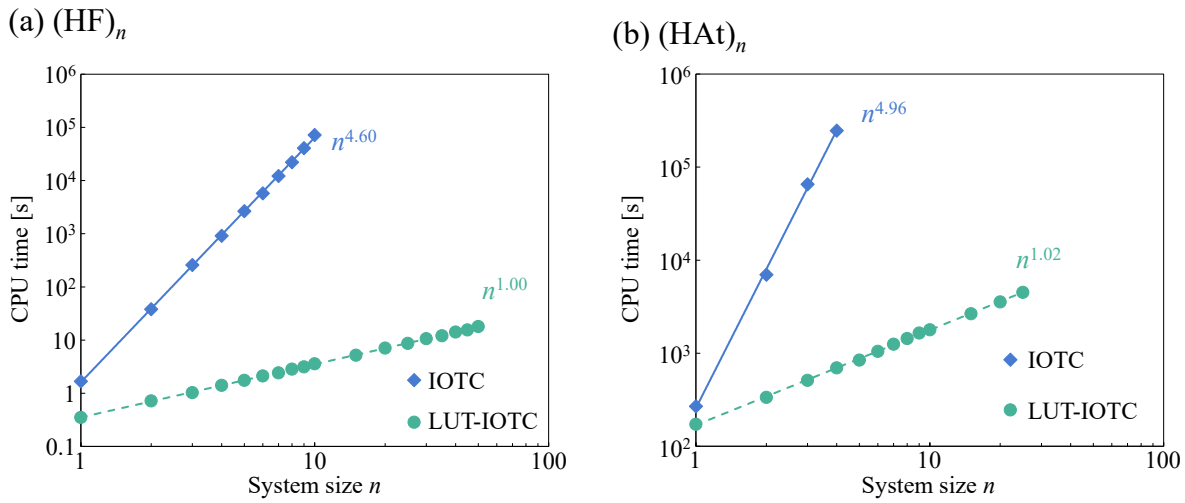

Figure 5.2. System-size dependence of CPU time (in s) for unitary transformation of TEIs required for range-separated two-electron operators using IOTC and LUT-IOTC Hamiltonian in calculation of $(HF)_n$ and $(HAt)_n$. CPU times were measured by a single core of AMD EPYC™ E7763 (2.45 GHz, 64 core).

Table 5.8. CPU time (in s) for TEIs of the range separated two-electron operator calculated by nonrelativistic (nonrel.), LUT-IOTC, and IOTC Hamiltonians. The results of TEIs of IOTC and one-center TEIs of LUT-IOTC are presented separately by term $\boldsymbol{g}_2^{\mathrm{sf}x}$ (x = 1-3).

molecule	n	Nonrel.	LUT-IOTC				IOTC		
			multicenter	one-center			sf1	sf2	sf3
				sf1	sf2	sf3			
HF									
	1	0.07	0.05	0.02	0.10	0.32	0.06	0.36	1.13
	2	0.93	0.89	0.03	0.20	0.64	0.92	5.03	15.18
	3	2.76	2.66	0.05	0.30	0.95	2.76	15.63	48.31
	4	6.56	6.29	0.07	0.39	1.26	6.36	36.08	111.25
	5	11.96	11.66	0.08	0.50	1.59	11.79	66.49	203.15
	6	18.70	18.59	0.10	0.59	1.89	19.44	107.17	323.73
	7	28.50	27.61	0.12	0.70	2.23	28.71	157.79	472.31
	8	38.46	37.89	0.13	0.79	2.53	38.27	216.31	649.44
	9	51.17	51.69	0.15	0.89	2.84	50.78	285.26	851.52
	10	66.62	65.47	0.16	0.99	3.16	66.15	366.72	1103.73
	15	176.76	176.38	0.24	1.48	4.74			
	20	369.22	373.73	0.33	1.99	6.33			
	25	680.70	688.53	0.42	2.49	7.97			
	30	1158.35	1150.44	0.48	2.95	9.46			
	35	1990.03	1845.46	0.56	3.45	11.05			
	40	2802.79	2815.33	0.65	3.95	12.61			
	45	4325.43	4276.73	0.73	4.43	14.22			
	50	5910.49	6310.03	0.81	4.94	15.80			

Table 5.8. Contined.

molecule	n	Nonrel.	LUT-IOTC				IOTC		
			multicenter	one-center			sf1	sf2	sf3
				sf1	sf2	sf3			
HAt									
	1	5.57	1.13	11.42	130.51	410.09	15.44	163.49	512.69
	2	40.13	31.13	22.93	261.14	819.51	164.69	1225.29	3595.62
	3	84.68	71.35	34.24	391.75	1230.67	185.01	1996.83	5816.54
	4	163.94	146.44	45.78	523.05	1639.91	351.65	3441.42	10972.12
	5	268.90	246.66	57.11	653.63	2050.69			
	6	400.22	373.45	68.52	785.41	2457.98			
	7	556.84	524.97	80.17	915.28	2872.11			
	8	736.39	702.23	91.54	1047.28	3280.02			
	9	945.02	905.82	102.65	1175.31	3687.59			
	10	1176.45	1137.52	114.21	1307.47	4097.00			
	15	2775.13	2732.68	173.27	1961.59	6147.84			
	20	5065.24	4944.40	228.33	2614.37	8205.08			
	25	8082.25	8288.18	288.25	3271.80	10254.28			
	30	11938.44							
	35	16902.63							

Table 5.9. CPU time (in s) for the unitary transformation of TEIs of the range separated two-electron operator calculated by LUT-IOTC and IOTC Hamiltonians. The results are presented separately by term $\boldsymbol{g}_2^{\mathrm{sfx}}$ (x = 1-3).

molecule	n	LUT-IOTC			IOTC		
		sf1	sf2	sf3	sf1	sf2	sf3
HF							
	1	0.12	0.12	0.11	0.56	0.60	0.53
	2	0.24	0.25	0.23	12.56	12.77	12.69
	3	0.34	0.35	0.33	88.23	80.53	90.39
	4	0.47	0.49	0.46	318.56	285.63	313.08
	5	0.58	0.60	0.56	893.87	880.73	887.36
	6	0.70	0.73	0.69	1940.88	1907.62	1918.54
	7	0.80	0.84	0.79	4105.41	4131.81	3987.98
	8	0.94	0.98	0.92	7277.17	7495.32	7349.18
	9	1.04	1.09	1.02	13315.92	14009.42	13550.42
	10	1.18	1.22	1.17	23737.53	24573.44	23753.49
	15	1.72	1.79	1.68			
	20	2.33	2.43	2.31			
	25	2.87	3.01	2.81			
	30	3.51	3.64	3.45			
	35	3.97	4.16	3.91			
	40	4.70	4.87	4.60			
	45	5.13	5.38	5.05			
	50	5.95	6.25	5.82			

Table 5.9. Continued.

molecule	*n*	LUT-IOTC			IOTC		
		sf1	sf2	sf3	sf1	sf2	sf3
HAt							
	1	51.59	60.19	60.73	78.85	94.40	95.94
	2	99.22	119.71	117.21	1966.05	2647.87	2385.97
	3	150.69	179.47	180.62	16248.97	27243.91	22105.43
	4	207.17	244.01	245.50	66911.04	93237.76	86627.50
	5	248.97	298.19	298.15			
	6	310.92	367.85	368.83			
	7	372.98	435.93	440.04			
	8	452.67	499.57	488.28			
	9	491.55	577.44	580.14			
	10	532.12	633.40	624.41			
	15	766.35	967.39	920.28			
	20	1052.08	1260.80	1245.02			
	25	1348.36	1578.57	1585.30			

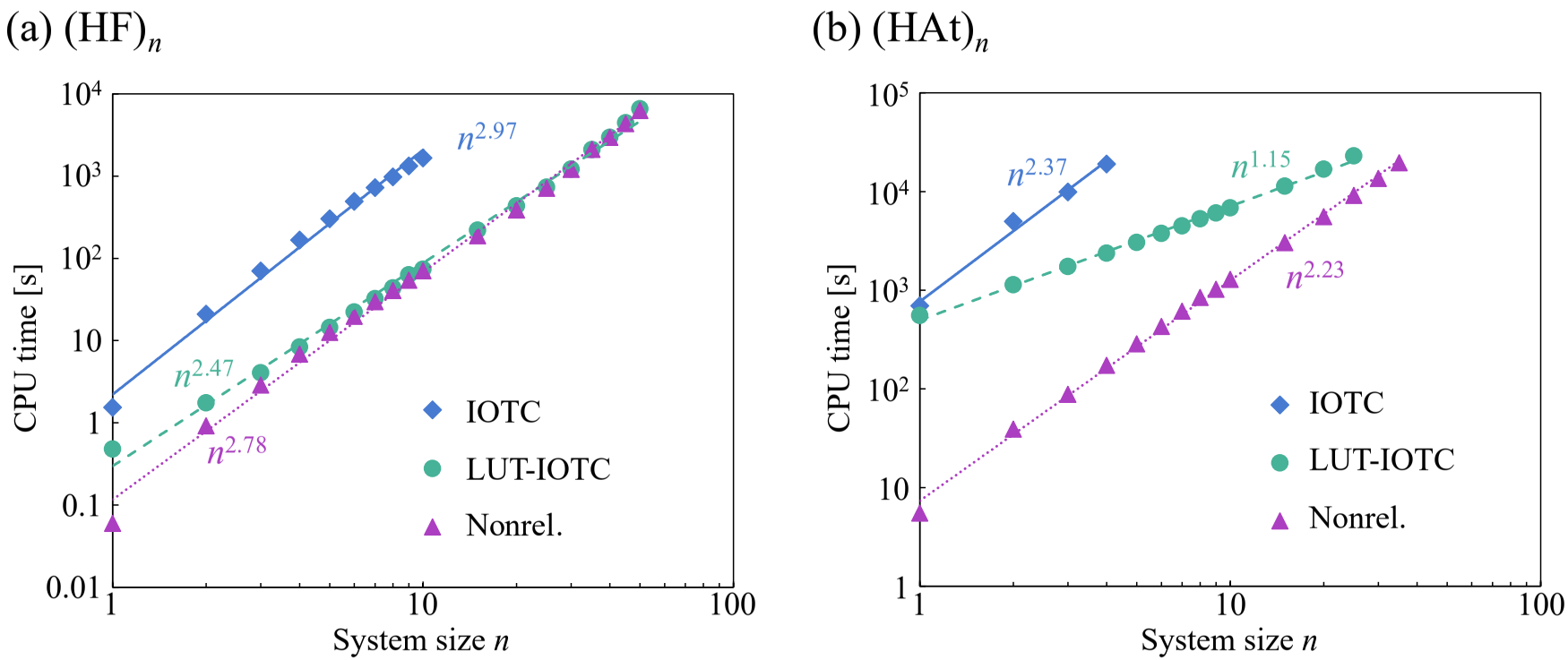

Figure 5.3. System-size dependence of the CPU time (in s) for the two-electron integrals using the IOTC LUT-IOTC and nonrelativistic (nonrel.) Hamiltonians in the calculation of $(HF)_n$ and $(HAt)_n$. CPU times were measured by a single core of AMD EPYC™ E7763 (2.45 GHz, 64 core).

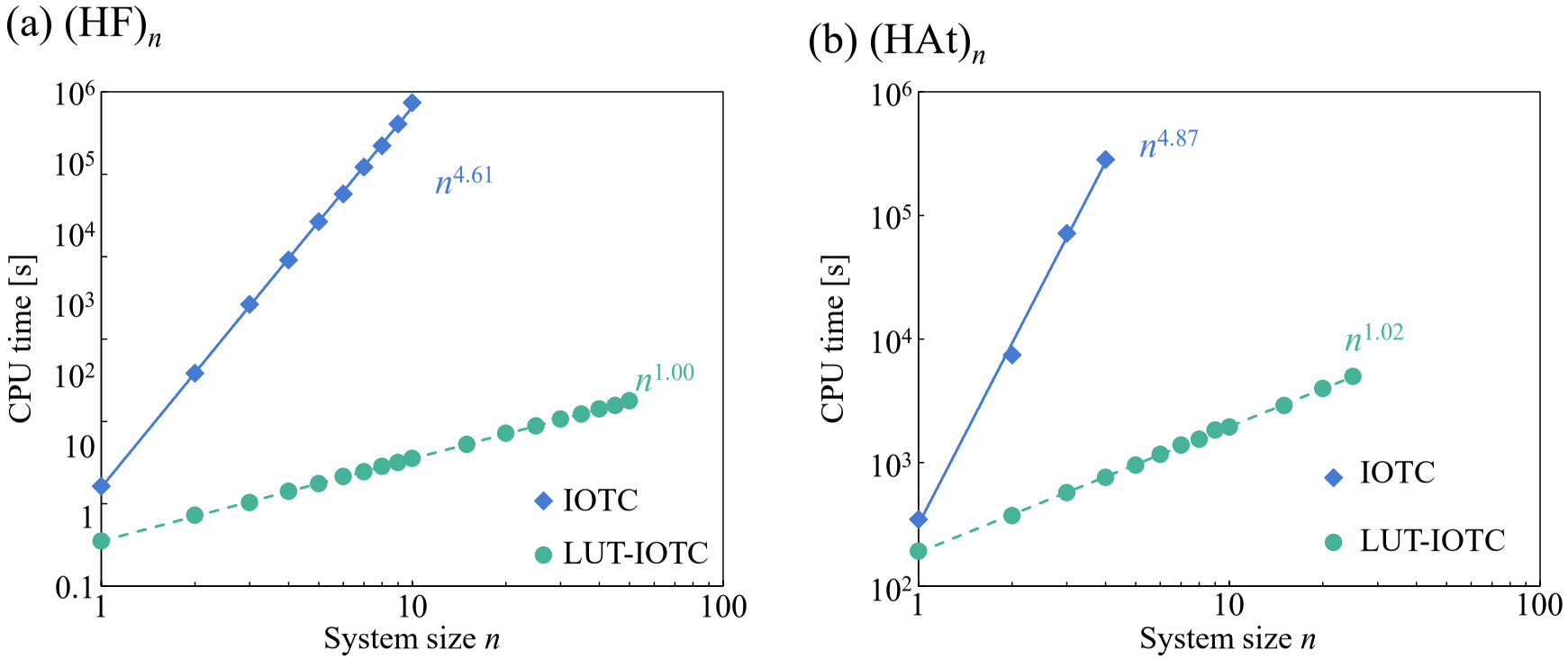

Figure 5.4. System-size dependence of the CPU time (in s) for the unitary transformation of the two-electron integrals using the IOTC and LUT-IOTC Hamiltonians in the calculation of $(HF)_n$ and $(HAt)_n$. CPU times were measured by a single core of AMD EPYC™ E7763 (2.45 GHz, 64 core).

Table 5.10. CPU time (in s) for TEIs of the full-range two-electron operator calculated by nonrelativistic, LUT-IOTC, and IOTC Hamiltonians. The results of TEIs of IOTC and one-center TEIs of LUT-IOTC are presented separately by term $\boldsymbol{g}_2^{\mathrm{sfx}}$ (x = 1-3).

molecule	n	Nonrelativistic	LUT-IOTC				IOTC		
			multicenter	one-center					
				sf1	sf2	sf3	sf1	sf2	sf3
HF									
	1	0.06	0.05	0.02	0.10	0.32	0.06	0.36	1.13
	2	0.92	0.89	0.03	0.20	0.64	0.93	4.98	15.14
	3	2.89	2.79	0.05	0.29	0.95	2.89	16.40	51.18
	4	6.85	6.64	0.06	0.39	1.26	6.76	38.98	121.56
	5	12.58	12.34	0.08	0.50	1.59	12.44	70.89	219.51
	6	19.80	19.69	0.10	0.59	1.89	20.78	117.12	356.29
	7	29.71	29.34	0.11	0.69	2.25	30.55	171.51	522.25
	8	40.79	40.26	0.13	0.78	2.52	40.75	232.94	709.28
	9	54.26	59.22	0.15	0.89	2.83	54.00	333.23	949.75
	10	71.04	69.70	0.16	0.98	3.15	71.54	398.37	1193.54
	15	188.31	214.50	0.24	1.47	4.73			
	20	389.65	427.49	0.32	1.96	6.30			
	25	714.70	725.08	0.41	2.48	7.96			
	30	1208.31	1203.74	0.48	2.93	9.44			
	35	2120.54	2092.82	0.56	3.43	11.01			
	40	2961.87	2942.25	0.64	3.92	12.58			
	45	4366.60	4441.46	0.72	4.39	14.16			
	50	6280.00	6579.24	0.80	4.89	15.77			

Table 5.10. Continued.

molecule	n	Nonrelativistic	LUT-IOTC				IOTC		
			multicenter	one-center			sf1	sf2	sf3
				sf1	sf2	sf3			
HAt									
	1	5.49	1.11	11.69	130.78	410.18	15.77	163.82	513.26
	2	38.96	30.10	23.42	261.66	819.80	166.27	1207.61	3607.52
	3	88.13	74.72	35.00	392.39	1231.11	240.65	2354.82	7283.52
	4	172.86	156.49	46.71	523.70	1640.84	506.50	4550.54	13939.67
	5	285.97	280.57	58.43	654.78	2053.42			
	6	428.07	432.22	71.43	793.21	2463.32			
	7	610.81	596.42	84.64	922.48	2876.15			
	8	841.40	826.23	98.12	1058.69	3284.20			
	9	1022.36	1058.86	108.24	1184.52	3691.54			
	10	1281.86	1281.48	118.91	1313.90	4100.46			
	15	3027.36	3022.94	179.04	1973.08	6152.17			
	20	5550.81	5690.26	236.40	2625.76	8213.67			
	25	9123.28	9109.21	295.63	3279.49	10258.66			
	30	13543.63							
	35	19559.52							

Table 5.11. CPU time (in s) for the unitary transformation TEIs of the full-range two-electron operator calculated by LUT-IOTC and IOTC Hamiltonians. The results are presented separately by term $\boldsymbol{g}_2^{\mathrm{sf}x}$ (x = 1–3).

molecule	n	LUT-IOTC			IOTC		
		sf1	sf2	sf3	sf1	sf2	sf3
HF							
	1	0.12	0.12	0.11	0.53	0.58	0.52
	2	0.24	0.25	0.24	12.65	12.93	12.79
	3	0.34	0.36	0.34	89.22	81.46	92.02
	4	0.47	0.49	0.46	303.19	286.97	317.21
	5	0.58	0.60	0.57	867.29	883.90	898.09
	6	0.71	0.73	0.70	1898.64	1920.19	1938.61
	7	0.80	0.84	0.80	4018.05	4135.23	4075.00
	8	0.93	0.97	0.93	7227.65	7539.66	7386.39
	9	1.04	1.09	1.03	13244.48	13895.36	13568.41
	10	1.17	1.22	1.16	23354.53	25040.81	25318.40
	15	1.73	1.80	1.71			
	20	2.35	2.45	2.35			
	25	2.88	3.03	2.86			
	30	3.51	3.65	3.49			
	35	4.01	4.20	4.01			
	40	4.68	4.86	4.63			
	45	5.11	5.38	5.09			
	50	5.86	6.10	5.84			
HAt							
	1	58.43	67.32	66.14	103.01	123.25	120.30
	2	113.19	133.58	124.96	2052.96	2859.13	2529.41
	3	174.35	200.96	195.23	18472.33	29557.57	23447.03
	4	232.68	267.61	258.11	75608.24	105996.79	102044.38
	5	292.88	335.90	324.17			
	6	356.77	411.61	398.80			
	7	422.62	491.42	469.02			
	8	467.07	556.59	517.96			
	9	556.98	649.93	623.84			
	10	590.22	697.34	653.76			
	15	870.85	1053.22	966.21			
	20	1207.20	1422.19	1345.41			
	25	1525.12	1755.10	1698.63			

5.3.4 Application to noble gas dimers

In this subsection, the proposed method is applied to noble gas dimers, which are typical examples of vdW interactions. Figure 5.5 shows the potential energy curves for the Rn dimer, calculated using the BOP, LC-BOP, and LC-BOP+LRD methods based on 1e2eLUT-IOTC Hamiltonian with $\boldsymbol{\delta}^{\mathrm{LUT}}$. BOP calculations yield an unbound potential, which is not suitable for representing vdW interactions. The LC method improves the potential curve, particularly around the equilibrium point, although it still remains unbound. By contrast, the potential obtained with LC-BOP+LRD is strongly bound and exhibits a clear equilibrium point. Furthermore, Figure 5.5 includes LC-BOP+LRD calculations based on the nonrelativistic Hamiltonian for comparison. When comparing nonrelativistic and LUT-IOTC calculations, the bottom of the potential is shifted towards smaller bond lengths due to the influence of relativistic effects. Additionally, potential energy curves for He_2, Ne_2, Ar_2, Kr_2, and Xe_2, calculated using the nonrelativistic and LUT-IOTC Hamiltonian with LC-BOP+LRD are depicted in Figure 5.6. These curves also exhibit strong binding and equilibrium points.

Table 5.12 presents equilibrium bond lengths R_e (in Å) and dissociation energies D_e (in kcal/mol) calculated using the LC-BOP+LRD method based on the nonrelativistic Hamiltonian, as well as the 1e2eLUT-IOTC Hamiltonian with $\boldsymbol{\delta}^{\mathrm{LUT}}$. As reference values, experimental results for He_2, Ne_2, Ar_2, Kr_2, and Xe_2,[52] as well as twice the vdW radius of Rn_2,[53] are also tabulated. Using LUT-IOTC, shorter R_e values are obtained than those obtained through nonrelativistic calculations. The deviations (Δ^{rel}) in bond length between LUT-IOTC and nonrelativistic calculations become more pronounced in higher-row elements. Accounting for relativistic effects through LUT-IOTC brings the calculated bond lengths closer to the reference values, reflecting the relativistic shrinkage of the vdW radius. D_e values obtained by nonrelativistic and LUT-IOTC Hamiltonians are similar. Δ^{rel} of Xe_2 and Rn_2 in D_e amount to only −0.005 [kcal/mol]. This suggests that relativistic effects on

D_e were not observed in the present calculations.

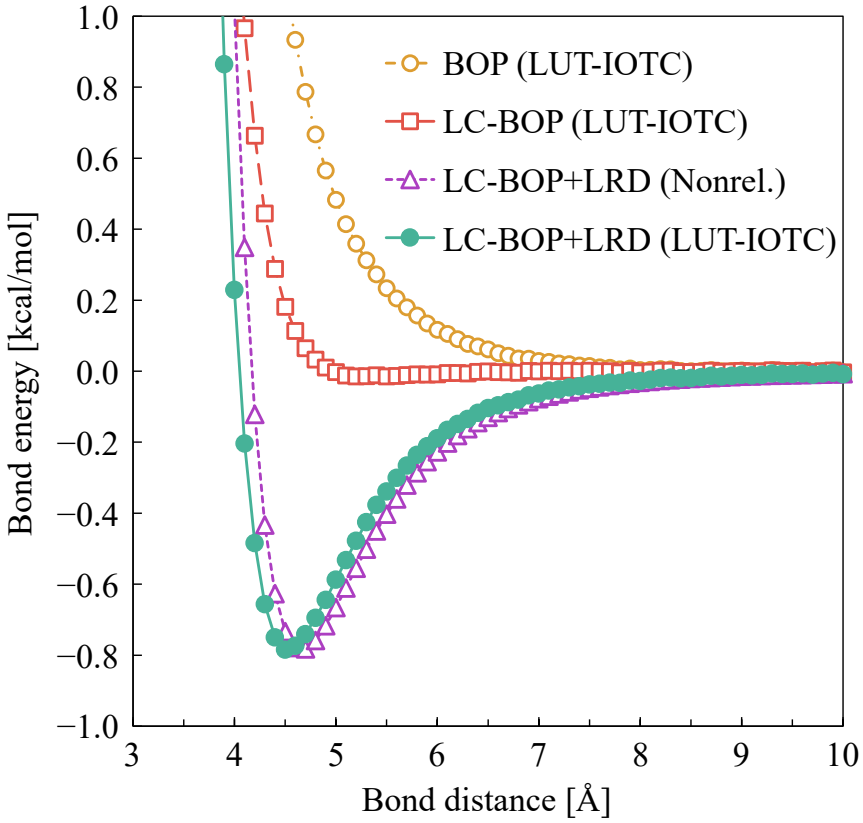

Figure 5.5. Potential energy curves of Rn dimer calculated by 1e2eLUT-IOTC Hamiltonian with $\boldsymbol{\delta}^{\mathrm{LUT}}$. As a functional, BOP and LC-BOP (μ = 0.47) with/without LRD method were examined. Nonrelativistic calculation of LC-BOP+LRD is also shown.

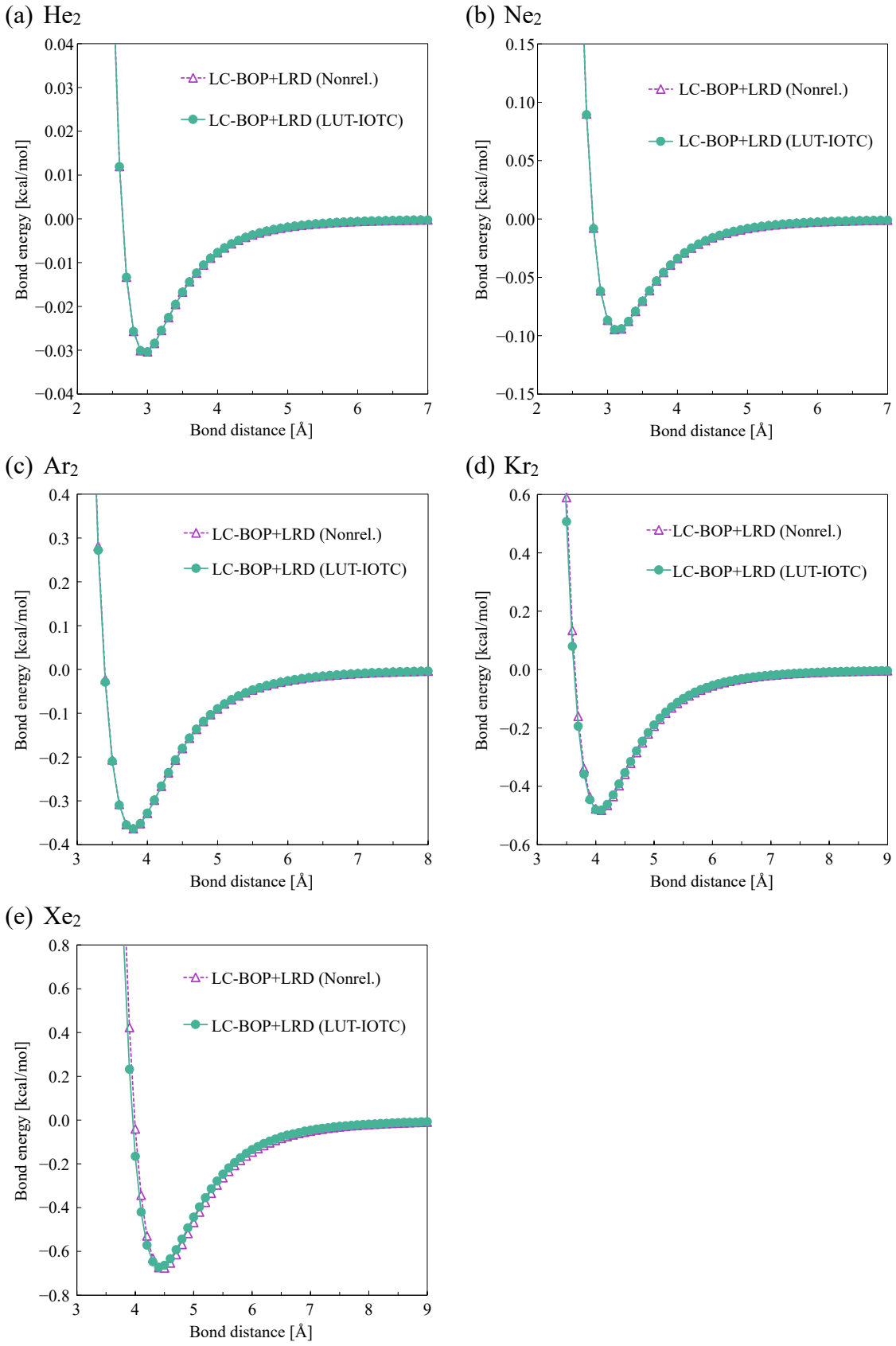

Figure 5.6. Potential energy curves of He_2, Ne_2, Ar_2, Kr_2, and Xe_2 calculated using the 1e2eLUT-IOTC Hamiltonian with $\boldsymbol{\delta}^{\mathrm{LUT}}$ and nonrelativistic Hamiltonian. LC-BOP+LRD method was used.

Table 5.12. Calculated equilibrium bond lengths R_e (in Å) and dissociation energies D_e (in kcal/mol) of noble gas dimers by nonrelativistic Hamiltonian (nonrel.) and 1e2eLUT-IOTC Hamiltonian with $\boldsymbol{\delta}^{LUT}$ (LUT-IOTC). LC-BOP (μ = 0.47) with LRD method was used as a functional. Δ^{rel} represents the deviations of LUT-IOTC from non-relativistic results. As references, experimental values of He_2, Ne_2, Ar_2, Kr_2, and Xe_2[52] and twice of vdW radius for Rn_2[53] are also shown.

	R_e				D_e			
	Nonrel.	LUT-IOTC	Δ^{rel}	Ref.	Nonrel.	LUT-IOTC	Δ^{rel}	Ref.
He_2	2.957	2.956	0.000	2.970	0.031	0.031	0.000	0.022
Ne_2	3.137	3.137	−0.001	3.091	0.095	0.095	0.000	0.084
Ar_2	3.786	3.784	−0.002	3.757	0.364	0.364	0.000	0.285
Kr_2	4.068	4.052	−0.016	4.008	0.483	0.484	0.001	0.400
Xe_2	4.455	4.417	−0.039	4.363	0.678	0.673	−0.005	0.561
Rn_2	4.659	4.533	−0.126	(4.40)	0.784	0.780	−0.005	-

5.3.5 Application to dissociation energies in heavy-element compounds

Table 5.13 provides dissociation energies for bond cleavage in two reactions: $Ge_2H_6 \rightarrow 2\ GeH_3$ and $Pb_2(CH_3)_2 \rightarrow 2\ PbCH_3$. These values were calculated using the nonrelativistic method and the 1e2eLUT-IOTC Hamiltonian with $\boldsymbol{\delta}^{\mathrm{LUT}}$. The differences in dissociation energies between the nonrelativistic and LUT-IOTC calculations are approximately 1 kcal/mol for $Ge_2H_6 \rightarrow 2\ GeH_3$ and range from 7–10 kcal/mol for $Pb_2(CH_3)_2 \rightarrow 2\ PbCH_3$. Relativistic effects reduce the dissociation energies in both reactions. Because both nonrelativistic and LUT-IOTC calculations were performed on the same structures, the covalency in the Pb-Pb and Ge-Ge bonds was weakened, corresponding to the relativistic shrinkage of *s* and *p* orbitals in the bonding region. Notably, relativistic effects are more pronounced in Pb compounds (sixth-row element) compared to Ge compounds (fourth-row element). Additionally, when comparing LC functionals to their non-LC counterparts, such as LC-BLYP to BLYP, or CAM-B3LYP to B3LYP, the use of LC functionals increases the dissociation energy. This is important as long-range interactions tend to stabilize binuclear molecules like Ge_2H_6 and $Pb_2(CH_3)_2$. This trend aligns with the values included in the HEAVYSB11 set, which become closer to the reference values when LC functionals are employed.[40] Furthermore, as shown in Table 5.14, the changes in dissociation energy due to the LUT-IOTC transformation of two-electron or density operators are less than 0.3 kcal/mol. This indicates that the treatment of one-electron operator plays a dominant role in the relativistic effects on reaction energies.

Table 5.13. Dissociation energies (in kcal/mol) of Ge and Pb compounds calculated by nonrelativistic (nonrel.) and 1e2eLUT-IOTC Hamiltonian with $\boldsymbol{\delta}^{\mathrm{LUT}}$ (LUT-IOTC).

	$Ge_2H_6 \rightarrow 2\ GeH_3$		$Pb_2(CH_3)_2 \rightarrow 2\ PbCH_3$	
	Nonrel.	LUT-IOTC	Nonrel.	LUT-IOTC
BLYP	65.2	64.4	44.5	37.5
LC-BLYP (μ = 0.47)	72.7	71.6	60.0	50.5
B3LYP	66.9	66.1	48.4	40.9
CAM-B3LYP	69.0	68.1	53.1	44.5

Table 5.14. Dissociation energies (in kcal/mol) of Ge and Pb compounds calculated by nonrelativistic, 1eLUT-IOTC, and 1e2eLUT-IOTC Hamiltonians with and without LUT-IOTC transformation of density operator $\boldsymbol{\delta}^{\mathrm{LUT}}$.

	Nonrelativistic	LUT-IOTC			
		1e	1e with $\boldsymbol{\delta}^{\mathrm{LUT}}$	1e2e	1e2e with $\boldsymbol{\delta}^{\mathrm{LUT}}$
$Ge_2H_6 \rightarrow 2\ GeH_3$					
BLYP	65.2	64.4	64.5	64.4	64.4
LC-BLYP (μ = 0.47)	72.7	71.6	71.6	71.6	71.6
B3LYP	66.9	66.1	66.1	66.1	66.1
CAM-B3LYP	69.0	68.1	68.1	68.1	68.1
$Pb_2(CH_3)_2 \rightarrow 2\ PbCH_3$					
BLYP	44.5	37.5	37.6	37.4	37.5
LC-BLYP (μ = 0.47)	60.0	50.6	50.7	50.4	50.5
B3LYP	48.4	40.9	41.0	40.8	40.9
CAM-B3LYP	53.1	44.6	44.7	44.4	44.5

5.4 Conclusion

This chapter developed a range separation method for the two-electron term based on the spin-free IOTC Hamiltonian and conducted the numerical assessment using the LC-DFT. Total energies and orbital energies of noble gas atoms demonstrated excellent agreement with 4c energies when employing the full IOTC transformation for one-electron operator, full-range and range-separated two-electron operators, and density operator. The LUT scheme was applied to range-separated terms of TEIs, one-electron integrals, full-range TEIs, and electron density in molecular calculations. Energy calculations for hydrogen halide molecules showed that the errors associated with the LUT scheme were sufficiently small compared to the errors introduced by the 2c transformation with the IOTC Hamiltonian. The calculations of HF and HAt polymers were also examined using both IOTC and LUT-IOTC Hamiltonians. The errors introduced by the LUT scheme were small, particularly when the system size increased. The CPU times for the evaluation and unitary transformation of TEIs were significantly reduced by the LUT scheme, resulting in linear scaling in $(HAt)_n$ calculations. The validity of the LUT scheme was confirmed for the range separation method. The method was applied to the investigation of spectroscopic constants for noble gas dimers. The equilibrium bond distances obtained by the LUT-IOTC Hamiltonian were shorter than those obtained by nonrelativistic calculations, particularly in heavier-element systems, indicating that vdW interactions are influenced by relativistic effects. Calculation of bond cleavage energies revealed the importance of relativistic treatment in reaction energies, particularly in heavy-element compounds.

References

1. W. Kohn and L.J. Sham, *Phys. Rev.* **140**, A1133 (1965).

2. T. Leininger, H. Stoll, H. Werner, and A. Savin, *Chem. Phys. Lett.* **275**, 151 (1997).

3. E.D. Hedegård, J. Toulouse, and H.J.A. Jensen, *J. Chem. Phys.* **148**, 214103 (2018).

4. A. Ferté, E. Giner, and J. Toulouse, *J. Chem. Phys.* **150**, 084103 (2019).

5. D.E. Taylor, J.G. Ángyán, G. Galli, C. Zhang, F. Gygi, K. Hirao, J.W. Song, K. Rahul, O. Anatole von Lilienfeld, R. Podeszwa, I.W. Bulik, T.M. Henderson, G.E. Scuseria, J. Toulouse, R. Peverati, D.G. Truhlar, and K. Szalewicz, *J. Chem. Phys.* **145**, 124105 (2016).

6. C. Kalai, B. Mussard, and J. Toulouse, *J. Chem. Phys.* **151**, 074102 (2019).

7. H. Iikura, T. Tsuneda, T. Yanai, and K. Hirao, *J. Chem. Phys.* **115**, 3540 (2001).

8. J. Heyd, G.E. Scuseria, and M. Ernzerhof, *J. Chem. Phys.* **118**, 8207 (2003).

9. Y. Tawada, T. Tsuneda, S. Yanagisawa, T. Yanai, and K. Hirao, *J. Chem. Phys.* **120**, 8425 (2004).

10. T. Yanai, D.P. Tew, and N.C. Handy, *Chem. Phys. Lett.* **393**, 51 (2004).

11. R. Baer and D. Neuhauser, *Phys. Rev. Lett.* **94**, 043002 (2005).

12. I.C. Gerber and J.G. Ángyán, *Chem. Phys. Lett.* **415**, 100 (2005).

13. O.A. Vydrov, J. Heyd, A.V. Krukau, and G.E. Scuseria, *J. Chem. Phys.* **125**, 074106 (2006).

14. J. Heyd, G.E. Scuseria, and M. Ernzerhof, *J. Chem. Phys.* **124**, 219906 (2006).

15. J. Song, T. Hirosawa, T. Tsuneda, and K. Hirao, *J. Chem. Phys.* **126**, 154105 (2007).

16. E. Livshits and R. Baer, *Phys. Chem. Chem. Phys.* **9**, 2932 (2007).

17. J. Song, S. Tokura, T. Sato, M.A. Watson, and K. Hirao, *J. Chem. Phys.* **127**, 154109 (2007).

18. J. Chai and M. Head-Gordon, *J. Chem. Phys.* **128**, 084106 (2008).

19. J. Chai and M. Head-Gordon, *Phys. Chem. Chem. Phys.* **10**, 6615 (2008).

20. T.M. Henderson, B.G. Janesko, and G.E. Scuseria, *J. Chem. Phys.* **128**, 194105 (2008).

21. Y. Akinaga and S. Ten-no, *Chem. Phys. Lett.* **462**, 348 (2008).

22. M.A. Rohrdanz, K.M. Martins, and J.M. Herbert, *J. Chem. Phys.* **130**, 054112 (2009).

23. J. Song, M.A. Watson, and K. Hirao, *J. Chem. Phys.* **131**, 144108 (2009).

24. Y. Imamura, R. Kobayashi, and H. Nakai, *J. Chem. Phys.* **134**, 124113 (2011).

25. M. Kamiya, T. Tsuneda, and K. Hirao, *J. Chem. Phys.* **117**, 6010 (2002).

26. M. Kamiya, H. Sekino, T. Tsuneda, and K. Hirao, *J. Chem. Phys.* **122**, 234111 (2005).

27. T. Tsuneda, J. Song, S. Suzuki, and K. Hirao, *J. Chem. Phys.* **133**, 174101 (2010).

28. O. Kullie and T. Saue, *Chem. Phys.* **395**, 54 (2012).

29. J. Paquier and J. Toulouse, *J. Chem. Phys.* **149**, 174110 (2018).

30. J. Paquier, E. Giner, and J. Toulouse, *J. Chem. Phys.* **152**, 214106 (2020).

31. J. Paquier and J. Toulouse, *Int. J. Quantum Chem.* **121**, (2021).

32. F. Aquino, N. Govind, and J. Autschbach, *J. Chem. Theory Comput.* **6**, 2669 (2010).

33. A. Nakata, T. Tsuneda, and K. Hirao, *J. Chem. Phys.* **135**, 224106 (2011).

34. T. Yoshizawa, W. Zou, and D. Cremer, *J. Chem. Phys.* **145**, 184104 (2016).

35. J. Seino and H. Nakai, *J. Chem. Phys.* **137**, 144101 (2012).

36. S. Grimme, *J. Chem. Phys.* **124**, 034108 (2006).

37. M. Hayami, J. Seino, Y. Nakajima, M. Nakano, Y. Ikabata, T. Yoshikawa, T. Oyama, K. Hiraga, S. Hirata, and H. Nakai, *J. Comput. Chem.* **39**, 2333 (2018).

38. G.M.J. Barca, C. Bertoni, L. Carrington, D. Datta, N. De Silva, J.E. Deustua, D.G. Fedorov, J.R. Gour, A.O. Gunina, E. Guidez, T. Harville, S. Irle, J. Ivanic, K. Kowalski, S.S. Leang, H. Li, W. Li, J.J. Lutz, I. Magoulas, J. Mato, V. Mironov, H. Nakata, B.Q. Pham, P. Piecuch, D. Poole, S.R. Pruitt, A.P. Rendell, L.B. Roskop, K. Ruedenberg, T. Sattasathuchana, M.W. Schmidt, J. Shen, L. Slipchenko, M. Sosonkina, V. Sundriyal, A. Tiwari, J.L. Galvez Vallejo, B. Westheimer, M. Włoch, P. Xu, F. Zahariev, and M.S. Gordon, *J. Chem. Phys.* **152**, 154102 (2020).

39. A.S.P. Gomes, T. Saue, L. Visscher, H.J.A. Jensen, R. Bast, I.A. Aucar, V. Bakken, K.G. Dyall, S. Dubillard, U. Ekström, E. Eliav, T. Enevoldsen, E. Faßhauer, T. Fleig, O. Fossgaard, L. Halbert, E.D. Hedegård, T. Helgaker, B. Helmich-Paris, J. Henriksson, M. Iliaš, Ch R. Jacob, S. Knecht, S. Komorovský, O. Kullie, J.K. Lærdahl, C.V. Larsen, Y.S. Lee, H.S. Nataraj, M.K. Nayak, P. Norman, G. Olejniczak, J. Olsen, J.M.H. Olsen, Y.C. Park, J.K. Pedersen, M. Pernpointner, R. Di Remigio, K. Ruud, P. Sałek, B. Schimmelpfennig, B. Senjean, A. Shee, J. Sikkema, A.J. Thorvaldsen, J. Thyssen, J. van Stralen, M.L. Vidal, S. Villaume, O. Visser, T. Winther, and S. Yamamoto, DIRAC19(2019) (available at http://dx.doi.org/10.5281/zenodo.3572669, see also http://www.diracprogram.org).

40. L. Goerigk, A. Hansen, C. Bauer, S. Ehrlich, A. Najibi, and S. Grimme, *Phys. Chem. Chem. Phys.* **19**, 32184 (2017).

41. K.P. Huber and G. Herzberg, Constants of diatomic molecules, in *Molecular Spectra and Molecular Structure: IV. Constants of Diatomic Molecules*, edited by K.P. Huber and G. Herzberg (Springer US, Boston, MA, 1979) pp. 8-689.

42. A.S. Pereira Gomes and L. Visscher, *Chem. Phys. Lett.* **399**, 1 (2004).

43. S.F. Boys and F. Bernardi, *Mol. Phys.* **19**, 553 (1970).

44. T. Sato and H. Nakai, *J. Chem. Phys.* **131**, 224104 (2009).

45. A.D. Becke, *Phys. Rev. A*, **38**, 3098 (1988).

46. C. Lee, W. Yang, and R.G. Parr, *Phys. Rev. B*, **37**, 785 (1988).

47. T. Tsuneda, T. Suzumura, and K. Hirao, *J. Chem. Phys.* **110**, 10664 (1999).

48. A.D. Becke, *J. Chem. Phys.* **98**, 5648 (1993).

49. T. Noro, M. Sekiya, and T. Koga, *Theor. Chem. Acc.* **109**, 85 (2003).

50. T. Noro, M. Sekiya, and T. Koga, *Theor. Chem. Acc.* **131**, 1124 (2012).

51. T. Noro, M. Sekiya, and T. Koga, *Theor. Chem. Acc.* **132**, 1363 (2013).

52. J.F. Ogilvie and F.Y.H. Wang, *J. Mol. Struct.* **273**, 277 (1992).

53. M. Mantina, A.C. Chamberlin, R. Valero, C.J. Cramer, and D.G. Truhlar, *J. Phys. Chem. A*, **113**, 5806 (2009).

Appendix

A5.1 Spin-dependent term of range-separated two-electron IOTC Hamiltonian

This section provides the spin-dependent terms of the two-electron IOTC Hamiltonian. Using Eqs. (2.3.12) and (2.3.13), the spin-free and spin-dependent terms are separated. The explicit expression of the electronic part of the two-electron IOTC Hamiltonian $\boldsymbol{g}_2^{++}$ is divided into spin-free terms $\boldsymbol{g}_2^{\mathrm{sf}x}$ and spin-dependent terms $\boldsymbol{g}_2^{\mathrm{sd}x}$ (x = 1-3):

$$\begin{aligned}\boldsymbol{g}_2^{++}(i,j) = \boldsymbol{g}_2^{\mathrm{sf1}}(i,j) + \boldsymbol{g}_2^{\mathrm{sf2}}(i,j) + \boldsymbol{g}_2^{\mathrm{sf3}}(i,j) \\ + \boldsymbol{g}_2^{\mathrm{sd1}}(i,j) + \boldsymbol{g}_2^{\mathrm{sd2}}(i,j) + \boldsymbol{g}_2^{\mathrm{sd3}}(i,j),\end{aligned} \tag{A5.1}$$

where

$$\boldsymbol{g}_2^{\mathrm{sd1}}(i,j) = P(i,j)\left(\boldsymbol{d}_i \boldsymbol{M}_j \left[\mathrm{i}\boldsymbol{\sigma}^i \cdot \boldsymbol{p}_i \frac{1}{r_{ij}} \mathbf{1}_2 \times \boldsymbol{p}_i \right] \boldsymbol{M}_j \boldsymbol{d}_i \right), \tag{A5.2}$$

$$\boldsymbol{g}_2^{\mathrm{sd2}}(i,j) = P(i,j)\left(\boldsymbol{d}_i \boldsymbol{d}_j \left[\mathrm{i}\boldsymbol{\sigma}^i \cdot \left(\boldsymbol{p}_i \left(\boldsymbol{p}_j \frac{1}{r_{ij}} \mathbf{1}_2 \cdot \boldsymbol{p}_j \right) \times \boldsymbol{p}_i \right) \right] \boldsymbol{d}_j \boldsymbol{d}_i \right), \tag{A5.3}$$

and

$$\boldsymbol{g}_2^{\mathrm{sd3}}(i,j) = -\boldsymbol{d}_i \boldsymbol{d}_j \left[\boldsymbol{\sigma}^i \cdot \left(\boldsymbol{p}_i \left(\boldsymbol{\sigma}^j \cdot \boldsymbol{p}_j \frac{1}{r_{ij}} \mathbf{1}_2 \times \boldsymbol{p}_j \right) \times \boldsymbol{p}_i \right) \right] \boldsymbol{d}_j \boldsymbol{d}_i . \tag{A5.4}$$

(See Eqs. (2.3.18)-(2.3.20) in Subsection 2.3 for spin free terms.)

Range separation terms are obtained replacing $1/r_{ij}$ in Eqs. (A5.2)-(A5.4) with $\left(1-\mathrm{erf}\left(\mu r_{ij}\right)\right)/r_{ij}$ and $\mathrm{erf}\left(\mu r_{ij}\right)/r_{ij}$ as in the case of spin-free terms. Short- and long-range parts of spin-dependent terms, $\boldsymbol{g}_2^{\mathrm{sd}x,\mathrm{sr}}$ and $\boldsymbol{g}_2^{\mathrm{sd}x,\mathrm{lr}}$ (x =1, 2, and 3) are as follows:

$$\boldsymbol{g}_2^{\mathrm{sd1,sr}}(i,j) = P(i,j)\left(\boldsymbol{d}_i \boldsymbol{M}_j \left[\mathrm{i}\boldsymbol{\sigma}^i \cdot \boldsymbol{p}_i \frac{1-\mathrm{erf}\left(\mu r_{ij}\right)}{r_{ij}} \mathbf{1}_2 \times \boldsymbol{p}_i \right] \boldsymbol{M}_j \boldsymbol{d}_i \right), \tag{A5.5}$$

$$\boldsymbol{g}_2^{\mathrm{sd2,sr}}(i,j)=P(i,j)\left(\boldsymbol{d}_i\boldsymbol{d}_j\left[\mathrm{i}\boldsymbol{\sigma}^i\cdot\left(\boldsymbol{p}_i\left(\boldsymbol{p}_j\frac{1-\mathrm{erf}\left(\mu r_{ij}\right)}{r_{ij}}\mathbf{1}_2\cdot\boldsymbol{p}_j\right)\times\boldsymbol{p}_i\right)\right]\boldsymbol{d}_j\boldsymbol{d}_i\right),$$

(A5.6)

$$\boldsymbol{g}_2^{\mathrm{sd3,sr}}(i,j)=-\boldsymbol{d}_i\boldsymbol{d}_j\left[\boldsymbol{\sigma}^i\cdot\left(\boldsymbol{p}_i\left(\boldsymbol{\sigma}^j\cdot\boldsymbol{p}_j\frac{1-\mathrm{erf}\left(\mu r_{ij}\right)}{r_{ij}}\mathbf{1}_2\times\boldsymbol{p}_j\right)\times\boldsymbol{p}_i\right)\right]\boldsymbol{d}_j\boldsymbol{d}_i,$$

(A5.7)

$$\boldsymbol{g}_2^{\mathrm{sd1,lr}}(i,j)=P(i,j)\left(\boldsymbol{d}_i\boldsymbol{M}_j\left[\mathrm{i}\boldsymbol{\sigma}^i\cdot\boldsymbol{p}_i\frac{\mathrm{erf}\left(\mu r_{ij}\right)}{r_{ij}}\mathbf{1}_2\times\boldsymbol{p}_i\right]\boldsymbol{M}_j\boldsymbol{d}_i\right),$$

(A5.8)

$$\boldsymbol{g}_2^{\mathrm{sd2,lr}}(i,j)=P(i,j)\left(\boldsymbol{d}_i\boldsymbol{d}_j\left[\mathrm{i}\boldsymbol{\sigma}^i\cdot\left(\boldsymbol{p}_i\left(\boldsymbol{p}_j\frac{\mathrm{erf}\left(\mu r_{ij}\right)}{r_{ij}}\mathbf{1}_2\cdot\boldsymbol{p}_j\right)\times\boldsymbol{p}_i\right)\right]\boldsymbol{d}_j\boldsymbol{d}_i\right),$$

(A5.9)

and

$$\boldsymbol{g}_2^{\mathrm{sd3,lr}}(i,j)=-\boldsymbol{d}_i\boldsymbol{d}_j\left[\boldsymbol{\sigma}^i\cdot\left(\boldsymbol{p}_i\left(\boldsymbol{\sigma}^j\cdot\boldsymbol{p}_j\frac{\mathrm{erf}\left(\mu r_{ij}\right)}{r_{ij}}\mathbf{1}_2\times\boldsymbol{p}_j\right)\times\boldsymbol{p}_i\right)\right]\boldsymbol{d}_j\boldsymbol{d}_i.$$

(A5.10)

Hereafter, the implementation of spin-dependent terms is briefly explained using the long-range terms as examples. The matrix representations of spin-dependent terms are

$$\begin{aligned}&\left\langle\chi_\mu\chi_\nu\left|\boldsymbol{g}_2^{\mathrm{sd1,lr}}\right|\chi_\lambda\chi_\sigma\right\rangle\\&=\sum_{k_ak_bk_ck_d}\left\langle\chi_\mu\left|\boldsymbol{d}_i\right|k_a\right\rangle\left\langle\chi_\nu\left|\boldsymbol{M}_j\right|k_b\right\rangle\left\langle k_ak_b\left|\mathrm{i}\boldsymbol{\sigma}^i\cdot\boldsymbol{p}_i\,\mathrm{erf}\left(\mu r_{ij}\right)/r_{ij}\,\mathbf{1}_2\times\boldsymbol{p}_i\right|k_ck_d\right\rangle\left\langle k_c\left|\boldsymbol{d}_i\right|\chi_\lambda\right\rangle\left\langle k_d\left|\boldsymbol{M}_j\right|\chi_\sigma\right\rangle,\end{aligned}$$

(A5.11)

$$\begin{aligned}&\left\langle\chi_\mu\chi_\nu\left|\boldsymbol{g}_2^{\mathrm{sd2,lr}}\right|\chi_\lambda\chi_\sigma\right\rangle\\&=\sum_{k_ak_bk_ck_d}\left\langle\chi_\mu\left|\boldsymbol{d}_i\right|k_a\right\rangle\left\langle\chi_\nu\left|\boldsymbol{d}_j\right|k_b\right\rangle\left\langle k_ak_b\left|\mathrm{i}\boldsymbol{\sigma}^i\cdot\left(\boldsymbol{p}_i\left(\boldsymbol{p}_j\,\mathrm{erf}\left(\mu r_{ij}\right)/r_{ij}\,\mathbf{1}_2\cdot\boldsymbol{p}_j\right)\times\boldsymbol{p}_i\right)\right|k_ck_d\right\rangle\left\langle k_c\left|\boldsymbol{d}_i\right|\chi_\lambda\right\rangle\left\langle k_d\left|\boldsymbol{d}_j\right|\chi_\sigma\right\rangle,\end{aligned}$$

(A5.12)

and

$$\left\langle \chi_\mu \chi_\nu \left| \boldsymbol{g}_2^{\mathrm{sd3,lr}} \right| \chi_\lambda \chi_\sigma \right\rangle$$
$$= \sum_{k_a k_b k_c k_d} \left\langle \chi_\mu \left| \boldsymbol{d}_i \right| k_a \right\rangle \left\langle \chi_\nu \left| \boldsymbol{d}_j \right| k_b \right\rangle \left\langle k_a k_b \left| -\boldsymbol{\sigma}^i \cdot \left(\boldsymbol{p}_i \left(\boldsymbol{\sigma}^j \cdot \boldsymbol{p}_j \operatorname{erf}\left(\mu r_{ij}\right) / r_{ij} \mathbf{1}_2 \times \boldsymbol{p}_j \right) \times \boldsymbol{p}_i \right) \right| k_c k_d \right\rangle \left\langle k_c \left| \boldsymbol{d}_i \right| \chi_\lambda \right\rangle \left\langle k_d \left| \boldsymbol{d}_j \right| \chi_\sigma \right\rangle.$$

(A5.13)

The TEIs that require explicit calculations for the spin-dependent terms are those three integrals:

$$\left\langle k_a k_b \left| \mathrm{i}\boldsymbol{\sigma}^i \cdot \boldsymbol{p}_i \operatorname{erf}\left(\mu r_{ij}\right) / r_{ij} \mathbf{1}_2 \times \boldsymbol{p}_i \right| k_c k_d \right\rangle$$

$$\left\langle k_a k_b \left| \mathrm{i}\boldsymbol{\sigma}^i \cdot \left(\boldsymbol{p}_i \left(\boldsymbol{p}_j \operatorname{erf}\left(\mu r_{ij}\right) / r_{ij} \mathbf{1}_2 \cdot \boldsymbol{p}_j \right) \times \boldsymbol{p}_i \right) \right| k_c k_d \right\rangle$$

$$\left\langle k_a k_b \left| -\boldsymbol{\sigma}^i \cdot \left(\boldsymbol{p}_i \left(\boldsymbol{\sigma}^j \cdot \boldsymbol{p}_j \operatorname{erf}\left(\mu r_{ij}\right) / r_{ij} \mathbf{1}_2 \times \boldsymbol{p}_j \right) \times \boldsymbol{p}_i \right) \right| k_c k_d \right\rangle.$$

Using the following equation,

$$\mathrm{i}\boldsymbol{\sigma} \cdot \boldsymbol{A} \times \boldsymbol{B} = \begin{pmatrix} \mathbf{0}_2 & \left(\boldsymbol{A} \times \boldsymbol{B}\right)_y \\ -\left(\boldsymbol{A} \times \boldsymbol{B}\right)_y & \mathbf{0}_2 \end{pmatrix} - \mathrm{i} \begin{pmatrix} \left(\boldsymbol{A} \times \boldsymbol{B}\right)_z & \left(\boldsymbol{A} \times \boldsymbol{B}\right)_x \\ \left(\boldsymbol{A} \times \boldsymbol{B}\right)_x & -\left(\boldsymbol{A} \times \boldsymbol{B}\right)_z \end{pmatrix}, \qquad \text{(A5.14)}$$

the first one is rewritten as

$$\left\langle k_a k_b \left| \mathrm{i}\boldsymbol{\sigma}^i \cdot \boldsymbol{p}_i \operatorname{erf}\left(\mu r_{ij}\right) / r_{ij} \mathbf{1}_2 \times \boldsymbol{p}_i \right| k_c k_d \right\rangle$$
$$= \begin{pmatrix} \mathbf{0}_2 & \left\langle k_a k_b \left| \left(\boldsymbol{p}_i \operatorname{erf}\left(\mu r_{ij}\right) / r_{ij} \mathbf{1}_2 \times \boldsymbol{p}_i \right)_y \right| k_c k_d \right\rangle \\ -\left\langle k_a k_b \left| \left(\boldsymbol{p}_i \operatorname{erf}\left(\mu r_{ij}\right) / r_{ij} \mathbf{1}_2 \times \boldsymbol{p}_i \right)_y \right| k_c k_d \right\rangle & \mathbf{0}_2 \end{pmatrix}$$
$$-\mathrm{i} \begin{pmatrix} \left\langle k_a k_b \left| \left(\boldsymbol{p}_i \operatorname{erf}\left(\mu r_{ij}\right) / r_{ij} \mathbf{1}_2 \times \boldsymbol{p}_i \right)_z \right| k_c k_d \right\rangle & \left\langle k_a k_b \left| \left(\boldsymbol{p}_i \operatorname{erf}\left(\mu r_{ij}\right) / r_{ij} \mathbf{1}_2 \times \boldsymbol{p}_i \right)_x \right| k_c k_d \right\rangle \\ \left\langle k_a k_b \left| \left(\boldsymbol{p}_i \operatorname{erf}\left(\mu r_{ij}\right) / r_{ij} \mathbf{1}_2 \times \boldsymbol{p}_i \right)_x \right| k_c k_d \right\rangle & -\left\langle k_a k_b \left| \left(\boldsymbol{p}_i \operatorname{erf}\left(\mu r_{ij}\right) / r_{ij} \mathbf{1}_2 \times \boldsymbol{p}_i \right)_z \right| k_c k_d \right\rangle \end{pmatrix},$$

(A5.15)

with

$$\left\langle k_a k_b \left| \left(\boldsymbol{p}_i \operatorname{erf}\left(\mu r_{ij}\right) / r_{ij} \mathbf{1}_2 \times \boldsymbol{p}_i \right)_x \right| k_c k_d \right\rangle$$
$$= \left\langle \frac{\partial k_a}{\partial y} k_b \left| \operatorname{erf}\left(\mu r_{ij}\right) / r_{ij} \mathbf{1}_2 \right| \frac{\partial k_c}{\partial z} k_d \right\rangle - \left\langle \frac{\partial k_a}{\partial z} k_b \left| \operatorname{erf}\left(\mu r_{ij}\right) / r_{ij} \mathbf{1}_2 \right| \frac{\partial k_c}{\partial y} k_d \right\rangle,$$

(A5.16)

$$\left\langle k_a k_b \left| \left(\boldsymbol{p}_i \operatorname{erf}\left(\mu r_{ij}\right)/r_{ij}\,\mathbf{1}_2 \times \boldsymbol{p}_i \right)_y \right| k_c k_d \right\rangle$$
$$= \left\langle \frac{\partial k_a}{\partial x} k_b \left| \operatorname{erf}\left(\mu r_{ij}\right)/r_{ij}\,\mathbf{1}_2 \right| \frac{\partial k_c}{\partial z} k_d \right\rangle - \left\langle \frac{\partial k_a}{\partial z} k_b \left| \operatorname{erf}\left(\mu r_{ij}\right)/r_{ij}\,\mathbf{1}_2 \right| \frac{\partial k_c}{\partial x} k_d \right\rangle, \tag{A5.17}$$

and

$$\left\langle k_a k_b \left| \left(\boldsymbol{p}_i \operatorname{erf}\left(\mu r_{ij}\right)/r_{ij}\,\mathbf{1}_2 \times \boldsymbol{p}_i \right)_z \right| k_c k_d \right\rangle$$
$$= \left\langle \frac{\partial k_a}{\partial x} k_b \left| \operatorname{erf}\left(\mu r_{ij}\right)/r_{ij}\,\mathbf{1}_2 \right| \frac{\partial k_c}{\partial y} k_d \right\rangle - \left\langle \frac{\partial k_a}{\partial y} k_b \left| \operatorname{erf}\left(\mu r_{ij}\right)/r_{ij}\,\mathbf{1}_2 \right| \frac{\partial k_c}{\partial x} k_d \right\rangle. \tag{A5.18}$$

The second integral is as follows:

$$\left\langle k_a k_b \left| \mathrm{i}\boldsymbol{\sigma}^i \cdot \left(\boldsymbol{p}_i \left(\boldsymbol{p}_j \operatorname{erf}\left(\mu r_{ij}\right)/r_{ij}\,\mathbf{1}_2 \cdot \boldsymbol{p}_j \right) \times \boldsymbol{p}_i \right) \right| k_c k_d \right\rangle$$
$$= \begin{pmatrix} \mathbf{0}_2 & \left\langle k_a k_b \left| \left(\boldsymbol{p}_i \left(\boldsymbol{p}_j \operatorname{erf}\left(\mu r_{ij}\right)/r_{ij}\,\mathbf{1}_2 \cdot \boldsymbol{p}_j \right) \times \boldsymbol{p}_i \right)_y \right| k_c k_d \right\rangle \\ -\left\langle k_a k_b \left| \left(\boldsymbol{p}_i \left(\boldsymbol{p}_j \operatorname{erf}\left(\mu r_{ij}\right)/r_{ij}\,\mathbf{1}_2 \cdot \boldsymbol{p}_j \right) \times \boldsymbol{p}_i \right)_y \right| k_c k_d \right\rangle & \mathbf{0}_2 \end{pmatrix}$$
$$-\mathrm{i} \begin{pmatrix} \left\langle k_a k_b \left| \left(\boldsymbol{p}_i \left(\boldsymbol{p}_j \operatorname{erf}\left(\mu r_{ij}\right)/r_{ij}\,\mathbf{1}_2 \cdot \boldsymbol{p}_j \right) \times \boldsymbol{p}_i \right)_z \right| k_c k_d \right\rangle & \left\langle k_a k_b \left| \left(\boldsymbol{p}_i \left(\boldsymbol{p}_j \operatorname{erf}\left(\mu r_{ij}\right)/r_{ij}\,\mathbf{1}_2 \cdot \boldsymbol{p}_j \right) \times \boldsymbol{p}_i \right)_x \right| k_c k_d \right\rangle \\ \left\langle k_a k_b \left| \left(\boldsymbol{p}_i \left(\boldsymbol{p}_j \operatorname{erf}\left(\mu r_{ij}\right)/r_{ij}\,\mathbf{1}_2 \cdot \boldsymbol{p}_j \right) \times \boldsymbol{p}_i \right)_x \right| k_c k_d \right\rangle & -\left\langle k_a k_b \left| \left(\boldsymbol{p}_i \left(\boldsymbol{p}_j \operatorname{erf}\left(\mu r_{ij}\right)/r_{ij}\,\mathbf{1}_2 \cdot \boldsymbol{p}_j \right) \times \boldsymbol{p}_i \right)_z \right| k_c k_d \right\rangle \end{pmatrix}, \tag{A5.19}$$

with

$$\left\langle k_a k_b \left| \left(\boldsymbol{p}_i \left(\boldsymbol{p}_j \operatorname{erf}\left(\mu r_{ij}\right)/r_{ij}\,\mathbf{1}_2 \cdot \boldsymbol{p}_j \right) \times \boldsymbol{p}_i \right)_x \right| k_c k_d \right\rangle$$
$$= \left\langle \frac{\partial k_a}{\partial y} k_b \left| \left(\boldsymbol{p}_j \operatorname{erf}\left(\mu r_{ij}\right)/r_{ij}\,\mathbf{1}_2 \cdot \boldsymbol{p}_j \right) \right| \frac{\partial k_c}{\partial z} k_d \right\rangle - \left\langle \frac{\partial k_a}{\partial z} k_b \left| \left(\boldsymbol{p}_j \operatorname{erf}\left(\mu r_{ij}\right)/r_{ij}\,\mathbf{1}_2 \cdot \boldsymbol{p}_j \right) \right| \frac{\partial k_c}{\partial y} k_d \right\rangle$$
$$= \left\langle \frac{\partial k_a}{\partial y} \left(\nabla_{\mathbf{r}_j} k_b \right) \right| \operatorname{erf}\left(\mu r_{ij}\right)/r_{ij}\,\mathbf{1}_2 \left| \frac{\partial k_c}{\partial z} \left(\nabla_{\mathbf{r}_j} k_d \right) \right\rangle - \left\langle \frac{\partial k_a}{\partial z} \left(\nabla_{\mathbf{r}_j} k_b \right) \right| \operatorname{erf}\left(\mu r_{ij}\right)/r_{ij}\,\mathbf{1}_2 \left| \frac{\partial k_c}{\partial y} \left(\nabla_{\mathbf{r}_j} k_d \right) \right\rangle, \tag{A5.20}$$

$$
\begin{aligned}
&\left\langle k_a k_b \left| \left(\boldsymbol{p}_i \left(\boldsymbol{p}_j \operatorname{erf}\left(\mu r_{ij}\right)/r_{ij}\, \mathbf{1}_2 \cdot \boldsymbol{p}_j \right) \times \boldsymbol{p}_i \right)_y \right| k_c k_d \right\rangle \\
&= \left\langle \frac{\partial k_a}{\partial x} k_b \left| \left(\boldsymbol{p}_j \operatorname{erf}\left(\mu r_{ij}\right)/r_{ij}\, \mathbf{1}_2 \cdot \boldsymbol{p}_j \right) \right| \frac{\partial k_c}{\partial z} k_d \right\rangle - \left\langle \frac{\partial k_a}{\partial z} k_b \left| \left(\boldsymbol{p}_j \operatorname{erf}\left(\mu r_{ij}\right)/r_{ij}\, \mathbf{1}_2 \cdot \boldsymbol{p}_j \right) \right| \frac{\partial k_c}{\partial x} k_d \right\rangle \\
&= \left\langle \frac{\partial k_a}{\partial x} \left(\nabla_{\mathbf{r}_j} k_b \right) \middle| \operatorname{erf}\left(\mu r_{ij}\right)/r_{ij}\, \mathbf{1}_2 \middle| \frac{\partial k_c}{\partial z} \left(\nabla_{\mathbf{r}_j} k_d \right) \right\rangle - \left\langle \frac{\partial k_a}{\partial z} \left(\nabla_{\mathbf{r}_j} k_b \right) \middle| \operatorname{erf}\left(\mu r_{ij}\right)/r_{ij}\, \mathbf{1}_2 \middle| \frac{\partial k_c}{\partial x} \left(\nabla_{\mathbf{r}_j} k_d \right) \right\rangle,
\end{aligned}
\tag{A5.21}
$$

and

$$
\begin{aligned}
&\left\langle k_a k_b \left| \left(\boldsymbol{p}_i \left(\boldsymbol{p}_j \operatorname{erf}\left(\mu r_{ij}\right)/r_{ij}\, \mathbf{1}_2 \cdot \boldsymbol{p}_j \right) \times \boldsymbol{p}_i \right)_z \right| k_c k_d \right\rangle \\
&= \left\langle \frac{\partial k_a}{\partial x} k_b \left| \left(\boldsymbol{p}_j \operatorname{erf}\left(\mu r_{ij}\right)/r_{ij}\, \mathbf{1}_2 \cdot \boldsymbol{p}_j \right) \right| \frac{\partial k_c}{\partial y} k_d \right\rangle - \left\langle \frac{\partial k_a}{\partial y} k_b \left| \left(\boldsymbol{p}_j \operatorname{erf}\left(\mu r_{ij}\right)/r_{ij}\, \mathbf{1}_2 \cdot \boldsymbol{p}_j \right) \right| \frac{\partial k_c}{\partial x} k_d \right\rangle \\
&= \left\langle \frac{\partial k_a}{\partial x} \left(\nabla_{\mathbf{r}_j} k_b \right) \middle| \operatorname{erf}\left(\mu r_{ij}\right)/r_{ij}\, \mathbf{1}_2 \middle| \frac{\partial k_c}{\partial y} \left(\nabla_{\mathbf{r}_j} k_d \right) \right\rangle - \left\langle \frac{\partial k_a}{\partial y} \left(\nabla_{\mathbf{r}_j} k_b \right) \middle| \operatorname{erf}\left(\mu r_{ij}\right)/r_{ij}\, \mathbf{1}_2 \middle| \frac{\partial k_c}{\partial x} \left(\nabla_{\mathbf{r}_j} k_d \right) \right\rangle.
\end{aligned}
\tag{A5.22}
$$

The third one is as follows:

$$
\begin{aligned}
&\left\langle k_a k_b \left| -\boldsymbol{\sigma}^i \cdot \left(\boldsymbol{p}_i \left(\boldsymbol{\sigma}^j \cdot \boldsymbol{p}_j \operatorname{erf}\left(\mu r_{ij}\right)/r_{ij}\, \mathbf{1}_2 \times \boldsymbol{p}_j \right) \times \boldsymbol{p}_i \right) \right| k_c k_d \right\rangle \\
&= \left\langle k_a k_b \left| \mathrm{i}\boldsymbol{\sigma}^i \cdot \left(\boldsymbol{p}_i \left(i\boldsymbol{\sigma}^j \cdot \boldsymbol{p}_j \operatorname{erf}\left(\mu r_{ij}\right)/r_{ij}\, \mathbf{1}_2 \times \boldsymbol{p}_j \right) \times \boldsymbol{p}_i \right) \right| k_c k_d \right\rangle \\
&= \begin{pmatrix} \mathbf{0}_2 & \left\langle k_a k_b \left| \left(\boldsymbol{p}_i \left(\mathrm{i}\boldsymbol{\sigma}^j \cdot \boldsymbol{p}_j \operatorname{erf}\left(\mu r_{ij}\right)/r_{ij}\, \mathbf{1}_2 \times \boldsymbol{p}_j \right) \times \boldsymbol{p}_i \right)_y \right| k_c k_d \right\rangle \\ -\left\langle k_a k_b \left| \left(\boldsymbol{p}_i \left(\mathrm{i}\boldsymbol{\sigma}^j \cdot \boldsymbol{p}_j \operatorname{erf}\left(\mu r_{ij}\right)/r_{ij}\, \mathbf{1}_2 \times \boldsymbol{p}_j \right) \times \boldsymbol{p}_i \right)_y \right| k_c k_d \right\rangle & \mathbf{0}_2 \end{pmatrix} \\
&-\mathrm{i} \begin{pmatrix} \left\langle k_a k_b \left| \left(\boldsymbol{p}_i \left(\mathrm{i}\boldsymbol{\sigma}^j \cdot \boldsymbol{p}_j \operatorname{erf}\left(\mu r_{ij}\right)/r_{ij}\, \mathbf{1}_2 \times \boldsymbol{p}_j \right) \times \boldsymbol{p}_i \right)_z \right| k_c k_d \right\rangle & \left\langle k_a k_b \left| \left(\boldsymbol{p}_i \left(\mathrm{i}\boldsymbol{\sigma}^j \cdot \boldsymbol{p}_j \operatorname{erf}\left(\mu r_{ij}\right)/r_{ij}\, \mathbf{1}_2 \times \boldsymbol{p}_j \right) \times \boldsymbol{p}_i \right)_x \right| k_c k_d \right\rangle \\ \left\langle k_a k_b \left| \left(\boldsymbol{p}_i \left(\mathrm{i}\boldsymbol{\sigma}^j \cdot \boldsymbol{p}_j \operatorname{erf}\left(\mu r_{ij}\right)/r_{ij}\, \mathbf{1}_2 \times \boldsymbol{p}_j \right) \times \boldsymbol{p}_i \right)_x \right| k_c k_d \right\rangle & -\left\langle k_a k_b \left| \left(\boldsymbol{p}_i \left(\mathrm{i}\boldsymbol{\sigma}^j \cdot \boldsymbol{p}_j \operatorname{erf}\left(\mu r_{ij}\right)/r_{ij}\, \mathbf{1}_2 \times \boldsymbol{p}_j \right) \times \boldsymbol{p}_i \right)_z \right| k_c k_d \right\rangle \end{pmatrix}.
\end{aligned}
\tag{A5.23}
$$

The matrix elements in Eq. (A5.23) are also rewritten as similar procedure as the first and second integrals using Eq. (A5.14). Therefore, the Gaussian-type TEIs of operator $\operatorname{erf}\left(\mu r_{ij}\right)/r_{ij}$ are explicitly evaluated.

Chapter 6 Evaluation of PCE on FON states in noble gas atom[§]

6.1 Introduction

The total energy of DFT is expressed as a functional of electron density[1] shown in Eq. (2.3.28) in Chapter 2. Because the exact functional form is unknown, approximate functionals are generally used. Despite the widespread use of DFT, the approximate functionals are limited by inaccurate definitions of chemical phenomena such as reaction barriers,[2,3] band gap,[4] polarizability,[5] and charge transfer.[6] The causes of these errors have been discussed in terms of the SIE, which stems from the exchange term of the approximate functional.[7] More inclusively, the definition of the delocalization error is proposed.[8,9]

The delocalization error occurs in the FON states.[8,10] The ground-state energy obtained by the exact functional varies piecewise linearly with respect to the FON electrons between two consecutive integers. However, the approximate functional deviates from the linearity. For example, the total energy change dependent on electron number with FON states becomes a concave curve in the HOMO.[10]

Several researchers have developed methods for correcting the delocalization error or SIE[7,11–15]; however, this aspect continues to be challenging in DFT.[16] Global and range-separated hybrid functionals, which mix certain ratios of HFx into exchange functional, reduce these errors to a certain extent. The LC-DFT,[17,18] which calculates exchange energy as long-range HFx and short-range exchange functional, indicates linear dependence of total energy on change of the occupation number of HOMO.[19] For the description of the linearity in core orbitals, the importance of short-range HFx is revealed by the LCgau

[§] Reproduced from the article by Chinami Takashima and Hiromi Nakai, DOI: 10.1007/s00214-023-03089-3

scheme[20] and core-valence-Rydberg functional.[21,22]

The accurate description of linearity is one measure of evaluating the performance of functionals. Orbital-specific hybrid functionals are constructed by imposing the linearity condition for orbitals of FON states, which reasonably reproduces the ionization potential and excitation energies involving core, valence, and Rydberg orbitals.[23–26] The localized orbital scaling correction was developed by enforcing the linearity condition for the relation between energy and electron number and correctly described phenomena such as polarizability, molecular dissociation, and band gap.[14,27–30]

In this chapter, the PCE of FON states is examined in the 2c relativistic theory based on the IOTC Hamiltonian. The remainder of this chapter is organized as follows. In Section 6.2, the linearity condition for FON states as the theoretical background is discussed. Section 6.3 explains the computational details. The results and discussion are presented in Section 6.4 followed by the conclusion in Section 6.5.

6.2 Linearity condition for FON states

The energy of the exact DFT with respect to FON electron is expressed as follows:

$$\begin{aligned} E\left(N+\Delta n\right) &= \left(1-\Delta n\right)E\left(N\right)+\Delta n E\left(N+1\right) \\ &= \left(E\left(N+1\right)-E\left(N\right)\right)\Delta n + E\left(N\right), \end{aligned} \tag{6.2.1}$$

where N is a positive integer, Δn is a fractional number ($0 \le \Delta n \le 1$), and $E(N)$ is the ground-state energy of an N-electron system.[31] The curve of E with respect to Δn becomes straight, which is termed the linearity condition for total energies.

According to Janak's theorem,[32] orbital energy ε_i, which is the eigen value of φ_i, is adherent to the following expression:

$$\frac{\partial E}{\partial f_i} = \varepsilon_i , \tag{6.2.2}$$

where f_i is the occupation number of the i-th orbital. The HOMO energy is equivalent to

the negative value of the first ionization potential.[33] Differentiating Eq. (6.2.2) by f_i in the range of 0 to 1 yields the following expression:

$$\left.\frac{\partial^2 E}{\partial f_i^2}\right|_{0\le f_i\le 1} = \left.\frac{\partial \varepsilon_i}{\partial f_i}\right|_{0\le f_i\le 1} = 0\,, \tag{6.2.3}$$

indicating that the orbital energy is constant for the change of occupation number of the corresponding orbital. This is the linearity condition for orbital energies.

6.3 Computational details

Noble gas atoms (Ne, Ar, Kr, Xe, and Rn) were numerically analyzed. Sapporo-TZP-2012+d basis sets for Ne, Ar,[34] and Sapporo-DKH3-TZP-2012+d basis sets for Kr, Xe, and Rn[35] were applied in an uncontracted manner.

The exchange-correlation functionals used in this study were 100% Becke's exchange (B88)[36] with Lee–Yang–Parr (LYP)[37] correlation (BLYP), Becke's half-and-half exchange (50% B88 + 50% HFx) with LYP correlation (BHHLYP),[38] 100% HFx with LYP correlation (HFLYP), and LC-BLYP with range-separation parameter 0.47.[3] The modified ratio of B88 and HFx, namely, 40% B88 + 60% HFx, 30% B88 + 70% HFx, 20% B88 + 80% HFx, and 10% B88 + 90% HFx, were also employed in conjunction with LYP correlation.

For the 2c calculation, the one-electron spin-free IOTC Hamiltonian[39] with two-electron Coulomb operator (1eIOTC) and one- and two-electron spin-free IOTC Hamiltonian[40] (1e2eIOTC) were used along with the PCC[41,42] ($\boldsymbol{\delta}^{\mathrm{sf}}$) and -uncorrected density operator, which are described in Chapter 2. FON energy was calculated self-consistently by varying the occupation numbers of HOMO or 1*s* orbital. All the calculations were performed with the modified version of the GAMESS program.[43]

6.4 Results and discussion

6.4.1 PCE on delocalization error

In this subsection, the PCEs on the delocalization error are examined. Figures 6.1–6.4 show the total energy deviation ΔE,

$$\Delta E = E\left(N+\Delta n\right)-\left[\left\{1-\left|\Delta n\right|\right\}E\left(N\right)+\left|\Delta n\right|E\left(N-1\right)\right], \tag{6.4.1}$$

with respect to Δn. According to the linearity condition, ΔE becomes 0 regardless of Δn in the exact energy.

Figure 6.1 provides the HOMO result of Ne, Ar, Kr, Xe, and Rn atoms obtained by the BLYP functional. As relativistic treatments, nonrelativistic Hamiltonian, 1eIOTC, 1eIOTC with $\boldsymbol{\delta}^{\mathrm{sf}}$, 1e2eIOTC, and 1e2eIOTC with $\boldsymbol{\delta}^{\mathrm{sf}}$ are compared. The right panels show the enlarged view near the minima. All elements and relativistic treatments show the concave curves. Comparing elements, the absolute value of ΔE is largest in Ne and smaller in Ar, Kr, Xe, and Rn in that order. Lighter elements have a larger delocalization error. In the results of Ne and Ar, the relativistic treatments indicate close values to nonrelativistic treatments. The relativistic treatments estimate lower ΔE of Kr, Xe, and Rn than the nonrelativistic treatment. The differences among 1eIOTC, 1eIOTC with $\boldsymbol{\delta}^{\mathrm{sf}}$, 1e2eIOTC, and 1e2eIOTC with $\boldsymbol{\delta}^{\mathrm{sf}}$ are hardly identified. PCEs of two-electron and density operators rarely affect the FON states of HOMO, which are over stabilized by one-electron relativistic effects.

Figure 6.2 presents the results for 1*s* orbital. Contrary to the case of HOMO shown in Figure 6.1, the absolute value of ΔE is largest in Rn and becomes relatively small in Xe, Kr, Ar, and Ne in that order. Heavier elements are limited from larger delocalization error in the FON states of 1*s* orbital. Comparing nonrelativistic and relativistic treatments, the differences are found in Ar, Kr, Xe, and Rn, which are minor in Ar and obvious for other elements in the order of magnitude Kr < Xe < Rn. The PCEs of two-electron and density

operators are also large. 1eIOTC (1eIOTC with $\boldsymbol{\delta}^{sf}$) yield lower ΔE than that of 1e2eIOTC (1e2eIOTCwith $\boldsymbol{\delta}^{sf}$). In terms of $\boldsymbol{\delta}^{sf}$, the ΔE obtained by 1eIOTC (1e2eIOTC) is higher than that obtained by 1eIOTC with $\boldsymbol{\delta}^{sf}$ (1e2eIOTC with $\boldsymbol{\delta}^{sf}$). For example, the ΔE of Rn at Δn = 0.5 is −155.6, −161.6, −137.6, and −143.7 eV for 1eIOTC, 1eIOTC with $\boldsymbol{\delta}^{sf}$, 1e2eIOTC, and 1e2eIOTC with $\boldsymbol{\delta}^{sf}$. The PCE of two-electron and density operator overestimates and underestimates delocalization error, respectively. The results of a comparative analysis of the difference owing to the picture change of two-electron and density operators show that the PCE of two-electron operators (~16 eV in Rn at Δn = 0.5) are larger than those of the density operator (~6 eV in Rn at Δn = 0.5).

Figures 6.3 and 6.4 show the results obtained by the HFLYP functional for HOMO and 1*s* orbital, respectively. Contrary to Figures 6.1 and 6.2, all curves are convex. HFx destabilizes the FON states. These errors are referred to as a localization error, which is derived from the lack of electron correlation in HFx.[8] The absolute values of ΔE are smaller than those of BLYP. Electron correlation in the exchange term is smaller than the error derived from the inexact form of exchange functional. In the results of HOMO shown in Figure 6.3, the localization error for the lighter elements increases. The differences between nonrelativistic and relativistic treatments, which is slightly observed in Rn, are small. The PCE values of two-electron and density operators are also small in all elements.

Opposite to the HOMO, the localization errors of 1*s* orbital shown in Figure 6.4 are larger in heavier elements. The effects of relativistic treatments are apparent in Ar, Kr, Xe, and Rn. The PCE of the two-electron operator, which overestimates the localization error, is clear in Xe and Rn. In contrast to the BLYP in Figure 6.2, the differences due to $\boldsymbol{\delta}^{sf}$ are so small as to be invisible. The exchange part of HFLYP is not affected by the PCE of density operator because it does not include electron density. Although the correlation part is influenced by the PCE of the density operator, the correlation energy is considerably smaller than the exchange energy. Therefore, the PCE of the density operator for HFLYP is

small.

Owing to the error cancellation of concave and convex characteristics of BLYP and HFLYP functionals, the curvature of ΔE becomes smaller when B88 exchange and HFx are mixed as shown in Figure A6.1 in Appendix of this chapter.

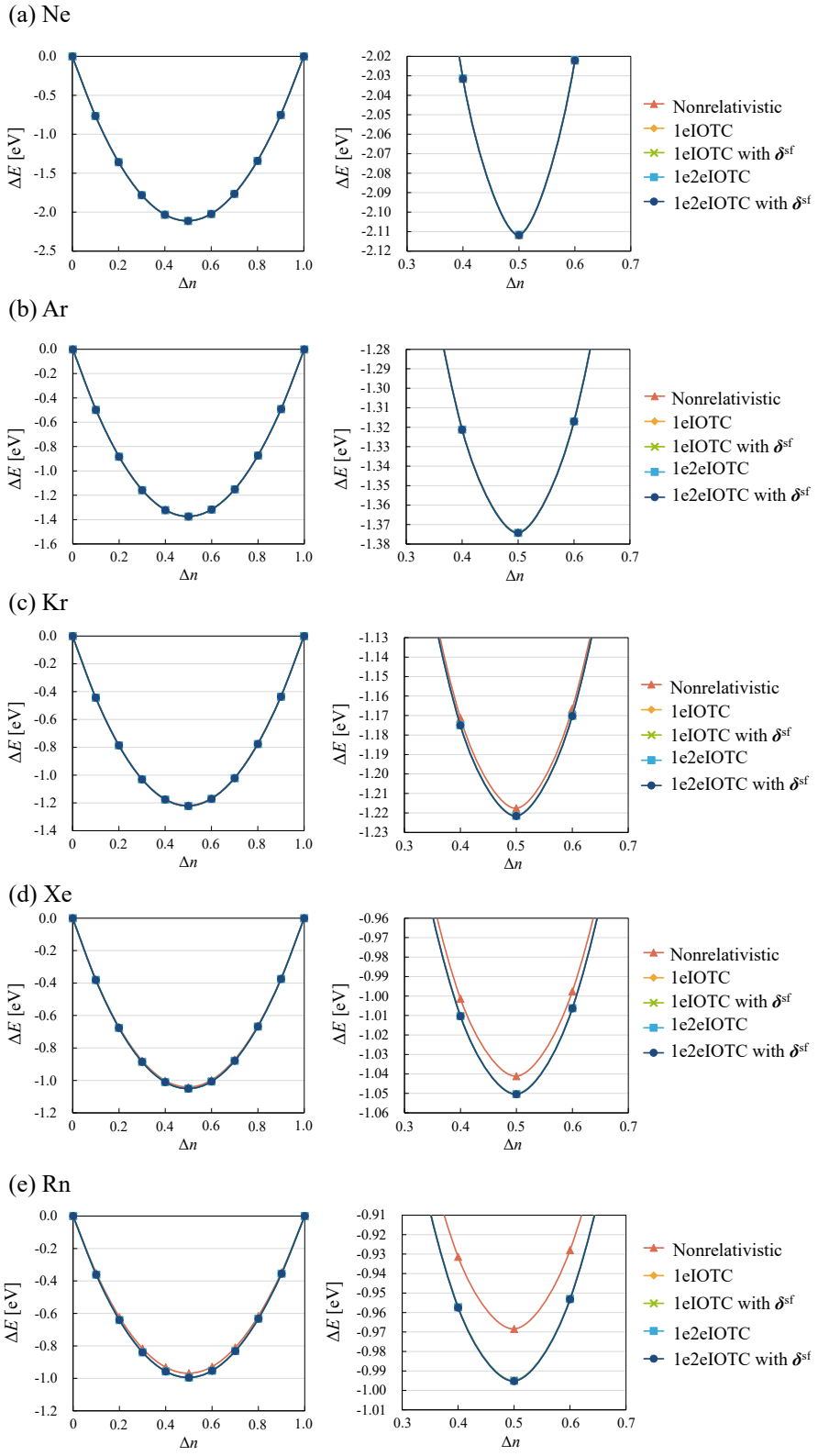

Figure 6.1. Total energy deviation (in eV) from ideal energy of FON states of HOMO in (a) Ne, (b) Ar, (c) Kr, (d) Xe, and (e) Rn atoms obtained by BLYP functionals with several relativistic treatments. Right panels show the enlarged view near the minima.

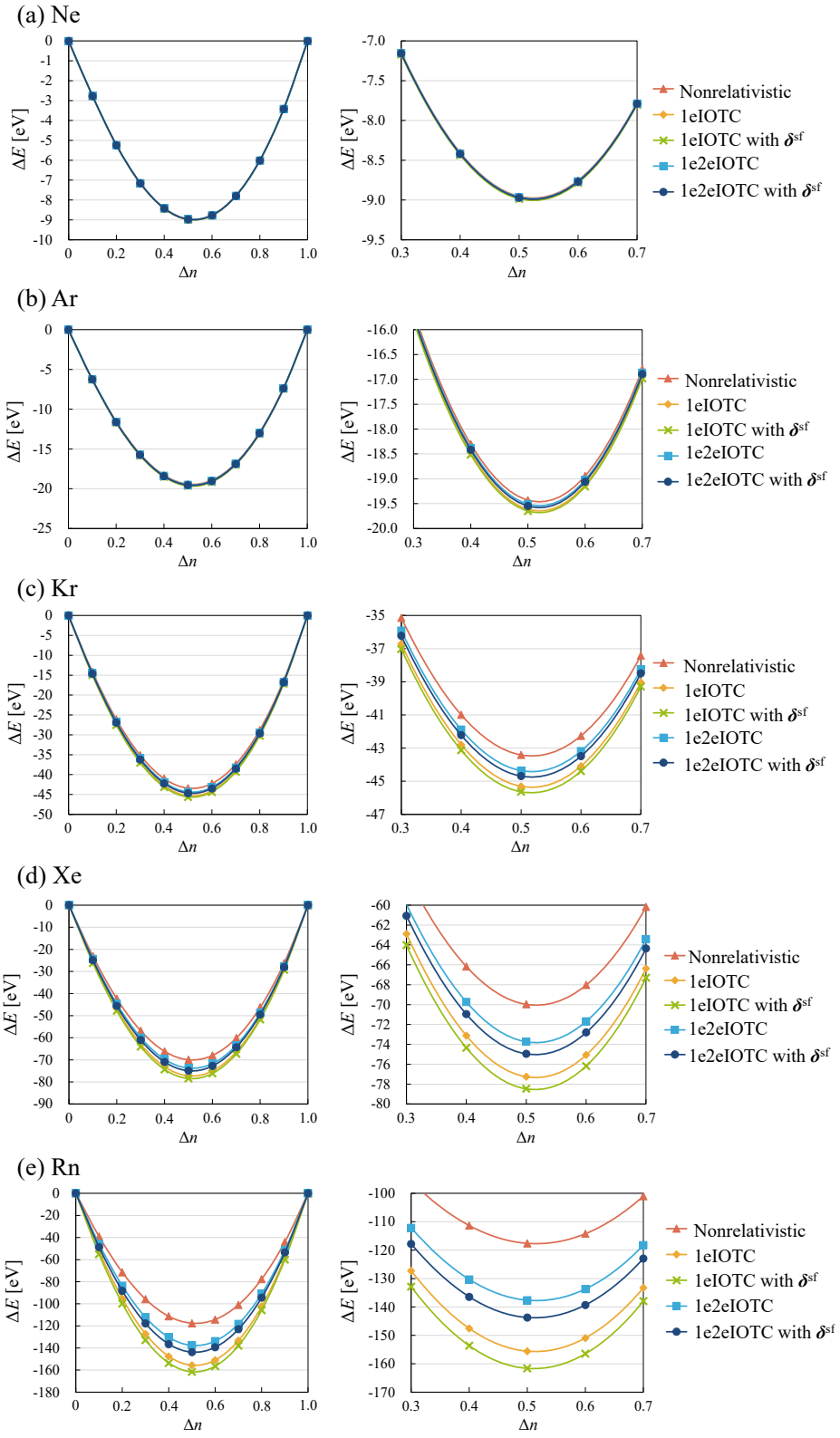

Figure 6.2. Total energy deviation (in eV) from ideal energy of FON states of 1*s* orbital in (a) Ne, (b) Ar, (c) Kr, (d) Xe, and (e) Rn atoms obtained by BLYP functionals with several relativistic treatments. Right panels show the enlarged view near the minima.

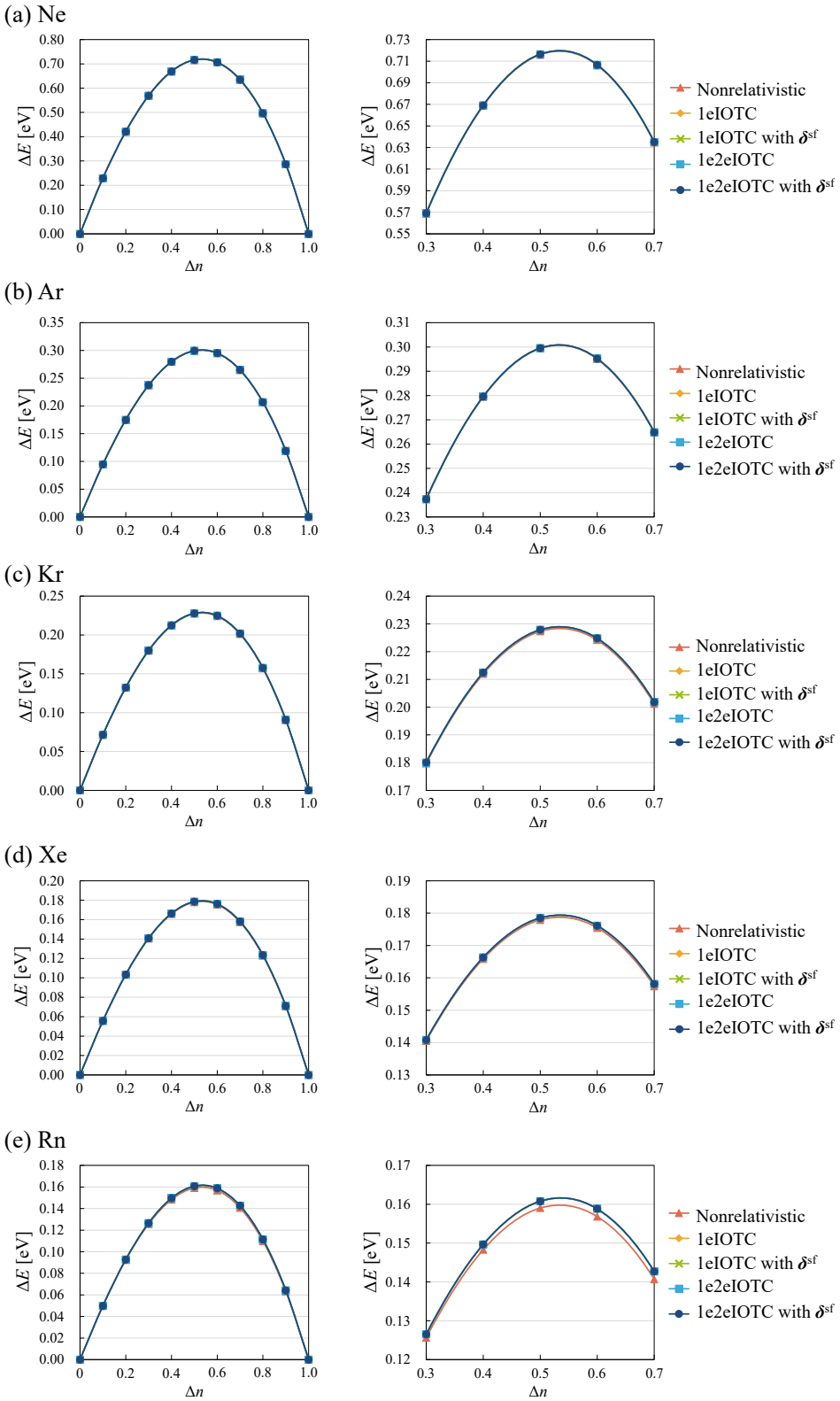

Figure 6.3. Total energy deviation (in eV) from ideal energy of FON states of HOMO in (a) Ne, (b) Ar, (c) Kr, (d) Xe, and (e) Rn atoms obtained by HFLYP functionals with several relativistic treatments. Right panels show the enlarged view near the minima.

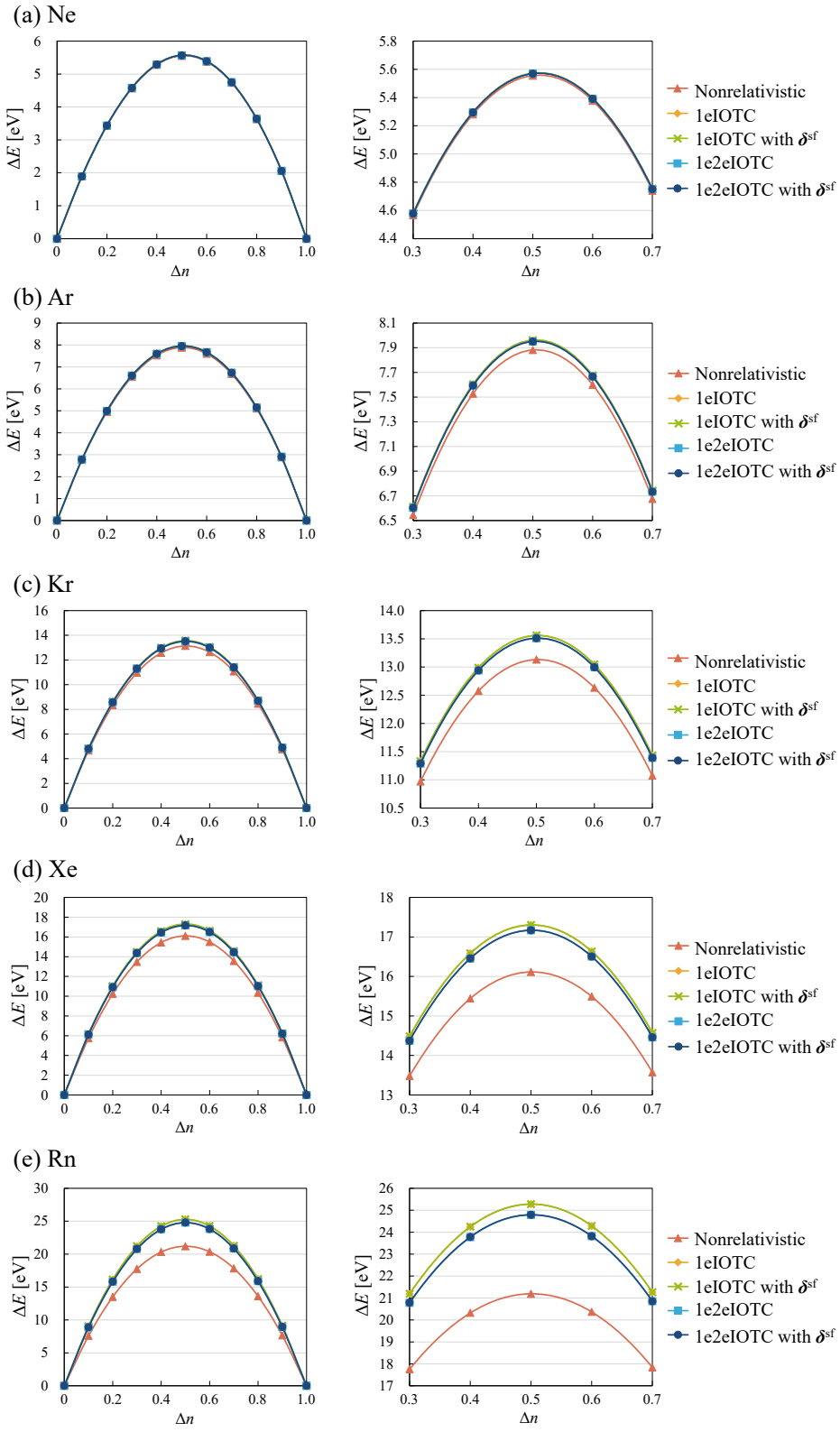

Figure 6.4. Total energy deviation (in eV) from ideal energy of FON states of 1s in (a) Ne, (b) Ar, (c) Kr, (d) Xe, and (e) Rn atoms obtained by HFLYP functionals with several relativistic treatments. Right panels show the enlarged view near the minima.

6.4.2 Orbital energy dependence of FON

This subsection examines the behaviors of orbital energy with respect to FON. Figures 6.5–6.8 demonstrate the orbital energies with respect to FON electron Δn. The results of the lightest and heaviest elements, Ne and Rn, are presented here. The slopes of the graphs of orbital energy with respect to Δn calculated using the least square method are tabulated in Tables 1–4. The results of other elements, Ar, Kr, and Xe, are provided in Figures A6.2–A6.7 and Tables A6.1–A6.5 in the appendix of this chapter.

Figure 6.5 shows the results for the HOMO of Ne. The corresponding slopes are shown in Table 6.1. The orbital energies $\varepsilon_{\mathrm{HOMO}}$ of BLYP monotonically increase as Δn increases. Upon adding HFx, the slope of $\varepsilon_{\mathrm{HOMO}}$ versus Δn graph becomes smaller. In the results of HFLYP, $\varepsilon_{\mathrm{HOMO}}$ decreases as Δn increases. Moreover, 30%B88+70%HFx+LYP shows the smallest absolute value of the slope, indicating the smallest FON dependence of $\varepsilon_{\mathrm{HOMO}}$. The slope of LC-BLYP is similar to that of BHHLYP. Nonrelativistic and relativistic treatments exhibit the above tendency and quantitatively similar orbital energies. One-electron relativistic effects and the PCE of two-electron and density operators are small in the HOMO of the Ne atom.

Figure 6.6 shows the results for 1*s* orbital of Ne. The corresponding slopes are shown in Table 6.2. The qualitative tendency of the orbital energies ε_{1s} with respect to Δn is similar to that of $\varepsilon_{\mathrm{HOMO}}$: ε_{1s} increases in BLYP and decreases in HFLYP as Δn increases and the combinations of B88 and HFx lie between BLYP and HFLYP. Moreover, 40%B88+60%HFx+LYP indicates the smallest absolute value of the slope, namely the smallest FON dependence of ε_{1s}. The magnitude of the slope is larger than that of the HOMO, indicating that ΔE of 1*s* orbital in Fig. 2(a) are larger than that of HOMO in Figure 6.1(a). The slope of LC-BLYP is larger than that of BHHLYP and closer to BLYP. As mentioned in previous studies,[20–22] the short-range HFx is important in inner shell orbitals. The relativistic effects and PCE are small, as in the results of HOMO.

Figure 6.7 shows the results for the HOMO of Rn. The corresponding slopes are shown in Table 6.3. The qualitative trends are similar to the results for HOMO of Ne, with the exception of the results of LC-BLYP. Among the combination of B88 and HFx, 10%B88+90%HFx+LYP indicates the smallest FON dependence of $\varepsilon_{\mathrm{HOMO}}$. $\varepsilon_{\mathrm{HOMO}}$ obtained by LC-BLYP, whose graph shows smaller slope than that of 10%B88+90%HFx+LYP, is almost independent from Δn. As in the case of Ne, the relativistic effects are small.

Figure 6.8 shows the results for 1*s* of Rn. The corresponding slopes are shown in Table 6.3. The qualitative trends are similar to the results for 1*s* orbital of Ne. Unlike Figures 6.5–6.7, the differences caused by the nonrelativistic and relativistic treatments are pronounced in the 1*s* orbital of Rn. The orbital energy changes of relativistic treatments are steeper than that of nonrelativistic Hamiltonian: the absolute values of the slopes obtained by relativistic treatments are apparently larger than those by nonrelativistic Hamiltonian. The changes of ε_{1s} (in eV) along the increase of FON, $0 < \Delta n < 1$ obtained by BLYP are −88176.8 to −87267.6 in nonrelativistic Hamiltonian, −99454.4 to −98240.7 in 1eIOTC, −99397.0 to −98129.5 in 1eIOTC with $\boldsymbol{\delta}^{\mathrm{sf}}$, −99671.6 to −98601.7 in 1e2eIOTC, and −99613.6 to −98489.3 in 1e2eIOTC with $\boldsymbol{\delta}^{\mathrm{sf}}$. The range of ε_{1s} in 1eIOTC is approximately 11000 eV lower than that of nonrelativistic Hamiltonian. Comparing 1eIOTC with 1e2eIOTC, the range of the ε_{1s} of 1e2eIOTC is more than 300 eV lower than that of 1eIOTC. Using $\boldsymbol{\delta}^{\mathrm{sf}}$ makes the range of ε_{1s} higher. The PCE of two-electron and density operators on the values of ε_{1s} cannot be disregarded while the relativistic effects are dominated by the one-electron term. The linearity of orbital energy is also influenced by PCE. The functional that yields the smallest slope of ε_{1s} versus Δn graph is 20%B88+80%HFx+LYP for nonrelativistic Hamiltonian and 1e2eIOTC and 10%B88+90%HFx+LYP for other relativistic treatments.

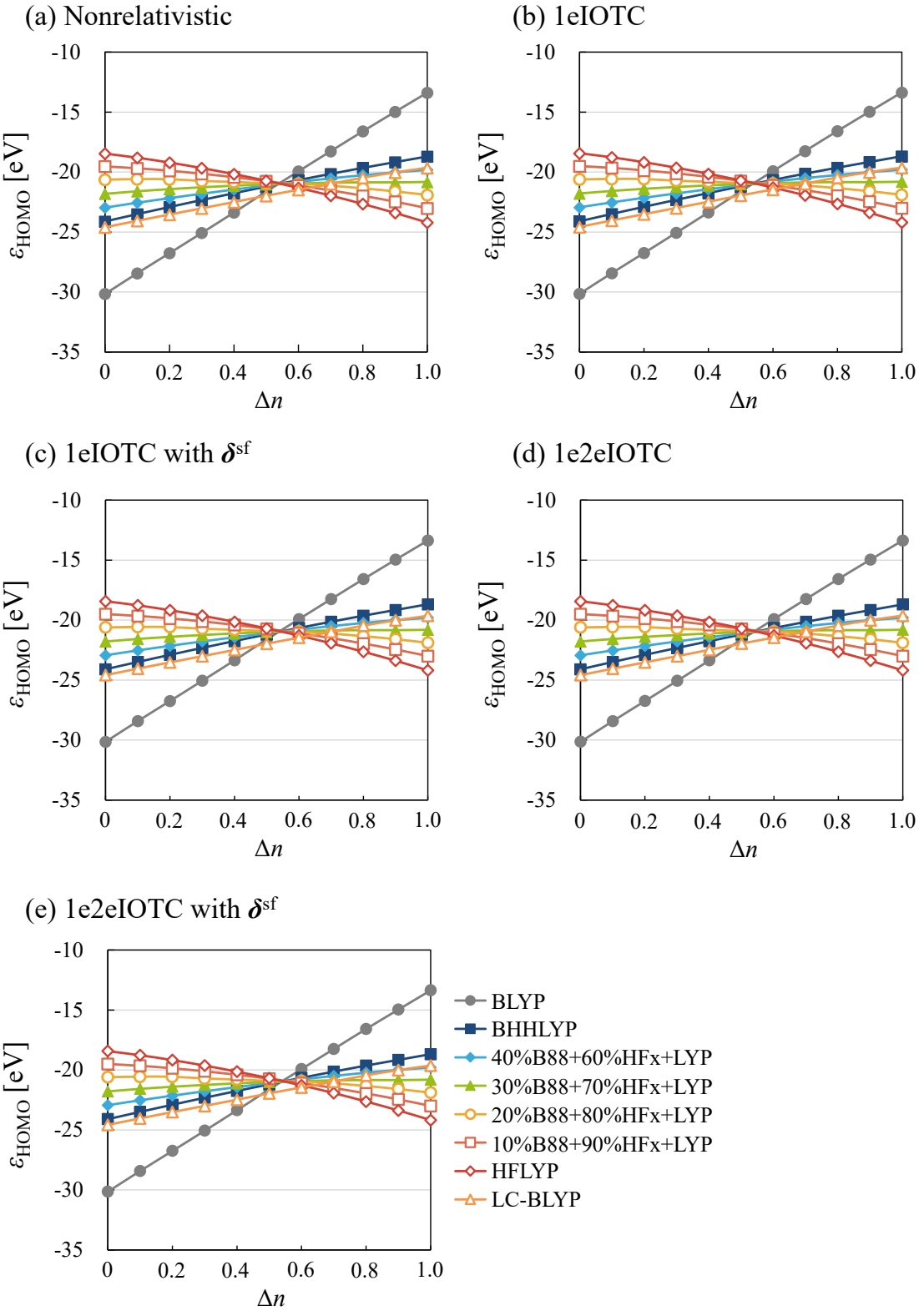

Figure 6.5. Orbital energy changes of HOMO, $\varepsilon_{\mathrm{HOMO}}$ (in eV) with respect to FON, Δn in Ne atom. Relativistic treatments are (a) nonrelativistic, (b) 1eIOTC, (c) 1eIOTC with $\boldsymbol{\delta}^{\mathrm{sf}}$, (d) 1e2eIOTC, and (e) 1e2eIOTC with $\boldsymbol{\delta}^{\mathrm{sf}}$.

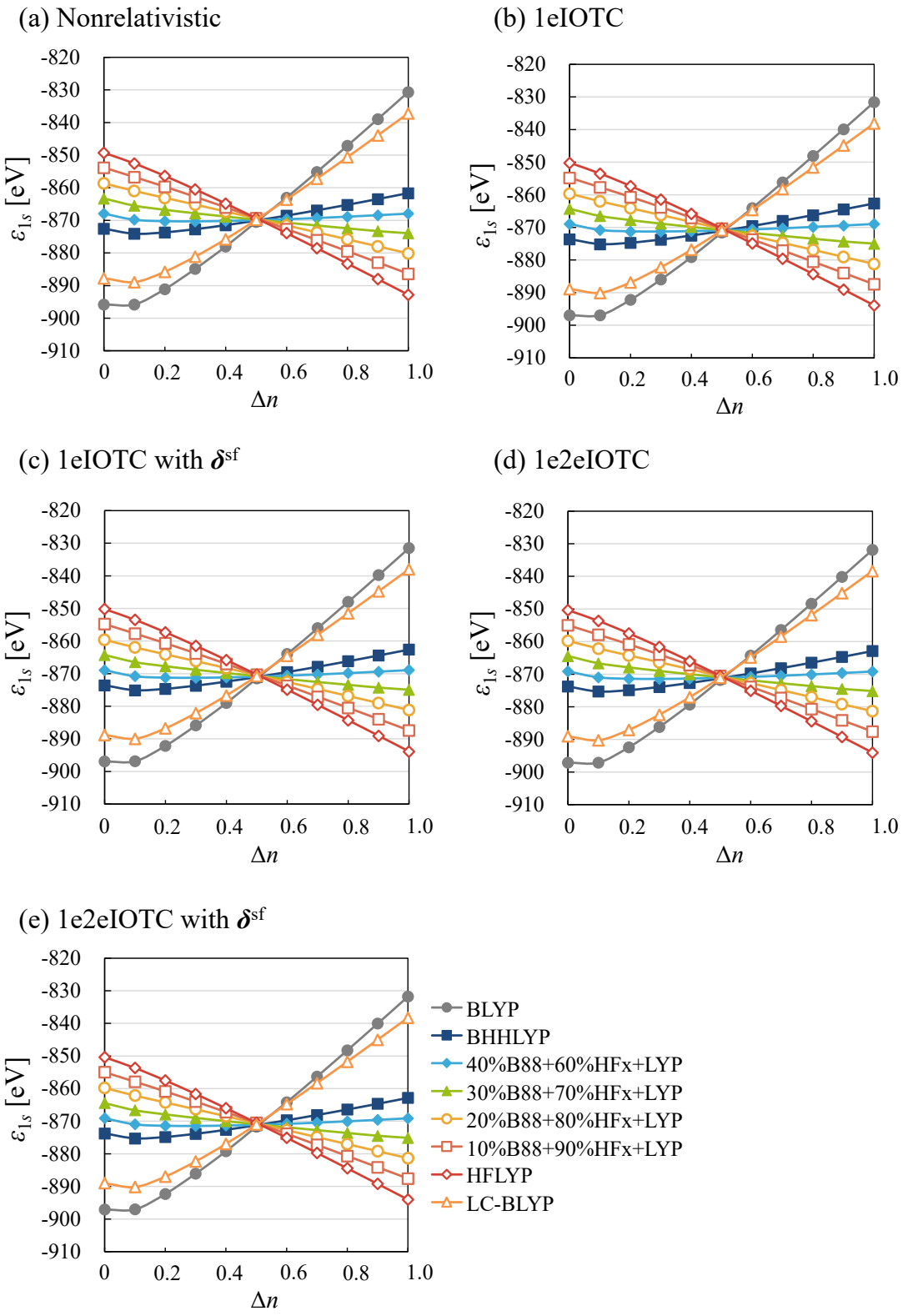

Figure 6.6. Orbital energy changes of 1*s* orbital, ε_{1s} (in eV) with respect to FON, Δn in Ne atom. Relativistic treatments are (a) nonrelativistic, (b) 1eIOTC, (c) 1eIOTC with $\boldsymbol{\delta}^{sf}$, (d) 1e2eIOTC, and (e) 1e2eIOTC with $\boldsymbol{\delta}^{sf}$.

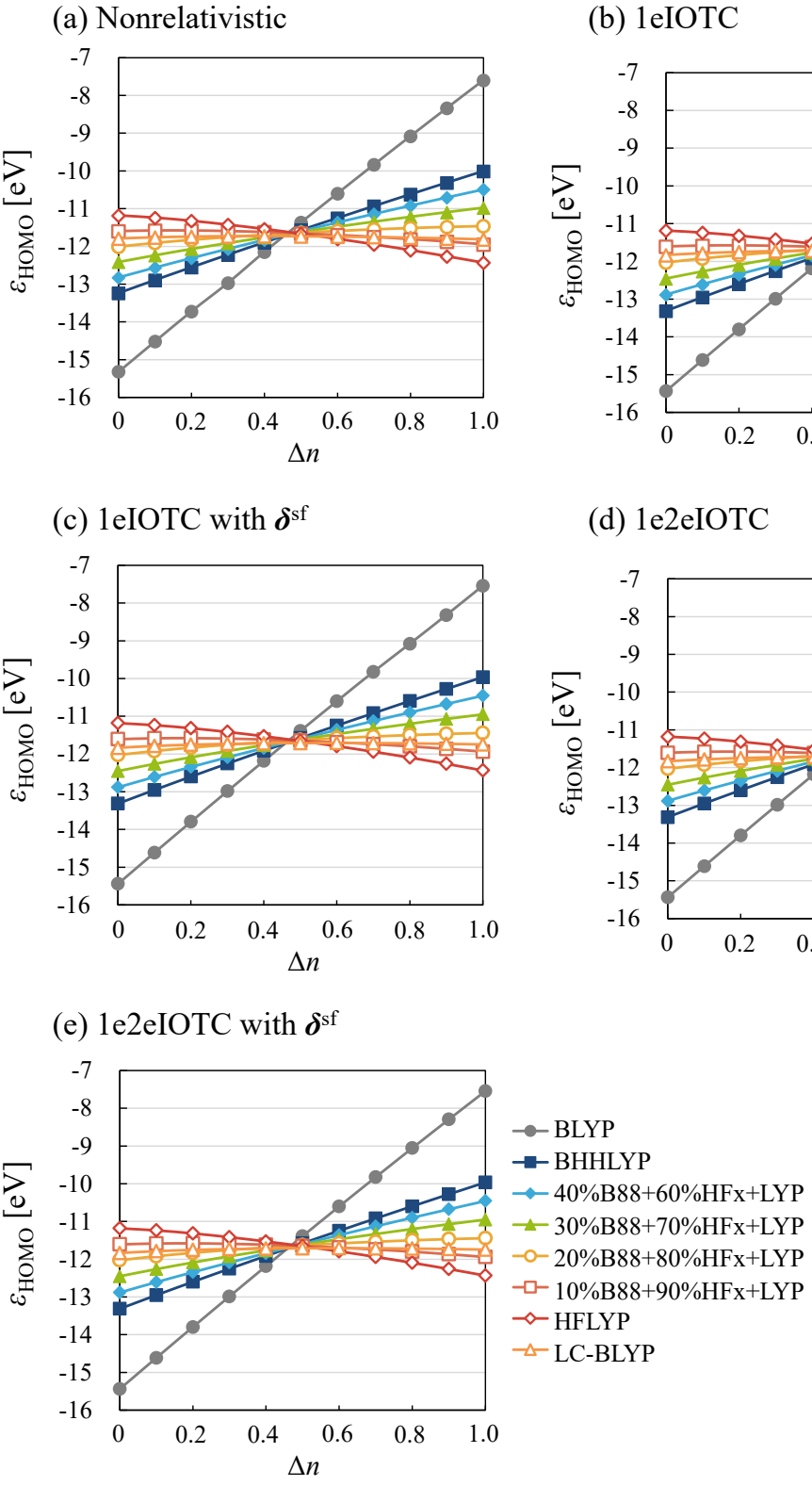

Figure 6.7. Orbital energy changes of HOMO, $\varepsilon_{\mathrm{HOMO}}$ (in eV) with respect to FON, Δn in Rn atom. Relativistic treatments are (a) nonrelativistic, (b) 1eIOTC, (c) 1eIOTC with $\boldsymbol{\delta}^{\mathrm{sf}}$, (d) 1e2eIOTC, and (e) 1e2eIOTC with $\boldsymbol{\delta}^{\mathrm{sf}}$.

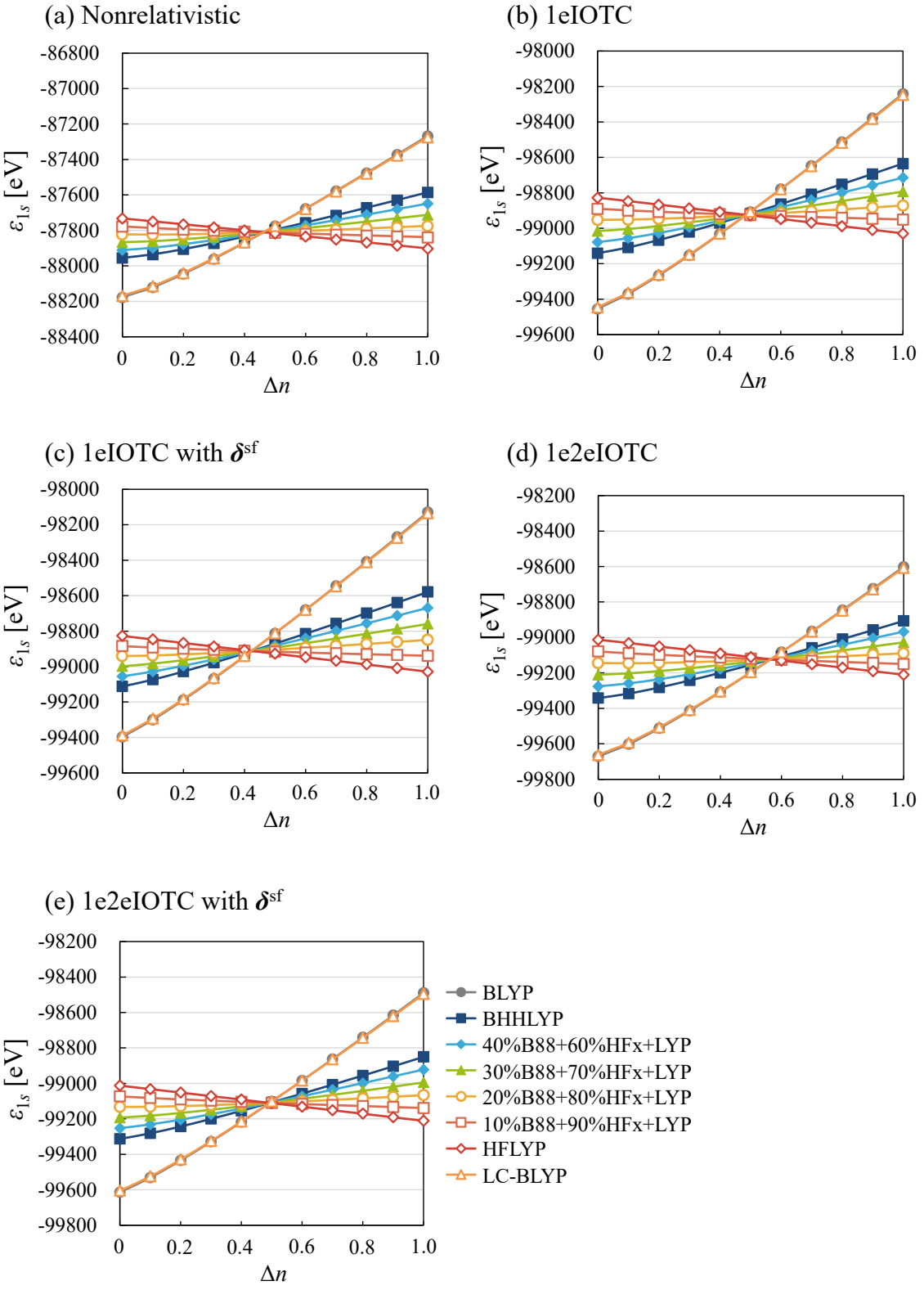

Figure 6.8. Orbital energy changes of 1*s*, ε_{1s} (in eV) with respect to FON, Δn in Rn atom. Relativistic treatments are (a) nonrelativistic, (b) 1eIOTC, (c) 1eIOTC with $\boldsymbol{\delta}^{sf}$, (d) 1e2eIOTC, and (e) 1e2eIOTC with $\boldsymbol{\delta}^{sf}$.

Table 6.1. Slopes of orbital energy change with respect to FON electron (in eV) in HOMO of Ne atoms in Figure 6.5.

	Nonrelativistic	1eIOTC	1e2eIOTC with $\boldsymbol{\delta}^{sf}$	1e2eIOTC	1e2eIOTC with $\boldsymbol{\delta}^{sf}$
BLYP	16.84	16.84	16.84	16.84	16.85
BHHLYP	5.42	5.42	5.42	5.42	5.42
40%B88+60%HFx +LYP	3.16	3.16	3.16	3.16	3.16
30%B88+70%HFx +LYP	0.96	0.96	0.96	0.96	0.96
20%B88+80%HFx +LYP	−1.25	−1.25	−1.25	−1.25	−1.25
10%B88+90%HFx +LYP	−3.49	−3.50	−3.50	−3.50	−3.50
HFLYP	−5.76	−5.76	−5.76	−5.76	−5.76
LC-BLYP	5.01	5.01	5.01	5.01	5.01

Table 6.2. Slopes of orbital energy change with respect to FON electron (in eV) in 1*s* orbital of Ne atoms in Figure 6.6.

	Nonrelativistic	1eIOTC	1e2eIOTC with $\boldsymbol{\delta}^{sf}$	1e2eIOTC	1e2eIOTC with $\boldsymbol{\delta}^{sf}$
BLYP	69.07	69.27	69.31	69.15	69.20
BHHLYP	12.45	12.48	12.51	12.42	12.45
40%B88+60%HFx +LYP	1.11	1.11	1.13	1.07	1.09
30%B88+70%HFx +LYP	−10.08	−10.12	−10.10	−10.14	−10.13
20%B88+80%HFx +LYP	−21.35	−21.42	−21.41	−21.43	−21.42
10%B88+90%HFx +LYP	−32.70	−32.80	−32.80	−32.80	−32.80
HFLYP	−44.13	−44.27	−44.27	−44.25	−44.25
LC-BLYP	54.41	54.60	54.65	54.49	54.54

Table 6.3. Slopes of orbital energy change with respect to FON electron (in eV) in HOMO of Rn atoms in Figure 6.7.

	Nonrelativistic	1eIOTC	1e2eIOTC with $\boldsymbol{\delta}^{sf}$	1e2eIOTC	1e2eIOTC with $\boldsymbol{\delta}^{sf}$
BLYP	7.74	7.90	7.88	7.90	7.90
BHHLYP	3.23	3.34	3.34	3.34	3.34
40%B88+60%HFx +LYP	2.33	2.42	2.42	2.42	2.42
30%B88+70%HFx +LYP	1.43	1.49	1.49	1.49	1.49
20%B88+80%HFx +LYP	0.53	0.57	0.57	0.57	0.57
10%B88+90%HFx +LYP	−0.36	−0.35	−0.35	−0.35	−0.35
HFLYP	−1.27	−1.27	−1.27	−1.27	−1.27
LC-BLYP	−0.03	0.08	0.08	0.08	0.08

Table 6.4. Slopes of orbital energy change with respect to FON electron (in eV) in 1*s* orbital of Rn atoms in Figure 6.8.

	Nonrelativistic	1eIOTC	1e2eIOTC with $\boldsymbol{\delta}^{sf}$	1e2eIOTC	1e2eIOTC with $\boldsymbol{\delta}^{sf}$
BLYP	927.94	1232.58	1282.72	1088.76	1139.60
BHHLYP	379.21	514.70	540.16	444.66	470.32
40%B88+60%HFx +LYP	269.49	371.29	391.70	316.00	336.56
30%B88+70%HFx +LYP	159.77	227.91	243.24	187.40	202.82
20%B88+80%HFx +LYP	50.06	84.57	94.80	58.86	69.14
10%B88+90%HFx +LYP	−59.64	−58.71	−53.63	−69.63	−64.52
HFLYP	−170.00	−202.12	−202.52	−198.23	−198.63
LC-BLYP	913.39	1217.87	1268.07	1074.04	1124.94

6.5 Conclusion

In this chapter, the PCE in the FON states of HOMO and 1*s* orbitals of noble gas atoms in the framework of the spin-free IOTC Hamiltonian was examined. Calculations of the delocalization error revealed that the FON electron states were over stabilized by relativistic treatments. The PCE of two-electron and density operators were remarkable in the core region of heavy elements: the former and the latter overestimated and underestimated the delocalization error, respectively. Corresponding to these results of total energies, the values of orbital energies and the slope of their changes to FON in core region of heavy elements were affected by PCE. The PCE of two-electron and density operators should be corrected when considering the linearity condition of total and orbital energies.

References

1. P. Hohenberg and W. Kohn, *Phys. Rev.* **136**, B864 (1964).

2. Y. Zhang and W. Yang, *J. Chem. Phys.* **109**, 2604 (1998).

3. J. Song, T. Hirosawa, T. Tsuneda, and K. Hirao, *J. Chem. Phys.* **126**, 154105 (2007).

4. J.P. Perdew, W. Yang, K. Burke, Z. Yang, E.K.U. Gross, M. Scheffler, G.E. Scuseria, T.M. Henderson, I.Y. Zhang, A. Ruzsinszky, H. Peng, J. Sun, E. Trushin, and A. Görling, *PNAS*, **114**, 2801 (2017).

5. D. Jacquemin, E.A. Perpète, G. Scalmani, M.J. Frisch, R. Kobayashi, and C. Adamo, *J. Chem. Phys.* **126**, 144105 (2007).

6. A.D. Becke, S.G. Dale, and E.R. Johnson, *J. Chem. Phys.* **148**, 211101 (2018).

7. J.P. Perdew and A. Zunger, *Phys. Rev. B*, **23**, 5048 (1981).

8. P. Mori-Sánchez, A.J. Cohen, and W. Yang, *Phys. Rev. Lett.* **100**, 146401 (2008).

9. A.J. Cohen, P. Mori-Sánchez, and W. Yang, *Science*, **321**, 792 (2008).

10. P. Mori-Sánchez, A.J. Cohen, and W. Yang, *J. Chem. Phys.* **125**, 201102 (2006).

11. T. Tsuneda, M. Kamiya, and K. Hirao, *J. Comput. Chem.* **24**, 1592 (2003).

12. O.A. Vydrov, G.E. Scuseria, J.P. Perdew, A. Ruzsinszky, and G.I. Csonka, *J. Chem. Phys.* **124**, 094108 (2006).

13. M.R. Pederson, A. Ruzsinszky, and J.P. Perdew, *J. Chem. Phys.* **140**, 121103 (2014).

14. C. Li, X. Zheng, N.Q. Su, and W. Yang, *Natl. Sci. Rev.* **5**, 203 (2017).

15. C.M. Diaz, T. Baruah, and R.R. Zope, *Phys. Rev. A* **103**, 042811 (2021).

16. K.R. Bryenton, A.A. Adeleke, S.G. Dale, and E.R. Johnson, *WIREs Comput. Mol. Sci.* **13**, (2023).

17. H. Iikura, T. Tsuneda, T. Yanai, and K. Hirao, *J. Chem. Phys.* **115**, 3540 (2001).

18. J. Heyd, G. E. Scuseria, and M. Ernzerhof, *J. Chem. Phys.* **118**, 8207 (2003).

19. O.A. Vydrov, G.E. Scuseria, and J.P. Perdew, *J. Chem. Phys.* **126**, 154109 (2007).

20. J. Song, M.A. Watson, A. Nakata, and K. Hirao, *J. Chem. Phys.* **129**, 184113 (2008).

21. A. Nakata, Y. Imamura, and H. Nakai, *J. Chem. Phys.* **125**, 064109 (2006).

22. A. Nakata, Y. Imamura, and H. Nakai, *J. Chem. Theory Comput.* **3**, 1295 (2007).

23. Y. Imamura, R. Kobayashi, and H. Nakai, *J. Chem. Phys.* **134**, 124113 (2011).

24. Y. Imamura, R. Kobayashi, and H. Nakai, *Chem. Phys. Lett.* **513**, 130 (2011).

25. Y. Imamura, R. Kobayashi, and H. Nakai, *J. Comput. Chem.* **34**, 1218 (2013).

26. Y. Imamura, K. Suzuki, T. Iizuka, and H. Nakai, *Chem. Phys. Lett.* **618**, 30 (2015).

27. C. Li, X. Zheng, A.J. Cohen, P. Mori-Sánchez, and W. Yang, *Phys. Rev. Lett.* **114**, 053001 (2015).

28. N.Q. Su, A. Mahler, and W. Yang, *J. Phys. Chem. Lett.* **11**, 1528 (2020).

29. Y. Mei, Z. Chen, and W. Yang, *J. Phys. Chem. Lett.* **11**, 10269 (2020).

30. Y. Mei, N. Yang, and W. Yang, *J. Chem. Phys.* **154**, 054302 (2021).

31. J.P. Perdew, R.G. Parr, M. Levy, and J.L. Balduz, *Phys. Rev. Lett.* **49**, 1691 (1982).

32. J.F. Janak, *Phys. Rev. B*, **18**, 7165 (1978).

33. C.-O. Almbladh and U. von Barth, *Phys. Rev. B*, **31**, 3231 (1985).

34. T. Noro, M. Sekiya, and T. Koga, *Theor. Chem. Acc.* **131**, 1124 (2012).

35. T. Noro, M. Sekiya, and T. Koga, *Theor. Chem. Acc.* **132**, 1363 (2013).

36. A.D. Becke, *Phys. Rev. A*, **38**, 3098 (1988).

37. C. Lee, W. Yang, and R.G. Parr, *Phys. Rev. B*, **37**, 785 (1988).

38. A.D. Becke, *J. Chem. Phys.* **98**, 1372 (1993).

39. M. Barysz and A.J. Sadlej, *J. Chem. Phys.* **116**, 2696 (2002).

40. J. Seino and M. Hada, *Chem. Phys. Lett.* **461**, 327 (2008).

41. T. Oyama, Y. Ikabata, J. Seino, and H. Nakai, *Chem. Phys. Lett.* **680**, 37 (2017).

42. Y. Ikabata, T. Oyama, M. Hayami, J. Seino, and H. Nakai, *J. Chem. Phys.* **150**, 164104 (2019).

43. G.M.J. Barca, C. Bertoni, L. Carrington, D. Datta, N. De Silva, J.E. Deustua, D.G. Fedorov, J.R. Gour, A.O. Gunina, E. Guidez, T. Harville, S. Irle, J. Ivanic, K. Kowalski,

S.S. Leang, H. Li, W. Li, J.J. Lutz, I. Magoulas, J. Mato, V. Mironov, H. Nakata, B.Q. Pham, P. Piecuch, D. Poole, S.R. Pruitt, A.P. Rendell, L.B. Roskop, K. Ruedenberg, T. Sattasathuchana, M.W. Schmidt, J. Shen, L. Slipchenko, M. Sosonkina, V. Sundriyal, A. Tiwari, J.L. Galvez Vallejo, B. Westheimer, M. Włoch, P. Xu, F. Zahariev, and M.S. Gordon, *J. Chem. Phys.* **152**, 154102 (2020).

Appendix

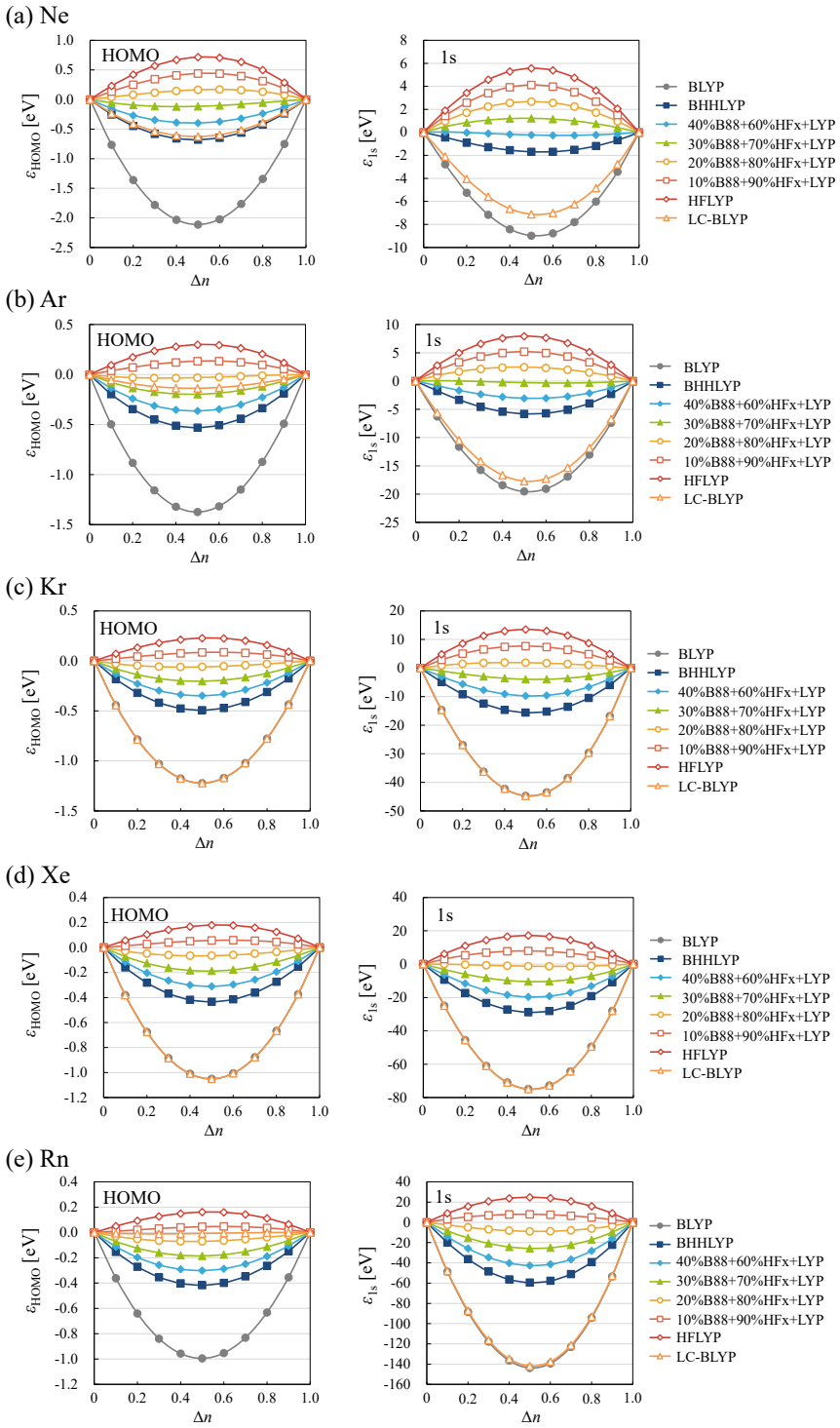

Figure A6.1. Total energy deviation (in eV) from ideal energy of FON states of HOMO (left panels) and 1*s* orbital (right panels) in (a) Ne, (b) Ar, (c) Kr, (d) Xe, and (e) Rn atoms obtained with 1e2eIOTC with $\boldsymbol{\delta}^{\mathrm{sf}}$.

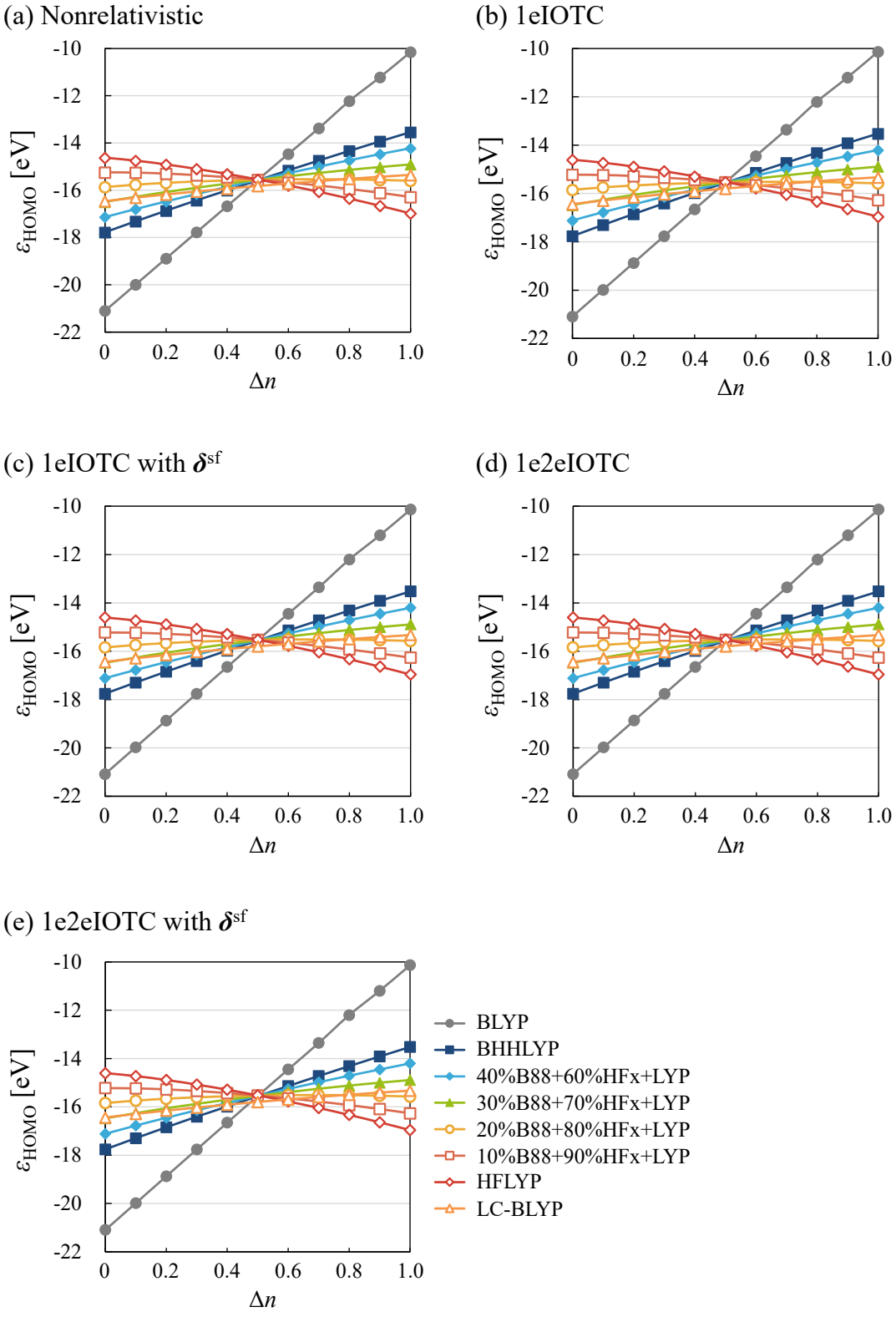

Figure A6.2. Orbital energy changes of HOMO, $\varepsilon_{\mathrm{HOMO}}$ (in eV) with respect to FON, Δn in Ar atom. Relativistic treatments are (a) nonrelativistic, (b) 1eIOTC, (c) 1eIOTC with $\boldsymbol{\delta}^{\mathrm{sf}}$, (d) 1e2eIOTC, and (e) 1e2eIOTC with $\boldsymbol{\delta}^{\mathrm{sf}}$.

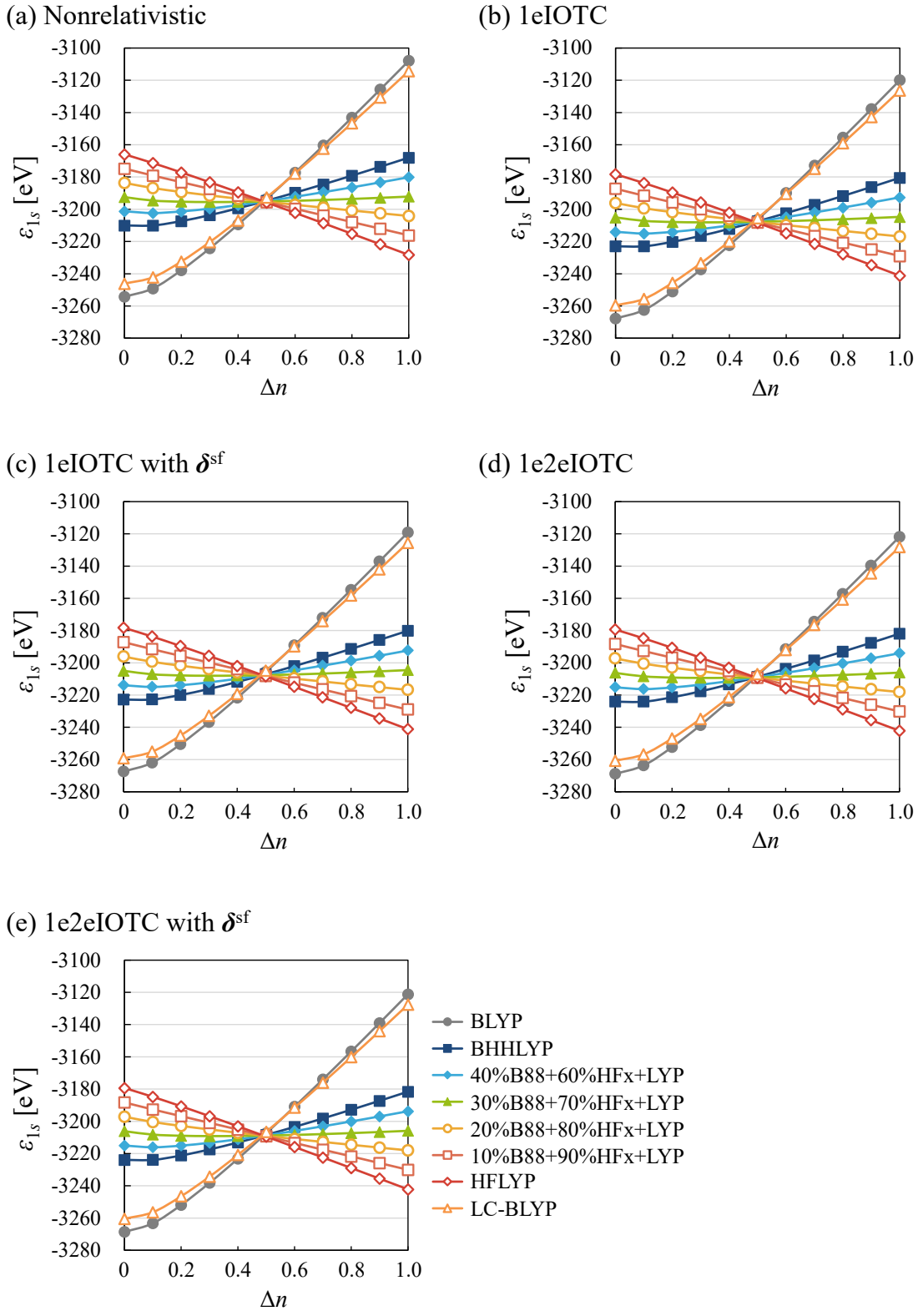

Figure A6.3. orbital energy changes of 1*s* orbital, ε_{1s} (in eV) with respect to FON, Δn in Ar atom. Relativistic treatments are (a) nonrelativistic, (b) 1eIOTC, (c) 1eIOTC with $\boldsymbol{\delta}^{sf}$, (d) 1e2eIOTC, and (e) 1e2eIOTC with $\boldsymbol{\delta}^{sf}$.

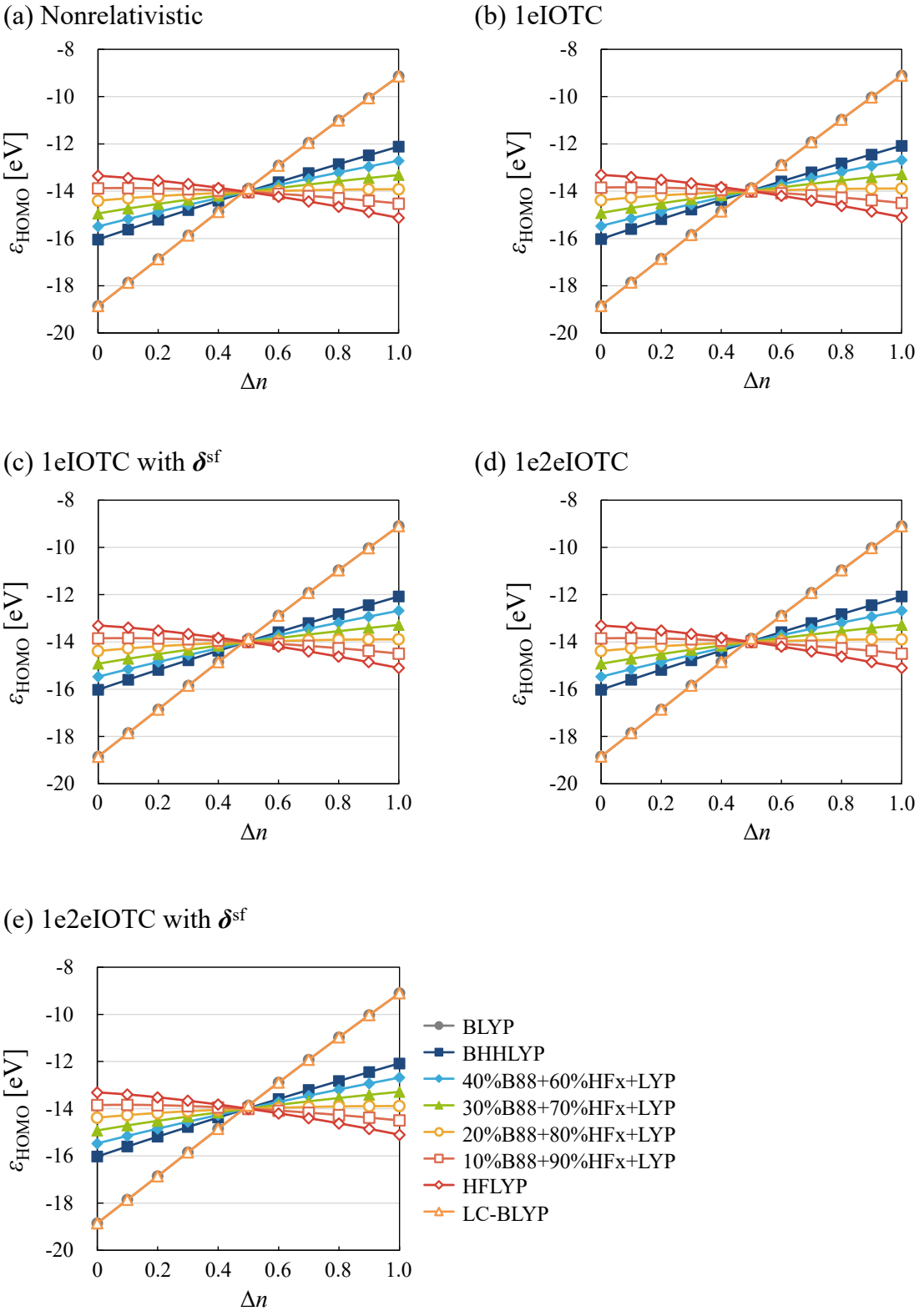

Figure A6.4. Orbital energy changes of HOMO, $\varepsilon_{\mathrm{HOMO}}$ (in eV) with respect to FON, Δn in Kr atom. Relativistic treatments are (a) nonrelativistic, (b) 1eIOTC, (c) 1eIOTC with $\boldsymbol{\delta}^{\mathrm{sf}}$, (d) 1e2eIOTC, and (e) 1e2eIOTC with $\boldsymbol{\delta}^{\mathrm{sf}}$.

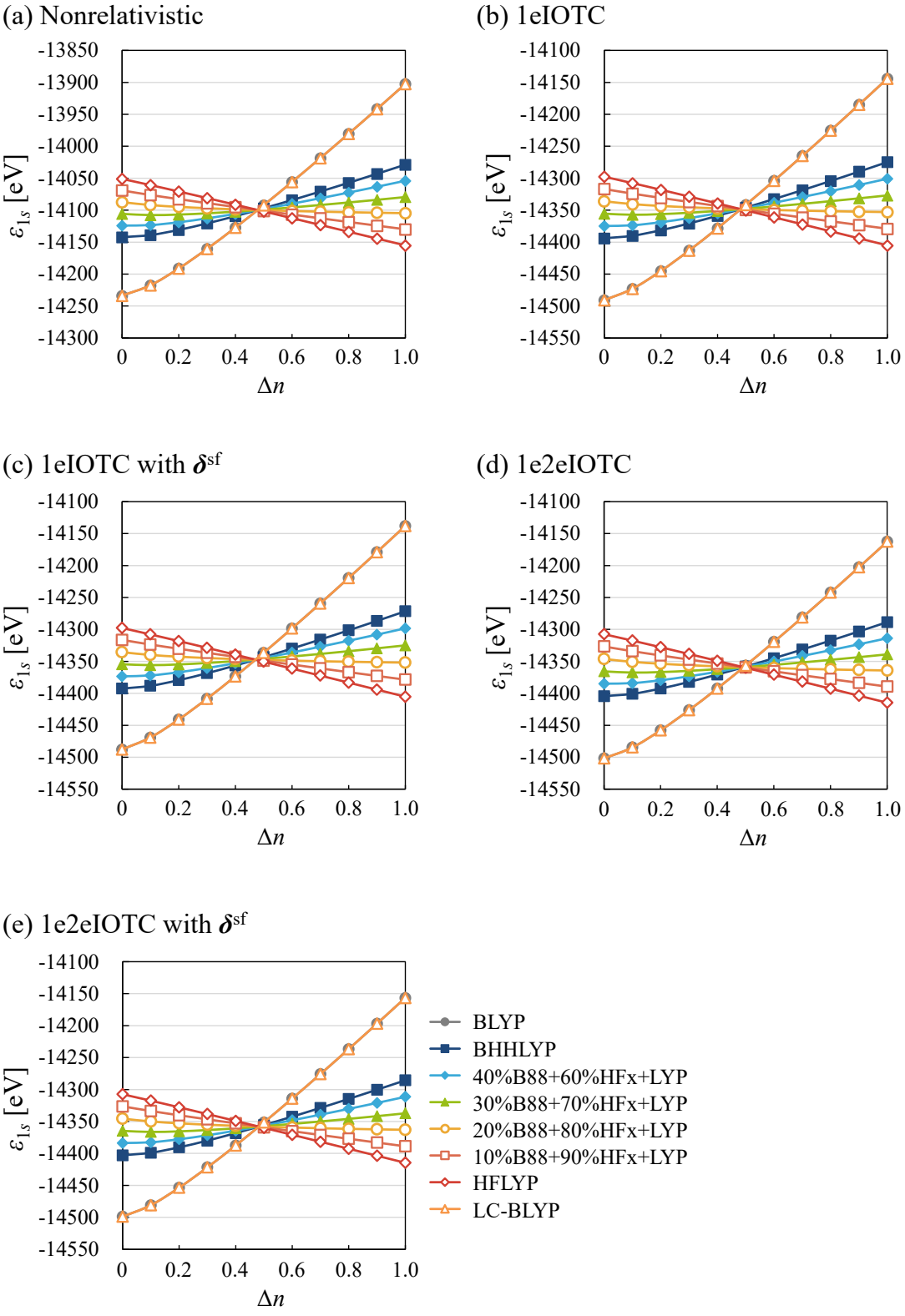

Figure A6.5. Orbital energy changes of 1*s* orbital, ε_{1s} (in eV) with respect to FON, Δn in Kr atom. Relativistic treatments are (a) nonrelativistic, (b) 1eIOTC, (c) 1eIOTC with $\boldsymbol{\delta}^{\mathrm{sf}}$, (d) 1e2eIOTC, and (e) 1e2eIOTC with $\boldsymbol{\delta}^{\mathrm{sf}}$.

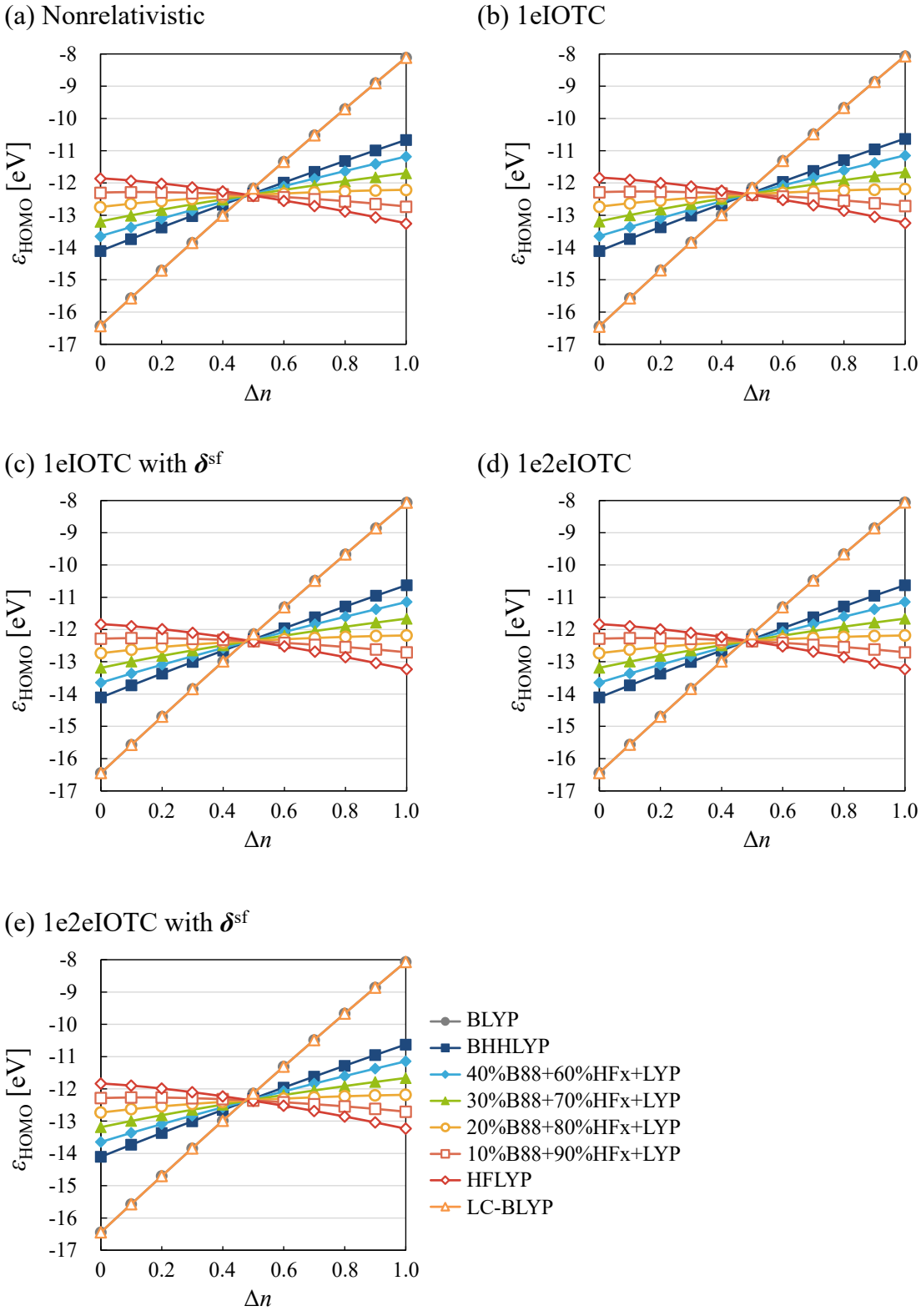

Figure A6.6. Orbital energy changes of HOMO, ε_{HOMO} (in eV) with respect to FON, Δn in Xe atom. Relativistic treatments are (a) nonrelativistic, (b) 1eIOTC, (c) 1eIOTC with $\boldsymbol{\delta}^{sf}$, (d) 1e2eIOTC, and (e) 1e2eIOTC with $\boldsymbol{\delta}^{sf}$.

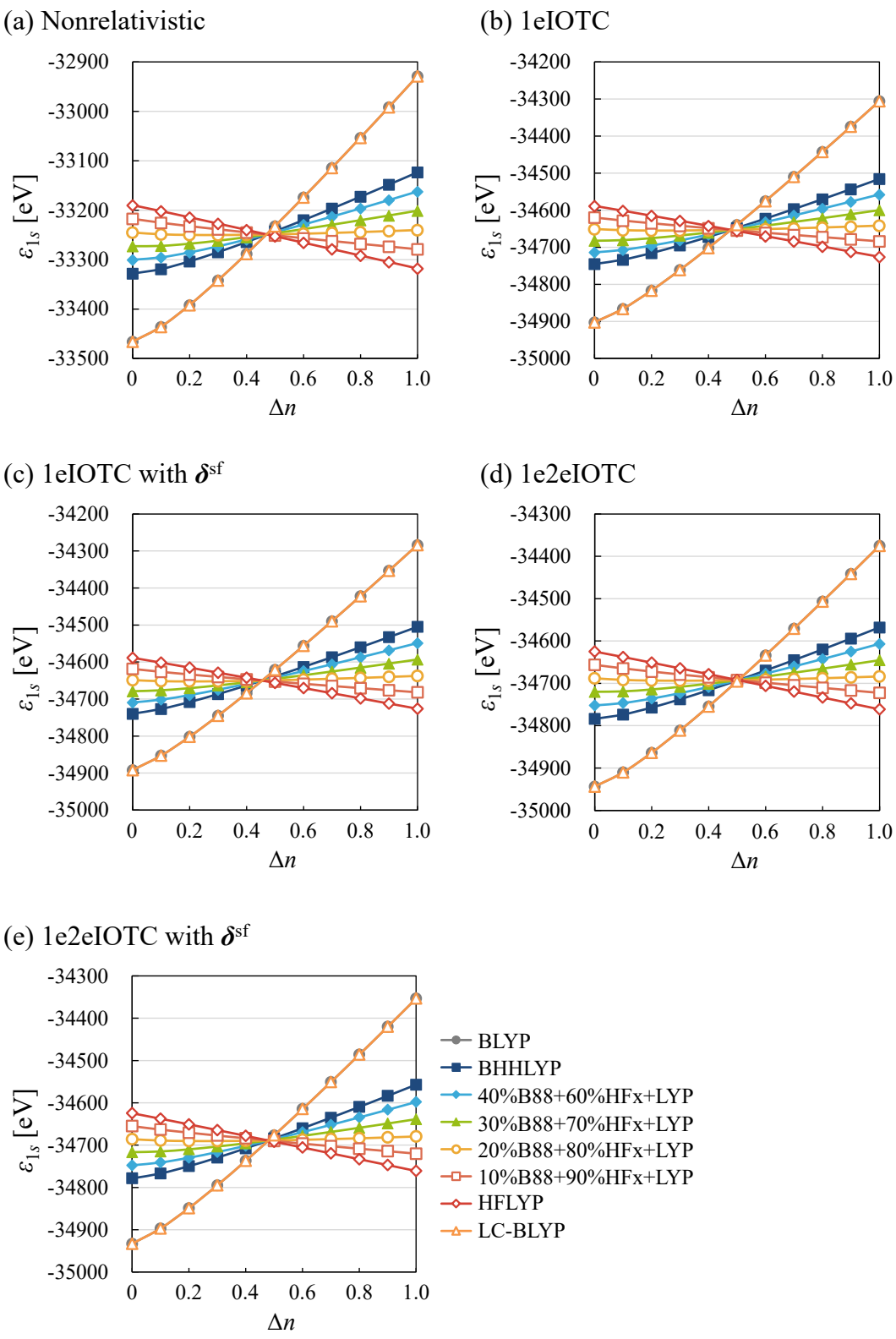

Figure A6.7. Orbital energy changes of 1*s* orbital, ε_{1s} (in eV) with respect to FON, Δn in Xe atom. Relativistic treatments are (a) nonrelativistic, (b) 1eIOTC, (c) 1eIOTC with $\boldsymbol{\delta}^{\mathrm{sf}}$, (d) 1e2eIOTC, and (e) 1e2eIOTC with $\boldsymbol{\delta}^{\mathrm{sf}}$.

Table A6.1. Slopes of orbital energy change with respect to FON electron (in eV) in HOMO of Ar atoms in Figure A6.2.

	Nonrelativistic	1eIOTC	1e2eIOTC with $\boldsymbol{\delta}^{sf}$	1e2eIOTC	1e2eIOTC with $\boldsymbol{\delta}^{sf}$
BLYP	10.99	10.99	10.99	10.99	10.99
BHHLYP	4.23	4.23	4.23	4.23	4.23
40%B88+60%HFx +LYP	2.91	2.91	2.91	2.91	2.91
30%B88+70%HFx +LYP	1.58	1.58	1.58	1.58	1.58
20%B88+80%HFx +LYP	0.26	0.26	0.26	0.26	0.26
10%B88+90%HFx +LYP	−1.06	−1.06	−1.06	−1.06	−1.06
HFLYP	−2.38	−2.38	−2.38	−2.38	−2.38
LC-BLYP	1.10	1.11	1.11	1.11	1.11

Table A6.2. Slopes of orbital energy change with respect to FON electron (in eV) in 1*s* orbital of Ar atoms in Figure A6.3.

	Nonrelativistic	1eIOTC	1e2eIOTC with $\boldsymbol{\delta}^{sf}$	1e2eIOTC	1e2eIOTC with $\boldsymbol{\delta}^{sf}$
BLYP	151.75	153.25	153.56	152.43	152.74
BHHLYP	44.43	44.84	45.01	44.47	44.65
40%B88+60%HFx +LYP	22.98	23.19	23.32	22.90	23.03
30%B88+70%HFx +LYP	1.54	1.54	1.63	1.34	1.44
20%B88+80%HFx +LYP	−19.88	−20.09	−20.03	−20.20	−20.13
10%B88+90%HFx +LYP	−41.31	−41.74	−41.71	−41.75	−41.72
HFLYP	−62.74	−63.38	−63.38	−63.30	−63.30
LC-BLYP	137.10	138.58	138.89	137.76	138.07

Table A6.3. Slopes of orbital energy change with respect to FON electron (in eV) in HOMO of Kratoms in Figure A6.4.

	Nonrelativistic	1eIOTC	1e2eIOTC with $\boldsymbol{\delta}^{sf}$	1e2eIOTC	1e2eIOTC with $\boldsymbol{\delta}^{sf}$
BLYP	9.74	9.77	9.77	9.77	9.78
BHHLYP	3.92	3.94	3.94	3.94	3.94
40%B88+60%HFx +LYP	2.77	2.78	2.78	2.78	2.78
30%B88+70%HFx +LYP	1.62	1.63	1.63	1.63	1.63
20%B88+80%HFx +LYP	0.48	0.48	0.48	0.48	0.48
10%B88+90%HFx +LYP	−0.67	−0.67	−0.67	−0.67	−0.67
HFLYP	−1.80	−1.81	−1.81	−1.81	−1.81
LC-BLYP	9.74	9.77	9.77	9.77	9.78

Table A6.4. Slopes of orbital energy change with respect to FON electron (in eV) in 1*s* orbital of Kr atoms in Figure A6.5.

	Nonrelativistic	1eIOTC	1e2eIOTC with $\boldsymbol{\delta}^{sf}$	1e2eIOTC	1e2eIOTC with $\boldsymbol{\delta}^{sf}$
BLYP	340.78	356.00	358.80	348.40	351.21
BHHLYP	117.91	123.77	125.19	120.15	121.58
40%B88+60%HFx +LYP	73.36	77.36	78.49	74.54	75.68
30%B88+70%HFx +LYP	28.82	30.95	31.81	28.95	29.80
20%B88+80%HFx +LYP	−15.72	−15.45	−14.88	−16.65	−16.09
10%B88+90%HFx +LYP	−60.25	−61.82	−61.54	−62.23	−61.95
HFLYP	−104.60	−108.03	−108.04	−107.63	−107.64
LC-BLYP	340.78	356.00	358.80	348.40	351.21

Table A6.5. Slopes of orbital energy change with respect to FON electron (in eV) in HOMO of Xe atoms in Figure A6.6.

	Nonrelativistic	1eIOTC	1e2eIOTC with $\boldsymbol{\delta}^{sf}$	1e2eIOTC	1e2eIOTC with $\boldsymbol{\delta}^{sf}$
BLYP	8.32	8.38	8.38	8.39	8.39
BHHLYP	3.43	3.47	3.47	3.47	3.47
40%B88+60%HFx +LYP	2.46	2.49	2.49	2.49	2.49
30%B88+70%HFx +LYP	1.49	1.51	1.51	1.51	1.51
20%B88+80%HFx +LYP	0.52	0.54	0.54	0.54	0.54
10%B88+90%HFx +LYP	−0.44	−0.44	−0.44	−0.44	−0.44
HFLYP	−1.42	−1.42	−1.42	−1.42	−1.42
LC-BLYP	8.32	8.38	8.38	8.39	8.39

Table A6.6. Slopes of orbital energy change with respect to FON electron (in eV) in 1*s* orbital of Xe atoms in Figure A6.7.

	Nonrelativistic	1eIOTC	1e2eIOTC with $\boldsymbol{\delta}^{sf}$	1e2eIOTC	1e2eIOTC with $\boldsymbol{\delta}^{sf}$
BLYP	550.33	609.40	619.62	581.17	591.47
BHHLYP	211.04	235.47	240.60	221.84	226.99
40%B88+60%HFx +LYP	143.07	160.68	164.82	150.00	154.14
30%B88+70%HFx +LYP	75.14	85.93	89.06	78.19	81.30
20%B88+80%HFx +LYP	7.21	11.24	13.31	6.42	8.49
10%B88+90%HFx +LYP	−60.72	−63.45	−62.43	−65.34	−64.31
HFLYP	−128.42	−137.81	−137.87	−136.75	−136.81
LC-BLYP	550.33	609.40	619.62	581.17	591.47

Chapter 7 Implementation of PCC method into GAMESS program**

7.1 Introduction

The spin-free 2c Hamiltonian is so to speak one-component Hamiltonian, because it ignores the spin-dependent term of 2c Hamiltonian. In terms of implementation, the spin-free 2c Hamiltonian can be handled with only a few corrections for nonrelativistic quantum chemical calculations. Therefore, the spin-free 2c relativistic Hamiltonians for one-electron operator are available in several quantum chemical program packages, such as GAMESS,[1] ORCA,[2] NWChem,[3] TURBOMOLE,[4] CFOUR,[5] MOLCAS,[6,7] and so on. Nakai group has also implemented the LUT scheme based on the IOTC Hamiltonian into GAMESS program.[8] The LUT-IOTC Hamiltonian is available with not only SCF calculations but also electron correlation methods such as MP2 and CC, DFT, DC[9,10] for large-scale calculations, and geometry optimization by analytical energy gradient. However, the PCC for two-electron operator is necessary to pursue the accuracy close to that of the 4c Hamiltonian. The density operator also requires the PCC in the case of 2c DFT. In this chapter, the IOTC transformation with and without the LUT scheme for two-electron[11,12] and density operators[13] is implemented into the public version of GAMESS program. The remainder of this chapter is organized as follows: Sec. 7.2 explains the details of the implementation. The numerical assessments are presented in the Sec. 7.3. The conclusion of this chapter is provided in the Sec. 7.4.

** The parts of the contents of this chapter are reproduced from the article by Chinami Takashima, Junji Seino, and Hiromi Nakai, *J. Comput. Chem. Jpn.* **19**, 128 (2020). Copyright 2021 Society of Computer Chemistry, Japan. DOI: 10.2477/jccj.2021-0002

7.2 Implementation

Figure 7.1 shows the algorithm for the energy calculation by PCC method. The Coulomb-interaction is adopted as a two-electron operator. The IOTC transformation of the two-electron operator requires three kinds of TEIs in Eq. (2.3.25)–(2.3.27). The evaluation of TEIs for PBFs, namely, the Coulomb-like $\langle k_a k_b | 1/r_{ij} \mathbf{1}_2 | k_c k_d \rangle$, Darwin-like $\langle k_a k_b | \boldsymbol{p}_i 1/r_{ij} \mathbf{1}_2 \cdot \boldsymbol{p}_i | k_c k_d \rangle$, and specific spin-free interaction terms $\langle k_a k_b | \boldsymbol{p}_i \left[\boldsymbol{p}_j 1/r_{ij} \mathbf{1}_2 \cdot \boldsymbol{p}_j \right] \cdot \boldsymbol{p}_i | k_c k_d \rangle$, are implemented. The program code for the Coulomb-like term is similar to that for the nonrelativistic TEIs, which evaluates the TEIs of the Coulomb operator. Focusing on the momentum of operator, $\boldsymbol{p} = -i\nabla$, the Darwin-like and specific spin-free interaction terms are rewritten as

$$\langle k_a k_b | \boldsymbol{p}_1 1/r_{12} \mathbf{1}_2 \cdot \boldsymbol{p}_1 | k_c k_d \rangle = \langle \nabla_{\mathbf{r}_1} k_a k_b | 1/r_{12} \mathbf{1}_2 | \nabla_{\mathbf{r}_1} k_c k_d \rangle \tag{7.2.1}$$

and

$$\langle k_a k_b | \boldsymbol{p}_1 \left[\boldsymbol{p}_2 1/r_{12} \mathbf{1}_2 \cdot \boldsymbol{p}_2 \right] \cdot \boldsymbol{p}_1 | k_c k_d \rangle = \langle \nabla_{\mathbf{r}_1} k_a \nabla_{\mathbf{r}_2} k_b | 1/r_{12} \mathbf{1}_2 | \nabla_{\mathbf{r}_1} k_c \nabla_{\mathbf{r}_2} k_d \rangle . \tag{7.2.2}$$

Because the basis sets applied in GAMESS program is Gaussian-type functions, $\{k\}$ is represented by Gaussian-type functions. Therefore, $\nabla_{\mathbf{r}_1} k_a$ is also expressed by Gaussian-type functions that have different angular momenta from those of k_a as referred in Chapter 5. The codes for evaluating the Darwin-like and specific spin-free interaction terms are similar to that used for $\langle k_a k_b | 1/r_{12} \mathbf{1}_2 | k_c k_d \rangle$. The implementation of these TEIs was based on Gauss-Rys quadrature codes. The transformations of these TEIs are implemented by modifying the existence codes for (LUT-)IOTC for one-electron operator.

For the calculation of PCC of density operator, the OEIs appeared in Eq. (2.3.35) were additionally required for the calculation of electron density. The direct calculation of Eq. (2.3.35) demands the transformation of matrix. According to Eqs. (2.3.43) and (2.3.44),

these OEIs are obtained by the product of transformed AOs shown in Eqs. (2.3.41) and (2.3.42), namely the inner product of vectors. The practical implementation adopted simpler codes using the vector expression instead of the matrix transformation. The gradient of electron density and kinetic energy density shown in Eqs. (2.3.46) and (2.3.48) are also implemented according to the expression of inner product of vectors. As shown in Eq. (2.3.53), the exchange-correlation integral has also different formula from that does not consider PCC. The routine for adding the exchange-correlation term in the construction of Fock matrix was modified along the Eq. (2.3.53).

Table 7.1 summarizes the major capabilities of the IOTC Hamiltonian in GAMESS program. The (LUT-)IOTC Hamiltonian for one-electron term is denoted as 1e(LUT-)IOTC and that for one- and two-electron terms is denoted as 1e2e(LUT-)IOTC. The present implementation enables electron correlation methods and the DC method based on the 1e2e(LUT-)IOTC. Furthermore, the analytical energy gradient is also available for LUT-IOTC because the nuclear-coordinate derivative of TEIs in the LUT scheme is the same as that of nonrelativistic method.

Figure 7.2 shows the sample input of the energy calculation of PCC-DFT based on the LUT-IOTC Hamiltonian. The 1e2eLUT-IOTC Hamiltonian are available by specifying "RELWFN=LUTIOTC2" in the $CONTRL name list, which sets the fundamental job options. In addition, the PCC of density operator can be performed by adding "PCCDFT=.T." to the $RELWFN name list, which specifies the details of relativistic treatments, for example, the speed of light and threshold τ for one-electron LUT scheme. Keywords for another options for IOTC Hamiltonians are tabulated in Table 7.1.

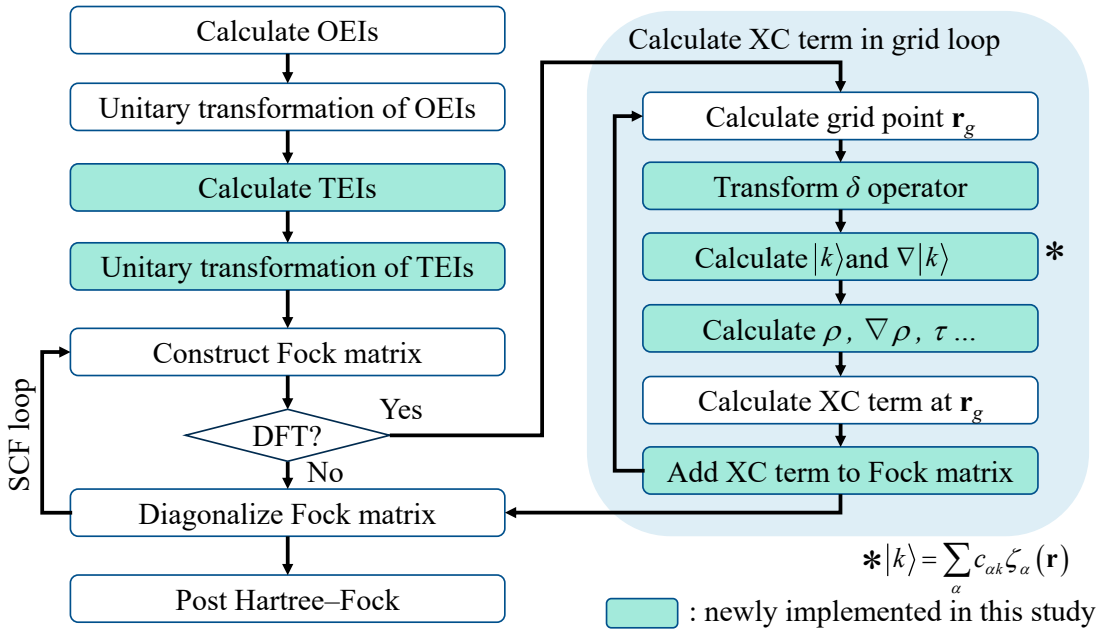

Figure 7.1. Schematic diagram of the algorithm for the energy calculation by PCC method. Items colored in green are the implemented parts in this chapter.

Table 7.1. Major capabilities of IOTC Hamiltonian in GAMESS. ✔ represents the previous work. ★ indicates the options that can be possible by the implementation of this chapter.

Hamiltonian	Keyword	Energy	Analytical gradient	Correlation (MP2, CC)	DC
1eIOTC	RELWFN=IOTC	✔	×	✔	✔
1eLUT-IOTC	RELWFN=LUT-IOTC	✔	✔	✔	✔
1e2eIOTC	RELWFN=IOTC2E	★	×	★	★
1e2eLUT-IOTC	RELWFN=LUTIOTC2	★	★	★	★
(LUT-)IOTC for $\boldsymbol{\delta}^{\mathrm{sf}}$	PCCDFT=.T.	★	★	-	-

```
 $CONTRL SCFTYP=RHF RUNTYP=ENERGY
  RELWFN=LUTIOTC2 DFTTYP=BLYP $END
 $RELWFN PCCDFT=.T. $END
 $BASIS GBASIS=SPKrDZC $END
 $DATA
 Sample input
C1
H    1.0   -0.46355   8.99463 0.00000
At  85.0   -1.61980  -0.92024 0.00000
...
 $END
```

Figure 7.2. Sample input of energy calculation of the PCC-DFT based on the LUT-IOTC method.

7.3 Numerical assessments

7.3.1 Accuracy

Table 7.2 shows the deviations in total energy from the 4c results at the BLYP[14,15]/Sapporo(-DKH3)-DZP-2012[16–18] level for diatomic molecules: CuH, Cu_2, AgH, Ag_2, AuH, and Au_2, whose bond distances were set to 1.4658, 2.2192, 1.6179, 2.5303, 1.5324, and 2.4719, respectively. The nonrelativistic, 1eIOTC, and 1e2eIOTC Hamiltonians were adopted. The effects of PCC for density operator by IOTC transformation $\boldsymbol{\delta}^{\mathrm{sf}}$ were also examined. Nonrelativistic Hamiltonian gives large deviations from 4c results. On the other hand, 1e2eIOTC with $\boldsymbol{\delta}^{\mathrm{sf}}$ showed an error of 0.007 hartree even for Au_2, which has the largest relativistic effects, and gives good agreement with 4c results in all molecules. The effects of PCC for two-electron Coulomb term and density operator are essential to obtain accurate results; The difference between 1eIOTC and 1e2eIOTC are several hartree as well as that between 1e2eIOTC with and without $\boldsymbol{\delta}^{\mathrm{sf}}$. In particular, 1eIOTC with $\boldsymbol{\delta}^{\mathrm{sf}}$ provides larger error than 1eIOTC without $\boldsymbol{\delta}^{\mathrm{sf}}$, which is due to the error cancellation from negative deviation of 1e2eIOTC Hamiltonian. The importance of comprehensive transformation of all operators was confirmed.

Table 7.3 shows the the error caused by the LUT scheme. The errors in all molecules are less than 1 millihartree and quite smaller than the deviation from 4c values shown in Table 7.2. The validity of the approximation of LUT scheme was confirmed.

Table 7.2. Total energy deviation (in hartree) of nonrelativistic and IOTC Hamiltonian from 4c Hamiltonian in the calculations of dimers of coinage metals, CuH, Cu_2, AgH, Ag_2, AuH, Au_2. IOTC transformations for one-electron (1e), two-electron (2e), and density operators ($\boldsymbol{\delta}^{sf}$) were examined. BLYP functional and uncontracted Sapporo(-DKH3)-DZP-2012 basis sets were applied. The reference 4c values are shown in parentheses.

	Nonrel.	1eIOTC	1eIOTC with $\boldsymbol{\delta}^{sf}$	1e2eIOTC	1e2eIOTC with $\boldsymbol{\delta}^{sf}$	(4c)
CuH	14.587504	0.275606	0.490224	−0.215161	−0.000194	(−1655.820950)
Cu_2	29.170984	0.551139	0.980329	−0.430280	−0.000391	(−3310.509041)
AgH	117.033352	1.490758	2.469700	−0.983365	−0.001923	(−5317.695585)
Ag_2	234.057976	2.981425	4.939251	−1.966657	−0.003834	(−10634.277804)
AuH	1158.437895	9.580662	15.360145	−5.808337	−0.003498	(−19028.891526)
Au_2	2316.820851	19.160914	30.719593	−11.616401	−0.007012	(−38056.629824)

Table 7.3. The deviation (in hartree) of total energy obtained by LUT-IOTC Hamiltonian from that obtained by IOTC Hamiltonian without LUT scheme. Transformations for one-electron (1e), two-electron (2e), and density operators ($\boldsymbol{\delta}$) were examined. BLYP functional and uncontracted Sapporo(-DKH3)-DZP-2012 basis sets were applied.

	1e	1e and $\boldsymbol{\delta}$	1e and 2e	1e, 2e, and $\boldsymbol{\delta}$
CuH	−0.000002	−0.000002	−0.000007	−0.000007
Cu_2	0.000000	0.000000	−0.000014	−0.000014
AgH	−0.000002	−0.000002	0.000004	0.000004
Ag_2	−0.000006	−0.000006	−0.000007	−0.000008
AuH	−0.000014	−0.000014	−0.000017	−0.000017
Au_2	0.000024	0.000024	0.000022	0.000022

7.3.2 Efficiency

Table 7.3 compares the CPU times of calculations of $Ir(ppy)_3$ using LUT-IOTC Hamiltonians at the PBE0[19]/Sapporo(-DKH3)-DZP-2012 level. LUT-IOTC transformation for one-electron, two-electron, and density operator was examined. For comparison, the CPU times for the nonrelativistic treatment are also given. The total CPU times and the components of time-consuming steps, namely, evaluation and transformation of TEIs and the first SCF cycle are shown. For measurement of the CPU times, one CPU core of Intel® Xeon® Gold 5122/3.60 GHz was used. The numbers of total SCF cycles were 39 and 31 for the nonrelativistic and LUT-IOTC calculations, respectively. The DFT calculations with the fine Lebedev grid (96 radial and 302 angular points) were performed in 15 cycles for nonrelativistic Hamiltonian, 14 cycles for 1e2eLUT-IOTC w/ $\boldsymbol{\delta}^{\mathrm{LUT}}$, and 13 cycles for others. In 1eLUT-IOTC Hamiltonian, the CPU times of TEIs and SCF are similar to those in the nonrelativistic Hamiltonian. In 1e2eLUT-IOTC with and without $\boldsymbol{\delta}^{\mathrm{LUT}}$, the CPU times of TEIs are approximately 16% larger than the others because of the use of local transformation. Using $\boldsymbol{\delta}^{\mathrm{LUT}}$ (i.e. in the calculation by 1eLUT-IOTC with $\boldsymbol{\delta}^{\mathrm{LUT}}$ and 1e2eLUT-IOTC w/ $\boldsymbol{\delta}^{\mathrm{LUT}}$), the CPU times of SCF are larger than those in the others. This is because the transformation for density operator is performed in all grid points. The 4c calculation was difficult in the present computing environment. In consequence, the most accurate calculation using 1e2eLUT-IOTC Hamiltonian with $\boldsymbol{\delta}^{\mathrm{LUT}}$ can be accomplished within three times of CPU times of nonrelativistic treatment.

Figure 7.3 provides the system-size dependence of CPU time for calculations of $(HF)_n$ molecules by the Hartree–Fock, MP2, CCSD, and CCSD(T) methods combined with the DC method. The intra and intermolecular distances of HF were fixed at 0.907 and 1.503 Å, respectively. The bond angles of H–F–H and F–H–F were set to 120° and 180°, respectively. Figure 7.3(a) shows the results obtained by nonrelativistic Hamiltonian. Figure 7.3(b) presents the results of the 1e2eIOTC Hamiltonian. For DC calculations, LUT scheme was

adopted in Figure 7.3(b). The DC method drastically reduced the CPU time and the order of scaling of the CPU time. Combination of DC and LUT provides similar results to those of the nonrelativistic calculation. Here, the CPU time for the DC-MP2 is shorter than that for DC-Hartree–Fock (DC-HF). DC-CCSD and DC-CCSD(T) show the smaller scales of the CPU times comparing with DC-HF. These results are owing to the dual buffer treatment, which utilizes the fact that the correlation energies are more localized than Coulomb and exchange energies.

Table 7.3. CPU time (in s) for calculation of $Ir(ppy)_3$ by nonrelativistic and LUT-IOTC Hamiltonians. LUT-IOTC transformation for one-electron (1e), two-electron (2e), and density operator ($\boldsymbol{\delta}^{\mathrm{LUT}}$) was examined. PBE0 functional and Sapporo(-DKH3)-DZP-2012 basis sets were adopted. The CPU time for Evaluation and transformation of TEIs, the first SCF cycle of DFT and total calculations are shown.

	TEIs	SCF	Total
Nonrelativistic	1175.17	359.35	12392.61
1e LUT-IOTC	1177.74	345.89	9994.87
1e LUT-IOTC with $\boldsymbol{\delta}^{\mathrm{LUT}}$	1195.72	1933.32	32360.91
1e2e LUT-IOTC	1368.86	341.39	10025.63
1e2e LUT-IOTC with $\boldsymbol{\delta}^{\mathrm{LUT}}$	1392.46	1949.37	34332.76

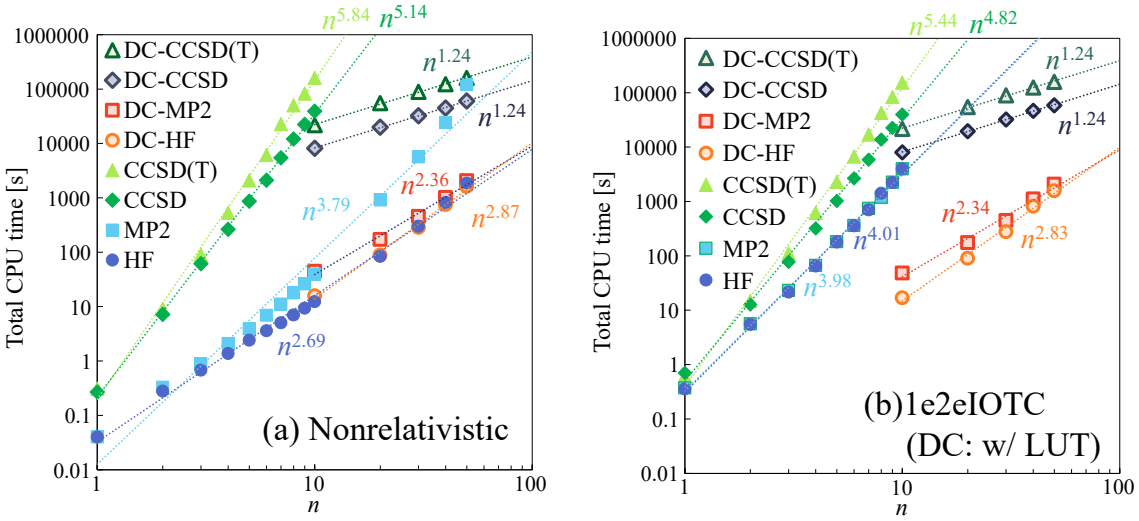

Figure 7.3. System-size dependence of CPU time (in s) in the Hartree–Fock (HF), MP2, CCSD, and CCSD(T) calculations of $(HF)_n$ molecules. (a) nonrelativistic and (b) 1e2eIOTC Hamiltonians are adopted with and without DC method. In the calculation of 1e2eIOTC, the DC method is combined with LUT scheme. As basis sets, uncontracted 6-311G** were applied.

7.4 Conclusion

This chapter presented the implementation of the PCC methods for the two-electron Coulomb interaction and density operators in the GAMESS program package, which enables accurate and efficient 2c relativistic calculations. The details of implementation and capability of the present methods were provided. Numerical assessments confirmed the accuracy and efficiency of the implementation In particular, the numerical result for the whole PCC of the one-electron, two-electron, and density operators clarified to be essential in order to obtain the results close to those of 4c treatment. Furthermore, its computational costs are slightly larger than but comparable with those of the nonrelativistic calculations. The GAMESS program including LUT-IOTC for two-electron and density operators was open to the public in July 2022.

References

1. G.M.J. Barca, C. Bertoni, L. Carrington, D. Datta, N. De Silva, J.E. Deustua, D.G. Fedorov, J.R. Gour, A.O. Gunina, E. Guidez, T. Harville, S. Irle, J. Ivanic, K. Kowalski, S.S. Leang, H. Li, W. Li, J.J. Lutz, I. Magoulas, J. Mato, V. Mironov, H. Nakata, B.Q. Pham, P. Piecuch, D. Poole, S.R. Pruitt, A.P. Rendell, L.B. Roskop, K. Ruedenberg, T. Sattasathuchana, M.W. Schmidt, J. Shen, L. Slipchenko, M. Sosonkina, V. Sundriyal, A. Tiwari, J.L. Galvez Vallejo, B. Westheimer, M. Włoch, P. Xu, F. Zahariev, and M.S. Gordon, *J. Chem. Phys.* **152**, 154102 (2020).

2. F. Neese, *WIREs Comput. Mol. Sci.* **2**, 73 (2012).

3. E. Aprà, E.J. Bylaska, W.A. de Jong, N. Govind, K. Kowalski, T.P. Straatsma, M. Valiev, H.J.J. van Dam, Y. Alexeev, J. Anchell, V. Anisimov, F.W. Aquino, R. Atta-Fynn, J. Autschbach, N.P. Bauman, J.C. Becca, D.E. Bernholdt, K. Bhaskaran-Nair, S. Bogatko, P. Borowski, J. Boschen, J. Brabec, A. Bruner, E. Cauët, Y. Chen, G.N. Chuev, C.J. Cramer, J. Daily, M.J.O. Deegan, T.H. Dunning Jr., M. Dupuis, K.G. Dyall, G.I. Fann, S.A. Fischer, A. Fonari, H. Früchtl, L. Gagliardi, J. Garza, N. Gawande, S. Ghosh, K. Glaesemann, A.W. Götz, J. Hammond, V. Helms, E.D. Hermes, K. Hirao, S. Hirata, M. Jacquelin, L. Jensen, B.G. Johnson, H. Jónsson, R.A. Kendall, M. Klemm, R. Kobayashi, V. Konkov, S. Krishnamoorthy, M. Krishnan, Z. Lin, R.D. Lins, R.J. Littlefield, A.J. Logsdail, K. Lopata, W. Ma, A.V. Marenich, J. Martin del Campo, D. Mejia-Rodriguez, J.E. Moore, J.M. Mullin, T. Nakajima, D.R. Nascimento, J.A. Nichols, P.J. Nichols, J. Nieplocha, A. Otero-de-la-Roza, B. Palmer, A. Panyala, T. Pirojsirikul, B. Peng, R. Peverati, J. Pittner, L. Pollack, R.M. Richard, P. Sadayappan, G.C. Schatz, W.A. Shelton, D.W. Silverstein, D.M.A. Smith, T.A. Soares, D. Song, M. Swart, H.L. Taylor, G.S. Thomas, V. Tipparaju, D.G. Truhlar, K. Tsemekhman, T. Van Voorhis, Á. Vázquez-Mayagoitia, P. Verma, O. Villa, A. Vishnu, K.D. Vogiatzis, D. Wang, J.H. Weare, M.J. Williamson, T.L. Windus, K. Woliński, A.T. Wong, Q. Wu, C.

Yang, Q. Yu, M. Zacharias, Z. Zhang, Y. Zhao, and R.J. Harrison, *J. Chem. Phys.* **152**, 184102 (2020).

4. S.G. Balasubramani, G.P. Chen, S. Coriani, M. Diedenhofen, M.S. Frank, Y.J. Franzke, F. Furche, R. Grotjahn, M. E. Harding, C. Hättig, A. Hellweg, B. Helmich-Paris, C. Holzer, U. Huniar, M. Kaupp, A. Marefat Khah, S. Karbalaei Khani, T. Müller, F. Mack, B.D. Nguyen, S.M. Parker, E. Perlt, D. Rappoport, K. Reiter, S. Roy, M. Rückert, G. Schmitz, M. Sierka, E. Tapavicza, D.P. Tew, C. van Wüllen, V.K. Voora, F. Weigend, A. Wodyński, and J.M. Yu, *J. Chem. Phys.* **152**, 184107 (2020).
5. D.A. Matthews, L. Cheng, M.E. Harding, F. Lipparini, S. Stopkowicz, T. Jagau, P.G. Szalay, J. Gauss, and J.F. Stanton, *J. Chem. Phys.* **152**, 214108 (2020).
6. F. Aquilante, L. De Vico, N. Ferré, G. Ghigo, P. Malmqvist, P. Neogrády, T.B. Pedersen, M. Pitoňák, M. Reiher, B.O. Roos, L. Serrano-Andrés, M. Urban, V. Veryazov, and R. Lindh, *J. Comput. Chem.* **31**, 224 (2010).
7. F. Aquilante, J. Autschbach, R.K. Carlson, L.F. Chibotaru, M.G. Delcey, L. De Vico, I. Fdez. Galván, N. Ferré, L.M. Frutos, L. Gagliardi, M. Garavelli, A. Giussani, C.E. Hoyer, G. Li Manni, H. Lischka, D. Ma, P.Å. Malmqvist, T. Müller, A. Nenov, M. Olivucci, T.B. Pedersen, D. Peng, F. Plasser, B. Pritchard, M. Reiher, I. Rivalta, I. Schapiro, J. Segarra-Martí, M. Stenrup, D.G. Truhlar, L. Ungur, A. Valentini, S. Vancoillie, V. Veryazov, V.P. Vysotskiy, O. Weingart, F. Zapata, and R. Lindh, *J. Comput. Chem.* **37**, 506 (2016).
8. Y. Nakajima, J. Seino, M.W. Schmidt, and H. Nakai, *J. Comput. Chem. Jpn.* **15**, 68 (2016).
9. T. Akama, M. Kobayashi, and H. Nakai, *J. Comput. Chem.* **28**, 2003 (2007).
10. H. Nakai, M. Kobayashi, T. Yoshikawa, J. Seino, Y. Ikabata, and Y. Nishimura, *J. Phys. Chem. A.* **127**, 589 (2023).
11. J. Seino and M. Hada, *Chem. Phys. Lett.* **461**, 327 (2008).
12. J. Seino and H. Nakai, *J. Chem. Phys.* **137**, 144101 (2012).

13. Y. Ikabata, T. Oyama, M. Hayami, J. Seino, and H. Nakai, *J. Chem. Phys.* **150**, 164104 (2019).

14. A.D. Becke, *J. Chem. Phys.* **98**, 5648 (1993).

15. C. Lee, W. Yang, and R.G. Parr, *Phys. Rev. B* **37**, 785 (1988).

16. T. Noro, M. Sekiya, and T. Koga, *Theor. Chem. Acc.* **109**, 85 (2003).

17. T. Noro, M. Sekiya, and T. Koga, *Theor. Chem. Acc.* **131**, 1124 (2012).

18. T. Noro, M. Sekiya, and T. Koga, *Theor. Chem. Acc.* **132**, 1363 (2013).

19. J.P. Perdew, M. Ernzerhof, and K. Burke, *J. Chem. Phys.* **105**, 9982 (1996).

Chapter 8 Relativistic effects on C–H activation of *N*-phenylbezamide using Ir complex[††]

8.1 Introduction

Relativistic effects have been discussed as essential factors of molecular structures, properties, and chemical reactions in heavy element systems.[1–7] The scalar relativistic effect contracts and stabilizes *s* and *p* orbitals, followed by the self-consistent expansion and activation of *d* and *f* orbitals.[8] This effect influences bond lengths, vibrational frequencies, orbital energies, and reactivities. Another relativistic effect originates from the spin-dependent effect, which is due to the hybridization and rotation of electronic spins.[9] This effect influences magnetic properties, such as the chemical shifts of NMR, the spin-orbit splitting of degenerated orbitals, and intersystem crossing in photophysical and photochemical processes. For heavy elements, these effects are more significant.

Relativistic effects in homogeneous catalytic reactions have been examined mainly for third-row transition metal complexes, but recently for the first- and second-row ones as well.[10–18] For example, the contraction of 6*s* and 6*p* orbitals, the expansion of 5*d* orbitals, and the spin-orbit splitting of 6*p* and 5*d* orbitals shift the energy levels of the HOMO and LUMO, which have been reported to rationalize the remarkable activities of homogeneous Au, Pt, and Hg catalysts.[11–13,16]

In recent years, C–H functionalization using Ir complexes has attracted considerable attention because of their high catalytic activities.[19–25] For example, the energy barrier in the C–H amination of benzamides with Ir catalysts has been reported to be lower than that with Rh catalysts.[26] Furthermore, the rate constant of an Ir-mediated C–N coupling reaction

[††] Reprinted with permission from the article by Chinami Takashima, Hisaki Kurita, Hideaki Takano, Yasuhiro Ikabata, Takanori Shibata, and Hiromi Nakai, *J. Phys. Chem.* A **126**, 7627 (2022). Copyright 2023 American Chemical Society.

was shown to be larger than that of the Rh case.[27] Further, various catalytic activities of cationic Ir complexes have been reported,[28–32] for example, the sp^2 C–H alkenylation of aryl ketones with alkynes,[28] the sp^3 C–H alkylation of pyridylamine with alkenes,[33] and C–H conjugate addition to α-substituted α,β-unsaturated esters.[31]

In this chapter, the author elucidates the relativistic catalytic activities of cationic Ir complexes in experimental and theoretical aspects. The difference in the catalytic reactivity between the Ir and Rh complexes reported in the deuteration of *N*-phenylbenzamide for C–H activation is theoretically analyzed using DFT calculations. The scalar relativistic effect is estimated based on a direct comparison of reaction energy diagrams, geometric parameters, and electronic structures calculated by relativistic calculations with those of their nonrelativistic counterparts. The remainder of this chapter is organized as follows. The next section describes the experimental backgrounds: the results of deuteration of *N*-phenylbenzamide. The computational details, results, and discussion are presented in the third section. The last section presents the conclusion of this chapter.

8.2 Experimental backgrounds

Scheme 8.1 shows deuteration of *N*-phenylbenzamide, which is covered by this chapter. *N*-phenylbenzamide was reacted with excess amounts of D_2O using cationic Ir(I) and Rh(I)-diphosphine catalysts possessing (*S*)-BINAP derivatives in 1,4-dioxane at 120 °C for 24 h under standard reaction conditions. Figure 8.1 illustrates the molecular formulas of (*S*)-BINAP and (*S*)-SEGPHOS ligands.

When the Ir–(*S*)-SEGPHOS or (*S*)-BINAP catalyst was used, significant D-content was observed at the *ortho* positions of the aromatic rings of *N*-phenylbenzamide: D^1 and D^2 contents were 57 and 60 %, respectively, with Ir–(*S*)-SEGPHOS and 73 and 74 %, respectively with Ir–(*S*)-BINAP. The high catalytic activity of the cationic Ir complex for C–H activation was ascertained. In contrast, the Rh counterparts were inactive.

The conceivable reaction mechanism of deuteration of *N*-phenylbenzamide is shown in Scheme 8.2. The reactions at the *ortho* position of amino and carbonyl groups are described in left and right cycles of Scheme 8.2, respectively. The precursor of these reactions is the Ir-diphosphine complex (**A**). The substrate, *N*-phenylbenzamide (**B**), is coordinated to **A** by an oxygen atom as a directing group (**C** or **C'**). The C–H bond cleaves by the oxidative addition of Ir through a TS (**D** or **D'**), which leads to form the Ir-D complex (**E** or **E'**). Then, the H-D exchange occurs on the Ir to form Ir-D complex (**F** or **F'**). The C-D bond is formed on the *ortho* position of the substrate (**G**→**H** or **G'**→**H'**). Finally, the deuterated *N*-phenylbenzamide (**I** or **I'**) is obtained by the elimination of the substrate. Note that the present quantum chemical calculations treated the C-H bond cleavage, namely, **C**→**D**→**E** and **C'**→**D'**→**E'**.

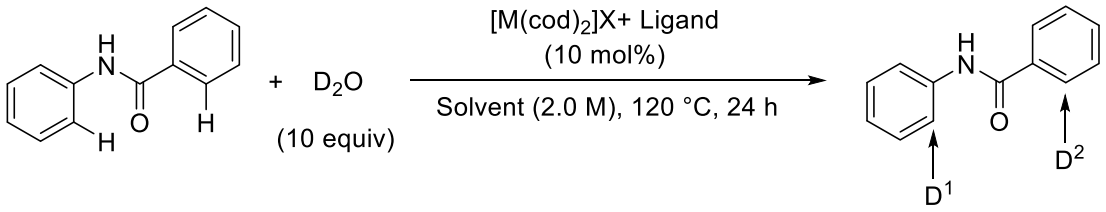

Scheme 8.1. Deuteration of *N*-phenylbenzamide using Ir- and Rh- catalysts.

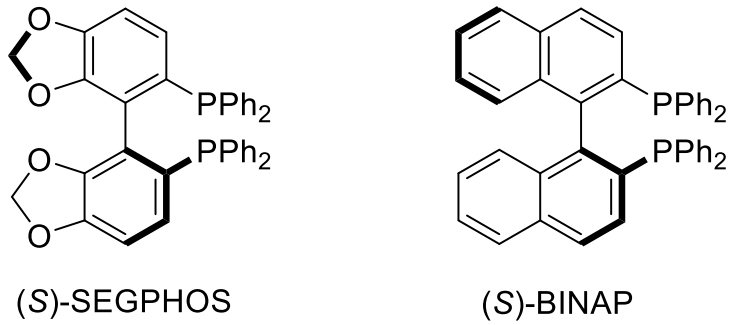

(*S*)-SEGPHOS (*S*)-BINAP

Figure 8.1. Molecular formulas of (*S*)-SEGPHOS and (*S*)-BINAP.

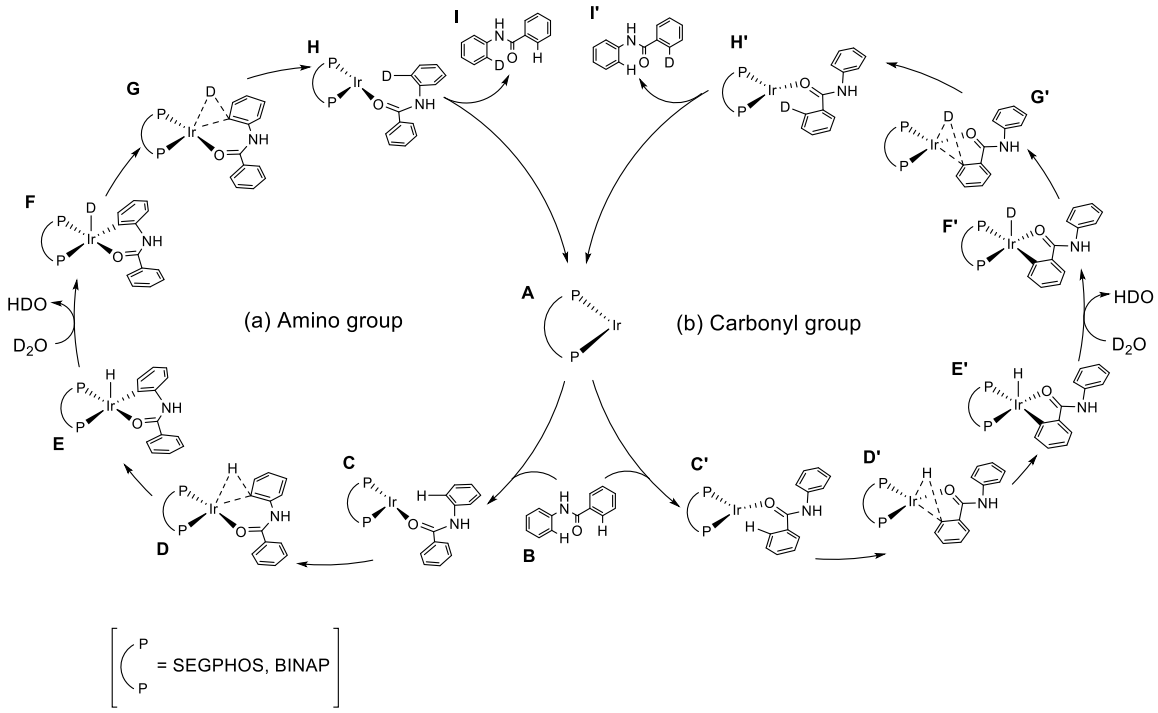

Scheme 8.2. Conceivable reaction mechanisms of deuteration of *N*-phenylbenzamide using Ir(I)-diphosphine catalysts. (a) and (b) correspond to the *ortho* position of amino and carbonyl groups, respectively.

8.3 Computational details

Using quantum chemical calculations, the author examined the oxidative addition of *N*-phenylbenzamide to the Ir and Rh complexes (**C→D→E** and **C'→D'→E'** in Scheme 8.2), which might be an elementary step in a series of H–D exchange reactions of *N*-phenylbenzamide in D_2O. This subsection describes the calculation conditions. Geometry optimizations were performed for the reactants, TSs, and products of the oxidative additions. In total, 16 patterns of conditions were considered because of the relativistic or nonrelativistic setting of the pseudopotential and valence basis set, transition metal elements (Ir or Rh), ligands (SEGPHOS or BINAP), and reaction positions (*ortho* position of amino or carbonyl group). Each combination was indicated by the following abbreviations: Rel/NR–Ir/Rh–S/B–A/C. For comparison, the geometry optimizations for the separated systems, namely, the Ir and Rh complexes and *N*-phenylbenzamide, were performed.

Harmonic vibrational frequencies were analytically calculated to examine whether the optimized structure had an equilibrium geometry or TS. TS structures were confirmed to connect the corresponding reactants and products using IRC[34–37] calculations. In Gibbs energy calculations, the temperature and pressure were set to 120 °C (393.15 K) and 1 atm, respectively. Solvation effects (1,4-dioxane, ε = 2.2099) were considered using the polarizable continuum model based on solute electron density.[38] Further, NBO analysis was performed using the NBO 6.0 program[39] to recognize the relativistic effect from the viewpoint of localized orbitals.

The above quantum chemical calculations were performed at the DFT level with the ωB97X-D exchange-correlation functional,[40] using the Gaussian 09 program package.[41] For the core electrons of Ir ([Kr]$4d^{10}4f^{14}$) and Rh ([Ar]$3d^{10}$), nonrelativistic and relativistic Stuttgart–Dresden (SDD)[42,43] pseudopotentials were used. As nonrelativistic and relativistic basis sets for the corresponding valence orbitals, (18*s*7*p*6*d*)/[4*s*2*p*2*d*] and

(20*s*9*p*8*d*)/[4*s*2*p*2*d*] were adopted, respectively. For the other atoms, such as C, H, N, O, and P, the 6-31G(d,p) all-electron basis sets[44,45] were used. Additionally, relativistic single-point calculations were performed with the all-electron basis sets at the optimized geometries using the above pseudopotentials. Sapporo-DKH3-DZP-2012 basis sets for Ir and Rh and Sapporo-DZP-2012 basis sets for H, C, N, O, and P were adopted. These all-electron calculations were performed by the GAMESS program.

8.4 Results and discussion

8.4.1 Geometry optimization

Figure 8.2 illustrates the optimized structures for relativistic treatment for the Ir complex with SEGPHOS as a ligand for C–H activation at the *ortho* position of the amino group: i.e., Rel–Ir–S–A. In this figure, two P atoms are distinguished by P_a and P_b.

Here, the geometries of the reaction centers for the Ir and Rh complexes with SEGPHOS at the amino-group reaction position calculated at the relativistic and nonrelativistic levels, i.e., Rel/NR–Ir/Rh–S–A are the subject. The reaction center consists of Ir or Rh, denoted as M, P_a and P_b of SEGPHOS coordinated to M, O of the carbonyl group being coordinated to M, and C and H of the C–H bond being activated. Table 8.1 lists six bond distances (Å) and six bond angles (degrees) of the reaction center, namely M–P_a, M–P_b, M–O, M–C, M–H, and C–H distances and P_a–M–P_b, P_a–M–O, P_b–M–C, P_a–M–H, P_b–M–H, and C–M–H angles. Δ represents the difference between the nonrelativistic and relativistic results.

In the separated systems, the geometric parameters of a free *N*-phenylbenzamide molecule are the same between the relativistic and nonrelativistic data because they involved only light elements, such as C, H, N, and O, which were uniquely treated at the nonrelativistic level with the 6-31G(d,p) basis sets. The C–H bond distance at the *ortho* position of the amino group was calculated to be 1.08 Å. Two M–P bond distances, i.e., M–

P_a and M–P_b, were equal because of the symmetry. The M–P bond distances in the Ir complex were calculated to be 2.19 and 2.28 Å at the relativistic and nonrelativistic levels. The shortening by 0.09 Å for the former was due to the relativistic shrinkage of the *d* orbitals of Ir. In contrast, the shortening of two M–P bond distances in the Rh complex was minor: 0.02 Å. Although the P_a–M–P_b bond angles in the Ir and Rh complexes were approximately right angles, the relativistic treatment afforded slightly increased values of 94.6 and 92.8 degrees in the Ir and Rh complexes, respectively.

In the reactants, *N*-phenylbenzamide was attached to the metal complex by forming an M–O bond. Regardless of the metal species and relativistic treatments, the C–H bond lengths of the reactants were not directly activated and were calculated to be 1.09 Å, which was not significantly different from that of the free *N*-phenylbenzamide molecule, i.e., 1.08 Å. The M–O distances were in the range of 2.16–2.26 Å. For both reaction positions, Δ values were −0.09 and −0.02 Å for the Ir and Rh complexes, respectively. This difference indicates that the relativistic effect shortened the M–O distance in the Ir complex than in the Rh complex. The M–C and M–H distances were calculated to be 2.58–2.71 and 2.61–2.74 Å, respectively, which were regarded as van der Waals contacts. The shortening of the M–C and M–H distances in the relativistic treatment was due to the above-mentioned shortening of the M–O bonds rather than the direct relativistic effect. Although the P_a–M–P_b bond angles slightly decreased from those of the isolated metal complexes, they were kept quasi-perpendicular. The P_a–M–O bond angles were calculated to be quasilinear. The M–P_a bond distances at the *trans* position were slightly elongated because the M–O bonds were newly formed. The P_a–M–C angles were estimated to be 147.2–152.2 degrees, which were remarkably smaller than the linear angles. The P_a–M–H and P_b–M–H angles were estimated to be larger than the right angles, 116.9–119.1 and 123.4–129.3 degrees, respectively.

In the products, the C–H bonds were cleaved as the distances were elongated to 2.41–

2.56 Å, and the M–C and M–H bonds were newly formed in addition to the M–O bond. Notably, the relativistic effect directly shortened the M–C and M–H distances in the Ir complex more than those in the Rh complex. As shown later, the reduced M–H and M–C distances led to the stabilization of the product. For the reactants, the P_a–M–P_b bond angles were conserved quasi-perpendicular. The P_a–M–O bond angles were calculated to be quasilinear. The newly formed M–C bonds, which were located at the *trans*-position of the M–P_b bond, elongated the M–P_b bond distances by approximately 0.2 Å in comparison with those in the isolated complexes and the reactants. The newly formed M–H bonds were located at the *cis* positions of the M–P_a and M–P_b bonds; the P_a–M–H and P_b–M–H bond angles were quasi-perpendicular. Consequently, the products had approximately square-pyramidal structures.

In the TSs, the differences in the C–H distances were characteristic. The relativistic treatment shortened the C–H distance by 0.24 Å in the Ir complex while such difference was estimated to be 0.11 Å in the Rh complex. The C–H distance was the main reaction coordinate for the C–H activation. The relatively short C–H distance of 1.45Å in the Ir complex indicates that the TS was closer to the reactant than the product. Similar trends were observed for the C–M–H bond angles. According to Hammond's postulate,[46] the relativistic and nonrelativistic treatments demonstrated the early and late TSs in the Ir complex, respectively, while both treatments showed the late TSs in the Rh complex. The relativistic results for the Ir complex were rather regarded as mid-TSs.

As shown in Table 8.1, for Rel/NR–Ir/Rh–S–A, the geometric parameters for the other cases, Rel/NR–Ir/Rh–S–C, Rel/NR–Ir/Rh–B–A, and Rel/NR–Ir/Rh–B–C, are tabulated in Tables A8.1–A8.3 in Appendix of this chapter. Table 8.2 summarizes the C–H distances and the C–M–H angles in all cases. For Rel/NR–Ir/Rh–S–C, relatively large differences between the relativistic and nonrelativistic treatments were obtained in the TSs of the Ir complexes. Conversely, relatively small differences were observed in the reactants

and products of the Ir and Rh complexes and the TS of the Rh complexes. As will be discussed in the next section, these differences were caused by the stabilization of the products by the relativistic effect in the Ir complexes, which led to the early or mid-TSs because of Hammond's postulate.

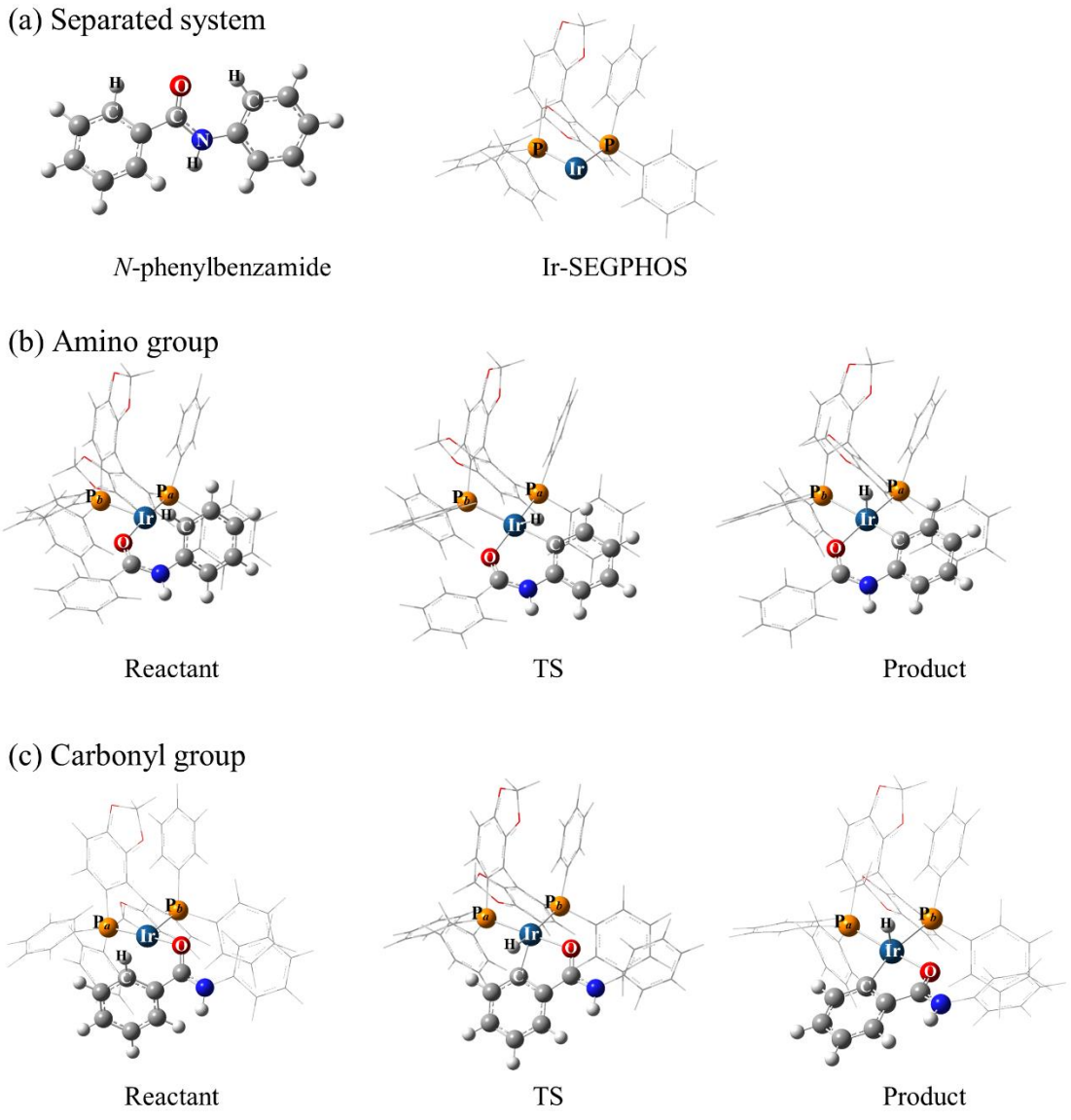

Figure 8.2. Schematic illustrations of optimized structures of separated systems, reactants, TSs, and products of the C-H bond cleavage at the *ortho* position of amino and carbonyl groups by the Ir complex with the SEGPHOS ligand, which were calculated at the relativistic treatment.

Table 8.1. Bond distances (in Å) and bond angles of reactants, TSs, and products of the C-H activation at the *ortho* positions of amino group by the Ir and Rh complexes with the SEGPHOS ligand. Those of separated systems, namely, free *N*-phenylbenzamide molecule and isolated metal complexes, are also tabulated. M designates the transition metal (Ir or Rh). Δ represents the difference between the results obtained by the relativistic (Rel) and nonrelativistic (NR) calculations.

	Ir			Rh		
	Rel	NR	Δ	Rel	NR	Δ
Separated System						
N-phenylbenzamide						
C-H	1.08	1.08	0.00	1.08	1.08	0.00
Metal Complexes						
M-P_a	2.19	2.28	−0.09	2.20	2.22	−0.02
M-P_b	2.19	2.28	−0.09	2.20	2.22	−0.02
P_a-M-P_b	94.6	91.1	3.5	92.8	91.3	1.6
Reactant						
M-P_a	2.25	2.33	−0.08	2.24	2.26	−0.02
M-P_b	2.22	2.31	−0.09	2.23	2.25	−0.02
M-O	2.16	2.26	−0.09	2.16	2.19	−0.02
M-C	2.63	2.71	−0.08	2.58	2.63	−0.05
M-H	2.71	2.74	−0.03	2.61	2.64	−0.03
C-H	1.09	1.09	0.00	1.09	1.09	0.00
P_a-M-P_b	92.7	90.6	2.0	92.1	91.1	1.0
P_a-M-O	174.8	177.1	−2.3	173.6	173.3	0.3
P_b-M-C	151.1	152.2	−1.1	148.7	147.2	1.6
P_a-M-H	119.1	117.7	1.3	117.5	116.9	0.6
P_b-M-H	127.7	129.3	−1.6	124.6	123.4	1.2
C-M-H	23.4	23	0.4	24.2	23.8	0.4

Table 8.1. Continued.

	Ir			Rh		
	Rel	NR	Δ	Rel	NR	Δ
Transition State						
M-P_a	2.29	2.37	−0.08	2.29	2.32	−0.03
M-P_b	2.37	2.48	−0.11	2.39	2.44	−0.05
M-O	2.11	2.16	−0.06	2.09	2.10	−0.02
M-C	2.14	2.16	−0.03	2.09	2.09	0.00
M-H	1.61	1.60	0.01	1.53	1.53	0.00
C-H	1.45	1.69	−0.24	1.65	1.76	−0.11
P_a-M-P_b	92.4	91.4	1.1	92.1	91.6	0.5
P_a-M-O	171.3	173.0	−1.6	167.6	171.1	−3.6
P_b-M-C	167.2	165.4	1.9	161.3	165.9	−4.6
P_a-M-H	96.7	93.0	3.6	93.5	92.6	0.9
P_b-M-H	126.5	116.5	10.0	112.0	112.4	−0.3
C-M-H	42.8	50.9	−8.1	51.4	55.6	−4.2
Product						
M-P_a	2.30	2.37	−0.07	2.29	2.32	−0.02
M-P_b	2.42	2.51	−0.10	2.42	2.45	−0.03
M-O	2.11	2.17	−0.06	2.10	2.11	−0.02
M-C	2.07	2.13	−0.06	2.04	2.06	−0.02
M-H	1.52	1.55	−0.03	1.49	1.49	−0.01
C-H	2.56	2.54	0.02	2.41	2.41	0.00
P_a-M-P_b	93.1	92.3	0.8	93.1	92.6	0.6
P_a-M-O	173.5	176.8	−3.3	173.4	174.4	−1.0
P_b-M-C	170.4	169.4	0.9	169.8	169.6	0.2
P_a-M-H	88.5	88.0	0.5	88.2	87.8	0.4
P_b-M-H	85.4	86.8	−1.4	88.9	89.0	−0.2
C-M-H	89.5	85.8	3.7	84.7	83.9	0.8

Table 8.2. C-H distances (in Å) and C-M-H angles in all cases, namely reactants, TSs, and products of the C-H activation at the *ortho* positions of amino and carbonyl groups with SEGPHOS and BINAP ligands. M designates the transition metal (Ir or Rh). Δ represents the difference between the results obtained by the relativistic (Rel) and nonrelativistic (NR) calculations.

	Amino group						Carbonyl group					
	Ir			Rh			Ir			Rh		
	Rel	NR	Δ	NR	Rel	Δ	NR	Rel	Δ	NR	Rel	Δ
SEGPHOS												
Separated System												
C-H	1.08	1.08	0.00	1.08	1.08	0.00	1.08	1.08	0.00	1.08	1.08	0.00
Reactant												
C-H	1.09	1.09	0.00	1.09	1.09	0.00	1.09	1.09	0.00	1.09	1.09	0.00
C-M-H	23.4	23.0	0.4	23.8	23.8	0.4	22.6	24.2	1.5	23.7	24	0.3
Transition State												
C-H	1.45	1.69	−0.24	1.76	1.65	−0.11	1.77	1.50	−0.27	1.74	1.76	0.01
C-M-H	42.8	50.9	−8.1	55.6	51.4	−4.2	55.6	46.3	−9.3	57	57.9	0.9
Product												
C-H	2.56	2.54	0.02	2.41	2.41	0.00	2.58	2.63	0.05	2.49	2.53	0.04
C-M-H	89.5	85.8	3.7	83.9	84.7	0.8	87.8	93.2	5.4	87.4	90.1	2.8
BINAP												
Separated System												
C-H	1.08	1.08	0.00	1.08	1.08	0.00	1.08	1.08	0.00	1.08	1.08	0.00
Reactant												
C-H	1.09	1.09	0.00	1.09	1.09	0.00	1.09	1.09	0.00	1.09	1.09	0.00
C-M-H	23.0	23.2	0.2	23.6	23.7	0.2	23.1	23.4	0.3	24.1	24.3	0.2
Transition State												
C-H	1.71	1.44	−0.27	1.75	1.66	−0.10	1.78	1.50	−0.28	1.74	1.74	0.00
C-M-H	51.5	42.2	−9.3	55.2	51.7	−3.5	56.1	46.4	−9.6	57.0	57.2	0.2
Product												
C-H	2.54	2.53	−0.01	2.42	2.42	0.01	2.60	2.64	0.04	2.50	2.51	0.01
C-M-H	85.8	88.3	2.5	84.1	85.2	1.0	88.8	93.2	4.4	87.8	89.0	1.3

8.4.2 Energy diagram

Figure 8.3 shows the electronic energy diagrams of the C–H activation, which compares the nonrelativistic and relativistic calculations and the Ir and Rh complexes. Four diagrams were used to show the ligands and reaction positions, Figures 8.3 (a), (b), (c), and (d), correspond to Rel/NR–Ir/Rh–S–A, Rel/NR–Ir/Rh–S–C, Rel/NR–Ir/Rh–B–A, and Rel/NR–Ir/Rh–B–C, respectively. The corresponding enthalpy and Gibbs energy diagrams under standard conditions are shown in Figures A8.1 and A8.2, respectively. Notably, the enthalpy and Gibbs energy diagrams, including the thermal correction, did not significantly change from the electronic energy diagrams in these systems.

The reaction energies for the Ir complexes were calculated to be in the range of −5.2–−0.1 and 21.3–25.3 kcal/mol by the relativistic and nonrelativistic treatments, respectively, while those for the Rh complexes were 15.1–17.9 and 23.5–26.3 kcal/mol, respectively. This indicates that the reaction of the Ir complexes was exothermic, according to the relativistic calculations, while the others were endothermic. The drastic differences were mainly due to the stabilization of products: the stabilization energies obtained by including the relativistic effect were 25.4–26.2 and 8.2–8.4 kcal/mol for the Ir and Rh complexes, respectively. As shown in Table 8.3, the additional calculations to dissociate the H atom from individual products for Rel/NR–Ir/Rh–S–A clarified that the relativistic effect increased the binding energies of Ir–H and Rh–H by 19.8 and 8.8 kcal/mol, respectively. Therefore, we speculated that the binding energies for the relativistic stabilizations of Ir–C and Rh–C were ~5 and ~0 kcal/mol, respectively.

The reaction barriers for the Ir complexes were calculated to be in the range of 7.2–13.1 and 27.9–30.8 kcal/mol for the relativistic and nonrelativistic treatments, respectively, while those for the Rh complexes were 19.6–22.3 and 26.3 – 28.9 kcal/mol, respectively. The reaction barriers decreased to 17.0–20.8 and 6.6–6.9 kcal/mol for the Ir and Rh complexes, respectively because of the relativistic effect. Notably, the large decreases in

the reaction barriers for the Ir and Rh complexes were mainly due to the changes in the TS structures, from the late TS to the mid-TS, as shown in the previous section.

The C–H activation by the cationic Ir catalyst played a key role in the H–D exchange reaction of the *N*-phenylbenzamide experimentally observed. The product of the C–H activation further accepted D_2O as a ligand of the Ir complex, followed by the H–D exchange between the ligands. To produce deuterated *N*-phenylbenzamide, the reverse reaction of the C–H activation should proceed. As shown in Figure 8.3, the reaction barriers of the reverse reactions for the Rh complexes were estimated to be 3.9–4.9 and 2.6–3.1 kcal/mol at the relativistic and nonrelativistic levels, respectively, when neglecting the energetic effect of the deuteration. The reverse reactions occurred more easily than the positive reactions. Similarly, those of the Ir complexes were estimated to be 4.8–6.8 kcal/mol at the nonrelativistic level. Conversely, the reaction barriers of the reverse reactions for the Ir complexes became slightly larger because of the relativistic treatment: 12.1–13.8 kcal/mol. Notably, the reaction barriers of the positive and reverse reactions for the Ir complexes were comparable at the relativistic level.

Based on the TS theory given by

$$k = \kappa \frac{k_B T}{h} \exp\left(-\frac{\Delta G^{\ddagger}}{RT}\right) = \kappa \frac{k_B T}{h} \exp\left(\frac{\Delta S^{\ddagger}}{R}\right) \exp\left(-\frac{\Delta H^{\ddagger}}{RT}\right), \tag{8.1}$$

the reaction constants at the standard condition, i.e., the absolute temperature (T) of 298.15 K, were estimated to be 3.2×10^5, 1.7×10^{-2}, and 8.7×10^{-10} s^{-1} for $\Delta G^{\ddagger}$ of 10, 20, and 30 kcal/mol, respectively. Here, k_B is the Boltzmann constant (1.38×10^{-23} $J \cdot K^{-1}$), h is the Planck constant (6.63×10^{-34} J·s), and R is the gas constant (8.31 $J \cdot K^{-1}$ mol^{-1}). The frequency factor κ was assumed to be 1. The reciprocals of the rate constants, which indicate the orders of reaction times, were estimated to be ~3 μs, ~1 min, and ~32 years for $\Delta G^{\ddagger}$ of 10, 20, and 30 kcal/mol, respectively. Therefore, the author concludes that the comparable reaction barriers obtained for the Ir complexes, which were provided by the

mid-TSs, were favorable for accomplishing the overall H–D exchange reactions.

Figure 8.4 shows the electronic energy diagram obtained by the all-electron relativistic calculation. The scalar-relativistic IOTC Hamiltonian with the LUT scheme was adopted for the relativistic all-electron calculations. The relativistic treatments were applied to the one-electron Dirac Hamiltonian, which is termed LUT-IOTC Hamiltonian. Single-point energy calculations were performed on the structure shown in Figure 8.2, namely the Ir and Rh complexes with the SEGPHOS ligands. The results of the all-electron calculations also indicated that the reaction barriers for the Ir complex were considerably smaller than those for the Rh complex.

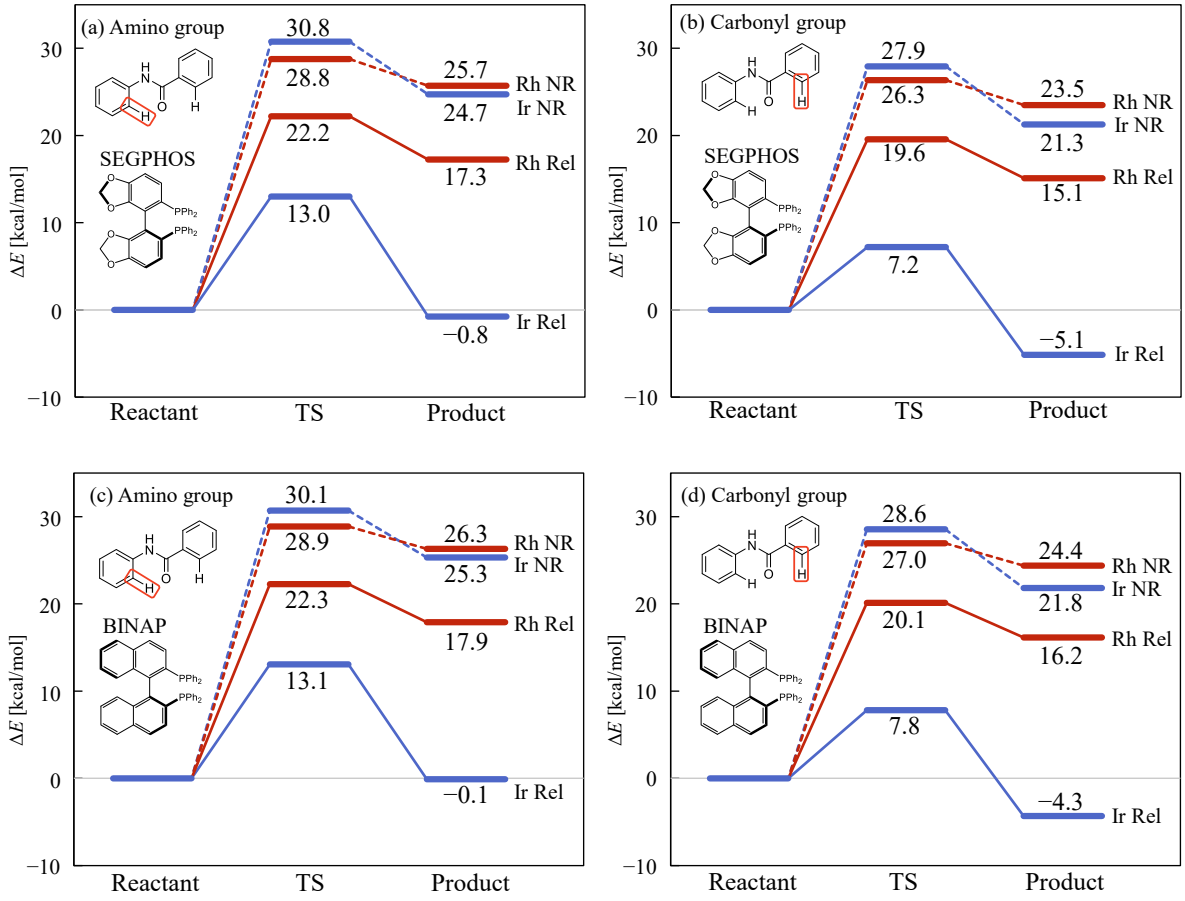

Figure 8.3. Energy diagrams of the C-H activation. (a) and (b) correspond to the SEGPHOS ligand and (c) and (d) to the BINAP ligand. (a) and (c) correspond to the *ortho* position of the amino group and (b) and (d) to that of the carbonyl group. Black and gray lines represent the results of the Ir and Rh complexes, respectively. Dashed and solid lines represent the results of the nonrelativistic (NR) and relativistic (Rel) calculations, respectively.

Table 8.3. Bond dissociation energies (in kcal/mol) of the Ir/Rh-H bond in product. ΔE_{bond} represents the difference between the results obtained by the relativistic (Rel) and nonrelativistic (NR) calculations.

	Rel	NR	ΔE_{bond}
Ir	86.3	66.5	19.8
Rh	73.3	64.5	8.8

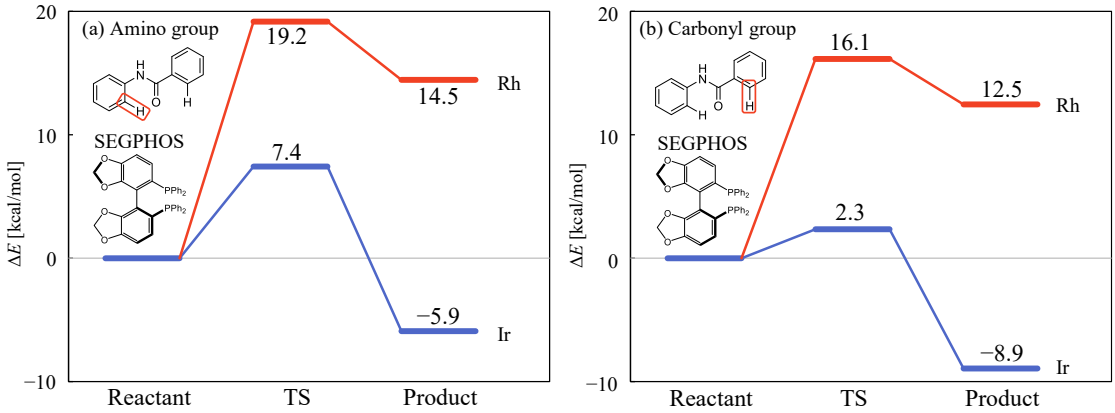

Figure 8.4. Calculated electronic energy diagrams obtained by the all-electron relativistic calculation with LUT-IOTC Hamiltonian.

8.4.3 Natural bond orbital analysis

This section provides a qualitative understanding of the relativistic catalytic activity of the cationic Ir complex in the C–H activation reactions. The Ir and Rh catalysts with the SEGPHOS ligand for the C–H activation at the *ortho* position of the amino group, i.e., Rel/NR–Ir/Rh–S–A, are used as typical examples; the other cases exhibit similar trends.

Table 8.4 shows the orbital energies of 11 NBOs in the valence region of the reactants and products for the Ir and Rh complexes, which were calculated using nonrelativistic and relativistic treatments. The corresponding occupation numbers are shown in parentheses in the table. Additionally, Table 8.4 shows the orbital energies and occupation numbers for the separated systems, i.e., the free *N*-phenylbenzamide and the isolated Ir and Rh complexes with the SEGPHOS ligand. The orbital characters given in Table 8.4 were assigned from the NBO figures shown in Figures A8.3–A8.5 and the NBO population analysis shown in Tables A8.4–A8.7 in the Appendix of this chapter. For the four different calculations, i.e., Rel/NR–Ir/Rh–S–A, the NBO data with the same orbital character were listed in the same column. Since the data were arranged in the order of orbital energy for Rel–Ir–S–A, the orbital energies were occasionally reversed in the other cases.

Figures 8.5 (a), (b), (c), and (d) show the orbital correlation diagrams of Rel–Ir–S–A, NR–Ir–S–A, Rel–Rh–S–A, and NR–Rh–S–A, respectively, illustrating the NBO analysis in Table 8.4. The vertical axis corresponds to the NBO energy. Both sides show the orbital levels of the separated systems, i.e., the metal complex and *N*-phenylbenzamide. The inset shows the orbital levels assigned to the Ir complex and *N*-phenylbenzamide in the reactant. The center corresponds to the product. Although the occupation number of NBOs is a non-integer, the orbital levels with and without up-and-down arrows are adopted to distinguish between the quasi-occupied and quasi-unoccupied orbitals.

Three NBOs of the free *N*-phenylbenzamide were one non-bonding orbital of O in the carbonyl group (n_O), one C–H bonding orbital ($\sigma_{C–H}$), and one C–H anti-bonding orbital

($\sigma^*_{C–H}$). Although these NBOs were partially occupied, n_O and $\sigma_{C–H}$ were assigned to quasi-occupied orbitals and $\sigma^*_{C–H}$ to quasi-unoccupied orbitals. Notably, the four data points in the same column are equivalent for the free *N*-phenylbenzamide. As shown in Table A8.4, the NBO populations of n_O are 58.1% and 41.8% for the 2*s* and 2*p* orbitals of O, respectively. The $\sigma_{C–H}$ and $\sigma^*_{C–H}$ populations were {19.5%, 44.8%, and 35.6%} and {10.8%, 24.8%, and 64.3%}, respectively, for the {C2*s*, C2*p*, H1*s*} orbitals, respectively.

The eight NBOs of the isolated Ir and Rh complexes were two M–P bonding orbitals ($\sigma_{M–Pa}$, $\sigma_{M–Pb}$), four non-bonding orbitals of metals, such as Ir and Rh (n_M), and two M–P bonding orbitals ($\sigma^*_{M–Pa}$, $\sigma^*_{M–Pb}$). Notably, n_M consists mainly of *d* orbitals and partially of the *s* orbitals of the metal. These results are consistent with the fact that the electron configurations of the Ir and Rh monocations are [Xe]$4f^{14}5d^7 6s^1$ and [Kr]$4d^7 5s^1$, respectively. The orbital energies of $\sigma_{M–Pa}$ and $\sigma^*_{M–Pb}$ obtained by the relativistic treatment were lower than those obtained by the nonrelativistic treatment for the Ir and Rh complexes. This indicates that the binding between the metal and the SEGPHOS ligand was relatively strong when the relativistic effect was included. The origin is the activation of the d orbitals, which was caused by the relativistic self-consistent expansion of the *d* orbitals. The orbital energies of n_M for the relativistic treatment were slightly higher than those for the nonrelativistic treatment. Furthermore, the aforementioned differences for the Ir complex were remarkably larger than those for the Rh complex, further showing that the relativistic effect becomes more remarkable in heavy elements.

Although 11 NBOs in the reactants were regarded as a combination of the separated systems, i.e., three NBOs of *N*-phenylbenzamide and eight NBOs of the metal complex, there were characteristic changes. The orders of n_O and $\sigma_{C–H}$ were opposite in all cases. n_O was not a purely non-bonding orbital but a lone-pair orbital coordinating to the metal, because the carbonyl group of *N*-phenylbenzamide was coordinated to the metal, of which the *trans* position was P_a. For the three-center-four-electron bond, denoted by A:B:C, the

NBO analysis generally separates one two-center bonding orbital and one non-bonding orbital, such as A:B and :C. Furthermore, the covalence between A and B is larger than that between B and C, although the opposite is true for the ionicity. The three-center-four-electron bond of P_a:M:O was separated into P_a: and M:O in this NBO analysis. Therefore, the M–P_a and M–O bonds were significantly covalent and ionic, respectively.

In the products, the C–H bond was cleaved, and the M–C and M–H bonds were newly formed, as discussed in Section 3.2. Therefore, instead of $\sigma_{C–H}$ and $\sigma^*_{C–H}$ vanishing, two bonding orbitals, $\sigma_{M–C}$ and $\sigma_{M–H}$, and two anti-bonding orbitals, $\sigma^*_{M–C}$ and $\sigma^*_{M–H}$, appeared. Although the *trans*-position of the M–H bond was vacant, P_b was located at the *trans*-position of the M–C bond. The three-center-four-electron bond of P_b:M:C was separated into P_b: and M:C by the NBO analysis. As mentioned above, the M–P_b and M–C bonds were significantly ionic and covalent, respectively. Furthermore, the binding of M–C and M–H was calculated to be stronger for the relativistic treatment than for the nonrelativistic treatment because of the self-consistent expansion of *d* orbitals. The relativistic effect was greater for the heavy Ir complex than for the Rh complex.

The products had three non-bonding metal orbitals (n_M), which only involved *d* orbitals. These results are consistent with the fact that the electron configurations of the Ir and Rh monocations are [Xe]$4f^{14}5d^6$ and [Kr]$4d^6$, respectively. The C–H activation led to the oxidation number of the metal from +I to +III. Notably, the newly formed M–C and M–H bonds were significantly covalent, which played a key role in the catalytic activity of the Ir complex.

The discussion based on the NBO analysis is summarized as follows; The *d* orbitals of Ir were activated by self-consistent expansion, followed by a strong interaction with the 1*s* orbital of H and the 2*s* and 2*p* orbitals of C, resulting in strong Ir–H and Ir–C covalent bonds. The stabilization of the product afforded mid-TS, resulting in the lowering of the reaction barriers, as described in Sections 3.2 and 3.3. This was confirmed to be the origin

of the relativistic catalytic activity observed for the Ir complexes.

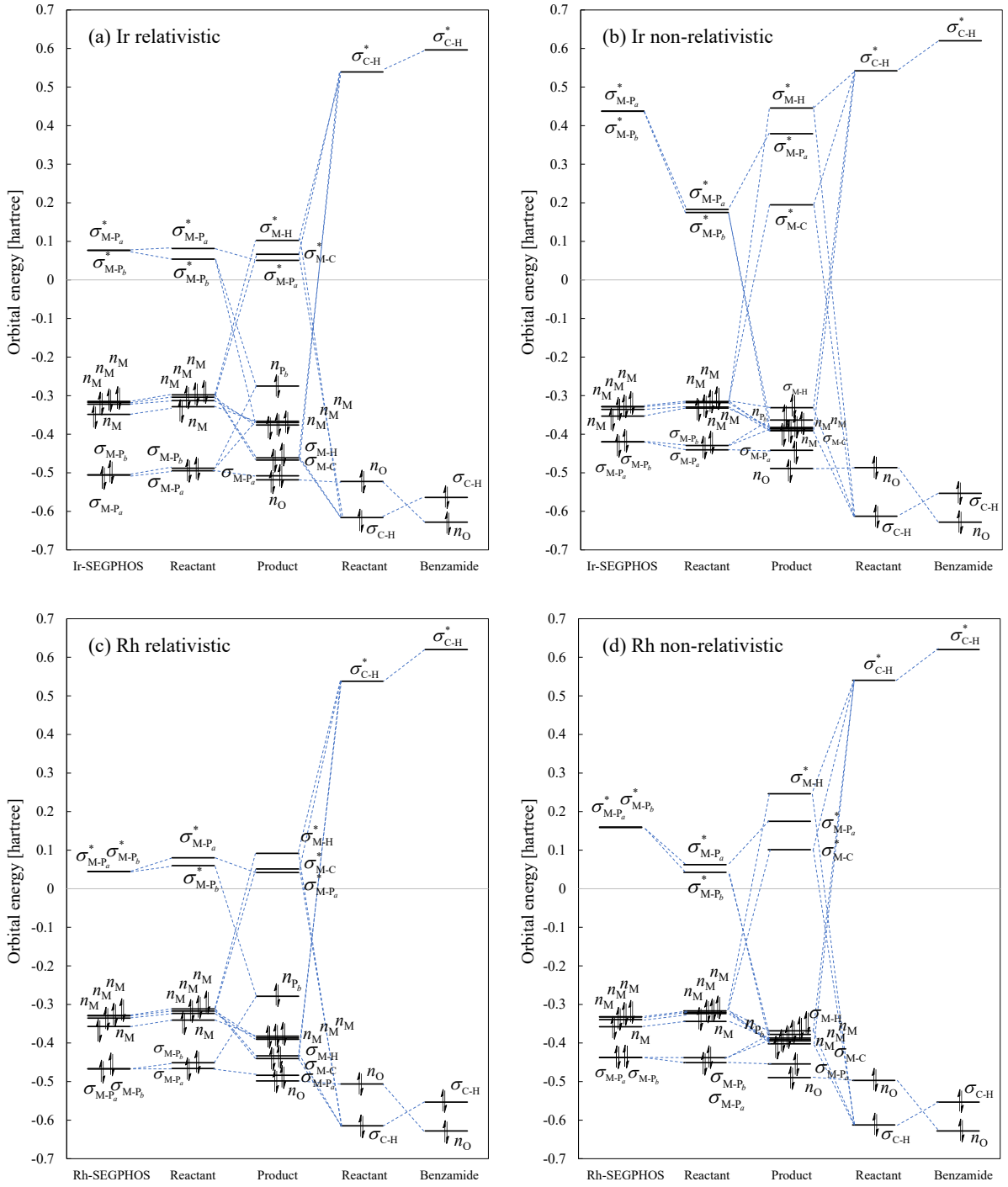

Figure 8.5. Orbital correlation diagram for the C-H activation at the *ortho* position of amino group by the metal complex with the SEGPHOS ligand. (a) and (b) correspond to the Ir complex, while (c) and (d) to the Rh complex. The orbital levels of (a) and (c) were estimated by the NBO analysis at the relativistic treatment, while those of (b) and (d) at the nonrelativistic treatment.

Table 8.4. NBO energy (in hartree) of reactant, TS, and product of the C-H activation with SEGPHOS at the *ortho* positions of amino groups. M designates the transition metal (Ir or Rh). Δ represents the difference between the results obtained by the nonrelativistic (NR) and relativistic (Rel) calculations. Occupation numbers of the orbitals are shown in parentheses.

	Ir					Rh				
	NR		Rel		Δ	NR		Rel		Δ
Separated System										
N-phenylbenzamide										
n_O	−0.628	(1.977)	−0.628	(1.977)	0.000	−0.628	(1.977)	−0.628	(1.977)	0.000
$\sigma_{C\text{-}H}$	−0.564	(1.982)	−0.564	(1.982)	0.000	−0.564	(1.982)	−0.564	(1.982)	0.000
$\sigma_{C\text{-}H^*}$	0.596	(0.014)	0.596	(0.014)	0.000	0.596	(0.014)	0.596	(0.014)	0.000
Metal Complex										
$\sigma_{M\text{-}Pa}$	−0.420	(1.825)	−0.505	(1.903)	−0.086	−0.438	(1.811)	−0.466	(1.869)	−0.029
$\sigma_{M\text{-}Pb}$	−0.420	(1.825)	−0.505	(1.903)	−0.086	−0.438	(1.814)	−0.451	(1.863)	−0.013
n_M	−0.353	(1.910)	−0.349	(1.878)	0.005	−0.358	(1.917)	−0.341	(1.921)	0.017
n_M	−0.336	(1.932)	−0.322	(1.901)	0.014	−0.339	(1.939)	−0.323	(1.903)	0.016
n_M	−0.328	(1.917)	−0.317	(1.888)	0.011	−0.332	(1.923)	−0.317	(1.936)	0.015
n_M	−0.329	(1.982)	−0.315	(1.977)	0.014	−0.332	(1.985)	−0.312	(1.982)	0.021
$\sigma^*_{M\text{-}Pb}$	0.438	(0.169)	0.077	(0.106)	−0.361	0.159	(0.185)	0.060	(0.180)	−0.099
$\sigma^*_{M\text{-}Pa}$	0.437	(0.170)	0.077	(0.106)	−0.361	0.160	(0.182)	0.080	(0.248)	−0.080

Table 8.4. Continued.

	Ir					Rh				
	NR		Rel		Δ	NR		Rel		Δ
Reactant										
$\sigma_{C\text{-}H}$	−0.613	(1.976)	−0.616	(1.975)	−0.003	−0.613	(1.975)	−0.615	(1.975)	−0.002
n_O	−0.487	(1.826)	−0.522	(1.795)	−0.036	−0.497	(1.826)	−0.506	(1.814)	−0.009
$\sigma_{M\text{-}Pa}$	−0.441	(1.849)	−0.495	(1.903)	−0.054	−0.451	(1.846)	−0.466	(1.869)	−0.015
$\sigma_{M\text{-}Pb}$	−0.429	(1.844)	−0.488	(1.899)	−0.059	−0.438	(1.841)	−0.451	(1.863)	−0.013
n_M	−0.332	(1.922)	−0.329	(1.892)	0.004	−0.344	(1.928)	−0.341	(1.921)	0.003
n_M	−0.330	(1.906)	−0.313	(1.869)	0.017	−0.324	(1.911)	−0.323	(1.903)	0.000
n_M	−0.318	(1.937)	−0.304	(1.909)	0.014	−0.320	(1.942)	−0.317	(1.936)	0.003
n_M	−0.315	(1.981)	−0.298	(1.978)	0.017	−0.317	(1.983)	−0.312	(1.982)	0.005
$\sigma^*_{M\text{-}Pb}$	0.175	(0.189)	0.054	(0.162)	−0.121	0.043	(0.193)	0.060	(0.180)	0.017
$\sigma^*_{M\text{-}Pa}$	0.183	(0.254)	0.082	(0.239)	−0.101	0.062	(0.257)	0.080	(0.248)	0.018
$\sigma^*_{C\text{-}H}$	0.542	(0.013)	0.539	(0.013)	−0.003	0.540	(0.013)	0.538	(0.013)	−0.002

Table 8.4. Continued.

		Ir					Rh				
		NR		Rel		Δ	NR		Rel		Δ
Product											
	n_O	−0.489	(1.766)	−0.518	(1.750)	−0.029	−0.490	(1.771)	−0.498	(1.765)	−0.009
	$\sigma_{M\text{-}Pa}$	−0.442	(1.873)	−0.508	(1.904)	−0.066	−0.454	(1.863)	−0.484	(1.878)	−0.029
	$\sigma_{M\text{-}C}$	−0.389	(1.873)	−0.467	(1.908)	−0.078	−0.402	(1.859)	−0.440	(1.877)	−0.038
	$\sigma_{M\text{-}H}$	−0.331	(1.856)	−0.461	(1.903)	−0.130	−0.369	(1.828)	−0.433	(1.853)	−0.065
	n_M	−0.391	(1.965)	−0.376	(1.948)	0.015	−0.395	(1.969)	−0.390	(1.965)	0.004
	n_M	−0.385	(1.961)	−0.370	(1.943)	0.016	−0.391	(1.967)	−0.387	(1.963)	0.004
	n_M	−0.383	(1.948)	−0.366	(1.922)	0.016	−0.387	(1.952)	−0.383	(1.945)	0.005
	n_{Pb}	−0.363	(1.632)	−0.275	(1.470)	0.088	−0.378	(1.633)	−0.279	(1.506)	0.099
	$\sigma^*_{M\text{-}Pa}$	0.379	(0.327)	0.051	(0.298)	−0.328	0.175	(0.342)	0.042	(0.323)	−0.133
	$\sigma^*_{M\text{-}C}$	0.195	(0.445)	0.067	(0.470)	−0.128	0.101	(0.458)	0.051	(0.461)	−0.050
	$\sigma^*_{M\text{-}H}$	0.446	(0.107)	0.102	(0.085)	−0.343	0.246	(0.125)	0.092	(0.109)	−0.154

8.5 Conclusion

This chapter elucidated that the relativistic effect is essential for the C–H activation of *N*-phenylbenzamide with cationic Ir catalysts. The deuteration experiments reported that the C–H activation of *N*-phenylbenzamide occurred using Ir–diphosphine catalysts and did not occur for Rh–diphosphine catalysts. DFT calculations suggest that the difference in reactivity originates from the relativistic effect. The self-consistent *d* orbital expansion causes the activation of the *d* orbitals of Ir, stabilizing TS and affording the product of the C–H activation. The relativistic effect of the Rh catalysts is similar but small in magnitude. Consequently, the origin of the catalytic activity was clarified from the viewpoint of the relativistic effect on the geometric parameters and electronic structures.

References

1. K.S. Pitzer, *Acc. Chem. Res.* **12**, 271 (1979).

2. P. Pyykko and J.P. Desclaux, *Acc. Chem. Res.* **12**, 276 (1979).

3. P. Pyykko, *Chem. Rev.* **88**, 563 (1988).

4. D.G. Fedorov, S. Koseki, M.W. Schmidt, and M.S. Gordon, *Int. Rev. Phys. Chem.* **22**, 551 (2003).

5. K.G. Dyall and K. Faegri, *Introduction to Relativistic Quantum Chemistry*, (Oxford University Press, New York, 2007) p. 544.

6. V. Pershina, Electronic Structure and Chemistry of the Heaviest Elements, in *Relativistic Methods for Chemists*, edited by Maria Barysz and Yasuyuki Ishikawa, (Springer Netherlands, Dordrecht, 2010) pp. 451-520.

7. M. Reiher and A. Wolf, *Relativistic quantum chemistry : the fundamental theory of molecular science / Markus Reiher and Alexander Wolf*, Second edition. ed. (Wiley-VCH, Weinheim an der Bergstrasse, Germany, 2015).

8. A. Sommerfeld, *Ann. Phys.* **356**, 1 (1916).

9. D.F. Mayers and D.R. Hartree, *Proc. R. soc. Lond. Ser. A-Contain. Pap. Math. Phys. Character*, **241**, 93 (1997).

10. Y. Kayaki, H. Tsukamoto, M. Kaneko, I. Shimizu, A. Yamamoto, M. Tachikawa, and T. Nakajima, *J. Organomet. Chem.* **622**, 199 (2001).

11. D.J. Gorin and F.D. Toste, *Nature* **446**, 395 (2007).

12. M. Pernpointner and A.S. Hashmi, *J. Chem. Theory Comput.* **5**, 2717 (2009).

13. M. Lein, M. Rudolph, S.K. Hashmi, and P. Schwerdtfeger, *Organometallics*, **29**, 2206 (2010).

14. M. Vasiliu, S. Li, A.J. Arduengo, and D.A. Dixon, *J. Phys. Chem. C*, **115**, 12106 (2011).

15. H. Xie, Q. Sun, G. Ren, and Z. Cao, *J. Org. Chem.* **79**, 11911 (2014).

16. A. Leyva-Pérez and A. Corma, *Angew. Chem. Int. Ed.* **51**, 614 (2012).

17. N.K. Dandu, J.A. Reed, and S.O. Odoh, *J. Phys. Chem. C*, **122**, 1024 (2018).

18. H. Braband, M. Benz, B. Spingler, J. Conradie, R. Alberto, and A. Ghosh, *Inorg. Chem.* **60**, 11090 (2021).

19. J.F. Hartwig, *Acc. Chem. Res.* **45**, 864 (2012).

20. S. Pan and T. Shibata, *ACS Catal.* **3**, 704 (2013).

21. T. Shibata, K. Tsuchikama, and S. Pan, *J. Synth. Org. Chem.* **71**, 1182 (2013).

22. J.F. Hartwig, *J. Am. Chem. Soc.* **138**, 2 (2016).

23. V.R. Landaeta and R.E. Rodríguez-Lugo, *J. Mol. Catal. A Chem.* **426**, 316 (2017).

24. J.F. Hartwig and E.A. Romero, *Tetrahedron*, **75**, 4059 (2019).

25. X. Li, W. Ouyang, J. Nie, S. Ji, Q. Chen, and Y. Huo, *ChemCatChem*, **12**, 2358 (2020).

26. T.M. Figg, S. Park, J. Park, S. Chang, and D.G. Musaev, *Organometallics*, **33**, 4076 (2014).

27. Y. Park, J. Heo, M. Baik, and S. Chang, *J. Am. Chem. Soc.* **138**, 14020 (2016).

28. K. Tsuchikama, M. Kasagawa, Y. Hashimoto, K. Endo, and T. Shibata, *J. Organomet. Chem.* **693**, 3939 (2008).

29. S. Pan, N. Ryu, and T. Shibata, *J. Am. Chem. Soc.* **134**, 17474 (2012).

30. T. Shibata, M. Michino, H. Kurita, Y. Tahara, and K.S. Kanyiva, *Chem. Eur. J.* **23**, 88 (2017).

31. T. Shibata, H. Kurita, S. Onoda, and K.S. Kanyiva, *Asian J. Org. Chem.* **7**, 1411 (2018).

32. T. Shibata, M. Kojima, S. Onoda, and M. Ito, *Org. Lett.* **23**, 8158 (2021).

33. Y. Tahara, M. Michino, M. Ito, K.S. Kanyiva, and T. Shibata, *Chem. Commun.* **51**, 16660 (2015).

34. K. Fukui, *J. Phys. Chem.* **74**, 4161 (1970).

35. K. Fukui, *Acc. Chem. Res.* **14**, 363 (1981).

36. C. Gonzalez and H.B. Schlegel, *J. Chem. Phys.* **90**, 2154 (1989).

37. C. Gonzalez and H.B. Schlegel, *J. Phys. Chem.* **94**, 5523 (1990).

38. A.V. Marenich, C.J. Cramer, and D.G. Truhlar, *J. Phys. Chem. B*, **113**, 6378 (2009).

39. E.D. Glendening, C.R. Landis, and F. Weinhold, *J. Comput. Chem.* **34**, 1429 (2013).

40. J. Chai and M. Head-Gordon, *Phys. Chem. Chem. Phys.* **10**, 6615 (2008).

41. M.J. Frisch, G.W. Trucks, H.B. Schlegel, G.E. Scuseria, M.A. Robb, J.R. Cheeseman, G. Scalmani, V. Barone, B. Mennucci, and G.A. Petersson, Gaussian 09 (Revision C.01), Gaussian, Inc., Wallingford CT(2010).

42. K.A. Peterson, D. Figgen, M. Dolg, and H. Stoll, *J. Chem. Phys.* **126**, 124101 (2007).

43. D. Figgen, K.A. Peterson, M. Dolg, and H. Stoll, *J. Chem. Phys.* **130**, 164108 (2009).

44. P.C. Hariharan and J.A. Pople, *Theor. Chim. Acta*, **28**, 213 (1973).

45. M.M. Francl, W.J. Pietro, W.J. Hehre, J.S. Binkley, M.S. Gordon, D.J. DeFrees, and J.A. Pople, *J. Chem. Phys.* **77**, 3654 (1982).

46. G.S. Hammond, *J. Am. Chem. Soc.* **77**, 334 (1955).

Appendix

Table A8.1. Bond distances (in Å) and bond angles of reactants, TSs, and products of the C-H bond activation at the *ortho* positions of carbonyl group by the Ir and Rh complexes with the SEGPHOS ligand. Those of separated systems, namely, free benzamide molecule and isolated metal complexes, are also tabulated. M designates the transition metal (Ir or Rh). Δ represents the difference between the results obtained by the nonrelativistic (NR) and relativistic (Rel) calculations.

	Ir			Rh		
	NR	Rel	Δ	NR	Rel	Δ
Separated System						
Benzamide						
C-H	1.08	1.08	0.00	1.08	1.08	0.00
Metal Complexes						
M-P_a	2.28	2.19	−0.09	2.22	2.20	−0.02
M-P_b	2.28	2.19	−0.09	2.22	2.20	−0.02
P_a-M-P_b	91.1	94.6	3.5	91.3	92.8	1.6
Reactant						
M-P_a	2.30	2.23	−0.06	2.25	2.23	−0.02
M-P_b	2.31	2.21	−0.09	2.25	2.22	−0.02
M-O	2.32	2.19	−0.13	2.23	2.20	−0.04
M-C	2.74	2.60	−0.14	2.63	2.61	−0.02
M-H	2.80	2.61	−0.19	2.66	2.62	−0.04
C-H	1.09	1.09	0	1.09	1.09	0
P_a-M-P_b	91.1	93.2	2.0	91.7	92.6	0.9
P_a-M-O	174.4	172.4	−1.9	173.1	172.5	−0.6
P_b-M-C	154.0	160.4	6.4	158.0	158.9	1.0
P_a-M-H	111.2	105.5	−5.7	107.3	106.0	−1.3
P_b-M-H	157.3	157.9	0.6	159.5	159.2	−0.3
C-M-H	22.6	24.2	1.5	23.7	24	0.3

Table A8.1. Continued.

	Ir			Rh		
	NR	Rel	Δ	NR	Rel	Δ
Transition State						
M-P_a	2.35	2.27	−0.09	2.28	2.27	−0.02
M-P_b	2.56	2.41	−0.15	2.47	2.46	−0.01
M-O	2.21	2.14	−0.07	2.14	2.13	−0.01
M-C	2.08	2.05	−0.02	2.00	1.99	−0.01
M-H	1.62	1.62	0	1.57	1.55	−0.03
C-H	1.77	1.50	−0.27	1.74	1.76	0.01
P_a-M-P_b	92.1	93.4	1.3	95.3	94.2	−1.1
P_a-M-O	177.9	175.1	−2.8	176.6	176.8	0.3
P_b-M-C	134.1	145.8	11.6	121.1	131.9	10.8
P_a-M-H	89.3	90.2	0.9	89.9	89.1	−0.7
P_b-M-H	169.5	165.5	−4.0	174.8	168.4	−6.4
C-M-H	55.6	46.3	−9.3	57	57.9	0.9
Product						
M-P_a	2.36	2.29	−0.08	2.31	2.28	−0.03
M-P_b	2.50	2.41	−0.09	2.46	2.42	−0.03
M-O	2.20	2.14	−0.06	2.14	2.12	−0.02
M-C	2.12	2.06	−0.06	2.05	2.04	−0.02
M-H	1.56	1.52	−0.03	1.50	1.49	−0.01
C-H	2.58	2.63	0.05	2.49	2.53	0.04
P_a-M-P_b	91.8	92.9	1.1	92.8	93.8	1.0
P_a-M-O	172.7	172.7	0.1	171.4	171.1	−0.3
P_b-M-C	168.5	166.8	−1.6	168.1	167.3	−0.9
P_a-M-H	84.5	85.8	1.3	82.5	83.9	1.4
P_b-M-H	95.4	92.4	−3.1	98.4	96.7	−1.7
C-M-H	87.8	93.2	5.4	87.4	90.1	2.8

Table A8.2. Bond distances (in Å) and bond angles of reactants, TSs, and products of the C-H bond activation at the *ortho* positions of amino group by the Ir and Rh complexes with the BINAP ligand. Those of separated systems, namely, free benzamide molecule and isolated metal complexes, are also tabulated. M designates the transition metal (Ir or Rh). Δ represents the difference between the results obtained by the nonrelativistic (NR) and relativistic (Rel) calculations.

	Ir			Rh		
	NR	Rel	Δ	NR	Rel	Δ
Separated System						
Benzamide						
C-H	1.08	1.08	0.00	1.08	1.08	0.00
Metal Complexes						
M-P_a	2.28	2.20	−0.08	2.22	2.20	−0.02
M-P_b	2.28	2.19	−0.09	2.22	2.20	−0.02
P_a-M-P_b	89.8	93.1	3.3	90.3	91.6	1.3
Reactant						
M-P_a	2.32	2.25	−0.07	2.26	2.24	−0.02
M-P_b	2.31	2.22	−0.09	2.25	2.23	−0.02
M-O	2.26	2.16	−0.10	2.18	2.16	−0.02
M-C	2.70	2.67	−0.04	2.65	2.63	−0.02
M-H	2.73	2.72	−0.01	2.67	2.65	−0.02
C-H	1.09	1.09	0.00	1.09	1.09	0.00
P_a-M-P_b	90.1	92.1	2.0	90.7	91.5	0.8
P_a-M-O	175.9	175.3	−0.7	174.5	175.0	0.4
P_b-M-C	151.4	151.8	0.4	150.0	150.6	0.5
P_a-M-H	119.4	118.0	−1.4	118.2	117.6	−0.6
P_b-M-H	128.5	128.6	0.2	126.5	126.8	0.4
C-M-H	23.0	23.2	0.2	23.6	23.7	0.2

Table A8.2. Continued.

	Ir			Rh		
	NR	Rel	Δ	NR	Rel	Δ
Transition State						
M-P_a	2.37	2.28	−0.09	2.32	2.29	−0.03
M-P_b	2.48	2.36	−0.12	2.42	2.38	−0.04
M-O	2.17	2.12	−0.06	2.11	2.09	−0.01
M-C	2.17	2.15	−0.02	2.10	2.09	−0.01
M-H	1.59	1.61	0.02	1.52	1.53	0.00
C-H	1.71	1.44	−0.27	1.75	1.66	−0.10
P_a-M-P_b	89.8	91.2	1.4	90.2	91.1	0.9
P_a-M-O	169.2	167.9	−1.2	167.4	165.8	−1.6
P_b-M-C	163.5	164.5	1.0	161.7	161.2	−0.6
P_a-M-H	93.0	95.4	2.4	92.0	93.0	1.1
P_b-M-H	113.6	124.0	10.4	108.2	111.2	3.0
C-M-H	51.5	42.2	−9.3	55.2	51.7	−3.5
Product						
M-P_a	2.38	2.30	−0.08	2.32	2.30	−0.02
M-P_b	2.50	2.40	−0.10	2.45	2.42	−0.03
M-O	2.17	2.11	−0.06	2.11	2.09	−0.01
M-C	2.13	2.07	−0.06	2.06	2.04	−0.02
M-H	1.55	1.52	−0.03	1.49	1.49	−0.01
C-H	2.54	2.53	−0.01	2.42	2.42	0.01
P_a-M-P_b	91.0	92.1	1.0	91.6	92.2	0.6
P_a-M-O	176.7	170.8	−5.9	173.7	172.7	−1.0
P_b-M-C	170.5	170.4	−0.1	170.3	170.6	0.3
P_a-M-H	88.6	89.0	0.4	87.7	87.9	0.3
P_b-M-H	87.3	86.1	−1.2	89.0	88.7	−0.3
C-M-H	85.8	88.3	2.5	84.1	85.2	1.0

Table A8.3. Bond distances (in Å) and bond angles of reactants, TSs, and products of the C-H bond activation at the *ortho* positions of carbonyl group by the Ir and Rh complexes with the BINAP ligand. Those of separated systems, namely, free benzamide molecule and isolated metal complexes, are also tabulated. M designates the transition metal (Ir or Rh). Δ represents the difference between the results obtained by the nonrelativistic (NR) and relativistic (Rel) calculations.

	Ir			Rh		
	NR	Rel	Δ	NR	Rel	Δ
Separated System						
Benzamide						
C-H	1.08	1.08	0.00	1.08	1.08	0.00
Metal Complexes						
M-P_a	2.28	2.20	−0.08	2.22	2.20	−0.02
M-P_b	2.28	2.19	−0.09	2.22	2.20	−0.02
P_a-M-P_b	89.8	93.1	3.3	90.3	91.6	1.3
Reactant						
M-P_a	2.31	2.23	−0.08	2.24	2.22	−0.02
M-P_b	2.31	2.21	−0.10	2.25	2.22	−0.02
M-O	2.30	2.19	−0.11	2.22	2.19	−0.03
M-C	2.68	2.66	−0.02	2.62	2.61	−0.01
M-H	2.74	2.70	−0.05	2.60	2.56	−0.04
C-H	1.09	1.09	0.00	1.09	1.09	0.00
P_a-M-P_b	90.4	92.4	2.0	91.1	91.9	0.9
P_a-M-O	174.0	171.5	−2.4	173.4	172.6	−0.8
P_b-M-C	159.6	161.4	1.9	157.6	157.8	0.2
P_a-M-H	110.5	106.5	−4.0	107.4	106.0	−1.4
P_b-M-H	156.5	157.0	0.5	159.9	160.2	0.3
C-M-H	23.1	23.4	0.3	24.1	24.3	0.2

Table A8.3. Continued.

	Ir			Rh		
	NR	Rel	Δ	NR	Rel	Δ
Transition State						
M-P_a	2.35	2.27	−0.09	2.29	2.27	−0.02
M-P_b	2.57	2.41	−0.16	2.47	2.45	−0.02
M-O	2.21	2.14	−0.07	2.14	2.12	−0.02
M-C	2.08	2.05	−0.02	2.00	1.99	−0.01
M-H	1.62	1.62	0.00	1.57	1.56	−0.02
C-H	1.78	1.50	−0.28	1.74	1.74	0.00
P_a-M-P_b	91.1	92.4	1.3	94.4	93.2	−1.2
P_a-M-O	178.9	176.8	−2.1	176.6	177.5	0.9
P_b-M-C	134.4	148.1	13.7	121.0	130.6	9.6
P_a-M-H	89.9	91.5	1.6	90.7	90.3	−0.3
P_b-M-H	168.9	162.9	−6.0	174.9	170.3	−4.6
C-M-H	56.1	46.4	−9.6	57.0	57.2	0.2
Product						
M-P_a	2.36	2.29	−0.08	2.31	2.28	−0.03
M-P_b	2.50	2.40	−0.10	2.45	2.42	−0.03
M-O	2.20	2.13	−0.07	2.12	2.11	−0.02
M-C	2.12	2.07	−0.05	2.06	2.05	−0.02
M-H	1.55	1.52	−0.03	1.50	1.49	−0.01
C-H	2.60	2.64	0.04	2.50	2.51	0.01
P_a-M-P_b	91.1	92.4	1.3	92.1	92.6	0.5
P_a-M-O	172.7	175.3	2.6	174.4	174.6	0.2
P_b-M-C	168.8	167.3	−1.4	168.5	168.1	−0.4
P_a-M-H	84.7	87.8	3.1	85.1	86.2	1.1
P_b-M-H	96.4	92.7	−3.7	97.6	96.7	−0.9
C-M-H	88.8	93.2	4.4	87.8	89.0	1.3

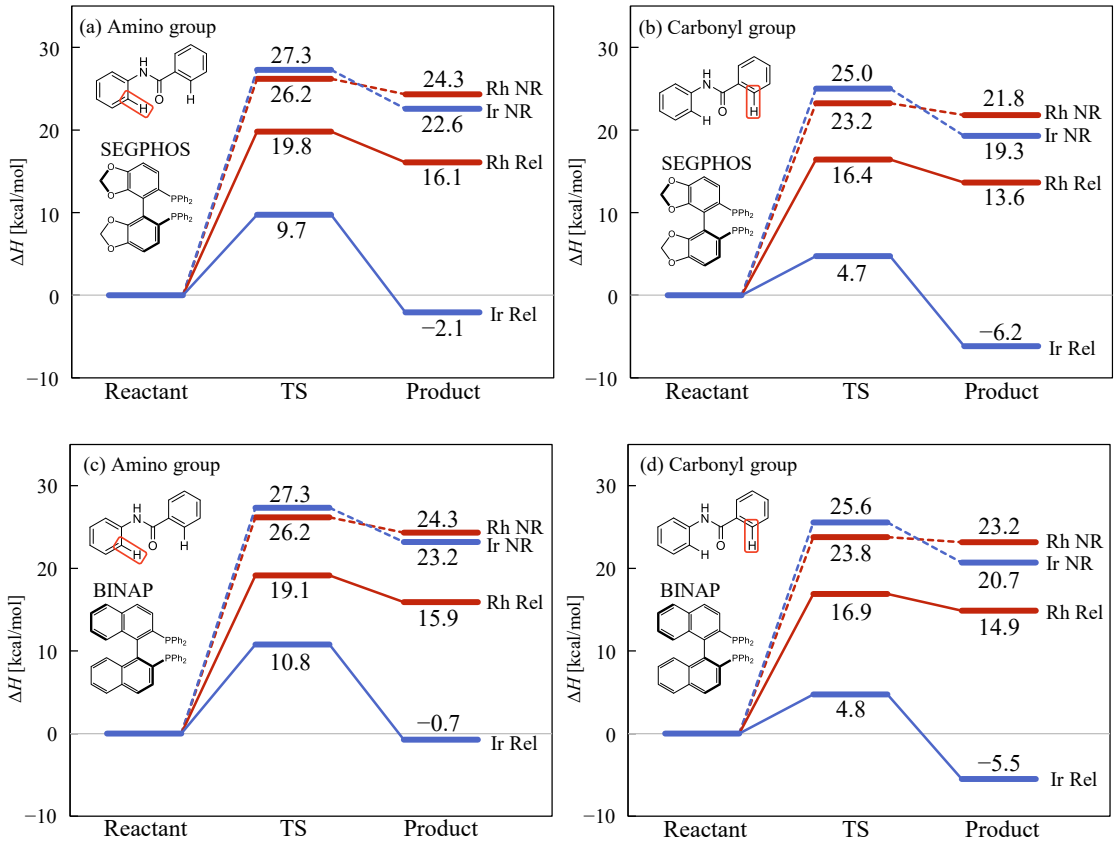

Figure A8.1. Enthalpy diagrams of the C-H bond activation. (a) and (b) correspond to the SEGPHOS ligand and (c) and (d) to the BINAP ligand. (a) and (c) correspond to the *ortho* position of the amino group and (b) and (d) to that of the carbonyl group. Black and gray lines represent the results of the Ir and Rh complexes, respectively. Dashed and solid lines represent the results of the nonrelativistic (NR) and relativistic (Rel) calculations, respectively.

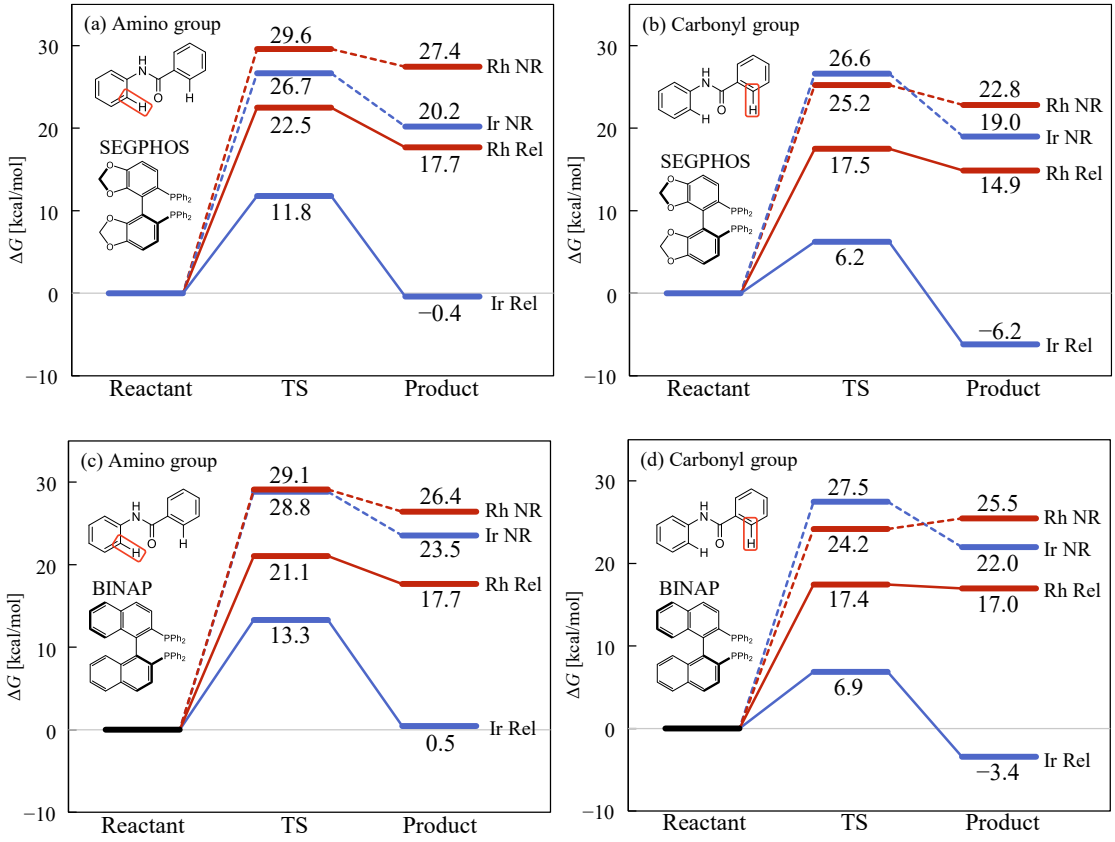

Figure A8.2. Gibbs energy diagrams of the C-H bond activation. (a) and (b) correspond to the SEGPHOS ligand and (c) and (d) to the BINAP ligand. (a) and (c) correspond to the *ortho* position of the amino group and (b) and (d) to that of the carbonyl group. Black and gray lines represent the results of the Ir and Rh complexes, respectively. Dashed and solid lines represent the results of the nonrelativistic (NR) and relativistic (Rel) calculations, respectively.

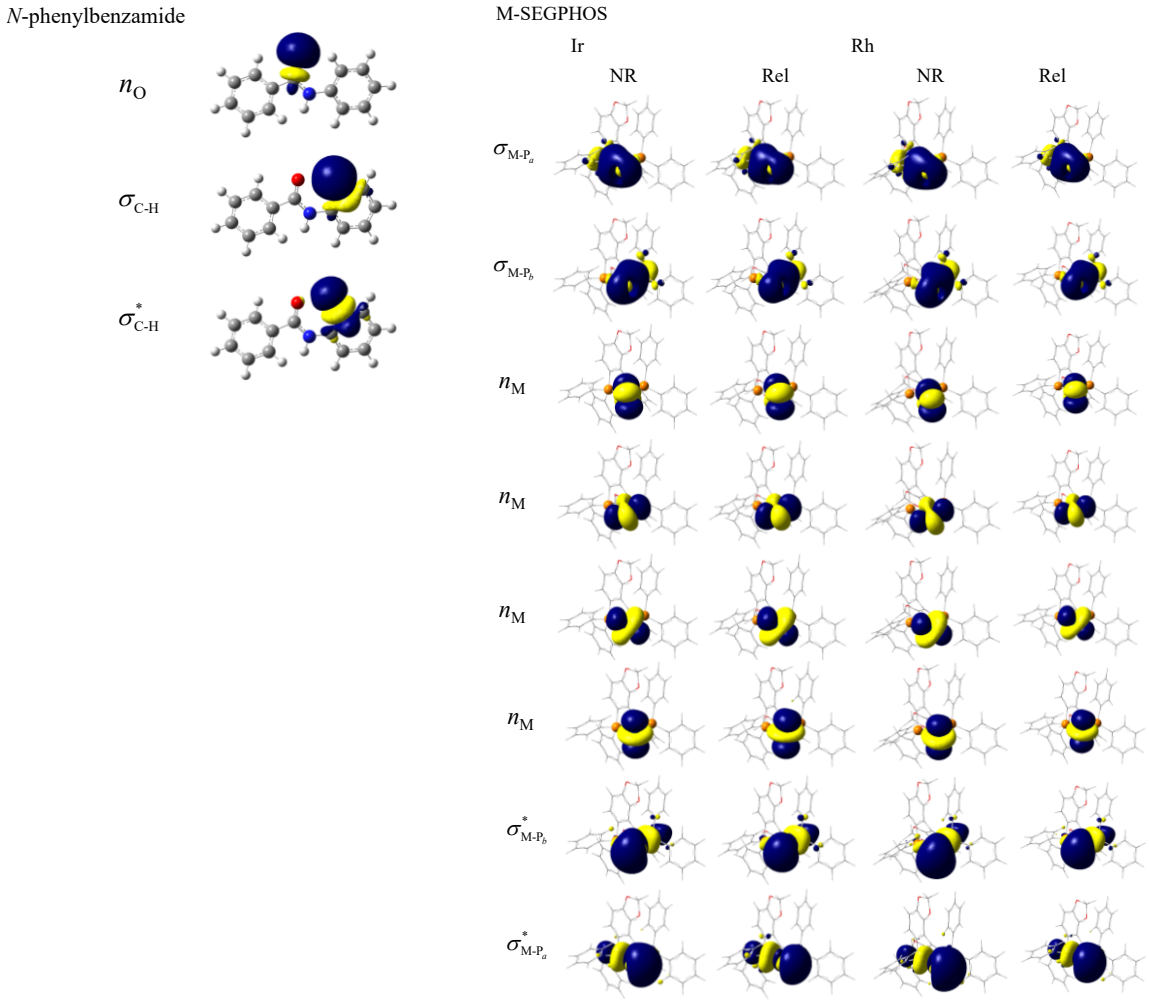

Figure A8.3. Visualization of NBOs in the valence region of the separated system, namely *N*-phenylbenzamide and Ir and Rh complexes with SEGPHOS ligand, which were calculated by the nonrelativistic (NR) and relativistic (Rel) treatments.

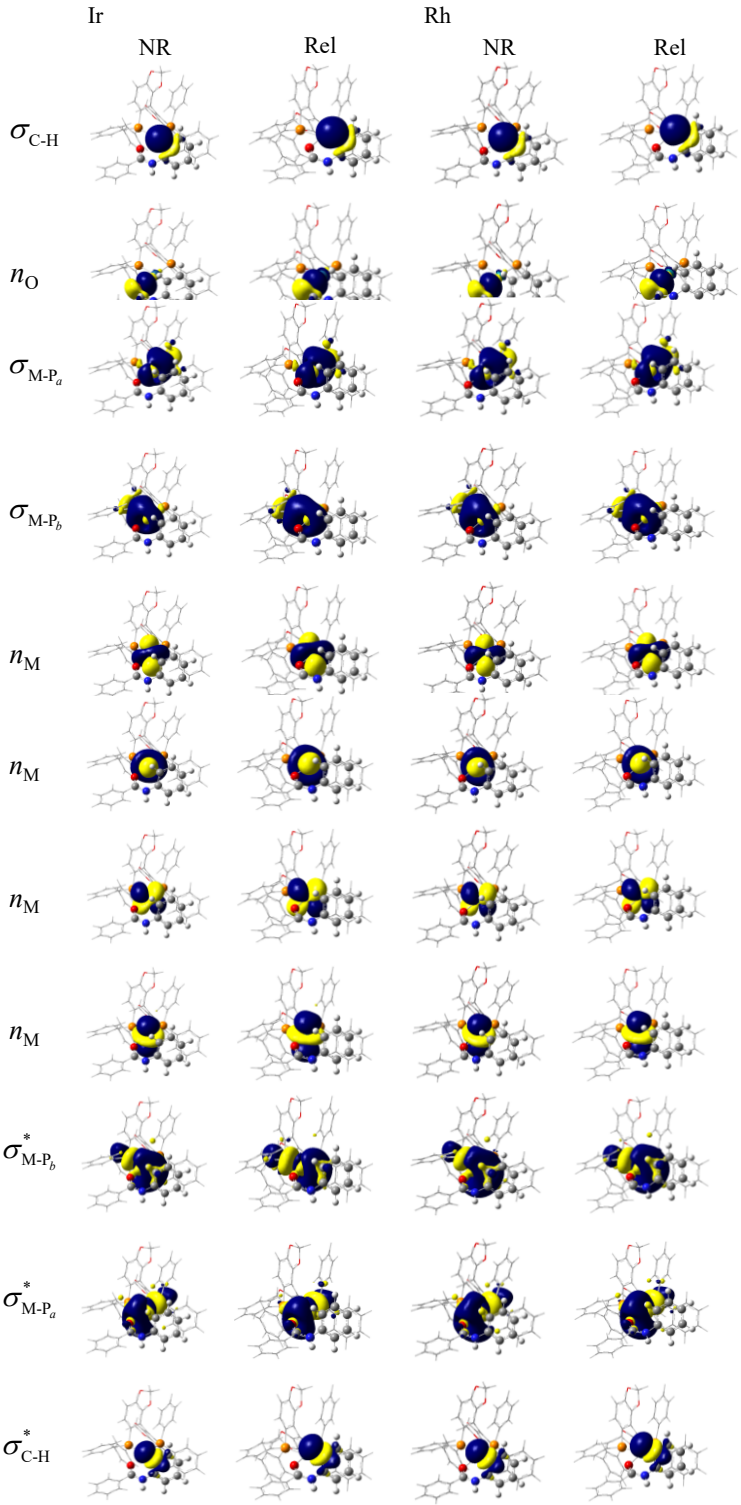

Figure A8.4. Visualization of NBOs in the valence region of the reactants of the C-H activation at the *ortho* position of amino group with SEGPHOS ligand, which were calculated by the nonrelativistic (NR) and relativistic (Rel) treatments.

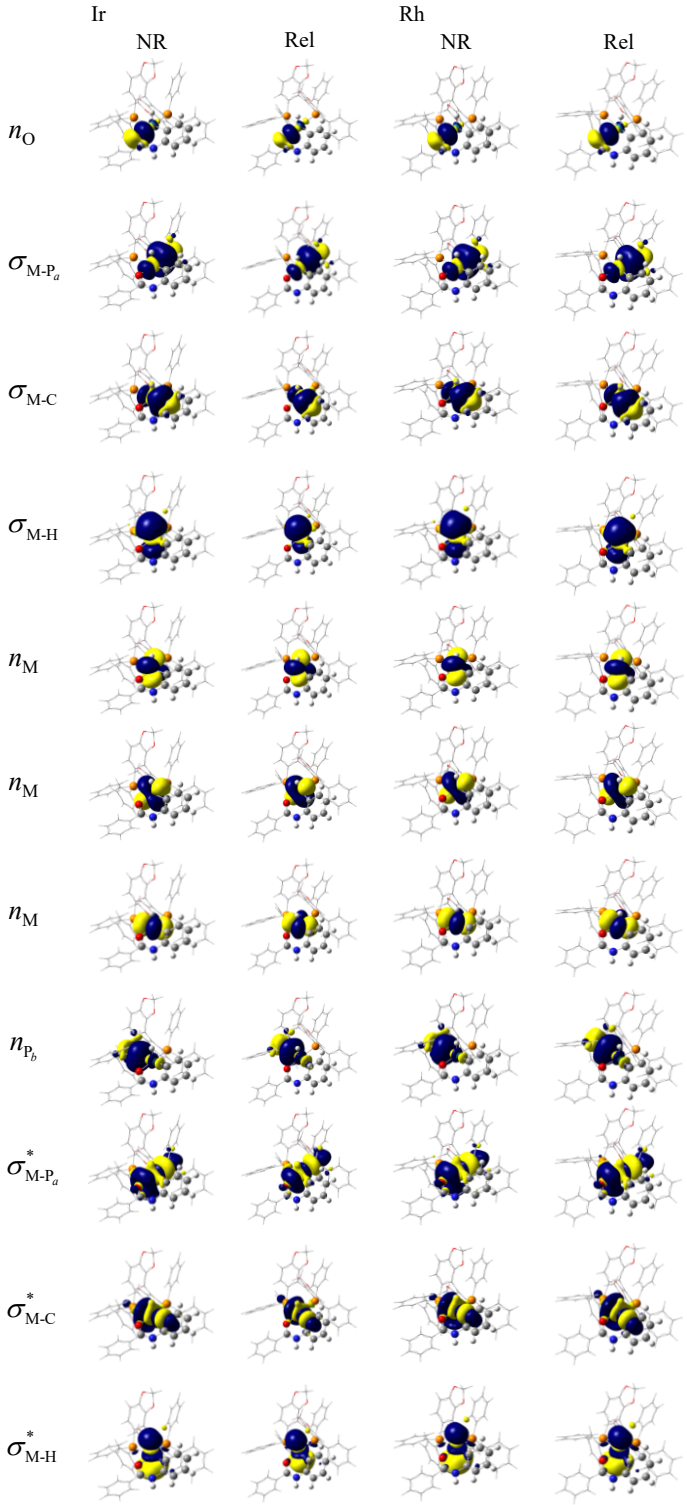

Figure A8.5. Visualization of NBOs in the valence region of the products of the C-H activation at the *ortho* position of amino group with SEGPHOS ligand, which were calculated by the nonrelativistic (NR) and relativistic (Rel) treatments.

Table A8.4. NBO population analysis (%) in the valence region of the Ir complexes with SEGPHOS ligand in the C-H activation at the *ortho* position of amino group calculated by the relativistic treatments.

	Ir		C		H
	5*d*	6*s*	2*s*	2*p*	1*s*
Separated System					
N-phenylbenzamide					
n_{O}	0.00	0.00	0.00	0.00	0.00
$\sigma_{C\text{-}H}$	0.00	0.00	19.54	44.81	35.59
$\sigma_{C\text{-}H^*}$	0.00	0.00	10.81	24.78	64.34
Metal Complex					
$\sigma_{M\text{-}Pa}$	18.84	16.30	-	-	-
$\sigma_{M\text{-}Pb}$	18.83	16.30	-	-	-
n_{M}	99.62	0.33	-	-	-
n_{M}	99.81	0.18	-	-	-
n_{M}	99.76	0.00	-	-	-
n_{M}	93.03	6.87	-	-	-
$\sigma^*_{M\text{-}Pb}$	34.64	29.99	-	-	-
$\sigma^*_{M\text{-}Pa}$	34.65	29.98	-	-	-
Reactant					
$\sigma_{C\text{-}H}$	0.00	0.00	19.47	45.07	35.40
n_{O}	0.00	0.00	0.00	0.00	0.00
$\sigma_{M\text{-}Pa}$	16.48	13.61	0.00	0.00	0.00
$\sigma_{M\text{-}Pb}$	16.67	16.50	0.00	0.00	0.00
n_{M}	99.79	0.17	0.00	0.00	0.00
n_{M}	99.84	0.07	0.00	0.00	0.00
n_{M}	99.78	0.21	0.00	0.00	0.00
n_{M}	95.38	4.60	0.00	0.00	0.00
$\sigma^*_{M\text{-}Pb}$	33.57	33.22	0.00	0.00	0.00
$\sigma^*_{M\text{-}Pa}$	38.25	31.56	0.00	0.00	0.00
$\sigma^*_{C\text{-}H}$	0.00	0.00	10.68	24.72	64.54
Product					
n_{O}	0.00	0.00	0.00	0.00	0.00
$\sigma_{M\text{-}Pa}$	21.02	12.39	0.00	0.00	0.00
$\sigma_{M\text{-}C}$	23.92	13.37	17.51	45.19	0.00
$\sigma_{M\text{-}H}$	42.57	15.48	0.00	0.00	41.83
n_{M}	99.68	0.24	0.00	0.00	0.00
n_{M}	99.98	0.00	0.00	0.00	0.00
n_{M}	99.96	0.01	0.00	0.00	0.00
n_{Pb}	0.00	0.00	0.00	0.00	0.00
$\sigma^*_{M\text{-}Pa}$	41.79	24.63	0.00	0.00	0.00
$\sigma^*_{M\text{-}C}$	40.22	22.48	10.41	26.89	0.00
$\sigma^*_{M\text{-}H}$	30.72	11.17	0.00	0.00	57.98

Table A8.4. Continued.

	P_a		P_b		O		Rest
	3*s*	3*p*	3*s*	3*p*	2*s*	2*p*	
Separated System							
N-phenylbenzamide							
n_O	-	-	-	-	58.13	41.82	0.05
$\sigma_{C\text{-}H}$	-	-	-	-	0.00	0.00	0.06
$\sigma_{C\text{-}H^*}$	-	-	-	-	0.00	0.00	0.07
Metal Complex							
$\sigma_{M\text{-}Pa}$	18.76	45.77	0.00	0.00	-	-	0.31
$\sigma_{M\text{-}Pb}$	0.00	0.00	18.77	45.78	-	-	0.32
n_M	0.00	0.00	0.00	0.00	-	-	0.05
n_M	0.00	0.00	0.00	0.00	-	-	0.01
n_M	0.00	0.00	0.00	0.00	-	-	0.24
n_M	0.00	0.00	0.00	0.00	-	-	0.10
$\sigma^*_{M\text{-}Pb}$	0.00	0.00	10.20	24.89	-	-	0.28
$\sigma^*_{M\text{-}Pa}$	10.21	24.90	0.00	0.00	-	-	0.28
Reactant							
$\sigma_{C\text{-}H}$	0.00	0.00	0.00	0.00	0.00	0.00	0.06
n_O	0.00	0.00	0.00	0.00	21.37	78.58	0.05
$\sigma_{M\text{-}Pa}$	23.23	46.51	0.00	0.00	0.00	0.00	0.17
$\sigma_{M\text{-}Pb}$	0.00	0.00	21.17	45.48	0.00	0.00	0.17
n_M	0.00	0.00	0.00	0.00	0.00	0.00	0.04
n_M	0.00	0.00	0.00	0.00	0.00	0.00	0.09
n_M	0.00	0.00	0.00	0.00	0.00	0.00	0.01
n_M	0.00	0.00	0.00	0.00	0.00	0.00	0.02
$\sigma^*_{M\text{-}Pb}$	0.00	0.00	10.51	22.60	0.00	0.00	0.11
$\sigma^*_{M\text{-}Pa}$	10.01	20.05	0.00	0.00	0.00	0.00	0.13
$\sigma^*_{C\text{-}H}$	0.00	0.00	0.00	0.00	0.00	0.00	0.06
Product							
n_O	0.00	0.00	0.00	0.00	20.21	79.73	0.06
$\sigma_{M\text{-}Pa}$	20.84	45.54	0.00	0.00	0.00	0.00	0.22
$\sigma_{M\text{-}C}$	0.00	0.00	0.00	0.00	0.00	0.00	0.00
$\sigma_{M\text{-}H}$	0.00	0.00	0.00	0.00	0.00	0.00	0.11
n_M	0.00	0.00	0.00	0.00	0.00	0.00	0.08
n_M	0.00	0.00	0.00	0.00	0.00	0.00	0.02
n_M	0.00	0.00	0.00	0.00	0.00	0.00	0.03
n_{Pb}	0.00	0.00	15.03	84.90	0.00	0.00	0.07
$\sigma^*_{M\text{-}Pa}$	10.48	22.90	0.00	0.00	0.00	0.00	0.19
$\sigma^*_{M\text{-}C}$	0.00	0.00	0.00	0.00	0.00	0.00	0.01
$\sigma^*_{M\text{-}H}$	0.00	0.00	0.00	0.00	0.00	0.00	0.14

Table A8.5. NBO population analysis (%) in the valence region of the Ir complexes with SEGPHOS ligand in the C-H activation at the *ortho* position of amino group calculated by the nonrelativistic treatments.

	Ir		C		H
	5*d*	6*s*	2*s*	2*p*	1*s*
Separated System					
N-phenylbenzamide					
n_{O}	0.00	0.00	0.00	0.00	0.00
$\sigma_{C\text{-}H}$	0.00	0.00	19.54	44.81	35.59
$\sigma_{C\text{-}H^*}$	0.00	0.00	10.81	24.78	64.34
Metal Complex					
$\sigma_{M\text{-}Pa}$	14.19	13.50	-	-	-
$\sigma_{M\text{-}Pb}$	14.22	13.50	-	-	-
n_{M}	99.89	0.08	-	-	-
n_{M}	99.95	0.04	-	-	-
n_{M}	99.83	0.00	-	-	-
n_{M}	97.97	2.02	-	-	-
$\sigma^*_{M\text{-}Pb}$	36.73	34.90	-	-	-
$\sigma^*_{M\text{-}Pa}$	36.72	34.94	-	-	-
Reactant					
$\sigma_{C\text{-}H}$	0.00	0.00	19.26	44.94	35.74
n_{O}	0.00	0.00	0.00	0.00	0.00
$\sigma_{M\text{-}Pa}$	13.74	11.66	0.00	0.00	0.00
$\sigma_{M\text{-}Pb}$	12.55	13.46	0.00	0.00	0.00
n_{M}	99.94	0.02	0.00	0.00	0.00
n_{M}	99.89	0.06	0.00	0.00	0.00
n_{M}	99.90	0.09	0.00	0.00	0.00
n_{M}	97.87	2.12	0.00	0.00	0.00
$\sigma^*_{M\text{-}Pb}$	35.66	38.24	0.00	0.00	0.00
$\sigma^*_{M\text{-}Pa}$	40.28	34.19	0.00	0.00	0.00
$\sigma^*_{C\text{-}H}$	0.00	0.00	10.72	25.02	64.20
Product					
n_{O}	0.00	0.00	0.00	0.00	0.00
$\sigma_{M\text{-}Pa}$	18.48	11.49	0.00	0.00	0.00
$\sigma_{M\text{-}C}$	25.65	12.90	15.88	45.57	0.00
$\sigma_{M\text{-}H}$	41.92	16.18	0.00	0.00	41.77
n_{M}	99.88	0.08	0.00	0.00	0.00
n_{M}	99.98	0.00	0.00	0.00	0.00
n_{M}	99.99	0.00	0.00	0.00	0.00
n_{Pb}	0.00	0.00	0.00	0.00	0.00
$\sigma^*_{M\text{-}Pa}$	43.04	26.77	0.00	0.00	0.00
$\sigma^*_{M\text{-}C}$	40.88	20.57	9.96	28.59	0.00
$\sigma^*_{M\text{-}H}$	30.15	11.64	0.00	0.00	58.08

Table A8.5. Continued.

	P_a		P_b		O		Rest
	3*s*	3*s*	3*s*	3*p*	2*s*	2*p*	
Separated System							
N-phenylbenzamide							
n_O	-	-	-	-	58.13	41.82	0.05
$\sigma_{C\text{-}H}$	-	-	-	-	0.00	0.00	0.06
$\sigma_{C\text{-}H^*}$	-	-	-	-	0.00	0.00	0.07
Metal Complex							
$\sigma_{M\text{-}Pa}$	20.55	51.43	0.00	0.00	-	-	0.33
$\sigma_{M\text{-}Pb}$	0.00	0.00	20.53	51.41	-	-	0.34
n_M	0.00	0.00	0.00	0.00	-	-	0.03
n_M	0.00	0.00	0.00	0.00	-	-	0.01
n_M	0.00	0.00	0.00	0.00	-	-	0.17
n_M	0.00	0.00	0.00	0.00	-	-	0.01
$\sigma^*_{M\text{-}Pb}$	0.00	0.00	7.95	19.89	-	-	0.53
$\sigma^*_{M\text{-}Pa}$	7.94	19.87	0.00	0.00	-	-	0.53
Reactant							
$\sigma_{C\text{-}H}$	0.00	0.00	0.00	0.00	0.00	0.00	0.06
n_O	0.00	0.00	0.00	0.00	16.38	83.55	0.07
$\sigma_{M\text{-}Pa}$	23.41	51.05	0.00	0.00	0.00	0.00	0.14
$\sigma_{M\text{-}Pb}$	0.00	0.00	22.83	51.04	0.00	0.00	0.13
n_M	0.00	0.00	0.00	0.00	0.00	0.00	0.04
n_M	0.00	0.00	0.00	0.00	0.00	0.00	0.05
n_M	0.00	0.00	0.00	0.00	0.00	0.00	0.01
n_M	0.00	0.00	0.00	0.00	0.00	0.00	0.01
$\sigma^*_{M\text{-}Pb}$	0.00	0.00	8.03	17.96	0.00	0.00	0.10
$\sigma^*_{M\text{-}Pa}$	7.99	17.41	0.00	0.00	0.00	0.00	0.13
$\sigma^*_{C\text{-}H}$	0.00	0.00	0.00	0.00	0.00	0.00	0.06
Product							
n_O	0.00	0.00	0.00	0.00	16.58	83.35	0.07
$\sigma_{M\text{-}Pa}$	20.91	48.93	0.00	0.00	0.00	0.00	0.19
$\sigma_{M\text{-}C}$	0.00	0.00	0.00	0.00	0.00	0.00	0.00
$\sigma_{M\text{-}H}$	0.00	0.00	0.00	0.00	0.00	0.00	0.13
n_M	0.00	0.00	0.00	0.00	0.00	0.00	0.04
n_M	0.00	0.00	0.00	0.00	0.00	0.00	0.02
n_M	0.00	0.00	0.00	0.00	0.00	0.00	0.01
n_{Pb}	0.00	0.00	48.18	51.80	0.00	0.00	0.02
$\sigma^*_{M\text{-}Pa}$	8.98	21.01	0.00	0.00	0.00	0.00	0.20
$\sigma^*_{M\text{-}C}$	0.00	0.00	0.00	0.00	0.00	0.00	0.00
$\sigma^*_{M\text{-}H}$	0.00	0.00	0.00	0.00	0.00	0.00	0.13

Table A8.6. NBO population analysis (%) in the valence region of the Rh complexes with SEGPHOS ligand in the C-H activation at the *ortho* position of amino group calculated by the relativistic treatments.

	Rh		C		H
	4*d*	5*s*	2*s*	2*p*	1*s*
Separated System					
N-phenylbenzamide					
n_O	0.00	0.00	0.00	0.00	0.00
$\sigma_{C\text{-}H}$	0.00	0.00	19.54	44.81	35.59
$\sigma_{C\text{-}H^*}$	0.00	0.00	10.81	24.78	64.34
Metal Complex					
$\sigma_{M\text{-}Pa}$	14.99	14.10	-	-	-
$\sigma_{M\text{-}Pb}$	14.78	14.11	-	-	-
n_M	99.89	0.11	-	-	-
n_M	99.95	0.05	-	-	-
n_M	100.00	0.00	-	-	-
n_M	97.48	2.52	-	-	-
$\sigma^*_{M\text{-}Pb}$	36.37	34.73	-	-	-
$\sigma^*_{M\text{-}Pa}$	36.53	34.37	-	-	-
Reactant					
$\sigma_{C\text{-}H}$	0.00	0.00	19.35	44.93	35.66
n_O	0.00	0.00	0.00	0.00	0.00
$\sigma_{M\text{-}Pa}$	14.21	12.13	0.00	0.00	0.00
$\sigma_{M\text{-}Pb}$	13.19	14.16	0.00	0.00	0.00
n_M	99.93	0.06	0.00	0.00	0.00
n_M	99.96	0.04	0.00	0.00	0.00
n_M	99.89	0.11	0.00	0.00	0.00
n_M	98.13	1.87	0.00	0.00	0.00
$\sigma^*_{M\text{-}Pb}$	35.02	37.61	0.00	0.00	0.00
$\sigma^*_{M\text{-}Pa}$	39.72	33.92	0.00	0.00	0.00
$\sigma^*_{C\text{-}H}$	0.00	0.00	10.74	24.92	64.28
Product					
n_O	0.00	0.00	0.00	0.00	0.00
$\sigma_{M\text{-}Pa}$	19.29	11.90	0.00	0.00	0.00
$\sigma_{M\text{-}C}$	25.97	13.24	16.21	44.56	0.00
$\sigma_{M\text{-}H}$	42.28	16.17	0.00	0.00	41.46
n_M	99.93	0.07	0.00	0.00	0.00
n_M	99.97	0.03	0.00	0.00	0.00
n_M	99.99	0.00	0.00	0.00	0.00
n_{Pb}	0.00	0.00	0.00	0.00	0.00
$\sigma^*_{M\text{-}Pa}$	42.54	26.24	0.00	0.00	0.00
$\sigma^*_{M\text{-}C}$	40.24	20.53	10.46	28.76	0.00
$\sigma^*_{M\text{-}H}$	30.03	11.49	0.00	0.00	58.37

Table A8.6. Continued.

	P_a		P_b		O		Rest
	3*s*	3*p*	3*s*	3*p*	2*s*	2*p*	
Separated System							
N-phenylbenzamide							
n_O	-	-	-	-	58.13	41.82	0.05
$\sigma_{C\text{-}H}$	-	-	-	-	0.00	0.00	0.06
$\sigma_{C\text{-}H^*}$	-	-	-	-	0.00	0.00	0.07
Metal Complex							
$\sigma_{M\text{-}Pa}$	20.67	50.06	0.00	0.00	-	-	0.18
$\sigma_{M\text{-}Pb}$	0.00	0.00	20.78	50.15	-	-	0.17
n_M	0.00	0.00	0.00	0.00	-	-	0.00
n_M	0.00	0.00	0.00	0.00	-	-	0.00
n_M	0.00	0.00	0.00	0.00	-	-	0.00
n_M	0.00	0.00	0.00	0.00	-	-	0.00
$\sigma^*_{M\text{-}Pb}$	0.00	0.00	8.45	20.38	-	-	0.08
$\sigma^*_{M\text{-}Pa}$	8.48	20.54	0.00	0.00	-	-	0.08
Reactant							
$\sigma_{C\text{-}H}$	0.00	0.00	0.00	0.00	0.00	0.00	0.06
n_O	0.00	0.00	0.00	0.00	19.54	80.40	0.06
$\sigma_{M\text{-}Pa}$	24.24	49.31	0.00	0.00	0.00	0.00	0.11
$\sigma_{M\text{-}Pb}$	0.00	0.00	23.20	49.33	0.00	0.00	0.11
n_M	0.00	0.00	0.00	0.00	0.00	0.00	0.01
n_M	0.00	0.00	0.00	0.00	0.00	0.00	0.00
n_M	0.00	0.00	0.00	0.00	0.00	0.00	0.00
n_M	0.00	0.00	0.00	0.00	0.00	0.00	0.00
$\sigma^*_{M\text{-}Pb}$	0.00	0.00	8.74	18.58	0.00	0.00	0.06
$\sigma^*_{M\text{-}Pa}$	8.67	17.64	0.00	0.00	0.00	0.00	0.05
$\sigma^*_{C\text{-}H}$	0.00	0.00	0.00	0.00	0.00	0.00	0.06
Product							
n_O	0.00	0.00	0.00	0.00	18.10	81.83	0.07
$\sigma_{M\text{-}Pa}$	21.22	47.44	0.00	0.00	0.00	0.00	0.15
$\sigma_{M\text{-}C}$	0.00	0.00	0.00	0.00	0.00	0.00	0.01
$\sigma_{M\text{-}H}$	0.00	0.00	0.00	0.00	0.00	0.00	0.09
n_M	0.00	0.00	0.00	0.00	0.00	0.00	0.00
n_M	0.00	0.00	0.00	0.00	0.00	0.00	0.00
n_M	0.00	0.00	0.00	0.00	0.00	0.00	0.01
n_{Pb}	0.00	0.00	14.09	85.86	0.00	0.00	0.05
$\sigma^*_{M\text{-}Pa}$	9.62	21.52	0.00	0.00	0.00	0.00	0.08
$\sigma^*_{M\text{-}C}$	0.00	0.00	0.00	0.00	0.00	0.00	0.02
$\sigma^*_{M\text{-}H}$	0.00	0.00	0.00	0.00	0.00	0.00	0.11

Table A8.7. NBO population analysis (%) in the valence region of the Rh complexes with SEGPHOS ligand in the C-H activation at the *ortho* position of amino group calculated by the nonrelativistic treatments.

	Rh		C		H
	4*d*	5*s*	2*s*	2*p*	1*s*
Separated System					
N-phenylbenzamide					
n_O	0.00	0.00	0.00	0.00	0.00
$\sigma_{C\text{-}H}$	0.00	0.00	19.54	44.81	35.59
$\sigma_{C\text{-}H^*}$	0.00	0.00	10.81	24.78	64.34
Metal Complex					
$\sigma_{M\text{-}Pa}$	13.88	13.16	-	-	-
$\sigma_{M\text{-}Pb}$	13.40	13.13	-	-	-
n_M	99.89	0.08	-	-	-
n_M	99.96	0.03	-	-	-
n_M	99.79	0.00	-	-	-
n_M	98.23	1.75	-	-	-
$\sigma^*_{M\text{-}Pb}$	37.03	36.26	-	-	-
$\sigma^*_{M\text{-}Pa}$	37.37	35.42	-	-	-
Reactant					
$\sigma_{C\text{-}H}$	0.00	0.00	19.23	44.87	35.85
n_O	0.00	0.00	0.00	0.00	0.00
$\sigma_{M\text{-}Pa}$	13.42	11.57	0.00	0.00	0.00
$\sigma_{M\text{-}Pb}$	12.15	13.19	0.00	0.00	0.00
n_M	99.92	0.05	0.00	0.00	0.00
n_M	99.91	0.02	0.00	0.00	0.00
n_M	99.90	0.09	0.00	0.00	0.00
n_M	98.52	1.47	0.00	0.00	0.00
$\sigma^*_{M\text{-}Pb}$	35.79	38.83	0.00	0.00	0.00
$\sigma^*_{M\text{-}Pa}$	40.26	34.70	0.00	0.00	0.00
$\sigma^*_{C\text{-}H}$	0.00	0.00	10.76	25.09	64.09
Product					
n_O	0.00	0.00	0.00	0.00	0.00
$\sigma_{M\text{-}Pa}$	18.55	11.43	0.00	0.00	0.00
$\sigma_{M\text{-}C}$	13.19	26.41	15.58	44.81	0.00
$\sigma_{M\text{-}H}$	42.01	16.52	0.00	0.00	41.40
n_M	99.90	0.05	0.00	0.00	0.00
n_M	99.96	0.02	0.00	0.00	0.00
n_M	99.99	0.00	0.00	0.00	0.00
n_{Pb}	0.00	0.00	0.00	0.00	0.00
$\sigma^*_{M\text{-}Pa}$	43.22	26.64	0.00	0.00	0.00
$\sigma^*_{M\text{-}C}$	20.12	40.27	10.22	29.39	0.00
$\sigma^*_{M\text{-}H}$	29.76	11.70	0.00	0.00	58.46

Table A8.7. Continued.

	P_a		P_b		O		Rest
	3*s*	3*s*	3*s*	3*p*	2*s*	2*p*	
Separated System							
N-phenylbenzamide							
n_O	-	-	-	-	58.13	41.82	0.05
$\sigma_{C\text{-}H}$	-	-	-	-	0.00	0.00	0.06
$\sigma_{C\text{-}H^*}$	-	-	-	-	0.00	0.00	0.07
Metal Complex							
$\sigma_{M\text{-}Pa}$	21.05	51.72	0.00	0.00	-	-	0.19
$\sigma_{M\text{-}Pb}$	0.00	0.00	21.35	51.93	-	-	0.19
n_M	0.00	0.00	0.00	0.00	-	-	0.03
n_M	0.00	0.00	0.00	0.00	-	-	0.01
n_M	0.00	0.00	0.00	0.00	-	-	0.21
n_M	0.00	0.00	0.00	0.00	-	-	0.02
$\sigma^*_{M\text{-}Pb}$	0.00	0.00	7.73	18.80	-	-	0.18
$\sigma^*_{M\text{-}Pa}$	7.82	19.21	0.00	0.00	-	-	0.18
Reactant							
$\sigma_{C\text{-}H}$	0.00	0.00	0.00	0.00	0.00	0.00	0.05
n_O	0.00	0.00	0.00	0.00	18.62	81.32	0.06
$\sigma_{M\text{-}Pa}$	24.11	50.80	0.00	0.00	0.00	0.00	0.11
$\sigma_{M\text{-}Pb}$	0.00	0.00	23.59	50.97	0.00	0.00	0.10
n_M	0.00	0.00	0.00	0.00	0.00	0.00	0.03
n_M	0.00	0.00	0.00	0.00	0.00	0.00	0.07
n_M	0.00	0.00	0.00	0.00	0.00	0.00	0.01
n_M	0.00	0.00	0.00	0.00	0.00	0.00	0.01
$\sigma^*_{M\text{-}Pb}$	0.00	0.00	8.01	17.31	0.00	0.00	0.06
$\sigma^*_{M\text{-}Pa}$	8.04	16.93	0.00	0.00	0.00	0.00	0.08
$\sigma^*_{C\text{-}H}$	0.00	0.00	0.00	0.00	0.00	0.00	0.06
Product							
n_O	0.00	0.00	0.00	0.00	16.88	83.05	0.07
$\sigma_{M\text{-}Pa}$	21.18	48.67	0.00	0.00	0.00	0.00	0.17
$\sigma_{M\text{-}C}$	0.00	0.00	0.00	0.00	0.00	0.00	0.00
$\sigma_{M\text{-}H}$	0.00	0.00	0.00	0.00	0.00	0.00	0.06
n_M	0.00	0.00	0.00	0.00	0.00	0.00	0.05
n_M	0.00	0.00	0.00	0.00	0.00	0.00	0.02
n_M	0.00	0.00	0.00	0.00	0.00	0.00	0.01
n_{Pb}	0.00	0.00	47.60	52.39	0.00	0.00	0.01
$\sigma^*_{M\text{-}Pa}$	9.09	20.89	0.00	0.00	0.00	0.00	0.16
$\sigma^*_{M\text{-}C}$	0.00	0.00	0.00	0.00	0.00	0.00	0.01
$\sigma^*_{M\text{-}H}$	0.00	0.00	0.00	0.00	0.00	0.00	0.09

Chapter 9 General conclusion

In this thesis, the author developed theories and computational programs for 2c relativistic quantum chemistry in terms of the PCC of two-electron and density operators. The application to the analysis of the C–H activation was also explained. This Chapter summarizes the thesis and presents the perspectives of this research field.

In Chapters 3 and 4, the author addressed the acceleration of computation of TEIs, which is the bottleneck of relativistic calculation. CD and LUD for TEI-matrices were formulated and implemented in Chapter 3. The proposed algorithm reduced the number of calculations within arbitrary accuracy. The reduction of computational costs was particularly large in heavy-element systems where relativistic effects are essential, which confirmed the utility of this matrix decomposition technique. Chapter 4 proposed the efficient algorithm of LUT based on the element-loop scheme. The proposed algorithm accelerated the unitary transformation of TEIs; combination with the database of one-center TEIs realized the constant computational costs for the unitary transformation regardless of the system size. Applications to heavy-element molecules, such as Au clusters and Pt complexes, showed the validity of the algorithm assisted by the database.

Chapters 5 and 6 provided approaches to topics related to DFT. Chapter 5 introduced the PCC of two-electron and density operators to the LC-DFT. The formulation and implementation were proposed based on the IOTC transformation with and without the LUT scheme. The considerations of both PCC for two-electron and density operators and LC for exchange functionals were important for the calculations of heavy-element properties. Chapter 6 discussed the relationship between PCEs and delocalization error, which is defined as the deviation from the exact behavior of DFT energy. The functionals with a small ratio of HFx did not satisfy the linearity condition, the constant energy with

respect to the FON, and gave large delocalization error. PCC of two-electron and density operators had remarkable effects on delocalization error in core orbitals of higher-row elements, which revealed the importance of PCC of arbitrary operators.

Chapter 7 explained the details of the publishment of PCC methods to the GAMESS program, which is one of the popular quantum chemical program packages. The author made the PCC methods for two-electron and density operators available based on the spin-free IOTC Hamiltonian with and without the LUT scheme. The PCC methods were connected to several functionalities in GAMESS, such as correlation methods and linear-scaling techniques. Combination of the PCC with the DC method enabled highly accurate large-scale relativistic calculations.

In Chapter 8, the author explored the reactivity of cationic Ir and Rh catalysts in the C–H activation of *N*-phenylbenzamide. Comparing relativistic and nonrelativistic calculations clarified the origin of the high catalytic activity of Ir complexes. The relativistic effects on orbitals of Ir causes the stabilization of the product of the Ir–H and Ir–C bonds leading to the low reaction barrier of TSs. The relativistic effects on Rh catalysts indicated the similar tendency, but the magnitude was small. Consequently, the relativistic effects brought about the differences in reactivity depending on the metal species.

The study in this thesis enhances the availability and applicability of relativistic quantum chemistry. The PCC methods developed in this thesis realize the accurate 2c calculations with the similar computational costs to the nonrelativistic theory. The public version of GAMESS program with the PCC methods was released in July 2022, which allows any researcher to use such accurate and efficient relativistic methods. The progress of this research field, including this thesis and previous work, completed the foundation for utilizing the 2c Hamiltonian. Solving the Dirac equation based on the 2c theory will be more common instead of the Schrödinger equation. In terms of chemical properties, relativistic effects on transition metals were revealed to play an important role in catalytic

reactions. The viewpoint of relativistic effects will help to elucidate the reaction mechanisms of various types of transition metal catalysts. From the examination of orbital energies and the linearity condition, PCC, the subject of this thesis, was clarified to be essential particularly in inner-shell orbitals. The proposed methods will be useful to capture properties involving core electrons, which requires all electron calculations. Furthermore, the linearity condition is one measure of evaluating the performance of exchange correlation functional. The relationship between PCE and the linearity condition will be useful to the development of relativistic exchange-correlation functional, which remains a challenge of the quantum chemistry. Although this thesis provided only the spin-free treatment, extension to the spin-dependent framework can be performed straightforwardly based on program packages that deal with complex variables. The author believes that the research presented in this thesis will help both theoretical and experimental researchers and contribute to the further development of relativistic chemistry.

Acknowledgement

The research of this thesis was conducted under the supervision of Professor Dr. Hiromi Nakai, Waseda University. Prof. Nakai enthusiastically guided the author in setting research goals, attitudes as a researcher, and how to write academic papers. Prof. Nakai also gave the author a lot of opportunities to present her research at international and domestic academic conferences and to participate in joint research both inside and outside the University. The author would like to express the gratitude.

The author acknowledges Professor Dr. Yukio Furukawa, Professor Dr. Kohei Imura, Associate Professor Dr. Junji Seino, and Associate Professor Dr. Aditya Wibawa Sakti, Waseda University, for their valuable comments and careful guidance as referees. The author also grateful to Assoc. Prof. Seino for his detailed guidance on relativistic quantum chemistry, especially as a co-researcher on the research in Chapters 4 and 7.

The author would like to thank many people for their cooperation and support in advancing her thesis. The research in Chapter 8 started with a topic presented by Professor Dr. Takanori Shibata, Waseda University, when the author was an undergraduate student. In this research, Associate Professor Dr. Yasuhiro Ikabata, now at Toyohashi University of Technology, provided the author attentive guidance on everything to start the research project such as calculation with Gaussian program and preparation of documents. The author also appreciates members of Shibata group: Assistant Professor Dr. Hideaki Takano, now at Nagoya University, Mr. Hisaki Kurita, and Mr. King Hung Nigel Tang.

The author would also like to thank all the current and former members of Nakai laboratory. Although she cannot mention their names individually, she sincerely appreciates their time and consideration.

The author is grateful to JST SPRING (Grant Number JPMJSP2128) for the financial support from the autumn of 2021. Thanks to this support, the author was able to work on

research with few financial worries.

Finally, the author would like to express sincere gratitude to her mother, father, younger brother, and relatives for giving her to the opportunity to study at the graduate school.

List of achievements

Academic papers

○ 1. “Evaluation of picture change effects on fractional occupation number states in noble gas atoms”
Chinami Takashima and Hiromi Nakai
Theoretical Chemistry Accounts, *in press.*

○ 2. “Range Separation Method for Density Functional Theory Based on Two-electron Infinite-order Two-component Hamiltonian”
Chinami Takashima and Hiromi Nakai
Journal of Chemical Theory and Computation, *in press.*

○ 3. “Matrix-decomposed two-electron integrals in the infinite-order two-component Hamiltonian”
Chinami Takashima and Hiromi Nakai
Chem. Phys. Lett. **828**, 140714-1-9 (2023). (Editor’s Choice)

○ 4. “Experimental and Theoretical Evidence for Relativistic Catalytic Activity in C–H Activation of *N*-Phenylbenzamide Using a Cationic Iridium Complex”
Chinami Takashima, Hisaki Kurita, Hideaki Takano, Yasuhiro Ikabata, Takanori Shibata, and Hiromi Nakai
J. Phys. Chem. A, **126** (42), 7627-7638 (2022). (Supplementary Journal Cover)

○ 5. “Database-assisted local unitary transformation method for two-electron integrals in two-component relativistic calculations”
Chinami Takashima, Junji Seino, and Hiromi Nakai
Chem. Phys. Lett. **777**, 138691-1-8 (2021). (Editor’s Choice)

○ 6. “Implementation of Picture Change Corrected Density Functional Theory Based on Infinite-Order Two-Component Method to GAMESS Program”
Chinami Takashima, Junji Seino, and Hiromi Nakai
J. Comput. Chem. Jpn. **19** (4), 128-130 (2020).

Reviews

1. “カチオン性イリジウム触媒を用いた均一系触媒反応における相対論効果”
   (Relativistic Effect on Homogeneous Catalytic Reaction by Cationic Iridium Catalysts)
   髙島千波, 五十幡康弘, 栗田久樹, 高野秀明, 柴田高範, 中井浩巳
   J. Comput. Chem. Jpn. **18** (3), 136-138 (2019).

Lectures

International conference/symposia (Poster presentation)

1. “Long-range corrected density functional theory calculation with the infinite-order two-component Hamiltonian”
   ○Chinami Takashima and Hiromi Nakai
   Theory and Applications of Computational Chemistry (TACC2023), Hokkaido Japan, September 2023.

2. “Implementation of matrix-decomposed two-electron integrals in the infinite-order two-component method”
   ○Chinami Takashima and Hiromi Nakai
   The 6th China-Japan-Korea tripartite Workshop on Theoretical and Computational Chemistry (CJK-WTCC-VI), Suwon Korea, June 2023.

3. “Implementation of picture-change corrected density functional theory based on infinite-order two-component relativistic method into GAMESS program”
   ○Chinami Takashima, Junji Seino, and Hiromi Nakai
   The 10th edition of the conference of the Asia Pacific Association of Theoretical and Computational Chemistry (APATCC-10), Quy Nhon Vietnam, February 2023.

4. “Acceleration of local unitary transformation method by utilizing database of atomic two-electron integrals”
   ○Chinami Takashima, Junji Seino, and Hiromi Nakai
   The 5th China-Japan-Korea tripartite Workshop on Theoretical and Computational Chemistry (CJK-WTCC-V), Aichi Japan (Online), January 2022.

Domestic conference/symposia (Oral presentation)

1. “無限次 2 成分法に基づく長距離補正密度汎関数理論の開発”
   ○髙島千波, 中井浩巳
   第 17 回分子科学討論会, 大阪, 2023 年 9 月.

2. “無限次 2 成分法に基づく Picture Change 補正密度汎関数理論の GAMESS への実装”
   ○髙島千波, 清野淳司, 中井浩巳
   日本コンピュータ化学会 2020 年秋季年会, 鹿児島 (オンライン), 2020 年 11 月.

3. “イリジウム触媒を用いたベンズアニリド類の C-H 結合活性化反応における相対論効果の解析”
   ○髙島千波, 五十幡康弘, 栗田久樹, 高野秀明, 柴田高範, 中井浩巳
   日本化学会第 99 春季年会, 兵庫, 2019 年 3 月.

Domestic conference/symposia (Poster presentation)

1. “無限次 2 成分法における LU 分解を用いた 2 電子積分の実装”
   ○髙島千波, 中井浩巳
   第 24 回理論化学討論会, 石川 (オンライン), 2022 年 5 月.

2. “2 成分相対論における Picture Change 補正法の GAMESS への実装”
   ○髙島千波, 清野淳司, 中井浩巳
   第 10 回 CSJ 化学フェスタ 2020, オンライン, 2020 年 10 月.

3. “カチオン性イリジウム触媒を用いた均一系触媒反応における相対論効果”
   ○髙島千波, 五十幡康弘, 栗田久樹, 高野秀明, 柴田高範, 中井浩巳
   日本コンピュータ化学会 2019 年春季年会, 東京, 2019 年 6 月.

4. “カチオン性金属触媒を用いた C-H 活性化反応に対する理論的研究”
   ○髙島千波, 五十幡康弘, 中井浩巳
   第 8 回量子化学スクール, 愛知, 2018 年 12 月.

Others

(Academic papers)

1. “Photoexcited charge manipulation in conjugated polymers bearing a Ru(II) complex catalyst for visible-light CO_2 reduction”
   Akinobu Nakada, Ryuichi Miyakawa, Ren Itagaki, Kosaku Kato, Chinami Takashima, Akinori Saeki, Akira Yamakata, Ryu Abe, Hiromi Nakai, and Ho-Chol Chang
   J. Mater. Chem. A, **10** (37), 19821-19828 (2022).

2. “Dynamic hetero-metallic bondings visualized by sequential atom imaging”
   Minori Inazu, Yuji Akada, Takane Imaoka, Yoko Hayashi, Chinami Takashima, Hiromi Nakai, and Kimihisa Yamamoto
   Nat. Commun. **13**, 2968 (2022).

(Lectures, international conference/symposia, poster presentation)

3. “Solving unstable behavior of divide-and-conquer self-consistent field calculations using level shift technique based on pair-excited perturbative selection”
   ○Rei Oshima, Chinami Takashima, Kazuki Tajima, Takeshi Yoshikawa, and Hiromi Nakai
   Theory and Applications of Computational Chemistry (TACC2023), Hokkaido Japan, September 2023.

(Lectures, domestic conference/symposia, oral presentation)

4. “遷移金属触媒を用いた 8-メチルキノリンの選択的 C-H 活性化の理論的研究”
   ○星野秀杜, 髙島千波, 堀尾優斗, 柴田高範, 中井浩巳
   日本コンピュータ化学会 2023 年秋季年会, 香川, 2023 年 11 月.

5. “カチオン性イリジウム触媒を用いたβ-置換α,β-不飽和エステルに対するエナンチオ選択的不斉共役付加反応に関する理論的研究”
   ○石丸優樹, 髙島千波, 柴田高範, 中井浩巳
   日本化学会第 103 春季年会, 千葉, 2023 年 3 月.

6. “イリジウム触媒によるベンズアニリド類の位置選択的かつエナンチオ選択的 C-H 共役付加 ならびに反応機構解析”
   ○栗田久樹, 髙島千波, 五十幡康弘, 高野秀明, Kyalo Stephen Kanyiva, 中井浩巳,柴田高範
   日本化学会第 99 春季年会, 兵庫, 2019 年 3 月.

(Lectures, domestic conference/symposia, poster presentation)

7. “汎用原子レベルシミュレータ Matlantis のフラグメント分子軌道法への適用”
   ○大島玲生, 髙島千波, 藤波美起登, 小野純一, 中嶋裕也, 中井浩巳
   日本コンピュータ化学会 2023 年秋季年会, 香川, 2023 年 11 月.

8. “カチオン性 Ir/Rh 触媒を用いた 8-methylquinoline に対する選択的 C–H 活性化における反応機構の解析”
   ○星野秀杜, 髙島千波, 堀尾優斗, 柴田高範, 中井浩巳
   第 13 回 CSJ 化学フェスタ 2023, 東京, 2023 年 10 月.

9. “対励起型摂動選択による軌道のレベルシフトを適用した分割統治法の開発”
   ○大島玲生, 髙島千波, 田嶋一輝, 吉川武司, 中井 浩巳
   第 17 回分子科学討論会, 大阪, 2023 年 9 月.

10. “汎用原子レベルシミュレータ Matlantis と波動関数理論および密度汎関数理論による分子物性の比較検証”
    ○大島玲生, 髙島千波, 藤波美起登, 中嶋裕也, 中井浩巳
    日本コンピュータ化学会 2022 秋季年会, 長野, 2022 年 11 月.

11. “ジェミナル型固有関数による Resolution of Identity 近似”
    ○大島玲生, 髙島千波, 中井浩巳
    日本コンピュータ化学会 2022 春季年会, 東京, 2022 年 6 月.

12. “高効率電子相関計算のための 2 電子相互作用に対する Hess 法の拡張”
    ○大島玲生, 髙島千波, 中井浩巳
    第 24 回理論化学討論会, 石川 (オンライン), 2022 年 5 月.

(Awards)

13. Poster Prize Award from HPC Systems Inc.
    Theory and Applications of Computational Chemistry (TACC2023), Hokkaido Japan, September 2023.

14. Physical Chemistry Chemical Physics (PCCP) Poster Award,
    the 10th edition of the conference of the Asia Pacific Association of Theoretical and Computational Chemistry (APATCC-10), February 2023.

15. 2020 年度関根吉郎賞, 早稲田大学稲化会, 2021 年 3 月.